Plasma Physics Reports, Vol. 29, No. 2, 2003, pp. 105–111. Translated from Fizika Plazmy, Vol. 29, No. 2, 2003, pp. 124–130.

TOKAMAKS

Equilibrium of Rotating and Nonrotating Plasmas in Tokamaks

V. D. Pustovitov

Russian Research Centre Kurchatov Institute, pl. Kurchatova 1, Moscow, 123182 Russia

Received March 4, 2002; in final form, June 20, 2002

Abstract—The equilibrium of a tokamak plasma with a toroidal flow is discussed. It is shown that the centrifugal force of this rotation always reduces the equilibrium beta limit. An opposite view is analyzed, and the arguments supporting this view are considered. It is shown that, although the equilibrium conditions may be locally improved through a special choice of the profile of the plasma rotation velocity, toroidal rotation, on the whole, has a negative effect on the plasma equilibrium. However, under typical tokamak conditions, a decrease in the equilibrium β limit due to plasma rotation is insignificant and, consequently, the effect of the rotation of a hot plasma on its equilibrium can be neglected. © *2003 MAIK "Nauka/Interperiodica".*

1. INTRODUCTION

The development of the theory of plasma equilibrium in tokamaks was motivated by the necessity of solving the practical problem of the radial displacement of the plasma column in the first tokamak experiments [1, 2]. During an uncontrolled outward motion along the major radius, the plasma came into contact with the limiter; as a result, the plasma column was partially cut off, contaminated with impurities, and cooled and the discharge current decreased [1]. The theory developed in [2–4] gave answers to practical questions, and, by exactly following its recommendations, it was possible to achieve the recognized progress in tokamak research in the 1960s [5–7]. To be specific, it is sufficient to mention the formula derived by V.D. Shafranov for the transverse field required to keep the plasma column at a given position [2, 3].

By the 1970s, the main problems related to equilibrium of a circular plasma in tokamaks had already been solved; therefore, the development of the theory of equilibrium of an axisymmetric plasma became, to a considerable extent, academic and, sometimes, not directly related to experiment. By that time, it had also become clear that, in order to progress toward thermonuclear temperatures, it was necessary to employ the injection of fast neutral beams as a means of additional plasma heating, which, however, could set a plasma into rotation. This stimulated the first papers analyzing the possible effect of rotation on the plasma equilibrium in tokamaks [8, 9].

These studies were ahead of their time, because there were no experimental results that would require the account of plasma rotation in the theory of plasma equilibrium. Afterward, no experimental results (similar to those described in [1]) that would require a substantial revision of the "canonical" equilibrium theory have appeared. However, with the development of injection techniques in the early 1980s, the plasma rotation velocities during the unbalanced injection in tokamaks achieved a level of 100–150 km/s [10–12]; hence, it was natural for theoreticians to turn again to the problem of the equilibrium of a rotating plasma.

In the 1980s, this problem was investigated both analytically and numerically [13–28]. The results of these studies were briefly summarized in the well-known review [29]. It was found that, under typical tokamak conditions, the rotation of the plasma does not lead to any significant macroscopic effect. That is why the equilibrium theory of a toroidal plasma continued to be developed as a theory of static equilibrium [29–34].

In a recent paper by Ilgisonis and Pozdnyakov [35], however, it was stated that the toroidal rotation of a tokamak plasma may produce a strong, "pronounced enough" effect; e.g., it may increase the equilibrium β limit (the ratio of the plasma pressure to the magnetic field pressure) by a factor of 1.6 to 2.5 in comparison with that in static equilibrium. Nothing of this kind was reported in [8–29]. Note that Ilgisonis and Pozdnyakov [35] considered the same plasma equilibrium and analyzed it by the well-known theoretical model described in [8, 9]. It was stated in the main conclusions of [35] that a substantial effect can be achieved "by an appropriate choice of the toroidal velocity profile, no matter how high the absolute value of the rotation velocity."

The conclusions of [35], confirmed in a more recent paper by Ilgisonis [36], must certainly attract the attention of experts in this field, because, being unusual and unexpected, they touch on a very important problem and predict a significant positive effect. The objective of the present paper is to analyze the results and conclusions obtained in [35, 36]. A stationary plasma rotation will only be discussed below.

2. GLOBAL FORCE BALANCE AND PLASMA ROTATION

The general equations for the equilibrium of a magnetically confined toroidal plasma with a steady flow

1063-780X/03/2902-0105$24.00 © 2003 MAIK "Nauka/Interperiodica"

are described in details in many papers [8, 13, 14, 16–20, 23, 25, 26, 37, 38], including the well-known reviews [29, 33]. Here, we write out only those that will be needed for our analysis.

We start with the force balance equation

$$\rho(\mathbf{v}\cdot\nabla)\mathbf{v} = -\nabla p + \mathbf{j}\times\mathbf{B}, \quad (1)$$

where ρ is the plasma density, $\mathbf{v}$ is the plasma velocity (usually called the plasma flow velocity), p is the plasma pressure, $\mathbf{B}$ is the magnetic field, and $\mathbf{j} = \nabla\times\mathbf{B}$ is the current density. It is assumed that the plasma flow is stationary; consequently, the term $\rho\partial\mathbf{v}/\partial t$ on the left-hand side of Eq. (1) is omitted.

Ilgisonis and Pozdnyakov [35] considered an axisymmetric plasma with purely toroidal rotation:

$$\mathbf{v} = v_t(r, z)\mathbf{e}_\zeta. \quad (2)$$

In this case, we have

$$\rho(\mathbf{v}\cdot\nabla)\mathbf{v} = -\frac{\rho v_t^2}{r}\mathbf{e}_r, \quad (3)$$

and thus, Eq. (1) becomes

$$\frac{\rho v_t^2}{r}\mathbf{e}_r - \nabla p + \mathbf{j}\times\mathbf{B} = 0. \quad (4)$$

Here and below, (r, ζ, z) are conventional cylindrical coordinates with their origin at the symmetry axis, ζ is the toroidal angle, and the unit vectors $\mathbf{e}_r$ and $\mathbf{e}_\zeta$ point in the directions of ∇r and $\nabla\zeta$.

Multiplying Eq. (4) by $\mathbf{e}_r$ and integrating over the entire plasma volume (under the assumption that $p = 0$ at the plasma boundary), we obtain the following integral condition for the plasma equilibrium along the major radius:

$$\int\frac{p + \rho v_t^2}{r}dV + \int\mathbf{e}_r\cdot(\mathbf{j}\times\mathbf{B})dV = 0. \quad (5)$$

Here, the first term describes the force that expands the plasma column in the radial direction. The higher the plasma pressure, the stronger this ballooning force. The plasma pressure can be increased until the electromagnetic forces $\mathbf{j}\times\mathbf{B}$ fail to counterbalance this force and prevent the plasma from leaving a given volume. The maximum possible plasma pressure at which equilibrium condition (5) can still be satisfied is called the equilibrium pressure limit. Condition (5) shows that, generally speaking, the toroidal plasma rotation should *lower* this limit.

This conclusion inevitably follows from simple physical considerations. Let an originally nonrotating plasma be at a given equilibrium position. Let the plasma be set into rotation, the other conditions remaining unchanged. The toroidal rotation gives rise to the centrifugal force, which is described by the first term in Eq. (4). This force will push the plasma column outward. In order to return the plasma column to its initial position, it is necessary to *decrease* the plasma pressure.

These considerations contradict the conclusion of [35, 36] that the equilibrium beta limit can be *increased* by means of the toroidal plasma rotation. In what follows, this contradiction will be analyzed in more detail. However, before proceeding further, we complete the qualitative analysis by obtaining the estimates that demonstrate the role of plasma rotation in Eqs. (4) and (5).

By definition, we have $p = n_iT_i + n_eT_e$ and $\rho = m_in_i$, which gives

$$\frac{p}{\rho} = v_{Ti}^2\left(1 + \frac{n_eT_e}{n_iT_i}\right), \quad (6)$$

where n_i and T_i are the ion density and ion temperature, n_e and T_e are the electron density and electron temperature, m_i is the mass of an ion, and

$$v_{Ti} \equiv \sqrt{\frac{T_i}{m_i}} \quad (7)$$

is the ion thermal velocity. Consequently, we obtain

$$\frac{\rho v_t^2}{p} < \frac{v_t^2}{v_{Ti}^2}. \quad (8)$$

For a hydrogen plasma, we have

$$v_{Ti} = 979\sqrt{\frac{T_i}{T_0}}\ \text{km/s}, \quad (9)$$

where $T_0 = 10$ keV. This velocity is fairly high. It is clear that, even for a toroidal rotation velocity of about 300 km/s, quantity (8) is small and, thus, the effect of the rotation on the equilibrium of a hot ($T_i > 10$ keV) plasma in a tokamak can be neglected. This can be explained by the fact that the plasma mass in the device is extremely small and, therefore, the centrifugal force is weak. For example, for a hydrogen plasma, we have $\rho = 1.5\times10^{-10}$ g/cm^3 at $n = 9\times10^{13}$ cm^{-3}. By the way, it is for this reason that the gravity force never appears in the theory of plasma equilibrium in magnetic confinement systems.

3. TWO-DIMENSIONAL EQUILIBRIUM EQUATION

As is known, the equilibrium of an axisymmetric plasma rotating in the toroidal direction is described by the equation

$$\nabla\cdot\frac{\nabla\psi}{r^2} = -4\pi^2\frac{\partial p}{\partial\psi} - \frac{FF'(\psi)}{r^2}. \quad (10)$$

Here, the poloidal flux ψ and the poloidal current F are related to the magnetic field by the equation

$$2\pi\mathbf{B} = \nabla\psi\times\nabla\zeta + F\nabla\zeta, \quad (11)$$

and the pressure p is a function of ψ and r such that

$$\frac{\partial p(\psi, r)}{\partial r} = \frac{\rho v_t^2}{r} = \rho r \Omega^2, \quad (12)$$

where the derivative with respect to r is taken at constant ψ and $\Omega = v_t/r$ is the angular rotation frequency. For $v_t = 0$, Eq. (10) becomes the Grad–Shafranov equation with $p = p(\psi)$. Note that, for axisymmetric configurations with stationary plasma rotation, we have $\Omega = \Omega(\psi)$ [13, 15–17, 19–23, 25–29].

The Grad–Shafranov equation was generalized to the case $\mathbf{v} \neq 0$ for the first time by Zehrfeld and Green [8], who took into account not only toroidal rotation but also stationary poloidal rotation. The exact analytic solutions to Eq. (10) were discussed by Maschke and Perrin [13]. In the 1980s, Eq. (10) became widely known due to a series of papers on the equilibrium of plasmas with stationary flows [13, 15, 17, 19–22, 25, 27]. At that time, computer codes for solving Eq. (10) numerically were developed [17, 19–21, 24, 25, 28]. The codes allowed a detailed investigation of the features of the equilibrium of a toroidally rotating plasma by modeling the actual experimental conditions. Equation (10), numerical codes for its solution, and the results obtained are described in a special section in review [29].

No significant effect of the plasma rotation on the plasma equilibrium was revealed in theory or in experiment (the physical reasons for this were outlined in the previous section). Interest in the problem waned and was maintained only due to sparse theoretical papers (see [37–40]). As a result, the studies on this subject that were published in the 1980s were virtually forgotten, which is evidenced by the "rediscovery" of Eq. (10) by Ilgisonis and Pozdnyakov [35].

In [35, 36], Eq. (10) served as a starting point for an analysis of the effects of plasma rotation. A strong effect of the toroidal rotation of a plasma on its equilibrium was attributed to the dependence of p on r at fixed ψ. Essentially, the authors of [35, 36] stated that this dependence allows one to make a configuration weakly sensitive (or even insensitive) to the plasma pressure. To prove this conclusion, they used a consequence of Eq. (10), namely, the equation for the shift of the magnetic surfaces, which is analogous to the equation derived in [8] and thoroughly discussed in [9]. In [35], the dependence of the shift on the plasma pressure was analyzed. In contrast to [35], we proceed further in a more straightforward way by using Eq. (10) itself, rather than its particular consequences obtained under simplifying assumptions.

We are interested in the dependence of the solutions to Eq. (10) on the plasma pressure. Let us transform the right-hand side of Eq. (10) in order to make this dependence more explicit.

It follows from Eqs. (10) and (11) that

$$4\pi^2 \frac{\partial p}{\partial \psi} + \frac{FF'(\psi)}{r^2} = 2\pi \mathbf{j} \cdot \nabla \zeta. \quad (13)$$

Integrating this equality yields

$$\frac{dJ}{dV} = \left\langle \frac{\partial p}{\partial \psi} \right\rangle + \frac{FF'(\psi)}{4\pi^2} \left\langle \frac{1}{r^2} \right\rangle. \quad (14)$$

Here,

$$J = \frac{1}{2\pi} \int_V \mathbf{j} \cdot \nabla \zeta dV \quad (15)$$

is the longitudinal current flowing within the magnetic surface; V is the volume enclosed by this surface; and the angular brackets stand for the canonical averaging over the layer between two nearby magnetic surfaces,

$$\langle X \rangle = \frac{d}{dV} \int_V X dV. \quad (16)$$

Using Eq. (14), we reduce Eq. (10) to the form

$$-\frac{r^2}{4\pi^2} \left\langle \frac{1}{r^2} \right\rangle \nabla \cdot \frac{\nabla \psi}{r^2} = \frac{dJ}{dV} + r^2 \frac{\partial p}{\partial \psi} \left\langle \frac{1}{r^2} \right\rangle - \left\langle \frac{\partial p}{\partial \psi} \right\rangle. \quad (17)$$

Some conclusions about the effect of the toroidal rotation on the plasma equilibrium can be drawn even without solving Eq. (17). For a given profile of the toroidal current, the implicit dependence on the plasma rotation is accounted for by the two terms with the plasma pressure on the right-hand side of Eq. (17). Let us discuss whether such a dependence can be used to diminish the contribution of these terms.

4. CONFIGURATIONS INSENSITIVE TO THE PLASMA PRESSURE

If we were able to diminish the contribution of the pressure terms to Eq. (17) by manipulating the quantity v_t, it would be possible to speak of the positive effect of the plasma rotation on the plasma equilibrium. The right-hand side of Eq. (17) could become independent of pressure if

$$r^2 \frac{\partial p}{\partial \psi} = C(\psi). \quad (18)$$

This condition is not satisfied in a conventional case of a nonrotating plasma, when $p = p(\psi)$. The consequences of this fact are the Shafranov shift and the Pfirsch–Schlüter current, which increase with pressure. Here, we are speaking about the toroidal systems, and it is the toroidicity that does not allow the terms with pressure in Eq. (17) to cancel completely. The degenerate case $p = \text{const}$ is not considered here because we are interested in the pressure profiles that decrease toward the plasma boundary.

In order to analyze condition (18), we use the following expression for p, which explicitly takes into account the stationary toroidal plasma rotation [13, 16, 17, 19, 27–29]:

$$p = \bar{p}(\psi)\exp\frac{M^2 x}{2}. \quad (19)$$

This expression is valid for axisymmetric systems, provided that the plasma temperature is constant on a magnetic surface, $T = T(\psi)$. Here,

$$x \equiv r^2/r_{ax}^2 - 1, \quad (20)$$

r_{ax} is the position of the magnetic axis, and the quantity $M = M(\psi) \equiv \Omega r_{ax}/v_{Ti}$ can be called the Mach number.

For $p \neq$ const, condition (18), which can be rewritten as

$$(x+1)\frac{\partial p(\psi, x)}{\partial \psi} = C_1(\psi), \quad (21)$$

can only be satisfied at the magnetic axis $x = 0$. The larger the distance x from the magnetic axis, the larger the degree to which this condition is violated. The expansion of the left-hand side of condition (21) in powers of x starts from the terms

$$(x+1)\frac{\partial p}{\partial \psi} \simeq \frac{d\bar{p}}{d\psi} + x\frac{d}{d\psi}\left[\bar{p}\left(1 + \frac{M^2}{2}\right)\right], \quad (22)$$

which implies that condition (21) is satisfied to first order in x if

$$\bar{p} = \bar{p}_0\frac{2 + M_0^2}{2 + M^2}, \quad (23)$$

where $\bar{p}_0$ and M_0 are the values of $\bar{p}$ and M at the magnetic axis.

Up to this point, we had only two free functions, $\bar{p}$ and M, that could be used to satisfy condition (18). Now, these functions are related by equality (23), which is the final answer: to first order in x, the terms with pressure on the right-hand side of Eq. (17) are cancelled for this $\bar{p}(\psi)$ profile.

In expression (19), $\bar{p}(\psi)$ is by definition the plasma pressure at the line $r = r_{ax}$. To yield a pressure profile p decreasing toward the plasma edge, the function $M(\psi)$ in Eq. (23) should increase away from the magnetic axis. Even in the extreme case of $M_0 = 0$, the value of p at $M = 1$ is smaller than $\bar{p}_0$ by a factor of only 1/3. It is clear that condition (23) does not enable the pressure $\bar{p}(\psi)$ to vanish at the plasma boundary. Consequently, solution (23) is physically unrealistic. It may be stated that none of the choices of $M(\psi)$ can satisfy condition (18) and eliminate the dependence of the right-hand side of Eq. (17) on the pressure under the natural assumption that the plasma pressure p should decrease to zero at the plasma boundary.

Solution (23) is, in fact, a fairly slight modification of the trivial solution $p =$ const at $M = 0$, which is very far from the actual profiles of p. Expression (23) shows that the plasma rotation might have a strong impact on the plasma equilibrium only for very large and, therefore, physically unacceptable values of M. Profile (23) with a small gradient and a nonzero value at the plasma boundary is far from realistic profiles of the pressure p. That is why it seems hardly conceivable that condition (18) could be satisfied (at least approximately) for typical experimental p profiles. In addition, the toroidal plasma rotation velocity in tokamak experiments is usually maximum at the center of the plasma column [41, 42], whereas condition (23) requires the opposite. This further confirms and strengthens the above qualitative arguments that the toroidal plasma rotation cannot have a strong positive effect on the plasma equilibrium.

5. PLASMA ROTATION AND PLASMA SHIFT

The main effects of the finite plasma pressure in tokamaks is the outward shift of the magnetic surfaces [3, 31]. The effect of the plasma rotation on the shift Δ was first studied by Zehrfeld and Green [8, 9]. In [9], they obtained the formula

$$\Delta' = \Delta_S' - \frac{a}{R}\frac{\overline{\rho v_t^2} - \rho \overline{v_t^2}}{B_\theta^2}. \quad (24)$$

Here, Δ_S' is the velocity-independent component of Δ'; the prime denotes the derivative with respect to the minor radius a of the magnetic surfaces; R is the major radius of the torus; $B_\theta(a) = J/(2\pi a)$ is the magnetic field of the longitudinal current J flowing inside a magnetic surface; and the overhead bar stands for averaging over the transverse cross section,

$$\bar{X} \equiv \frac{2}{a^2}\int_0^a X\rho\, d\rho, \quad (25)$$

where ρ is the running minor radius of the magnetic surfaces. Recall that force balance equation (1) is written in a system of units in which the magnetic field pressure is $\mathbf{B}^2/2$. This corresponds to $\mathbf{B}^2/(8\pi)$ in [3, 31] and to $\mu_0\mathbf{B}^2/2$ in [8, 9].

The quantity Δ_S' was calculated by Shafranov [3, 31]:

$$\Delta_S' = -\frac{a}{R}\left[\frac{l_i}{2} + 2\frac{\bar{p} - p}{B_\theta^2}\right], \quad (26)$$

where $l_i \equiv \overline{B_\theta^2}/B_\theta^2$ is the internal inductance per unit length of the plasma column.

For pressure profiles decreasing toward the plasma edge, the quantity Δ'_S is obviously negative. As can be seen from Eq. (24), the toroidal rotation with a decreasing profile of ρv_t^2 leads to an increase in the quantity $|\Delta'|$ and, accordingly, to a larger shift of the magnetic surfaces. However, the quantity $|\Delta'|$ can be decreased by making ρv_t^2 the increasing function of a to obtain $\overline{\rho v_t^2} < \rho v_t^2$. Both of these conclusions were precisely formulated in [9]. In [35], the latter conclusion about the "positive" effect of the toroidal plasma rotation was presented as an original one, without reference to [9], although the analysis carried out in [35] nearly coincides with that of [9], including the use of an expression equivalent to Eq. (24). A really new assertion of [35] is that the absolute value of the plasma rotation velocity is unimportant for a substantial reduction of $|\Delta'|$. However, according to Eq. (24), this assertion is wrong. This can be seen even without recourse to Eq. (24): the basic equation (4) clearly shows that the effect of the toroidal rotation of a plasma on its equilibrium is determined by the absolute value of the quantity ρv_t^2.

Expression (24) is the result of solving Eq. (10) in the large aspect ratio approximation under the condition that the cross sections of the magnetic surfaces are shifted nested circles. In the previous section, expression (23) was derived for the pressure profile for which, to first order in x, it might be possible to obtain a favorable result: the independence of the solution to equilibrium equation (10) on plasma pressure. Solution (23) is valid for all configurations, regardless of the aspect ratio and the shape of the magnetic surfaces. According to this solution, Zehrfeld and Green's conclusion [9] that ρv_t^2 should increase with distance from the magnetic axis in order to reduce the plasma pressure effect on the solution to the equilibrium equation inside the plasma column remains valid even in the most general case.

At this point, it should be emphasized that the aforesaid is true only for a certain part of the plasma column. A decrease in $|\Delta'|$ in a central plasma region does not yet guarantee an increase in the maximum possible plasma pressure, as was erroneously thought in [35]. A complete solution of the equilibrium problem should include the integration of Δ' over the entire cross section of the plasma column, which was not done in [35]. The increase in ρv_t^2 away from the magnetic axis changes somewhere to a decrease, resulting in a negative effect, as can easily be seen from Eq. (24). However, even without recourse to formula (24), it is clear that, in any case, regardless of the ρv_t^2 profile, the centrifugal force of the toroidal plasma rotation is directed outward; therefore, the total effect must be negative. In particular, this is seen from integral force balance condition (5). In order to see this negative integral effect in terms of the conventional description based on expressions (24) and (26), let us apply expression (24) to the boundary magnetic surface $a = b$:

$$\Delta'(b) = -\frac{b}{R}\left[\frac{l_i}{2} + \beta_J + \frac{\overline{\rho v_t^2}}{B_J^2}\right]. \qquad (27)$$

Here, all of the quantities are taken at the plasma boundary; hence, l_i is the total internal inductance, $\beta_J = 2\bar{p}/B_J^2$ is the total poloidal beta, and B_J is the mean poloidal field at the boundary. It is also assumed that the conditions $p = 0$ and $\rho v_t^2 = 0$ are satisfied at the plasma boundary.

Expression (27) differs from the well-known formula for the static case [31] only in that it contains the term with the toroidal velocity v_t. As was expected, the contribution of this term is negative, which indicates an increase in $|\Delta'|$. A similar effect was revealed in the problem of the static equilibrium of a plasma with an anisotropic pressure, e.g., because of the presence of particles with high toroidal velocities [4, 31].

An increase in $|\Delta'|$ at the plasma edge should inevitably *reduce* the equilibrium beta limit. To demonstrate this once again, let us turn to the formula [43, 34]

$$B_\perp = -B_J\frac{b}{2R}\left[\ln\frac{8R}{b} - \frac{3}{2} - \frac{R}{b}\Delta'\right], \qquad (28)$$

which gives the strength of the external transverse field $B_\perp$ required to keep the plasma column in a tokamak at a given equilibrium position. Substituting expression (27) into (28) yields

$$B_\perp = -B_J\frac{b}{2R}\left[\ln\frac{8R}{b} - \frac{3}{2} + \frac{l_i}{2} + \beta_J + \frac{\overline{\rho v_t^2}}{B_J^2}\right]. \qquad (29)$$

For $v_t = 0$, this formula reproduces the classical result obtained by Shafranov [2, 3, 31]. It is this result that formed a basis for the development of equilibrium control systems in tokamaks, and it is this field that was mentioned in the first paragraph of the Introduction.

It can be seen from formula (29) that the transverse magnetic field must be stronger for a rotating plasma. As was explained in [31], the equilibrium limit for a plasma column with a circular cross section is achieved when the inner X-point of the magnetic separatrix approaches the plasma boundary. This means that there is an upper limit to the quantity $|B_\perp|$. Let us assume that this limit has been reached and $|B_\perp|$ cannot be increased further. It is clear that, for a given value of $|B_\perp|$, the higher values of β_J will be obtained for a nonrotating plasma.

Hence, we again arrive at the conclusion that the toroidal rotation can only reduce the equilibrium β limit. The opposite, very optimistic conclusion of [35] is

wrong because, in that paper, only the possibility of reducing the quantity $|\Delta'|$ at the center of the plasma column was considered, the equation for the shift was not completely integrated, and the boundary conditions were not discussed at all.

6. CONCLUSION

The possibility of the local improvement of the equilibrium conditions (or the possibility of decreasing $|\Delta'|$) for a tokamak plasma rotating in such a way that ρv_t^2 increases away from the magnetic axis was predicted as far back as 1973 by Zehrfeld and Green [9]. For about the next 30 years, no facts or predictions appeared (the only exception being papers [35, 36]) indicating that this effect should be taken into account in analyzing the integral equilibrium conditions. The reason is that the effect in question is fairly weak, which can be seen from the final formulas derived in [9] for the shift Δ, although this point was not directly mentioned in that paper. In addition, based exclusively on the fact that the equilibrium conditions can locally be improved in the plasma core, it cannot, however, be concluded that the rotation of a plasma has a favorable effect on its equilibrium.

The above analysis clearly shows that, in contrast to the conclusions reached in [35, 36], the effect in question is actually weak and the global effect is negative. This has been shown by all possible analytical means: by obtaining simple estimates (6)–(9) for the role of the plasma rotation in the global force balance, by solving the general problem of how to choose the velocity and pressure profiles in order to make the right-hand side of basic equilibrium equation (10) independent of the plasma pressure, and by examining the solution to Eq. (10) in the traditional model of circular shifted magnetic surfaces.

The effect of the plasma rotation on equilibrium is determined primarily by the absolute value of the rotation velocity, or, more precisely, by the quantity ρv_t^2 [see formulas (4), (5), (12), (23), (24), (27), (29)]. The assertions of Ilgisonis and Pozdnyakov [35, 36] that this effect is governed by the profile of the rotation velocity, rather than by its absolute value, are false. The conclusion about the strong positive effect of the toroidal plasma rotation [35, 36], in particular, about the possibility of substantially increasing (by a factor of 1.6 to 2.5) the equilibrium β limit [35], is also wrong. In fact, the equilibrium beta limit for a rotating plasma should be lower than that for a nonrotating plasma. This can be seen in basic equation (4); in its integral consequence (5); and, even better, in final expressions (27) and (29). For a hot plasma, the rotation-related decrease in the equilibrium β limit is insignificant, provided that the rotation velocity is lower than the plasma thermal velocity. That the effect is weak is a natural consequence of the smallness of parameter (8) for typical tokamak conditions. In any case, regardless of the value of the rotation velocity, this effect is negative, in contrast to the very optimistic predictions of [35, 36].

The above discussion was concentrated on the plasma equilibrium only; hence, the conclusion about the negative (although fairly weak) effect of the toroidal plasma rotation also applies only to plasma equilibrium, when the global force balance is important. On the other hand, plasma rotation may play a significant role in the processes that are governed by the local (rather than global) parameters. Thus, the rotation of a plasma can substantially affect its stability [44, 45]. In particular, it is well known that sufficiently rapid plasma rotation stabilizes the so-called resistive wall modes [41, 46, 47]. The solution of the problem of the stability of these modes with allowance for plasma rotation requires an adequate description of the dissipative processes occurring in a thin layer around a resonant magnetic surface. The stability problem requires quite different approaches and separate consideration.

ACKNOWLEDGMENTS

I am grateful to my colleagues at the Kurchatov Institute for bringing this problem to my attention and for their keen interest in establishing truth. This work was supported in part by the Russian Foundation for Basic Research, project no. 00-15-96526 (under the program “Leading Scientific Schools”).

REFERENCES

1. L. A. Artsimovich and K. B. Kartashev, Dokl. Akad. Nauk SSSR **146**, 1305 (1962) [Sov. Phys. Dokl. **7**, 919 (1963)].
2. V. D. Shafranov, At. Energ. **13**, 521 (1962).
3. V. D. Shafranov, *Reviews of Plasma Physics*, Ed. by M. A. Leontovich (Gosatomizdat, Moscow, 1963; Consultants Bureau, New York, 1966), Vol. 2.
4. V. S. Mukhovatov and V. D. Shafranov, Nucl. Fusion **11**, 605 (1971).
5. L. A. Artsimovich, *Closed Plasma Configurations* (Nauka, Moscow, 1969).
6. L. A. Artsimovich, Nucl. Fusion **12**, 215 (1972).
7. V. S. Mukhovatov, *Itogi Nauki Tekh., Ser. Fiz. Plazmy*, Ed. by V. D. Shafranov (VINITI, Moscow, 1980), Vol. 1, Part 1, p. 6.
8. H. P. Zehrfeld and B. J. Green, Nucl. Fusion **12**, 569 (1972).
9. H. P. Zehrfeld and B. J. Green, Nucl. Fusion **13**, 750 (1973).
10. S. Suckewer, H. P. Eubank, R. J. Goldston, *et al.*, Nucl. Fusion **21**, 1301 (1981).
11. K. Brau, M. Bitter, R. J. Goldston, *et al.*, Nucl. Fusion **23**, 1643 (1983).
12. R. C. Isler, Nucl. Fusion **24**, 1599 (1984).
13. E. K. Maschke and H. Perrin, Plasma Phys. **22**, 579 (1980).

14. W. A. Cooper and A. J. Wootton, Plasma Phys. **24**, 1183 (1982).
15. E. Hameiri, Phys. Rev. A **27**, 1259 (1983).
16. E. Hameiri, Phys. Fluids **26**, 230 (1983).
17. L. L. Lao, Comput. Phys. Commun. **31**, 201 (1984).
18. W. Kerner and H. Weitzner, Comput. Phys. Commun. **31**, 249 (1984).
19. W. Kerner and O. Jandl, Comput. Phys. Commun. **31**, 269 (1984).
20. S. Semenzato, R. Gruber, and H. P. Zehrfeld, Comput. Phys. Rep. **1**, 389 (1984).
21. R. A. Clemente and R. Farengo, Phys. Fluids **27**, 776 (1984).
22. W. A. Cooper, Plasma Phys. Controlled Fusion **26**, 1351 (1984).
23. Y. Z. Agim and J. A. Tataronis, J. Plasma Phys. **34**, 337 (1985).
24. K. Elsässer and A. Z. Heimsoth, Z. Naturforsch. A **41**, 883 (1986).
25. W. Kerner and S. Tokuda, Z. Naturforsch. A **42**, 1154 (1987).
26. A. Bhattacharjee, in *Theory of Fusion Plasmas (Proceedings of the International School of Plasma Physics "Piero Caldirola," Varenna, 1987)*, Ed. by A. Bondeson, E. Sindoni, and F. Troyon (Compositori, Bologna, 1988), p. 47.
27. J. W. Connor, S. C. Cowley, R. J. Hastie, and L. R. Pan, Plasma Phys. Controlled Fusion **29**, 919 (1987).
28. W. A. Cooper and S. P. Hirshman, Plasma Phys. Controlled Fusion **29**, 933 (1987).
29. T. Takeda and S. Tokuda, J. Comput. Phys. **93**, 1 (1991).
30. G. Beitman, *MHD Instabilities* (MIT Press, Cambridge, 1978; Énergoizdat, Moscow, 1982).
31. L. E. Zakharov and V. D. Shafranov, *Reviews of Plasma Physics*, Ed. by M. A. Leontovich and B. B. Kadomtsev (Énergoizdat, Moscow, 1982; Consultants Bureau, New York, 1986), Vol. 11.
32. V. D. Pustovitov and V. D. Shafranov, *Reviews of Plasma Physics*, Ed. by B. B. Kadomtsev (Énergoatomizdat, Moscow, 1987; Consultants Bureau, New York, 1990), Vol. 15.
33. B. J. Braams, Plasma Phys. Controlled Fusion **33**, 715 (1991).
34. V. D. Pustovitov, *Reviews of Plasma Physics*, Ed. by B. B. Kadomtsev and V. D. Shafranov (Consultants Bureau, New York, 2000), Vol. 21, p. 1.
35. V. I. Ilgisonis and Yu. I. Pozdnyakov, Pis'ma Zh. Éksp. Teor. Fiz. **71**, 454 (2000) [JETP Lett. **71**, 314 (2000)].
36. V. I. Ilgisonis, Plasma Phys. Controlled Fusion **43**, 1255 (2001).
37. R. Żelazny and A. Gałkowski, J. Plasma Phys. **50**, 385 (1993).
38. R. Żelazny, R. Stankiewicz, A. Gałkowski, and S. Potempski, Plasma Phys. Controlled Fusion **35**, 1285 (1993).
39. H. Tasso and G. N. Throumoulopoulos, Phys. Plasmas **5**, 2378 (1998).
40. Ch. Simintzis, G. N. Throumoulopoulos, and G. Pantis, Phys. Plasmas **8**, 2641 (2001).
41. A. M. Garofalo, A. D. Turnbull, M. E. Austin, *et al.*, Phys. Rev. Lett. **82**, 3811 (1999).
42. D. Testa, C. Giroud, A. Fasoli, *et al.*, Phys. Plasmas **9**, 243 (2002).
43. J. M. Greene, J. L. Johnson, and K. E. Weimer, Phys. Fluids **14**, 671 (1971).
44. M. S. Chu, L. Chen, L.-J. Zheng, *et al.*, Nucl. Fusion **39**, 2107 (1999).
45. M. Furukawa, Y. Nakamura, S. Hamaguchi, and M. Wakatani, Phys. Plasmas **8**, 4889 (2001).
46. A. Bondeson, C. G. Gimblet, and R. J. Hastie, Phys. Plasmas **6**, 637 (1999).
47. A. M. Garofalo, E. J. Strait, J. M. Bialek, *et al.*, Nucl. Fusion **40**, 1491 (2000).

Translated by O.E. Khadin

Plasma Physics Reports, Vol. 29, No. 2, 2003, pp. 112–117. Translated from Fizika Plazmy, Vol. 29, No. 2, 2003, pp. 131–136.

PLASMA ELECTRONICS

Nonlinear Theory of the Excitation of Azimuthal Surface Waves during Dissipative Instability

V. O. Girka, A. N. Kondratenko, and S. Yu. Puzyr'kov

Kharkiv National University, pl. Svobody 4, Kharkiv, 61077 Ukraine

e-mail: girka@pem.kharkov.ua

Received March 5, 2002

Abstract—A theoretical study is made of the surface electromagnetic eigenmodes that are excited by an annular charged-particle beam due to dissipative instability and propagate across the external axial magnetic field in a cylindrical metal waveguide partially filled with plasma. A self-consistent set of differential equations for a cold low-density charged-particle beam moving above the plasma surface is constructed in the single-mode approximation and is solved numerically. It is shown that the larger the dissipation, the slower the instability growth rate and the larger the wave amplitude in the saturation stage of the instability. An increase in the transverse dimensions of a charged-particle beam results in a slower growth of the dissipative instability, in which case, however, the beam transfers a larger fraction of its kinetic energy to the wave. © *2003 MAIK "Nauka/Interperiodica".*

1. INTRODUCTION

The investigation of the interaction of charged-particle beams with hybrid waveguide structures is important for radio engineering and plasma electronics because of the possibility of developing small-scale radio engineering devices capable of generating electromagnetic waves over a broad frequency band. Different aspects of the problem of the interaction of charged particle beams with the eigenmodes of plasma-filled waveguides were studied in [1–4]. The results of theoretical research on the beam–plasma interaction find applications in fusion experiments with beam-heated plasmas [5] and in physical experiments in space [6, 7]. In this paper, we develop a nonlinear theory of the interaction of charged-particle beams with the eigenmodes of a short scale-length plasma electronics device capable of generating continuously tunable radiation.

Among the issues that have been studied by now in considerable detail are the conditions for the onset of beam instabilities and the nonlinear interaction of charged-particle beams with plasmas in an infinitely strong external magnetic field and in a magnetic field of finite strength. The effect of the spectra of the generated waves on the characteristic features of the beam–plasma interaction has also been analyzed, but without allowance for the effect of plasma boundaries. The finite plasma dimensions not only change the excitation dynamics of bulk waves, but also provide conditions favorable for the onset of surface waves (SWs) [8–11].

It is the distinctive features of the interaction of charged-particle beams with plasma waveguide structures of finite dimensions that motivated the choice of the subject for our study. Specifically, we investigated the excitation of an extraordinarily polarized surface mode, which is the eigenmode of a cylindrical metal waveguide partially filled with a cold magnetized plasma, due to dissipative instability. This mode, which propagates in the azimuthal direction strictly transverse to a constant external axial magnetic field, is called an azimuthal surface wave (ASW) [12]. In the plasma region, the ASW field is described in terms of a superposition of the modified Bessel functions and their derivatives. In the vacuum region, where a low-density electron beam propagates, it is expressed in terms of the first- and second-order Bessel functions [13]. The numerical results obtained on the basis of the nonlinear theory of the excitation of an ASW by a charged-particle beam during the resonant beam-driven instability were reported in [14]. In that paper, it was shown that the growth rate of the resonant beam-driven instability of an ASW increases with the azimuthal mode number m and there exists an optimum value of m/R_1 (where R_1 is the radius of the plasma column) at which the instability growth rate is maximum. The excitation of SWs by an annular beam in the interaction with a plasma cylinder was also investigated in [15, 16].

The dissipative instability of ASWs was studied in [17] in the linear approximation. The growth rate of this instability was found to be slower than that of the resonant beam-driven instability of an ASW; moreover, it was found to decrease with increasing azimuthal mode number m. The nonlinear excitation of other types of SWs during the dissipative instability was studied in, e.g., [8, 18]. Our objective here was to investigate the nonlinear interaction of an ASW with an electron beam during this instability.

1063-780X/03/2902-0112$24.00

2. FORMULATION OF THE PROBLEM

It is proposed to excite ASWs in a cylindrical metal waveguide of radius R_2 with a coaxial plasma column of smaller radius R_1. An annular electron beam moves in the gap between the plasma and the metal waveguide wall. The beam density n_b is assumed to be much lower than the plasma density n_p, and the gap width is assumed to be sufficiently small ($R_2 - R_1 \ll R_2$). The constant external magnetic field $\mathbf{H}_0$ is oriented along the z-axis, which is the symmetry axis of the cylinder.

The electrical conductivity of the metal waveguide wall is assumed to be high enough for the tangential component of the electric field of an ASW to satisfy the boundary condition $E_\tau(R_2)$ at the metal surface. In the z direction, the system is assumed to be uniform; hence, the electromagnetic perturbations under consideration are independent of the z coordinate.

The desired set of the differential equations describing the nonlinear stage of the dissipative instability of an ASW can be obtained from the hydrodynamic equations for the plasma, Maxwell's equations, and the equation of motion for the beam electrons in the region $R_2 > r > R_1$. Since the beam density is much lower than the plasma density ($n_b \ll n_p$), we can neglect both the effect of the beam on the dispersion properties of an ASW and the effect of the self-field of the beam on the electromagnetic field in which the beam propagates. The dissipative processes in the plasma are described by introducing the effective collision frequency into the dispersion relation for an ASW.

3. BASIC EQUATIONS

In the cold plasma approximation, Maxwell's equations can be split into two independent subsets of equations by representing the dependence of the wave electromagnetic field on the time t and the azimuthal angle φ in the form

$$E, H = f(r)\exp(im\varphi - i\omega t). \quad (1)$$

One of the subsets describes the ASW field with extraordinary polarization, the electric field of the ASW being perpendicular to the external magnetic field $\mathbf{H}_0$. For the magnetic component H_z of the ASW field, it is possible to obtain a second-order differential equation whose solution is expressed in terms of the modified Bessel functions [13],

$$\frac{\partial^2 H_z}{\partial \xi^2} + \frac{1}{\xi}\frac{\partial H_z}{\partial \xi} - \left(1 + \frac{m^2}{\xi^2}\right)H_z = 0, \quad (2)$$

in which case the components of the wave electric field in a plasma cylinder $r < R_1$ are related to the above magnetic component by

$$E_r = \frac{\varepsilon_2}{k\varepsilon_1\psi^2}\frac{\partial H_z}{\partial r} + \frac{mH_z}{kr\psi^2}, \quad (3)$$

$$E_\varphi = \frac{im\varepsilon_2 H_z}{kr\varepsilon_1\psi^2} + \frac{i}{k\psi^2}\frac{\partial H_z}{\partial r}, \quad (4)$$

where $\xi = kr\psi$, $k = \omega c^{-1}$, c is the speed of light, $\psi^2 = (\varepsilon_2^2 - \varepsilon_1^2)\varepsilon_1^{-1}$, and ε_1 and ε_2 are the elements of the dielectric tensor of a cold magnetized plasma (see, e.g., [19]).

In the plasma region, the solution to Eqs. (2)–(4) that describes the H_z component of the ASW field is expressed through the modified Bessel functions $I_m(\xi)$ and the solutions describing the E_r and E_φ components are represented as linear combinations of the functions $I_m(\xi)$ and their derivatives $I_m'(\xi)$ with respect to the argument. This is valid under the assumption that the ASW field at the waveguide axis $r = 0$ is finite.

In the beam region, the electromagnetic field of an ASW is described by the following set of differential equations, which differ from Eqs. (2)–(4):

$$\frac{\partial^2 H_z}{\partial \zeta^2} + \frac{1}{\zeta}\frac{\partial H_z}{\partial \zeta} - \left(1 - \frac{m^2}{\zeta^2}\right)H_z = F_b, \quad (5)$$

$$E_r = \frac{4\pi}{i\omega}j_r - \frac{mH_z}{\zeta}, \quad (6)$$

$$E_\varphi = \frac{4\pi}{i\omega}j_\varphi - i\frac{\partial H_z}{\partial \zeta}, \quad (7)$$

where

$$F_b = -\frac{4\pi}{\omega\zeta}\left[\frac{\partial}{\partial \zeta}(j_\varphi \zeta) - imj_r\right], \quad \zeta = kr,$$

$$j_r = -|e|\sum_{i=1}^{N}\delta(r - r_i)\delta(\varphi - \varphi_i)\frac{\partial r}{\partial t},$$

$$j_\varphi = -|e|\sum_{i=1}^{N} r\delta(r - r_i)\delta(\varphi - \varphi_i)\frac{\partial \varphi}{\partial \tau},$$

and $\delta(x - x_0)$ is the delta function.

Equations (5)–(7) were solved by the method of variation of a constant. The components of the ASW field in the region $R_1 < r < R_2$ are expressed in terms of the Bessel functions of the first kind $J_m(\xi)$, the Bessel functions of the second kind $N_m(\xi)$, their derivatives with respect to the argument [13], and the components j_r and j_φ of the beam current density.

In order to derive the equations for the envelope and phase of the wave, we turn to the following boundary conditions:

(i) the tangential electric field of an ASW vanishes at the metal surface of the waveguide wall, $E_\varphi(R_2) = 0$;

(ii) the tangential field component E_φ is continuous at the plasma boundary $r = R_1$, $\{E_\varphi(R_1)\} = 0$; and

(iii) there are no currents at the metal surface of the waveguide wall and at the plasma–vacuum interface, $j_\varphi(R_1) = j_\varphi(R_2) = 0$.

Taking into account the dissipative processes in the plasma and using the standard procedures for averaging and singling out the slow time (see, e.g., [2, 8]), we can obtain equations for the envelope and phase of the eigenmodes excited in the waveguide. This can be done by introducing the effective collision frequency into the elements of the plasma dielectric tensor:

$$\frac{\partial A}{\partial t} = -\frac{A\beta}{P}\mathrm{Im}\,D(\omega) - \frac{\alpha D_p}{N\beta PL}\sum_{i=1}^{N}\left[\frac{m}{w}\frac{\partial R_i}{\partial t}L_1(\zeta_i)\sin(m\varphi_i + \Theta - \omega t) + R_i^2\frac{\partial \varphi_i}{\partial t}L_2(\zeta_i)\cos(m\varphi_i + \Theta - \omega t)\right], \quad (8)$$

$$\frac{\partial \Theta}{\partial t} = -\frac{\alpha D_p}{N\beta PLA}\sum_{i=1}^{N}\left[R_i^2\frac{\partial \varphi_i}{\partial t}L_2(\zeta_i)\sin(m\varphi_i + \Theta - \omega t) - \frac{m}{w}\frac{\partial R_i}{\partial t}L_1(\zeta_i)\sin(m\varphi_i + \Theta - \omega t)\right], \quad (9)$$

where $A = E_y B_0^{-1}$ is the dimensionless wave amplitude, Θ is the wave phase, $\alpha = n_b n_p^{-1}$, $\beta = |\omega_e|\Omega_e^{-1}$, $w = \omega\Omega_e^{-1}$, $R_i = r_i\Omega_e c^{-1}$, $\zeta_i = kR_i$, ω_e is the electron cyclotron frequency, Ω_e is the electron Langmuir frequency,

$$L = J_m(\zeta_1)N_m'(\zeta_2) - J_m'(\zeta_2)N_m(\zeta_1),$$

$$\zeta_1 = kR_1, \quad \zeta_2 = kR_2,$$

$$L_1(\zeta_i) = J_m(\zeta_i)N_m'(\zeta_2) - J_m'(\zeta_2)N_m(\zeta_i),$$

$$L_2(\zeta_i) = J_m'(\zeta_i)N_m'(\zeta_2) - J_m'(\zeta_2)N_m'(\zeta_i),$$

$$D_p = \frac{I_m'(\psi\zeta_1)}{\psi I_m(\psi\zeta_1)} + \frac{m\varepsilon_2}{\varepsilon_1\psi^2\zeta_1}, \quad P = \frac{d}{dw}\left[D_p + \frac{L_2(\zeta_1)}{L}\right],$$

$$\mathrm{Im}\,D(\omega) \approx \frac{\nu}{2\omega}\left[\frac{I_{m+1}(\xi_1)}{\psi I_m(\xi_1)} + \frac{2|m|\omega^2}{\Omega_e^2\zeta_1}\right],$$

and ν is the effective collision frequency of the plasma particles.

The equation of motion for the beam electrons can be conveniently written in terms of the electron momentum $\mathbf{p} = \gamma m_e\mathbf{v}$ (where γ is the relativistic factor):

$$\frac{d\mathbf{p}}{dt} = e\mathbf{E} + \frac{e}{c}[\mathbf{v}\times(\mathbf{H} + \mathbf{H}_0)]. \quad (10)$$

Substituting the ASW field components calculated in the region $R_1 < r < R_2$ yields the following set of equations for the ith electron:

$$\frac{dR_i}{dt} = |\omega_e|\frac{V_i}{\beta\gamma_i}, \quad (11)$$

$$\frac{d\varphi_i}{dt} = |\omega_e|\frac{u_i}{\beta\gamma_i R_i} + |\omega_e|\frac{\varepsilon}{\beta R_i}, \quad (12)$$

$$\frac{dV_i}{dt} = -|\omega_e|\frac{u_i}{\gamma_i}\left(1 - \frac{u_i}{\beta R_i}\right) + AR_1\left(\frac{m}{R_1} - w\frac{u_i}{\gamma_i}\right)\left(\frac{1}{\zeta_1 D_p} - R_\alpha\right)\sin(m\varphi_i + \Theta - \omega t), \quad (13)$$

$$\frac{du_i}{dt} = |\omega_e|\frac{V_i}{\gamma_i}\left(1 - \frac{u_i}{\beta R_i}\right) + \frac{AwR_1}{\zeta_1}\left[R_\alpha - 1 + \frac{R_\alpha}{D_p}\left(\frac{m^2}{\zeta_1} - \zeta_1\right)\right]\cos(m\varphi_1 + \Theta - \omega t) + \frac{AwR_1V_i}{\gamma_i}\left(\frac{1}{\zeta_1 D_p} - R_\alpha\right)\sin(m\varphi_1 + \Theta - \omega t), \quad (14)$$

where $R_\alpha = r_i R_1^{-1} - 1$, $V = p_r m_e^{-1}c^{-1}$, $u = p_\varphi m_e^{-1}c^{-1}$, and V_i and u_i are the dimensionless radial and azimuthal momenta of the ith electron, respectively.

Equations (13) and (14) were derived under the basic assumption that the region where the beam propagates is relatively narrow, $R_2 - R_1 \ll R_1$. This assumption made it possible to significantly simplify these equations by using the asymptotic expansions of the cylindrical Bessel functions and their Wronskians (see, e.g., [13]) and, thus, to substantially reduce the computation time required for the direct calculation of all cylindrical functions in Eqs. (8) and (9). The nonlinear interaction of an ASW with an annular electron beam was investigated by solving Eqs. (8), (9), and (11)–(14) numerically.

4. RESULTS OF NUMERICAL INVESTIGATIONS OF THE DISSIPATIVE INSTABILITY OF AN ASW

The model set of equations was solved by using the fourth-order Runge–Kutta method, which is one of the best standard methods for the numerical integration of differential equations and which makes it possible, on the one hand, to reduce the number of computational operations required to calculate their right-hand sides and, on the other, to ensure a high computational accuracy. The time integration step was varied depending on

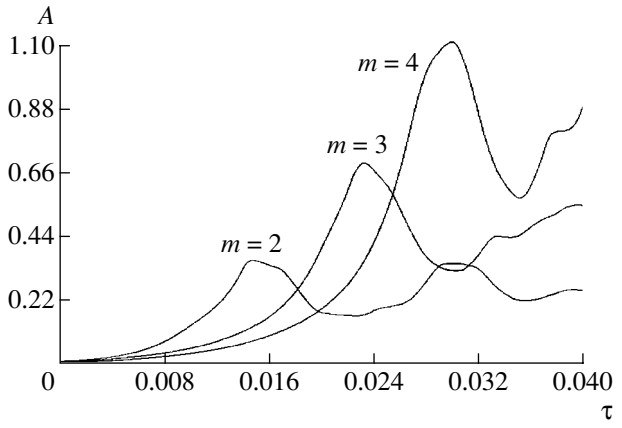

Fig. 1. Time dependences of the amplitudes of ASWs with different azimuthal mode numbers for ν = 0.

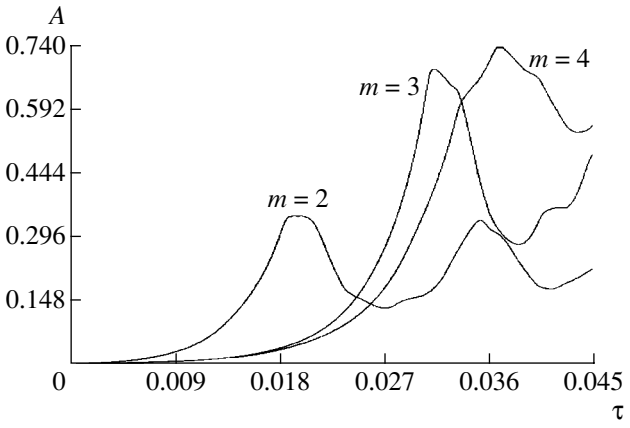

Fig. 2. Development of the dissipative instability of ASWs with different azimuthal mode numbers *m* for ν = 0.1.

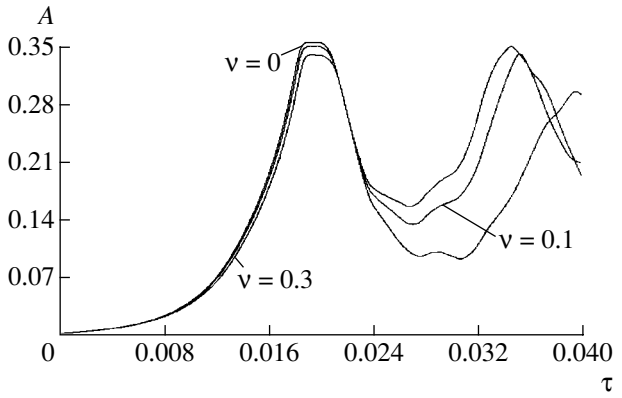

Fig. 3. Time dependences of the amplitude of an ASW with *m* = 2 for different collision frequencies of the plasma particles.

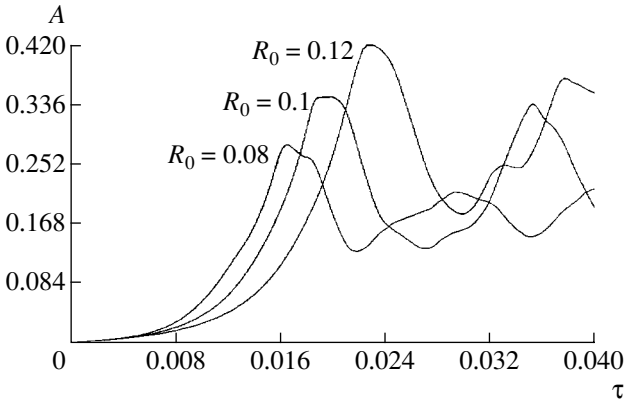

Fig. 4. Time dependences of the amplitude of an ASW with *m* = 2 for ν = 0.1 and for different transverse dimensions of the beam ($R_0 = R_2/R_1 - 1$).

the rate at which the functions changed during the process of numerical integration.

The number of particles used to model an electron beam was $N = 500$, because, with larger numbers of particles, the final results were found to remain essentially the same. The interaction of the beam electrons with the plasma boundary and metal waveguide wall was simulated using the mirror reflection model, which implies that the electrons do not disappear in such interactions, but rather their radial momenta are reversed by mirror reflection and they are reflected back into the region $R_1 < r < R_2$. This model is frequently used and is best suited for describing a beam–solid body boundary [8].

The results of numerical simulations of the development of the resonant beam-driven instability of an ASW are illustrated in Figs. 1–4. The initial wave amplitude, wave phase, and the radial momentum of all beam electrons were assumed to be $A = 10^{-3}$, $\Theta = 0$, and $V_i = 0$, respectively. The simulations were carried out for three different gap widths: $R_2 - R_1 = 0.08R_1$, $R_2 - R_1 = 0.1R_1$, and $R_2 - R_1 = 0.12R_1$. The initial distribution of the beam electrons over the azimuthal angle in the range $0 \le \varphi \le 2\pi$ was chosen to be approximately uniform with a small random deviation ($\Delta\varphi = \pm 1\%$). Over the radius, the beam electrons were initially distributed in a random manner in the spatial region $R_1 + \frac{1}{3}(R_2 - R_1) < r < R_1 + \frac{2}{3}(R_2 - R_1)$. In most of the simulations, the initial angular momentum u_i of the beam electrons was set equal to βR_i with a small random spread of $\pm 1\%$.

As was shown in [14], there is an effective wavenumber $k_{\text{eff}} = mcR_1^{-1}\Omega_e$, in the immediate vicinity of which the growth rate of the beam-driven instability of an ASW is maximum. In the case at hand, the effective wavenumber is approximately equal to $k_{\text{eff}}^* \approx 0.4$. That is why, for simulations, we chose the corresponding

values of R_1 for different azimuthal mode numbers. Our analysis of how the choice of the value of k_{eff} affects the development of the dissipative instability confirmed the results obtained in [14]. In fact, we found that, if the k_{eff} value was chosen to differ from k_{eff}^*, then the ASW amplitude increased at a slower rate. Our numerical analysis also confirmed the suggestion that the only waves that are excited resonantly are ASWs with positive values of the azimuthal mode number m; these waves propagate in the direction in which the beam electrons gyrate in an external axial magnetic field. The waves with $m < 0$ are not excited. It was established that the excitation of an ASW is highly sensitive to the beam electron density. The lower the beam density, the smaller the wave amplitude in the saturation stage of the instability and the longer the time scale on which the instability saturates. A decrease in the ratio $|\omega_e|\Omega_e^{-1}$ also reduces the time scale on which the ASW amplitude increases from its initial value to the maximum. Note that all of the curves in the figures presented here were computed for $|\omega_e| = 0.01\Omega_e$ and $n_b = 0.05n_p$.

Figure 1 illustrates how ASWs with different azimuthal mode numbers m are excited during the beam-driven instability ($\nu = 0$). We can see that, with increasing azimuthal mode number m, the ASW amplitude increases significantly in the saturation stage of the beam instability and the instability itself grows faster.

The results of investigations of the amplitudes of ASWs with different azimuthal mode numbers m during the dissipative instability ($\nu \neq 0$) are illustrated in Fig. 2. It can be seen from this figure that the larger the azimuthal mode number m, the larger the ASW amplitude in the saturation stage of the dissipative instability and the slower the instability growth rate.

In Fig. 3, we illustrate the results of investigations of the effect of the dissipation rate ν on the growth of the ASW amplitude during the development of the dissipative instability. It can be seen that the higher the dissipation rate ν, the smaller the ASW amplitude in the saturation stage of the instability and the slower the instability growth rate.

Figure 4 illustrates the results of a numerical analysis of the effect of the transverse dimensions of a beam on the amplitude of the wave envelope in the saturation stage of the dissipative instability and on the instability growth rate. We can see that the larger the transverse beam dimensions, the larger the fraction of the beam kinetic energy that is transferred to the wave and the longer the time required for the dissipative instability to saturate. This result stems from the distinctive features of the spatial distribution of the ASW field and from the fact that the larger the gap width $R_2 - R_1$, the larger the distance between the beam and the plasma surface, at which the SW amplitude is known to be maximum (see, e.g., [19]).

5. CONCLUSION

We have studied the excitation of ASWs with frequencies in the range $|\omega_e| < \omega < \sqrt{\Omega_e^2 + \omega_e^2/4} - |\omega_e|/2$ by an annular electron beam rotating around the plasma column that partially fills a cylindrical metal waveguide immersed in an external axial magnetic field. The resonant dissipative instability of an ASW has been investigated in the single-mode approximation.

We have derived a two-dimensional set of model equations describing the evolution of the envelope of the wave field, the phases of ASWs, and the coordinates and momenta of the electrons of a low-density beam. We have numerically analyzed the effect of the waveguide and beam parameters on the development of the resonant beam instability. We have shown that changing the sign of the azimuthal mode number (or, equivalently, reversing the propagation direction of the ASW) leads to the suppression of instability. ASWs with larger azimuthal mode numbers m are excited at slower rates, but their amplitudes in the saturation stage of the instability are larger. This is explained by the fact that the larger the azimuthal mode number m, the higher the phase velocity of the ASW [17] and, accordingly, the larger difference between the wave phase velocity and the beam velocity (note that it is this difference that determines how much of the beam energy is transferred to the wave [8]). The growth rates $\text{Im}\gamma$ of the resonant dissipative instability of ASWs are slower than those of the resonant beam-driven instability; moreover, an increase in the effective collision frequency results in an additional slowing of the growth rates $\text{Im}\gamma$. By increasing the transverse dimensions of the beam, it is possible to increase the difference between the beam velocity and the wave phase velocity and, consequently, to achieve larger amplitudes of the wave envelope in the saturation stage of the dissipative instability.

Finally, we point out the following two advantages of the proposed model of a hybrid waveguide structure excited by an annular charged-particle beam: first, the eigenfrequency of the structure can be continuously tuned by varying the plasma density and, second, the axial dimensions of the structure are small because the beam interacts with a wave propagating in the azimuthal direction.

REFERENCES

1. A. A. Rukhadze, L. S. Bogdankevich, S. E. Rosinskiĭ, and V. G. Rukhlin, *Physics of High-Current Relativistic Electron Beams* (Atomizdat, Moscow, 1980).
2. M. V. Kuzelev and A. A. Rukhadze, *Electrodynamics of Dense Electron Beams in a Plasma* (Nauka, Moscow, 1990).
3. R. B. Miller, *Introduction to the Physics of Intense Charged Particle Beams* (Plenum, New York, 1982; Mir, Moscow, 1984).

4. Ya. B. Faĭnberg, Fiz. Plazmy **11**, 1398 (1985) [Sov. J. Plasma Phys. **11**, 803 (1985)].
5. M. Fujiwara, O. Komeko, A. Komori, *et al.*, Plasma Phys. Controlled Fusion **41**, 157 (1999).
6. E. P. Kontar', V. I. Lapshin, and V. N. Mel'nik, Fiz. Plazmy **24**, 832 (1998) [Plasma Phys. Rep. **24**, 772 (1998)].
7. C. Krafft and A. S. Volokitin, Plasma Phys. Controlled Fusion **41**, 305 (1999).
8. A. N. Kondratenko and V. M. Kuklin, *Fundamentals of Plasma Electronics* (Énergoatomizdat, Moscow, 1988).
9. R. Ando, V. A. Balakirev, K. Kamada, *et al.*, Fiz. Plazmy **23**, 1042 (1997) [Plasma Phys. Rep. **23**, 964 (1997)].
10. B. A. Al'terkop, A. S. Volokitin, S. E. Rosinskiĭ, *et al.*, Fiz. Plazmy **3**, 173 (1977) [Sov. J. Plasma Phys. **3**, 100 (1977)].
11. A. N. Kondratenko, V. M. Kuklin, and I. Kh. Peneva, Izv. Vyssh. Uchebn. Zaved., Radiofiz. **20**, 56 (1977).
12. V. A. Girka, I. A. Girka, A. N. Kondratenko, and V. I. Tkachenko, Radiotekh. Élektron. **33**, 1031 (1988).
13. D. S. Kuznetsov, *Special Functions* (Vysshaya Shkola, Moscow, 1968).
14. V. A. Girka, A. M. Kondratenko, and A. E. Sporov, Zh. Tekh. Fiz. **69** (7), 84 (1999) [Tech. Phys. **44**, 814 (1999)].
15. O. V. Dolzhenko, A. V. Zosimov, and A. A. Rukhadze, Zh. Tekh. Fiz. **44**, 977 (1974) [Sov. Phys. Tech. Phys. **19**, 618 (1975)].
16. B. A. Al'terkop, S. E. Rosinskiĭ, and V. N. Tarakanov, Fiz. Plazmy **5**, 281 (1979) [Sov. J. Plasma Phys. **5**, 164 (1979)].
17. V. A. Girka, I. A. Girka, and V. I. Tkachenko, Zh. Tekh. Fiz. **66** (4), 114 (1996) [Tech. Phys. **41**, 357 (1996)].
18. V. N. Dubovik, V. M. Kuklin, and I. P. Panchenko, Fiz. Plazmy **11**, 1327 (1985) [Sov. J. Plasma Phys. **11**, 760 (1985)].
19. A. N. Kondratenko, *Surface and Internal Waves in a Bounded Plasma* (Énergoatomizdat, Moscow, 1985).

Translated by I.A. Kalabalyk

Plasma Physics Reports, Vol. 29, No. 2, 2003, pp. 118–129. Translated from Fizika Plazmy, Vol. 29, No. 2, 2003, pp. 137–149.

NONLINEAR PHENOMENA

Theory of Harmonic Generation in a Plasma Produced by the Photoionization of Gas Atoms with Electrons in the *np* States

V. P. Silin and P. V. Silin

Lebedev Physical Institute, Russian Academy of Sciences, Leninskiĭ pr. 53, Moscow, 117924 Russia

Received June 6, 2002

Abstract—For a plasma produced by the photoionization of hydrogen-like atoms with electrons in the *np* states, a theory is developed that describes the nonlinear plasma polarizability due to electron–ion collisions, which governs the bremsstrahlung-induced coherent harmonic generation. The effective partial collision frequencies are obtained as functions of the pump field intensity for the first four *p* states of hydrogen-like atoms and for the third, fifth, seventh, ninth, and eleventh harmonics. These analytic results make it possible to establish the scalings of the collision frequencies with pump field intensity, the principal quantum number, and the number of the generated harmonic. In the case of pump fields of comparatively low intensities, some qualitative differences are revealed between these scalings and the corresponding scalings obtained for the Bethe regime of suppression of the photoionization barrier in a gas of hydrogen-like atoms with electrons in the *ns* states.

1. In this paper, we present the results of a theory of the generation of the third, fifth, seventh, ninth, and eleventh harmonics in a plasma photoionized in the Bethe regime of suppression of the ionization barrier [1, 2]. We consider the plasma state within a relatively short period of time after the gas ionization, when the number of collisions between the electrons is still too small for them to forget information about their preionization states in the atoms. An important point is that, in this paper, we will assume that the electrons are initially in the *np* states (a similar analysis for *ns* states is performed in [3]).

In Section 2, we present the basic (common for our analysis) relationships that describe the effective nonlinear partial collision frequencies, which characterize the nonlinear conductivities of the plasma for different harmonics of the pump field. In Section 3, we describe the nonlinear collision frequencies that govern the generation of the third, fifth, and seventh harmonics. In Section 4, we consider the generation of the ninth harmonic, and Section 5 is devoted to the generation of the eleventh harmonic. Section 6 is a limiting asymptotic description of nonlinear collision frequencies for the pump fields of both high and low intensities (in the latter case, the nonlinear collision frequencies have power series expansions). Finally, in Section 7, we discuss the results of our theoretical analysis.

2. According to Bethe [1] (see also [2, 3]), the regime of suppression of the ionization barrier occurs when the electric field strength E satisfies the condition

$$E \geq \frac{I_Z^2}{4Z|e|^3}, \tag{2.1}$$

where Z is the nuclear charge, I_Z is the ionization potential, e is the charge of an electron, and m is its mass. For a hydrogen-like atom, we have

$$I_Z = \frac{Z^2 me^4}{2n^2\hbar^2},$$

where n is the principal quantum number. In the Bethe regime, an electron is almost freely removed from an atom. Consequently, the velocity spread of an electron with respect to its directed motion in an electric field is given by the distribution function of its state in an atom before ionization. The distribution function of the *np* states of unpolarized electrons is written as [4]

$$f_{np}(V) = \frac{N_e}{3\pi^2}\left(\frac{n}{2V_Z}\right)^5 \frac{V^2 c_n^2(mV)}{[(1/4) + (nV/2V_Z)^2]^6}, \tag{2.2}$$

where N_e is the electron density, $V_Z = Ze^2/\hbar$ is the Coulomb velocity unit [5], and the coefficients c_n are given in Appendix 1.

We represent the electric field of the pump wave in the form

$$\mathbf{E}(t) = \mathbf{E}\cos\omega t, \tag{2.3}$$

1063-780X/03/2902-0118$24.00

and denote the electron oscillatory velocity in the pump field by

$$V_E = |eE|/m\omega. \quad (2.4)$$

In the dipole approximation [6–9], the coherent oscillations of electrons in their collisions with plasma ions give a nonlinear collisional contribution to the electric current density $\delta\mathbf{j}$, which is represented as the expansion

$$\delta\mathbf{j} = \sum_{N=0}^{\infty} \frac{e^2 N_e}{m\omega^2} \nu^{(2N+1)}(np, E)\mathbf{E}\cos[(2N+1)\omega t] \quad (2.5)$$

in odd harmonics $2N + 1$ of the pump field [4]. Calculations yield the following expressions for the effective nonlinear partial collision frequencies $\nu^{(2N+1)}(np, E)$:

$$\nu^{(2N+1)}(np, E) = \nu_Z H\left[2N+1, np, \frac{V_E}{V_Z}\right], \quad (2.6)$$

where we have introduced the notation

$$\nu_Z = \frac{16e^2 e_i^2 N_i \Lambda}{m^2 V_Z^3}, \quad (2.7)$$

$$H\left[2N+1, np, \frac{V_E}{V_Z}\right] \equiv n^3 A\left[2N+1, np, \frac{nV_E}{V_Z}\right], \quad (2.8)$$

$$A[2N+1, np, x] = \frac{1}{x^3}[D_{np}\alpha[2N+1, b, x]]_{b=1}, \quad (2.9)$$

$$\alpha[2N+1, b, x] = \frac{d}{db}\left(\operatorname{arcsinh}\left(\frac{x}{b}\right) - \frac{(\sqrt{x^2+b^2}-b)^{2N}}{(2N+1)x^{2N-1}} - \sum_{k=1}^{N} \frac{2b}{(2N-2k+1)} \frac{(\sqrt{x^2+b^2}-b)^{2N-2k+1}}{x^{2N-2k+1}}\right). \quad (2.10)$$

The differential operators D_{np} are given in Appendix 2. The consequences of formulas (2.6)–(2.9) are the subject of further analysis.

In what follows, it is convenient to use the representation

$$A[2N+1, np] = \frac{1}{x^3}(\operatorname{arcsinh} x + a[2N+1, np, x]), \quad (2.11)$$

The algebraic functions $a[2N + 1, np, x]$ for different harmonics and different np states will be determined below.

3. In this section, we consider the nonlinear partial collision frequencies corresponding to the generation of the third, fifth, and seventh harmonics. We analyze these harmonics simultaneously because, as will be seen below, they are described by the analogous analytic consequences of general relationships (2.6)–(2.9). We start with the following consequence of formula (2.10) for the third harmonic (cf. [6]):

$$\alpha[3, b, x] = \operatorname{arcsinh}\left(\frac{x}{b}\right) + \frac{8b}{3x} - \frac{8b^2 + 7x^2}{3x\sqrt{b^2+x^2}}. \quad (3.1)$$

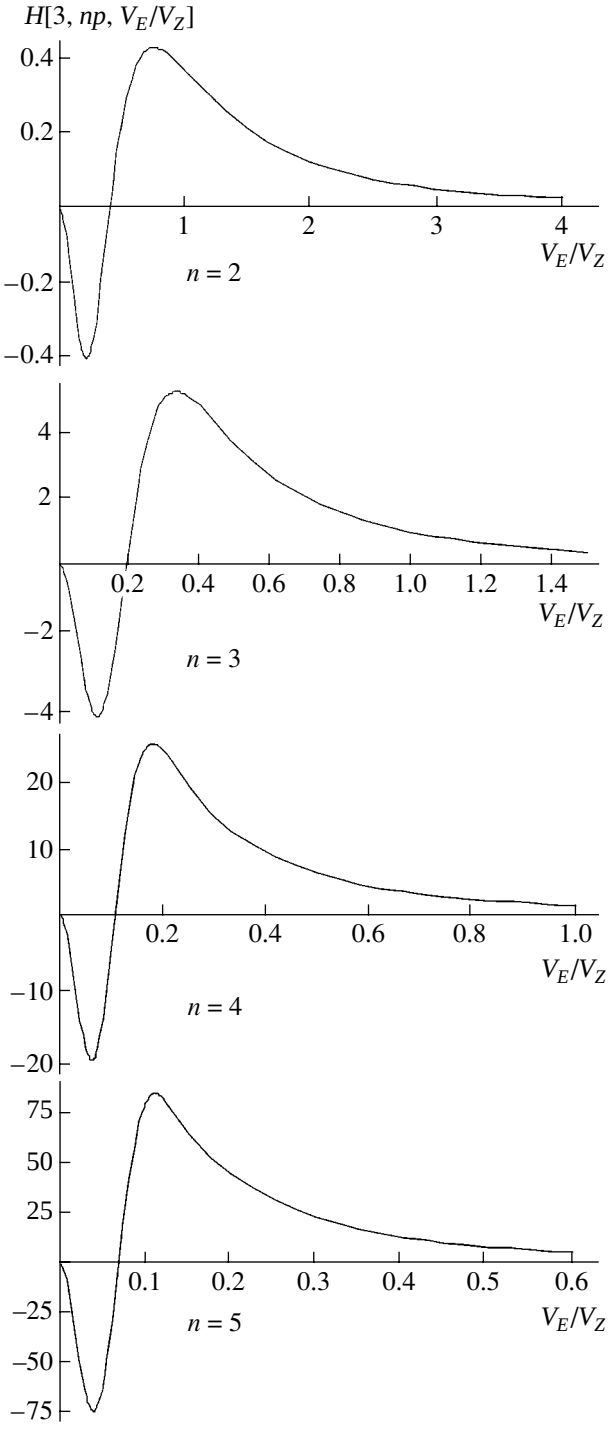

Fig. 1. Functions $H[3, np, V_E/V_Z]$ for different values of the principal quantum number.

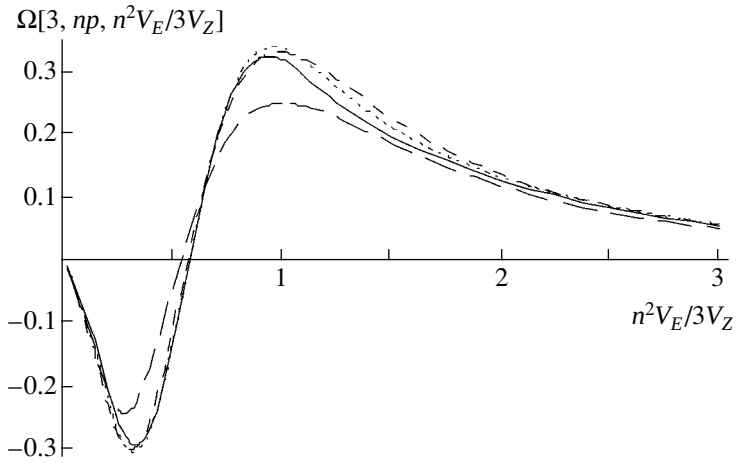

Fig. 2. Functions $\Omega[3, np, n^2V_E/3V_Z]$. The solid curve is for the $5p$ state, the dotted curve is for the $4p$ state, the short dashes are for the $3p$ state, and the long dashes are for the $2p$ state.

This formula, along with formula (2.9) and the differential operators presented in Appendix 2, allows us to find the function $a[3, np, x]$ for the third harmonic:

$$a[2N+1, np, x] = \frac{x}{(1+x^2)^{2n+(1/2)}} P_{4n}[2N+1, np, x], \tag{3.2}$$

where $P_{4n}[2N+1, np, x]$ are $4n$th-degree polynomials comprising even powers of x. In the case of formula (3.1), relationship (3.2) should be used with $2N+1=3$. However, relationship (3.2) is also valid for the fifth and seventh harmonics. That is why these two harmonics are considered together with the third harmonic. Let us now return to the third harmonic, in which case the polynomials $P_{4n}[2N+1, np, x]$ for the first four np states have the form

$$P_8[3, 2p, x] = -\frac{1}{45}(45 + 195x^2 + 356x^4 + 222x^6 + 51x^8),$$

$$P_{12}[3, 3p, x] = -\frac{1}{105}(105 + 665x^2 + 2219x^4 + 1461x^6 + 1429x^8 + 561x^{10} + 89x^{12}),$$

$$P_{16}[3, 4p, x] = -\frac{1}{315}(315 + 2625x^2 + 14098x^4 - 4052x^6 + 34074x^8 + 9754x^{10} + 6520x^{12} + 1860x^{14} + 225x^{16}), \tag{3.3}$$

$$P_{20}[3, 5p, x] = -\frac{1}{495}(495 + 5115x^2 + 41459x^4 - 107283x^6 + 413952x^8 - 206276x^{10} + 176310x^{12} + 28395x^{14} + 14425x^{16} + 3225x^{18} + 315x^{20}).$$

The plots of the four functions $H[3, np, V_E/V_Z]$ for $n = 2, 3, 4$, and 5 are shown in Fig. 1. For comparatively small values of the argument, these polynomials, which, according to formula (2.6), directly characterize the effective nonlinear collision frequencies, are very different for different values of the principal quantum number. A unified scaling for such different frequencies can be constructed using the functions

$$\Omega\left[2N+1, np, \frac{n^2V_E}{(2N+1)V_Z}\right] = \frac{(2N+1)^3}{n^{5/2}} A\left[2N+1, np, \frac{nV_E}{V_Z}\right]. \tag{3.4}$$

In accordance with formulas (2.6) and (2.8), we have

$$\nu^{(2N+1)}(np, E) = \nu_Z \frac{n^{11/2}}{(2N+1)^3} \Omega\left[2N+1, np, \frac{n^2V_E}{(2N+1)V_Z}\right]. \tag{3.5}$$

Figure 2 shows the plots of the four functions $\Omega[3, np, n^2V_E/3V_Z]$. The larger the principal quantum number, the more closely spaced the functions in the regions of their extremes. This yields an approximate scaling for the values of the function $\Omega[3, np, n^2V_E/3V_Z]$ and the approximate scaling

$$\sim \frac{n^2V_E}{V_Z}. \tag{3.6}$$

For the fifth harmonic, relationship (2.10) gives (cf. [7])

$$\alpha[5, b, x] = \operatorname{arcsinh}\left(\frac{x}{b}\right) + \frac{24b}{5x} + \frac{64b^3}{15x^3} - \frac{64b^4 + 104b^2x^2 + 43x^4}{15x^3\sqrt{b^2 + x^2}}. \quad (3.7)$$

In accordance with expression (2.9), this formula leads to a relationship of form (2.2), in which case the polynomials $P_{4n}[5, np, x]$ are as follows:

$$P_8[5, 2p, x] = -\frac{1}{15}(15 + 65x^2 + 108x^4 + 90x^6 + 25x^8),$$

$$P_{12}[5, 3p, x] = -\frac{1}{105}(105 + 665x^2 + 1771x^4 + 3029x^6 + 1765x^8 + 785x^{10} + 145x^{12}),$$

$$P_{16}[5, 4p, x] = -\frac{1}{525}(525 + 4375x^2 + 16\,030x^4 + 46\,260x^6 + 19\,382x^8 + 41\,942x^{10} + 15\,720x^{12} + 4780x^{14} + 655x^{16}), \quad (3.8)$$

$$P_{20}[5, 5p, x] = -\frac{1}{165}(165 + 1705x^2 + 7953x^4 + 36\,399x^6 - 20\,944x^8 + 113\,460x^{10} + 954x^{12} + 27\,417x^{14} + 7683x^{16} + 1779x^{18} + 193x^{20}).$$

The plots of the functions $H[5, np, V_E/V_Z]$ calculated from formulas (2.8), (2.11), (3.1), and (3.8) are displayed in Fig. 3, showing a strong dependence on the principal quantum number. The plots of the four functions $\Omega[5, np, n^2V_E/5V_Z]$ in Fig. 4 allow us to arrive at an approximate scaling analogous to the scaling that can be inferred from Fig. 2.

Finally, for the seventh harmonic, formula (2.10) becomes

$$\alpha[7, b, x] = \operatorname{arcsinh}\left(\frac{x}{b}\right) + \frac{b}{105x^2}(720x^4 + 1600x^2b^2 + 1152b^4) - \frac{1}{105x^5\sqrt{b^2 + x^2}}(337x^6 + 1376x^4b^2 + 2176x^2b^4 + 1152b^6). \quad (3.9)$$

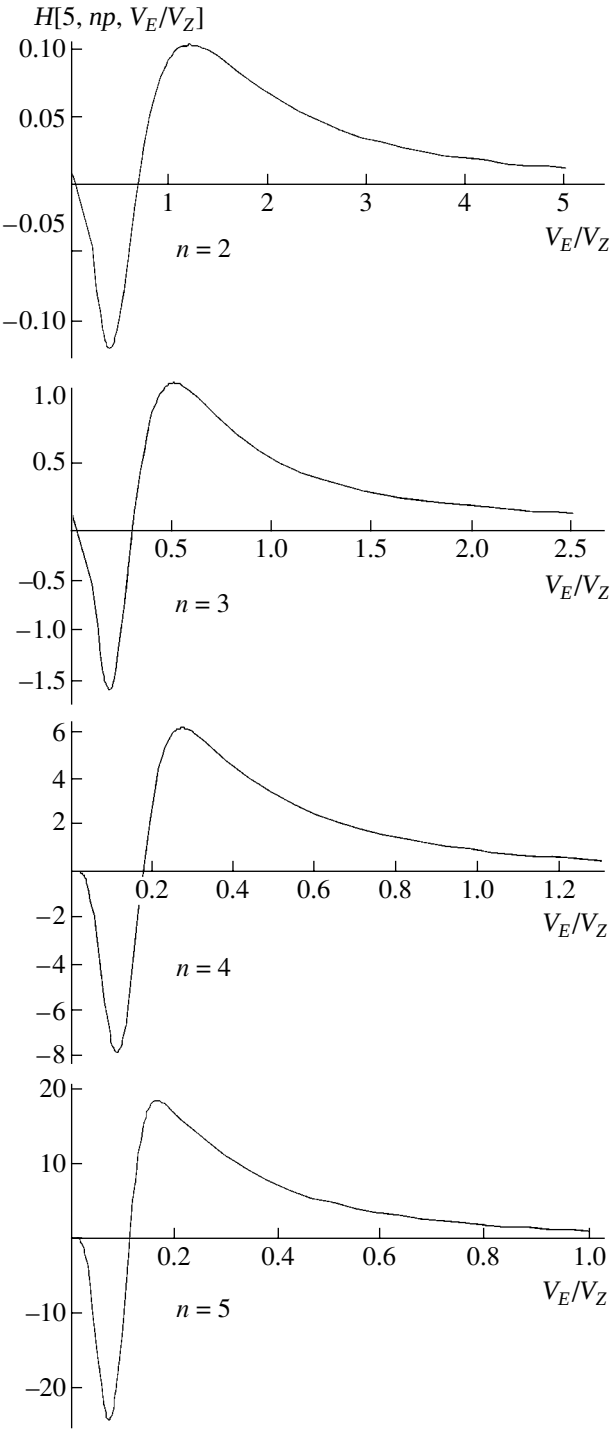

Fig. 3. Functions $H[5, np, V_E/V_Z]$ for different values of the principal quantum number.

In accordance with relationship (2.9), this formula reduces to a relationship of form (3.2), the polynomials $P_{4n}[7, np, x]$ being

$$P_8[7, 2p, x] = -\frac{1}{105}(105 + 455x^2 + 756x^4 + 582x^6 + 211x^8),$$

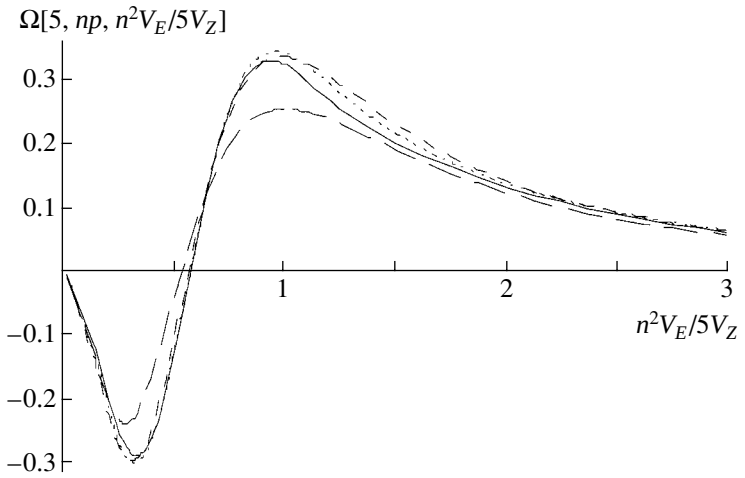

Fig. 4. Functions $\Omega[5, np, n^2V_E/5V_Z]$. The solid curve is for the $5p$ state, the dotted curve is for the $4p$ state, the short dashes are for the $3p$ state, and the long dashes are for the $2p$ state.

$$P_{12}[7, 3p, x] = -\frac{1}{105}(105 + 665x^2 + 1771x^4 + 2549x^6 + 2461x^8 + 809x^{10} + 181x^{12}),$$

$$P_{16}[7, 4p, x] = -\frac{1}{105}(105 + 875x^2 + 3206x^4 + 6756x^6 + 11\,662x^8 + 4702x^{10} + 4680x^{12} + 1052x^{14} + 167x^{16}), \quad (3.10)$$

$$P_{20}[7, 5p, x] = -\frac{1}{1155}(1155 + 11\,935x^2 + 55\,671x^4 + 154\,473x^6 + 433\,928x^8 - 19164x^{10} + 579\,690x^{12} + 68\,367x^{14} + 81\,501x^{16} + 14\,301x^{18} + 1747x^{20}).$$

The functions $H[7, np, V_E/V_Z]$ corresponding to these expressions are shown in Fig. 5. In Fig. 6, we plot the functions $\Omega[7, np, n^2V_E/7V_Z]$ for the first four np states. Analyzing Fig. 6, we again arrive at an approximate scaling analogous to the scalings that were inferred from Figs. 2 and 4 for the third and fifth harmonics, respectively.

4. In this section, we consider the ninth harmonic, for which we have

$$\alpha[9, b, x] = \operatorname{arcsinh}\left(\frac{x}{b}\right) + \frac{b}{315x^7}(2800x^6 + 11\,200x^4b^2 + 18\,816x^2b^4 + 10\,240b^6) - \frac{1}{315x^7\sqrt{b^2 + x^2}}(1091x^8 + 6688x^6b^2 + 19\,328x^4b^4 + 23\,936x^2b^6 + 10\,240b^8). \quad (4.1)$$

Using relationships (2.9) and (2.11) and taking into account expression (4.1) and the expressions for the differential operators from Appendix 2, we can write the relationship

$$a[9, np, x] = \frac{1}{x^7(1 + x^2)^{2n + (1/2)}}R_{4n + 8}[9, np, x] + \frac{1}{x^7}Q_0[9, np], \quad (4.2)$$

where

$$Q_0[9, 2p] = -\frac{65\,536}{189}, \quad Q_0[9, 3p] = -\frac{655\,360}{315}, \quad Q_0[9, 4p] = -\frac{1\,310\,720}{189}, \quad Q_0[9, 5p] = -\frac{3\,276\,800}{189}, \quad (4.3)$$

and the polynomials $R_{4n + 8}[9, np, x]$ have the form

$$R_{16}[9, 2p, x] = \frac{1}{945}(327\,680 + 1\,474\,560x^2 + 2\,580\,480x^4 + 2\,150\,400x^6 + 805\,455x^8 + 76\,545x^{10} - 13524x^{12} - 3798x^{14} - 2139x^{16}),$$

$$R_{20}[9, 3p, x] = \frac{1}{315}(655\,360 + 4\,259\,840x^2 + 11\,714\,560x^4 + 17\,571\,840x^6 + 15\,375\,045x^8 + 7\,685\,685x^{10} + 1\,916\,607x^{12} + 129\,633x^{14} - 14\,903x^{16} - 2107x^{18} - 623x^{20}),$$

$$R_{24}[9, 4p, x] = \frac{1}{945}(6\,553\,600 + 55\,705\,600x^2$$

$$+ 208\,896\,000x^4 + 452\,608\,000x^6 + 622\,335\,055x^8$$
$$+ 560\,094\,525x^{10} + 326\,697\,546x^{12} + 116\,627\,196x^{14} \quad (4.4)$$
$$+ 21\,798\,210x^{16} + 1\,125\,910x^{18} - 81\,480x^{20}$$
$$- 8988x^{22} - 1743x^{24}),$$

$$R_{28}[9, 5p, x] = \frac{1}{10395}(180\,224\,000 + 1\,892\,352\,000x^2$$
$$+ 8\,988\,672\,000x^4 + 25\,467\,904\,000x^6$$
$$+ 47\,752\,309\,605x^8 + 62\,077\,908\,585x^{10}$$
$$+ 56\,904\,346\,961x^{12} + 36\,580\,297\,743x^{14}$$
$$+ 16\,001\,944\,728x^{16} + 4\,440\,951\,676x^{18} + 666\,654\,870x^{20}$$
$$+ 27\,020\,217x^{22} - 1\,361\,829x^{24} - 128\,709x^{26} - 18\,363x^{28}).$$

Although formulas (4.2) and (3.2) are significantly different, the plots of the functions $H[9, np, V_E/V_Z]$ shown in Fig. 7 have much in common with those in Figs. 1, 3, and 5. Moreover, the approximate scaling that can be inferred from the functions $\Omega[9, np, n^2V_E/9V_Z]$ shown in Fig. 8 is similar to the scaling that follows from Figs. 2, 4, and 6 for the third, fifth, and seventh harmonics.

5. Finally, we analyze the case of the eleventh harmonic, when relationship (2.10) becomes

$$\alpha[11, b, x] = \operatorname{arcsinh}\left(\frac{x}{b}\right) + \frac{b}{3465x^9}(37\,800x^8$$
$$+ 235\,200x^6b^2 + 677\,376x^4b^4 + 829\,440x^2b^6$$
$$+ 358\,400b^8) - \frac{1}{3465x^9\sqrt{b^2 + x^2}}(12\,701x^{10} \quad (5.1)$$
$$+ 108\,568x^8b^2 + 492\,608x^6b^4 + 1\,047\,596x^4b^6$$
$$+ 1\,008\,640x^2b^8 + 358\,400b^{10}).$$

Using formulas (2.9), (2.11), and (4.1) and the expressions given in Appendix 2, we obtain

$$a[11, np, x] = \frac{1}{x^9(1 + x^2)^{2n + (1/2)}}R_{4n + 10}[11, np, x]$$
$$+ \frac{1}{x^9}Q_2[11, np, x], \quad (5.2)$$

where the polynomials $Q_2[11, np, x]$ have the form

$$Q_2[11, 2p, x] = -\frac{65\,536(56 + 27x^2)}{693},$$

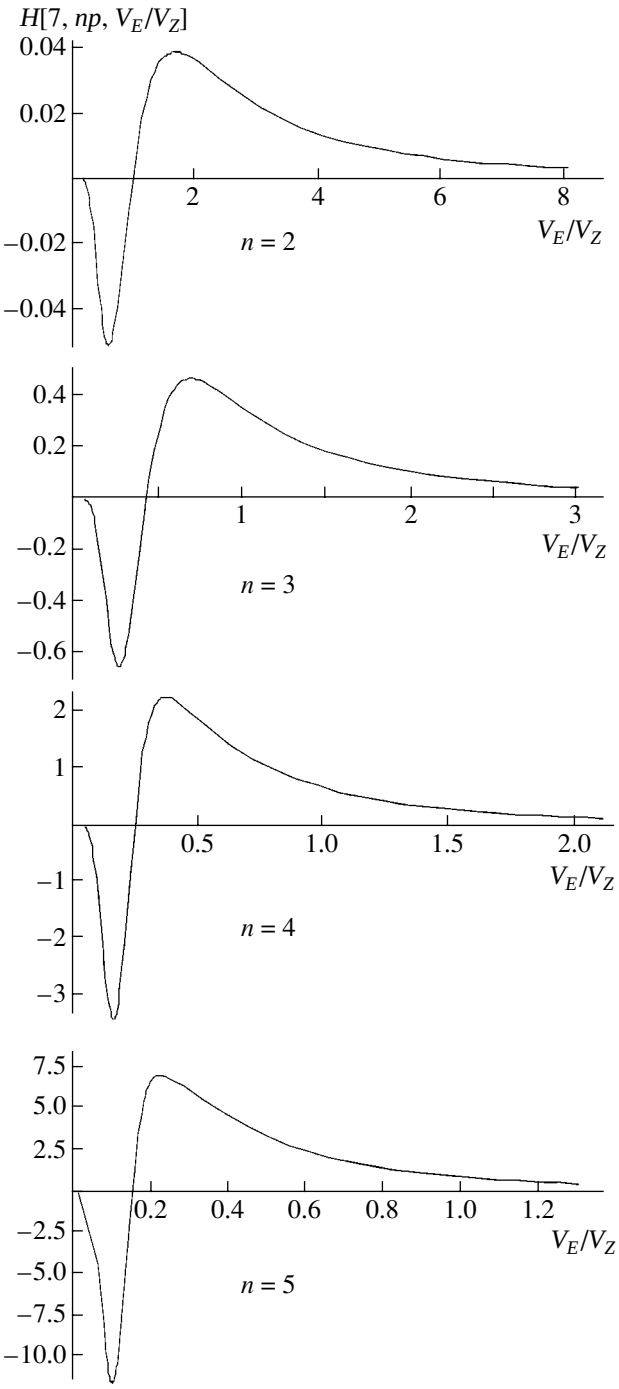

Fig. 5. Functions $H[7, np, V_E/V_Z]$ for different values of the principal quantum number.

$$Q_2[11, 3p, x] = -\frac{131\,072(280 + 81x^2)}{693},$$
$$Q_2[11, 4p, x] = -\frac{262\,144(728 + 135x^2)}{693}, \quad (5.3)$$
$$Q_2[11, 5p, x] = -\frac{655\,360(1064 + 135x^2)}{693}$$

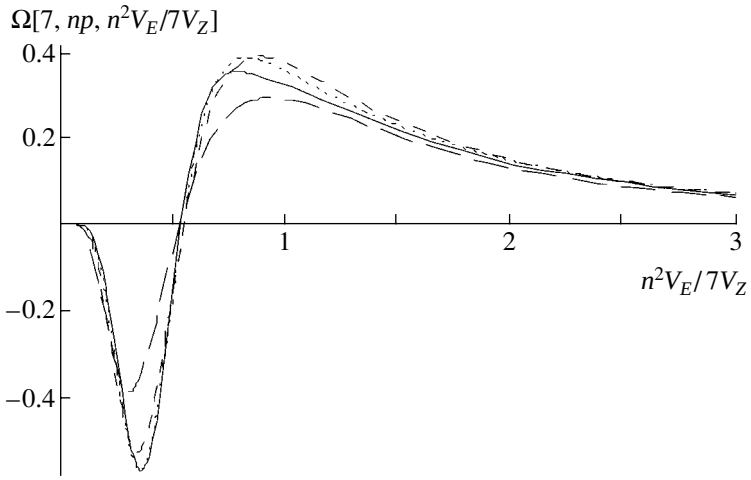

Fig. 6. Functions $\Omega[7, np, n^2V_E/7V_Z]$. The solid curve is for the $5p$ state, the dotted curve is for the $4p$ state, the short dashes are for the $3p$ state, and the long dashes are for the $2p$ state.

and, accordingly, the polynomials $R_{4n+10}[11, np, x]$ are written as

$$R_{18}[11, 2p, x] = \frac{1}{3465}(18350080 + 91422720x^2 + 184320000x^4 + 190095360x^6 + 103219200x^8 + 26285175x^{10} + 1785945x^{12} - 125748x^{14} - 5526x^{16} - 8543x^{18}),$$

$$R_{22}[11, 3p, x] = \frac{1}{3465}(183500800 + 1245839360x^2 + 3625123840x^4 + 5868994560x^6 + 5728419840x^8 + 3397951095x^{10} + 1160817735x^{12} + 194055477x^{14} + 8633163x^{16} - 364133x^{18} - 16177x^{20} - 7553x^{22}),$$

$$R_{26}[11, 4p, x] = \frac{1}{3465}(954204160 + 8287682560x^2 + 31919308800x^4 + 71539916800x^6 + 102832537600x^8 + 98353977975x^{10} + 62694099765x^{12} + 25811279802x^{14} + 6335935452x^{16} + 767413570x^{18} + 23714530x^{20} - 625800x^{22} - 27356x^{24} - 7091x^{26}),$$

(5.4)

$$R_{30}[11, 5p, x] = \frac{1}{3465}(3486515200 + 37050777600x^2 + 178534809600x^4 + 514751283200x^6 + 986302464000x^8 + 1318137673335x^{10} + 1253223426595x^{12} + 847364751387x^{14} + 399405057381x^{16} + 125286814576x^{18} + 23811668412x^{20} + 2221803150x^{22} + 50046899x^{24} - 910623x^{26} - 38703x^{28} - 6821x^{30}).$$

The plots of the functions $H[11, np, V_E/V_Z]$ are depicted in Fig. 9. The approximate scaling that can be inferred from the essential quantitative difference between these functions for the first four np states reduces to the scaling that describes the dependence on the principal quantum number and corresponds to the plots of the functions $\Omega[11, np, n^2V_E/11V_Z]$ shown in Fig. 10.

In order to show how accurate the scaling demonstrated by Fig. 10 is, note that, for $2N + 1 = 11$, all of the four curves in this figure cross the horizontal axis in the interval 0.52–0.54 of the values of the argument

$$n^2V_E/(2N + 1)V_Z. \quad (5.5)$$

Table

$2N + 1$	$a[2N + 1, 2p, \infty]$	$a[2N + 1, 3p, \infty]$	$a[2N + 1, 4p, \infty]$	$a[2N + 1, 5p, \infty]$
3	−1.13	−0.85	−0.71	−0.64
5	−1.67	−1.38	−1.25	−1.17
7	−2.01	−1.72	−1.59	−1.51
9	−2.26	−1.98	−1.84	−1.77
11	−2.46	−2.18	−2.05	−1.97

6. Here, we consider how the effective nonlinear collision frequencies depend on the pump fields of low and high intensities. We start by discussing the limit of strong pump fields such that

$$\frac{nV_E}{V_Z} \gg 1. \tag{6.1}$$

In accordance with representation (2.11), we can write the following asymptotic formula:

$$A\left[2N+1, np, \frac{nV_E}{V_Z}\right] = \frac{V_Z^3}{(nV_E)^3}\left\{\ln\frac{nV_E}{V_Z} + a[2N+1, np, \infty]\right\}. \tag{6.2}$$

In particular, according to formulas (3.3), (3.8), (4.4), and (5.4), the numbers $a[2N+1, ns(p), \infty]$ are on the order of unity, as can be seen from the table. Using formulas (2.6) and (2.8), we obtain the following asymptotic dependence of the effective partial collision frequencies on the pump field of high intensity:

$$\nu^{(2N+1)}(np, E) = \nu_Z\frac{V_Z^3}{V_E^3}\ln\left[\frac{2V_E}{V_Z}\right]. \tag{6.3}$$

We can see that, in the limit of strong pump fields, the effective collision frequencies are approximately independent of both the harmonic number and the value of the principal quantum number. The latter is valid at least for the comparatively small values of the principal quantum number that have been considered above.

Now, we will analyze the opposite limit of weak pump fields such that

$$\frac{nV_E}{V_Z} \ll 1. \tag{6.4}$$

In this limit, we can use the relationship

$$J_{2N+1}(\varsigma) \simeq \frac{1}{(2N+1)!}\left(\frac{\varsigma}{2}\right)^{2N+1}, \tag{6.5}$$

to reduce formula (2.9) to

$$A\left[2N+1, np, \frac{nV_E}{V_Z}\right] \simeq \left(\frac{nV_E}{2V_Z}\right)^{2N}\frac{N+1}{(2N+1)(2N+3)}U[2N+1, np], \tag{6.6}$$

where

$$U[2N+1, np] = D_{np}\frac{1}{b^{2N+3}}\bigg|_{b=1}. \tag{6.7}$$

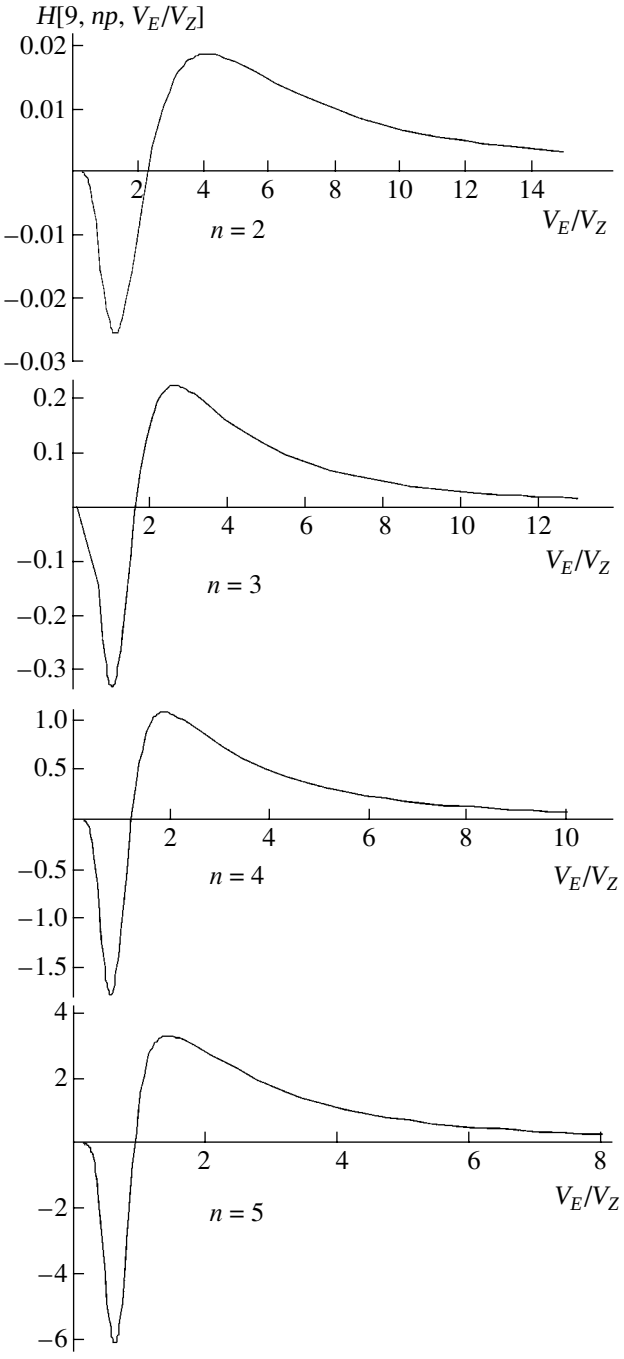

Fig. 7. Functions $H[9, np, V_E/V_Z]$ for different values of the principal quantum number.

For the first four *np* states, expressions (6.7) take the form

$$U[2N+1, 2p] = -\frac{16}{45}N(24 + 26N + 9N^2 + N^3),$$

$$U[2N+1, 3p] = -\frac{32}{315}N(264 + 478N + 355N^2 + 135N^3 + 26N^4 + 2N^5),$$

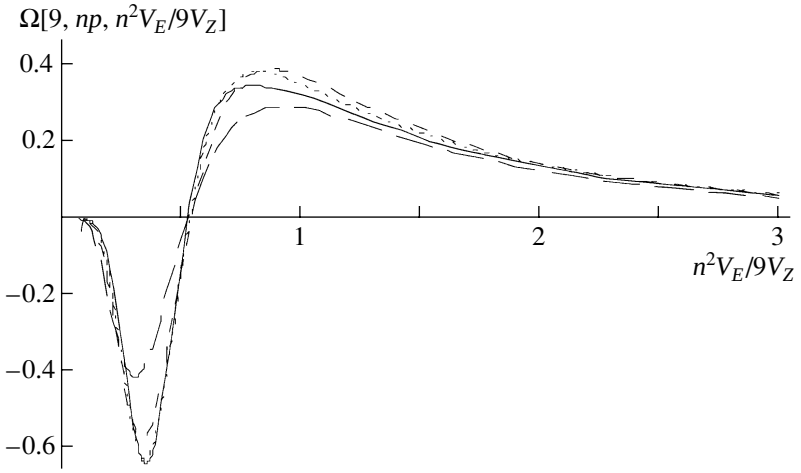

Fig. 8. Functions $\Omega[9, np, n^2V_E/9V_Z]$. The solid curve is for the $5p$ state, the dotted curve is for the $4p$ state, the short dashes are for the $3p$ state, and the long dashes are for the $2p$ state.

$$U[2N+1, 4p] = -\frac{64}{4725}N(3960 + 9282N + 9677N^2 + 5821N^3 + 2180N^4 + 508N^5 + 68N^6 + 4N^7), \quad (6.8)$$

$$U[2N+1, 5p] = -\frac{32}{467775}N(1297080 + 3583026N + 4563717N^2 + 3515233N^3 + 1804422N^4 + 641406N^5 + 158448N^6 + 26352N^7 + 2688N^8 + 128N^9).$$

For the $2p$ state, a comparison between the results for the generation of the third and eleventh harmonics yields $U[3, 2p] = -64/3$ and $U[11, 2p] = -896$, which corresponds to the approximate dependence $\sim(2N+1)^{2.8}$. For the $5p$ state, we have $U[3, 5p] = -3200/3$ and $U[11, 5p] = -9788672/3$, which corresponds to the dependence $\sim(2N+1)^{6.2}$. Hence, from formulas (6.6) and (6.8), we can see that, in the limit of weak pump fields, the effective partial collision frequencies depend very strongly on both the harmonic number and the value of the principal quantum number of p states.

7. In this last section, we discuss the results obtained. We begin with a comparative analysis of the differences between the regular features revealed above for a plasma produced by the photoionization of atoms with electrons in the np states and the corresponding theoretical results for the nonlinear partial conductivities of a plasma photoionized from atoms with electrons in the ns states. According to [3, 6, 7], for the first five ns states, the effective nonlinear collision frequencies and, consequently, the partial conductivities have a constant sign. In contrast, for the np states considered above, the effective partial collision frequencies are found to change sign because of their nonlinear dependence on the pump field. On the one hand, in the limit of weak pump fields such that condition (6.4) holds, the effective collision frequencies are negative, in accordance with formula (6.8). On the other hand, in the limit of strong pump fields satisfying condition (6.1), the effective collision frequencies are positive, in accordance with formula (6.3). Figures 2, 4, 6, 8, and 10 show that the values of argument (5.5) at which the effective collision frequencies change sign are close to each other. The plots of the functions $\Omega[2N+1, 5p, 25V_E/(2N+1)V_Z]$ for the third, fifth, seventh, ninth, and eleventh harmonics are displayed in Fig. 11. We can see that, in the regions of the positive extremes of these functions, formula (3.5) provides an approximate scaling of the effective partial collision frequencies with principal quantum number, harmonic number, and argument (5.5). This scaling is similar to that established for the ns states [3]. The difference is that formula (3.5) contains the factor $n^{11/2}$, in contrast to the factor n^5 obtained earlier for the ns states. In addition, the dependence on scale argument (5.5) is radically different. In the range of their negative values, the functions $\Omega[2N+1, 5p, 25V_E/(2N+1)V_Z]$ provide an insufficiently accurate scaling with harmonic number. That is why, in Fig. 12, we show the plots of the functions

$$\Xi\left[2N+1, np, \frac{n^2V_E}{(2N+1)V_Z}\right] = \frac{(2N+1)^{5/2}}{n^{5/2}}A\left[2N+1, np, \frac{nV_E}{V_Z}\right] \quad (7.1)$$

for the $5p$ states and for the five pump field harmonics under consideration. Using functions (7.1), we can represent the effective nonlinear collision frequencies as

$$\nu^{(2N+1)}(np, E) = \nu_Z\frac{n^{11/2}}{(2N+1)^{5/2}}\Xi\left[2N+1, np, \frac{n^2V_E}{(2N+1)V_Z}\right]. \quad (7.2)$$

In the regions of their negative extremes, functions (7.1) provide a better approximation to the scaling of the effective collision frequencies with a harmonic number.

Using the above scalings of the effective collision frequencies, we can obtain an expression for the harmonic generation efficiency. For a plane pump wave and a spatially unbounded homogeneous plasma, we, as usual, (see [6]) define the harmonic generation efficiency as the ratio of the energy flux densities of the generated harmonic and the pump wave. In accordance with this definition, we have

$$\eta^{(2N+1)}(n,E) = \left[\frac{(2N+1)}{4N(N+1)}\frac{\nu^{(2N+1)}(n,E)}{\omega}\right]^2. \quad (7.3)$$

In the limit of strong pump fields such that condition (6.1) holds, we can use this condition to reduce relationship (7.3) to the form

$$\eta^{(2N+1)}(n,E) \simeq \left(\frac{\nu_Z}{\omega}\right)^2\left(\frac{(2N+1)}{4N(N+1)}\frac{V_Z^3}{V_E^3}\ln\left[\frac{2V_E}{V_Z}\right]\right)^2. \quad (7.4)$$

For pump field intensities corresponding to the vicinity of the positive extreme of function (3.4), formula (3.5) permits us to represent relationship (7.3) as

$$\eta^{(2N+1)}(n,E) \simeq \left(\frac{\nu_Z}{\omega}\right)^2\left(\frac{n^{11/2}\Omega\left[2N+1, np, \frac{n^2V_E}{(2N+1)V_Z}\right]}{4N(N+1)(2N+1)^2}\right)^2. \quad (7.5)$$

For pump field intensities corresponding to the vicinity of the negative extreme of function (3.4), we arrive at the formula

$$\eta^{(2N+1)}(n,E) \simeq \left(\frac{\nu_Z}{\omega}\right)^2\left(\frac{n^{11/2}\Xi\left[2N+1, np, \frac{n^2V_E}{(2N+1)V_Z}\right]}{4N(N+1)(2N+1)^{3/2}}\right)^2. \quad (7.6)$$

To give better insight into the order of magnitude of the harmonic generation efficiency, we turn to the plots of the scale functions shown in Figs. 11 and 12 and to the approximate scaling laws provided by formulas (7.4)–(7.6) for the collision frequencies as functions of harmonic number and the principal quantum number and also present the following expression:

$$\frac{\nu_Z}{\omega} \simeq 4.7\times10^{-4}\frac{Z_i}{Z^3}\left(\frac{I_H}{10\hbar\omega}\right)\left(\frac{\Lambda}{10}\right)\frac{N_e}{10^{18}\ \mathrm{cm}^{-3}}, \quad (7.7)$$

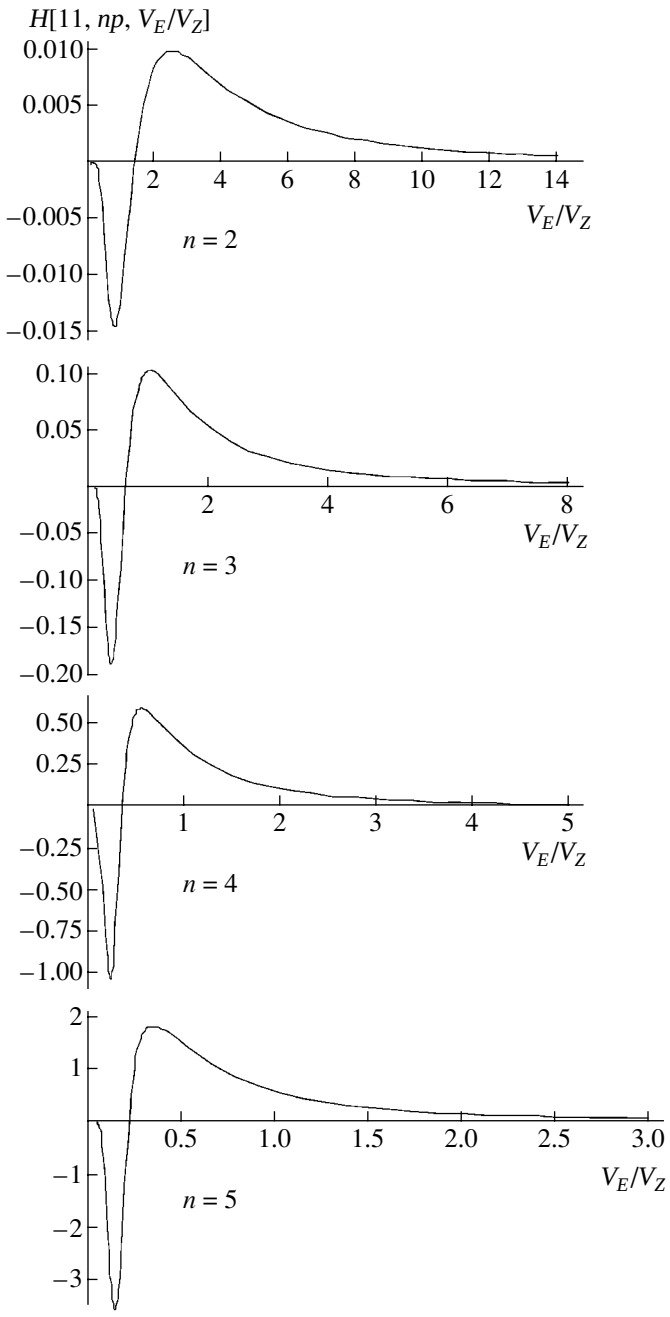

Fig. 9. Functions $H[11, np, V_E/V_Z]$ for different values of the principal quantum number.

where I_H is the ionization potential of a hydrogen atom and Z_i is the ion charge number. Finally, we write out the expression for the energy flux density of the pump field:

$$q = 9\times10^{13}Z^2\left(\frac{V_E}{V_Z}\right)^2\left(\frac{10\hbar\omega}{I_H}\right)^2\frac{\mathrm{W}}{\mathrm{cm}^2}. \quad (7.8)$$

Energy flux density (7.8) is determined by the ratio of the electron oscillatory velocity to the Coulomb veloc-

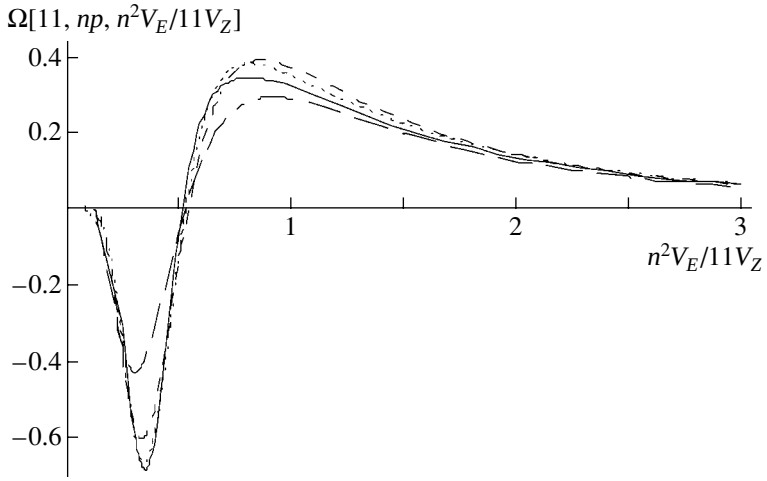

Fig. 10. Functions $\Omega[11, np, n^2V_E/11V_Z]$. The solid curve is for the $5p$ state, the dotted curve is for the $4p$state, the short dashes are for the $3p$ state, and the long dashes are for the $2p$ state.

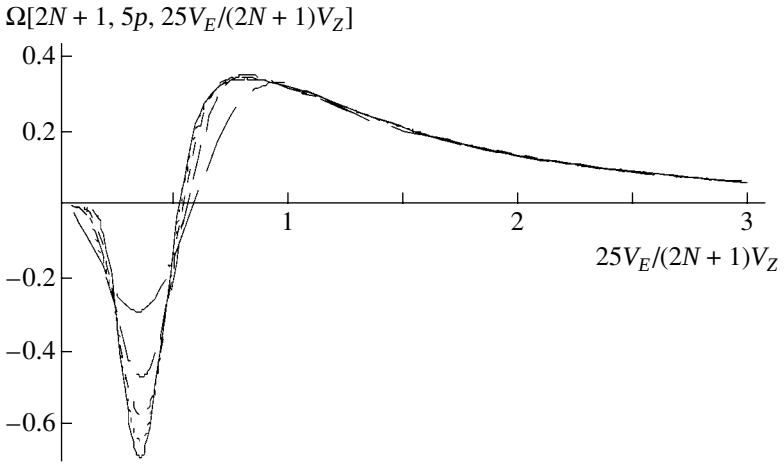

Fig. 11. Functions $\Omega[2N + 1, 5p, 25V_E/(2N + 1)V_Z]$. The long dashes are for the third harmonic, the intermediate-length dashes are for the fifth harmonic, the short dashes are for the seventh harmonic, the dotted curve is for the ninth harmonic, and the solid curve is for the eleventh harmonic.

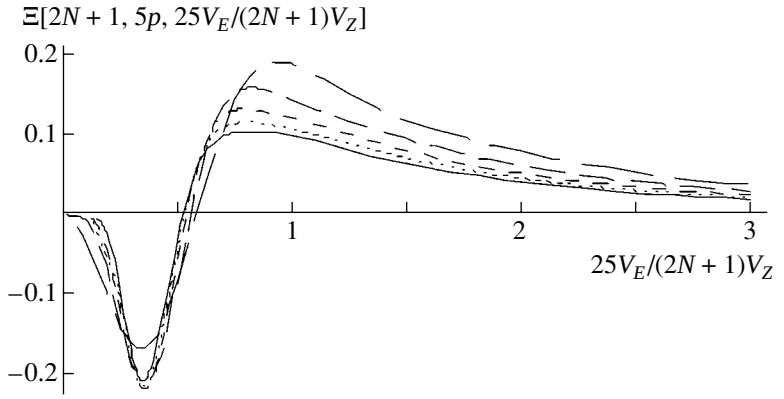

Fig. 12. Functions $\Xi[2N + 1, 5p, 25V_E/(2N + 1)V_Z]$. The long dashes are for the third harmonic, the intermediate-length dashes are for the fifth harmonic, the short dashes are for the seventh harmonic, the dotted curve is for the ninth harmonic, and the solid curve is for the eleventh harmonic.

ity unit. In turn, this ratio enters into the arguments of the functions that were used above to construct scalings for the effective nonlinear collision frequencies.

In summary, using the general approach developed in [8] (see also [9]) as a constituent of the theory of bremsstrahlung-induced coherent harmonic generation in a plasma photoionized from atoms with electrons in the first four *np* states in the Bethe regime of suppression of the ionization barrier, we have established scaling laws for the first five effective nonlinear collision frequencies, which determine the generation efficiencies of the third, fifth, seventh, ninth, and eleventh harmonics as functions of the pump field intensity. The approximate scalings for these effective nonlinear collision frequencies have been derived for the vicinities of their extremes and in the limits of weak and strong pump fields. The regular features revealed above may help to understand the mechanism for harmonic generation in a plasma produced by the photoionization of a gas with neutrals in excited states (cf. [10]). On the other hand, our analysis makes it possible to discern what would be the desired results of future experiments with which to complete the theory developed here.

ACKNOWLEDGMENTS

This work was supported in part by the Russian Foundation for Basic Research (project no. 02-02-16078) and the Federal Program "Support of Scientific Schools."

APPENDIX 1

Here, we present expressions for the coefficients $c_n(p)$, which characterize the values of distribution function (2.2) for the first four *np* states:

$$c_2(p) = 1,$$

$$c_3(p) = \sqrt{6}\left(1 - \frac{1}{2[(1/4) + (3p/2mV_Z)^2]}\right),$$

$$c_4(p) = \sqrt{20}\left(1 - \frac{6}{5[(1/4) + (2p/mV_Z)^2]} + \frac{3}{10[(1/4) + (2p/mV_Z)^2]^2}\right),$$

$$c_5(p) = \sqrt{50}\left(1 - \frac{21}{10[(1/4) + (5p/2mV_Z)^2]} + \frac{6}{5[(1/4) + (5p/2mV_Z)^2]^2} - \frac{1}{5[(1/4) + (5p/2mV_Z)^2]^3}\right).$$

APPENDIX 2

Here, we present expressions for the differential operators D_{np} for the first four *np* states:

$$D_{2p} = 1 - \frac{d}{db} + \frac{1}{3}\frac{d^2}{db^2} - \frac{1}{45}\frac{d^4}{db^4},$$

$$D_{3p} = 1 - \frac{d}{db} + \frac{1}{3}\frac{d^2}{db^2} - \frac{1}{45}\frac{d^5}{db^5} - \frac{1}{315}\frac{d^6}{db^6},$$

$$D_{4p} = 1 - \frac{d}{db} + \frac{1}{3}\frac{d^2}{db^2} + \frac{1}{45}\frac{d^4}{db^4} - \frac{2}{45}\frac{d^5}{db^5} - \frac{34}{1575}\frac{d^6}{db^6} - \frac{2}{525}\frac{d^7}{db^7} - \frac{1}{4725}\frac{d^8}{db^8},$$

$$D_{5p} = 1 - \frac{d}{db} + \frac{1}{3}\frac{d^2}{db^2} + \frac{2}{45}\frac{d^4}{db^4} - \frac{1}{15}\frac{d^5}{db^5} - \frac{19}{315}\frac{d^6}{db^6} - \frac{4}{189}\frac{d^7}{db^7} - \frac{2}{567}\frac{d^8}{db^8} - \frac{4}{14\,175}\frac{d^9}{db^9} - \frac{4}{467\,775}\frac{d^{10}}{db^{10}}.$$

Using these expressions, we can calculate functions (2.9).

REFERENCES

1. H. A. Bethe, *Handbuch der Physik*, B. 1: *Quantenmechanik der Ein- und Zwei-Electronenprobleme* (Berlin, 1933; ONTI, Moscow, 1935).
2. M. V. Fedorov and J. Peatross, Phys. Rev. A **52**, 504 (1995).
3. V. P. Silin and P. V. Silin, submitted to Fiz. Plazmy.
4. V. P. Silin and P. V. Silin, Fiz. Plazmy **28**, 1015 (2002) [Plasma Phys. Rep. **28**, 936 (2002)].
5. L. D. Landau and E. M. Lifshitz, *Quantum Mechanics: Non-Relativistic Theory* (GIFML, Moscow, 1963; Pergamon, New York, 1977).
6. V. P. Silin, Phys. Lett. A **286**, 190 (2001).
7. V. P. Silin, Zh. Éksp. Teor. Fiz. **121**, 291 (2002) [JETP **94**, 244 (2002)].
8. V. P. Silin, Zh. Éksp. Teor. Fiz. **47**, 2254 (1964) [Sov. Phys. JETP **20**, 1510 (1965)].
9. H. Haberland, M. Bonitz, and D. Kremp, Phys. Rev. E **64**, 026405 (2001).
10. F. B. Fedotov, A. N. Naumov, V. P. Silin, *et al.*, Phys. Lett. A **271**, 407 (2000).

Translated by I.A. Kalabalyk

Plasma Physics Reports, Vol. 29, No. 2, 2003, pp. 130–136. Translated from Fizika Plazmy, Vol. 29, No. 2, 2003, pp. 150–156.

SOLID-STATE PLASMA

Dissipation of the Energy of a Fast Charged Particle in a Solid-State Plasma

V. P. Zhurenko*, S. I. Kononenko*, V. I. Karas', and V. I. Muratov***

**Karazin National University, pl. Svobody 4, Kharkiv, 61077 Ukraine*

***National Science Center Kharkiv Institute of Physics and Technology, ul. Akademicheskaya 1, Kharkiv, 310108 Ukraine*

Received February 21, 2002; in final form, September 23, 2002

Abstract—Results are presented from experimental investigations of mechanisms for the dissipation of the energy of light ions in metal plasmas by using the method of secondary electron emission. It is shown that the coefficient of anisotropy of energy transfer from fast light ions is about 1.7. It is also shown that plasma oscillations excited by an ion significantly influence the production and emission of low-energy electrons, especially in the case of projectile molecular ions. © *2003 MAIK "Nauka/Interperiodica".*

1. INTRODUCTION

Because of the wide use of high-energy sources in science and engineering, more attention is being paid to the processes of interaction of charged particle flows with matter, in particular, to mechanisms for the transfer of energy from the particles to the medium. These mechanisms can be investigated by measuring the secondary effects that occur during the passage of a charged particle through a solid. A fast nonrelativistic particle moving in a solid-state plasma excites weakly damped collective oscillations of the electron density (electron wake waves), or so-called plasmons [1]. A particle moving with a velocity such that $v \gg v_0$ (where v_0 is the Bohr orbital velocity of an electron in a hydrogen atom in the ground state) transfers the main portion of its energy to the electron subsystem [2, 3]. The transfer occurs in two different ways: a fraction of the particle energy goes into the excitation of plasmons, and the remaining fraction is converted into the energy of individual electrons in collisions (in particular, in ionizing collisions with atoms). The ionization process that may also come into play when the energy transferred to an atomic electron is sufficiently large is avalanche ionization (by collision cascades) [2]. In turn, plasmons propagating in the medium can give rise to the ionization of atoms in the fields of plasma oscillations, thereby producing new free electrons. The mean energy of the electrons produced by this mechanism is higher than the electron thermal energy (some of the electrons may be even far more energetic). These nonequilibrium electrons are capable of overcoming the potential barrier and thus escaping from the medium. The electrons emitted from the matter carry information about the processes that have occurred in the ionization track of an ion. Hence, by studying electron effects during the passage of a charged particle in a solid, it may be possible to estimate the role of different mechanisms in energy dissipation.

The main features of the mechanism for electron production through ionization by plasma oscillations are associated with a relatively long lifetime of the wake waves and with the continuous excitation of these waves along the entire ionization track. Because of the large lifetime of the wake wave, the secondary ionization inside the track proceeds over a long period of time after the passage of a charged particle. The amount of slow electrons produced in cascade ionization is large when the cascade is initiated by a fast electron. A consequence of the long mean free path of a fast electron in the medium is that, in the cascade ionization, most of the slow electrons are produced over a distance on the order of its mean free path. Consequently, the distribution function of the ionization-produced electrons near the axis of the particle track is dominated by ionization by the wake field, while the distribution at distances from the track axis that are on the order of the mean free path of a fast electron is dominated by cascade ionization [2]. Since the impact ionization is induced only during the propagation of a particle through the medium and since the wake waves play the role of a linear source of secondary electrons, which operates for a long period of time after the passage of a charged particle, the temporal behavior of the ionization processes is completely governed by the wake waves.

Theoretically, it is estimated that a fast particle moving with velocity v expends a comparatively large fraction of its energy on the excitation of collective oscillations [2]:

$$\Delta E_k/\Delta E = \ln(v/10v_0)/2\ln(v/v_0), \qquad (1)$$

where ΔE_k is the fraction of energy that has gone into the excitation of collective oscillations, ΔE is the total energy loss of a fast charged particle in a solid-state

1063-780X/03/2902-0130$24.00

plasma, and v_0 is the Bohr orbital velocity of an electron in a hydrogen atom in the ground state. Since the energy of the wake waves is comparable in order of magnitude to the total energy that the particle transfers to the matter, the energy loss to wake waves can be regarded as an important aspect of the process of dissipation of the energy of a fast particle.

A particle propagating through a medium produces free electrons, some of which, with the proper values and directions of momentum, can escape from the medium. This process is called secondary electron emission (SEE). At present, it is proven theoretically and experimentally that the SEE coefficient in the case of light ions is directly proportional to the mean specific ionization loss dE/dx of an ion in a medium [4, 5]. Consequently, the investigation of SEE makes it possible to derive information about the energy lost by an ion as it moves through a solid-state plasma and about how this energy is distributed between different electron groups. The mean specific ionization loss dE/dx of an ion at each point in a medium can be represented as a sum of the losses associated with the energy transfer to the electrons that move in the same direction as the primary ion, $(dE/dx)_F$ and with the energy transfer to the electrons that move in the opposite direction, $(dE/dx)_B$: $dE/dx = (dE/dx)_F + (dE/dx)_B$. In our opinion, it is quite natural that the quantities $(dE/dx)_F$ and $(dE/dx)_B$ are proportional to the coefficients of SEE in the propagation direction of a fast light ion (in the forward direction), γ_F, and in the opposite (backward) direction, γ_B, respectively. Hence, by investigating the kinetic ion–electron emission from a thin film in the forward and backward directions, it is possible to study the anisotropy of energy transfer from a primary ionizing charged particle.

A high-energy ion propagating through a medium produces a large amount of nonequilibrium electrons (see above), whose energy distribution can be approximated by a power law [6]. Both of the above mechanisms for the energy transfer from the primary particle to the electrons in the medium (the collisional and plasmon mechanisms) contribute to the electron energy distribution. A study of the energy spectra of the electrons that are produced from the SEE induced by fast ions will make it possible to obtain new data on the energy contribution of the wake field to the formation of the nonequilibrium electron distribution function.

The excitation of plasma oscillations is more intense in the case of projectile molecular ions [7–9]. This indicates that an investigation of the kinetic electron emission induced by atomic and molecular ions also provides a promising way of studying the effect of plasma oscillations in a medium on the electron distribution function.

In this paper, we present the results of measurements of the SEE coefficients and electron energy distributions in the forward and backward directions. Generalizing the results obtained in three different experiments makes it possible to determine the mechanisms for energy losses of a fast ion propagating in a solid-state plasma.

2. ANISOTROPY OF THE ENERGY TRANSFER FROM AN ION

In direct (head-on) collisions, a fast primary particle produces the so-called δ electrons. The velocity of the δ electrons that corresponds to the maximum possible momentum transfer can be defined as $v_\delta = 2v_P\cos\theta$, where v_P is the velocity of a bombarding ion and the angle θ is measured from its propagation direction [10]. In further collisions, these fast electrons produce slow electrons as a result of a cascade process [4]. In the medium, the motion of slow electrons produced in the avalanche and in the ionization by a wake field is isotropic, while fast δ electrons move predominantly in the propagation direction of the primary ion. Also, a moving ion entrains some of the free and ionization-produced electrons within the substance. The velocity of these entrained electrons, which are called "accompanying" or "convoy" electrons [11], coincides in magnitude with the velocity of the ion, $v_e = v_P$, and has the same direction [12]. Consequently, in the energy spectrum of the electrons produced from the SEE, we can distinguish between three electron groups: (i) slow electrons with energies $E < E_p$ (where E_p is the energy of the plasma oscillations), which are produced from the ionization by plasma oscillations and from direct collisions with large impact parameters, which are accompanied by small momentum transfers; (ii) moderate-energy electrons, which are produced exclusively in direct collisions accompanied by small momentum transfers; and (iii) fast electrons, which move preferentially in the propagation direction of the ion and can be regarded as being represented by convoy electrons and by δ electrons produced from direct collisions with small impact parameters, which are accompanied by large momentum transfers.

Since a fast primary ion transfers a substantial fraction of its energy to the electrons that move in its propagation direction (convoy electrons and δ electrons), we can speak of the anisotropic energy transfer from an ion.

Experiments aimed at investigating the anisotropy of the energy transfer from a fast ion were carried out on a device whose schematic diagram is shown in Fig. 1. Vacuum chamber *1* was equipped with primary particle source *2*, target *3*, and collector *5*. The pressure of the residual gases in the chamber was no higher than 10^{-6} torr. A 5.15-MeV α-particle flow with the intensity $I_{\alpha 0} = 4.64 \times 10^6$ particles per second was emitted into a half-space by an MIR3-A Pu^{239} radioisotope source. An α-particle flow penetrated target *3* and reached massive collector *5*, which was made of the same material as the target. The experiments were carried out with aluminum, copper, and nickel collector–target pairs. The tar-

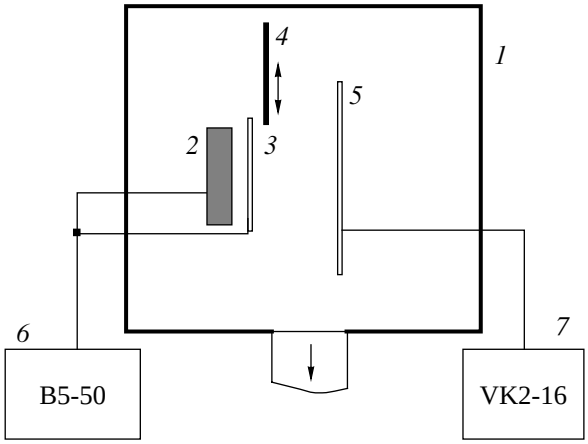

Fig. 1. Schematic of the experimental device: (*1*) vacuum chamber, (*2*) Pu^{239} radioisotope source of α particles, (*3*) target, (*4*) movable diaphragm, (*5*) collector, (*6*) B5-50 dc source, and (*7*) electrometric voltmeter.

gets were in the form of foils 5.6 μm (Al), 2.01 μm (Cu), and 0.27 μm (Ni) thick. The target thicknesses was chosen to be less than the mean free path of α particles with the above energy in a given substance. After passage through the target, α particles had energies no larger than E_{max} (the energy corresponding to the penetration in a direction perpendicular to the target plane). The radioisotope source was connected electrically to the target. A voltage of 300 V of either polarity was applied between the collector and the target by means of B5-50 dc source *6*. In the case of a voltage of positive polarity, the SEE coefficient γ_B was measured from the collector (backward emission), and, in the case of a voltage of negative polarity, the SEE coefficient γ_F was measured from the outer target surface (forward emission). The SEE current I_c was measured in the collector circuit by VK2-16 electrometric voltmeter *7*. The measurement system was adjusted by using movable diaphragm *4*, which was placed between the collector and the target and cut off the particle flow.

The coefficient γ was determined from the formula

$$\gamma_F = 2\frac{k_F I_{\alpha 0} + I_c}{k_F I_{\alpha 0}}, \quad \gamma_B = 2\frac{I_c - k_F I_{\alpha 0}}{k_F I_{\alpha 0}}, \qquad (2)$$

where $I_{\alpha 0}$ is the current of α particles from a radioisotope source and k_F is the fraction of α particles that have passed through the target. The ratio R of the forward SEE coefficient γ_F to the backward one γ_B,

$$R = \gamma_F/\gamma_B, \qquad (3)$$

was measured to be 1.57 for aluminum, 1.69 for copper, and 1.82 for nickel. According to these data, the ratios R for different substances differ insignificantly, by no more than 10% of the mean value.

Rothard and his colleagues [13] carried out a series of measurements of the coefficient γ of SEE induced in a thin carbon film by the ions with different charge numbers. Measurements on both sides of the film showed a considerable difference between the coefficients of SEE from the front surface irradiated by the ions (backward emission) and from the rear surface (forward emission) [13].

An analysis of the above results of our measurements and of the data from experiments [13], carried out with a carbon target and with Li^{2+} ions, which are close in mass, energy ($0.86 \le E \le 1.15$ MeV/amu), and charge state to the α particles used in our experiments, allows us to suggest that the ratios of the fractions of energy that are transferred from a light ion to the electrons moving in the propagation direction of the ion and in the opposite direction are fairly close to each other for different target substances. In the case in question, the energy loss of a light ion (He^{2+}, Li^{2+}) to the electrons moving in its propagation direction is larger than the loss to the electrons moving in the opposite direction by a factor of approximately 1.7.

Presumably, the above difference in the forward and backward SEE coefficients with the same energy of the bombarding ions stems from the presence of convoy and δ electrons, which are emitted predominantly in the propagation direction of the ions. For the targets investigated in our experiments, the energy E_{max} of α particles varied from 0.8 to 1 MeV/amu; consequently, the maximum energies of the emitted convoy electrons and δ electrons are about 0.5 and 2 keV, respectively. The relative amount γ_δ of these electrons can be determined from the difference between the forward and backward SEE coefficients, $\gamma_\delta = \gamma_F - \gamma_B$. Recall that, for light ions, the SEE coefficient is proportional to the mean specific ionization loss dE/dx of an ion in a medium. Therefore, the ratio R_δ of the energy going into the production of convoy and δ electrons to the total energy losses of an ion in a medium can be defined as $R_\delta = \gamma_\delta/\gamma$, where $\gamma = \gamma_F + \gamma_B$ is the total coefficient of the forward and backward SEE. In the case under consideration, with allowance for the experimentally measured values of R, the ratio R_δ is from 0.22 to 0.29. Hence, the δ and convoy electrons can carry away approximately 22–29% of the energy that the ion transfers to the electrons in different substances.

3. ENERGY DISTRIBUTION AMONG DIFFERENT ELECTRON GROUPS

In a number of papers, it was shown theoretically and experimentally that, when ion-induced SEE takes place in a medium, the presence of a flux generated in momentum space by a source (ionization) and a sink (electron emission) results in the formation of a steady-state nonequilibrium power-law electron distribution function in a solid-state plasma:

$$N(E) = AE^{-s}, \qquad (4)$$

where s is the power index and A is a constant [6, 14]. Also, in formula (4), E is the total electron energy in a solid body, $E = \varphi + E_F + eU$, where φ is the work function, E_F is the Fermi energy, and the energy eU is measured from the vacuum energy. The experimentally measured energy distribution functions of the electrons produced from the ion-induced SEE are piecewise power functions with different power indices s for different energy intervals [6, 15].

An important role in the production of free electrons (and, accordingly, in the emission process) is played by the wake-field oscillations. The energy loss to these oscillations can be estimated from formula (1). The energy $E_p = \hbar\omega_p$ of the plasma oscillations, which is usually lower than 25 eV, is nonetheless sufficiently high in comparison with the energy required to excite an electron from its valence band to the conduction band where they are freely mobile. The energy of the electrons produced by ionization by the wake-field oscillations cannot exceed E_p. Consequently, slow electrons produced in this ionization process are distributed in the emission spectrum over its low-energy part, which is bounded from above by the plasmon energy.

Under conditions close to those mentioned above, we experimentally measured the energy spectra of the electrons produced from the backward SEE induced in a beryllium foil by 4.9-MeV α particles [15]. The measurements were carried out in the energy range from 0 to $E^* = 100$ eV. The experimentally obtained power-law energy spectrum may be divided into two parts, the boundary between which is determined by the energy $E_p = 18.9$ eV of a plasmon within the beryllium target. One part of the spectrum is represented by the slow electrons of the first group (see Section 2), and the other, by the moderate-energy electrons of the second group. Since the number of emitted electrons is proportional to the specific energy loss of the primary ion, we can estimate the fractions of the energy lost by the ion to the slow electrons from the first group and to the electrons from the second group. We separately integrate these two parts of the experimental emission spectrum $N(E)$ over energy and determine the number N_1 of electrons from the first group and the number N_2 of electrons from the second group for beryllium:

$$N_1 = \int_{\varphi + E_F + eU}^{E_p} N(E)\sqrt{E}dE, \qquad N_2 = \int_{\varphi + E_F + E^*}^{E_p} N(E)\sqrt{E}dE. \tag{5}$$

The fractions of the energy lost by the ion to the electrons from the first and the second group can be estimated as the ratios of N_1 and N_2 to the total number $N_0 = N_1 + N_2$ of emitted electrons:

$$K_1 = N_1/N_0 = 0.63 \text{ and } K_2 = N_2/N_0 = 0.37. \tag{6}$$

In other words, the energy transferred from the ion to the slow electrons from the first group is about twice as large as the fraction of the ion energy that is lost to the electrons from the second group.

According to the above results on the anisotropy of the energy transfer, approximately one-quarter of the energy lost by a charged particle is converted into the energy of the electrons in direct collisions accompanied by large momentum transfers (δ electrons) and also into the energy of the convoy electrons. The remaining fraction of the energy of a charged particle moving in a solid-state plasma is lost through the following two dissipation mechanisms: first, in direct collisions accompanied by small momentum transfers and, second, by the excitation of plasmons. The fraction of energy that goes into the production of slow electrons ($E < \hbar\omega_p$) can be defined as $\Delta E_{\text{slow}}/\Delta E = K_1(1 - R_\delta)$. In the case at hand, this fraction, which is transferred to electrons by the above two mechanisms, is from 45 to 49% of the total energy lost by an ion in the substance. In our opinion, theoretical formula (1) somewhat overestimates the fraction of the energy $\Delta E_k/\Delta E$ lost to the wake waves: $\Delta E_k/\Delta E \approx 40\%$.

Earlier, it was established that the experimentally measured energy distribution functions of the electrons produced from the ion-induced SEE are piecewise power functions with different power indices s for different energy intervals [6, 15]. Such distribution functions of the electrons that were produced in silver, copper, and nickel thin films from both forward and backward SEE induced by He^+ ions with energies from 1 to 3 MeV were measured in our experiments. Analyzing the experimental SEE spectra, we determined how the power index s_1 for the first energy interval (corresponding to slow electrons with energies $E < 35$ eV) depends on the specific ionization losses of an ion in the medium. Our experimental data show that, over this energy interval, the power index decreases with increasing energy losses of a fast ion [16].

According to the Bethe–Bloch formula [3]

$$-dE/dx = (4\pi Z_1^2 e^4/mv^2) Z_2 N \ln(2mv^2/I) \tag{7}$$

(where m is the mass of an electron, Z_1 is the charge of the incident particle, Z_2 is the charge of the atoms of the decelerated medium, and I is their mean excitation potential), the energy lost by a fast ion decreases with increasing its velocity. Consequently, the higher the velocity (energy) of a fast ion, the larger the relative amount of fast electrons with energies above E_P. This tendency was also pointed out by Hasselcamp *et al.* [17]. In other words, as the velocity of a fast ion increases, the plasmon mechanism for slow electron production becomes less efficient. This result, however, does not follow from formula (1), which implies that the energy $\Delta E_k/\Delta E$ lost by an ion to wake waves only weakly depends on its velocity.

4. MOLECULAR IONS

A great deal of information on wake-field oscillations in a medium penetrated by a fast ion can be obtained by studying the kinetic SEE from metal surfaces bombarded by molecular ions. Such experiments were carried out in a number of papers [7–9]. Hasselcamp and Scharmann [7] studied the energy spectra of the secondary electrons knocked out of a massive copper target by H^+, H_2^+, and H_3^+ ions with an energy of 200 keV/amu. According to the results reported in that paper, measurements in the energy interval $E \le 35$ eV gave power-law spectra of the secondary electrons produced by both atomic and molecular ions. The yields γ of secondary electrons produced from the emission induced by H^+, H_2^+, and H_3^+ bombarding ions are in the ratio 1 : 2 : 3. This ratio fails to hold for the differential electron yield $\gamma(E)$, where E is the energy of the secondary electrons. As was shown by Hasselcamp and Hippler [8], the coefficient $R_\gamma(E)$, defined as

$$R_\gamma(E) = \gamma_{H_2}(E)/2\gamma_{H_1}(E), \quad (8)$$

changes substantially within the energy range 0–200 eV of the secondary electrons. The data published in [8] show that, for a golden target bombarded by primary ions with energies from 75 to 300 keV/amu, the curve $R_\gamma(E)$ has two maxima. For low-energy secondary electrons, the coefficient is $R_\gamma(E) < 1$. It should be noted that, with increasing the energy of the primary ions, the first maximum and the intersection point with the straight line $R_\gamma = 1$ both shift toward lower energies, while the second maximum shifts toward higher energies. Hasselcamp and Hippler [8] pointed out that the electron velocity corresponding to the second maximum is equal to the velocity of the bombarding ions.

As a molecular ion enters the medium, it breaks into fragments, each of which excites plasma oscillations. In studying kinetic electron emission induced by CO^+, C^+, and O^+ ions, Frischkorn *et al.* [9] showed that the interference between the plasma oscillations excited by different fragments of a molecular ion influence the total electron yield.

When a medium is penetrated by a diatomic molecule (rather than by an atom or ion), the processes of the trapping and loss of electrons by the molecule become important at velocities close to those of the bound electrons of the atoms in the medium, as is the case with a bombarding atom. Because of ionization, the ions composing the molecule experience Coulomb repulsion. This repulsion becomes strong so rapidly that it is possible to speak of a Coulomb explosion. As a result, a diatomic molecule moving in the medium breaks into two ions [18]. As a fast hydrogen molecular ion moves through the target substance, it is completely ionized and breaks into fragments—atomic ions—which propagate over distances that only slightly exceed the radius r of their Coulomb screening. For metals, we have $r \sim 10^{-8}$ cm. The diameter of the ionization track is determined by the length of a collision cascade and is approximately equal to 10^{-6} cm; this indicates that both fragments of a molecular ion move in the same track.

A molecule with an energy of $E \ge 100$ keV per nucleon starts to be stripped of electrons as it propagates through just the first several outer monolayers of the target; i.e., the constituent ions of the molecule begin to experience Coulomb repulsive forces immediately after the molecule enters the target and, as a result, the distance between the ions begins to increase with time. An experimental analysis showed that the ions fly away from their mutual center of mass in an asymmetric fashion [19]. The observed asymmetry can be explained as being due to the effect of plasma oscillations excited by the ion fragments and indicates that, as the fragments fly apart, they undergo an additional interaction with matter.

The interaction of atomic and molecular ions with target substances was investigated in the experimental device described in detail in [16]. We studied secondary electron emissions from silver, copper, and nickel thin foils in the forward direction, i.e., in the propagation direction of the primary ion. As in the experiments reported above, the thicknesses of the targets were less than the mean free paths of ions with given energies in the corresponding substances and were chosen to be 2.0 μm for silver, 2.1 μm for copper, and 1.1 μm for nickel. The targets were produced by chemical means. In most experiments, the beam current density at the target was no greater than 0.1 μA/cm^2. A small-aperture retarding-potential spectrometer was oriented at an angle of 40° to the ion beam. Earlier, it was shown that the functional dependence of the emission spectra is insensitive to the measurement direction. As a recording and storage terminal system, we used an AI-1024-95 pulse analyzer connected to a computer. The energy width of each of the analyzer channels was 0.044 eV, the total number of channels was 1024. The measured data were processed by a computer.

Figure 2 shows representative energy spectra of the SEE induced in a silver target by 1-MeV H^+ ions and by 2-MeV H_2^+ ions. According to our experimental results, the distribution functions of the nonequilibrium electrons emitted from all kinds of targets are power-law functions with power indices close to those given in [6]. In order to reveal the differences between the energy spectra from SEE induced by molecular and atomic hydrogen ions, we calculated the differential coefficient $R_\gamma(E)$, which was defined in formula (8). Figure 3 illustrates the coefficient $R_\gamma(E)$ as a function of the energy of the secondary electrons for the three kinds of targets used in our experiments. We can see that the plots obtained for different targets have the same shape and differ exclusively in amplitude. It is worth noting that the positions at which the coefficient $R_\gamma(E)$ is maximum are different for different targets. The larger the specific energy loss dE/dx of an ion, the lower the

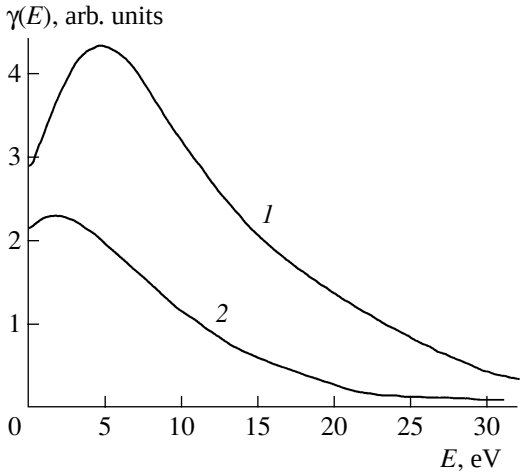

Fig. 2. Energy spectra of the secondary electrons produced from a silver target by (*1*) H_2^+ ions with an energy of 2 MeV and (*2*) H^+ ions with an energy of 1 MeV.

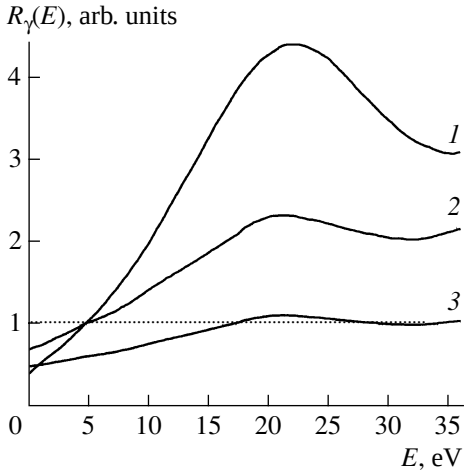

Fig. 3. Experimental dependences of the coefficient $R_\gamma(E)$ on the energy of the secondary electrons for (*1*) Cu, (*2*) Ni, and (*3*) Ag.

energy of the secondary electrons at the maximum in the curve $R_\gamma(E)$ and the larger the amplitude of the curves. The curves $R_\gamma(E)$ obtained in [8] for a massive gold target are similar to those shown in Fig. 3. Analogous curves were also derived from experiments with primary ions of lower energies.

In analyzing the experimental curves presented in Fig. 3, it is important to take into account that each of them has a maximum and that, for secondary-electron energies lower than 10 eV, the differential coefficient is smaller than unity, $R_\gamma(E) < 1$. Presumably, the presence of the maxima can be explained as follows. When propagating through the medium, a diatomic molecule loses a larger fraction of energy than do two atomic ions [2]; moreover, the fraction of the energy that goes into the excitation of the wake waves is substantially larger. The energy of the plasma oscillations is fixed for a given substance [1]; consequently, the energy loss to plasma oscillations is associated with a certain part of the electron energy spectrum, specifically, with electrons whose energy is no greater than the plasmon energy. These considerations indicate that the maxima in the curves $R_\gamma(E)$ may be of plasmon origin.

The fact that, in the SEE spectra, there are energy intervals over which molecular ions (diatomic molecules) produce low-energy electrons less efficiently than do their constituents can possibly be explained as follows. In the low-energy range over which $R_\gamma(E) < 1$, the electrons are produced not only by the plasmon mechanism but also in direct collisions of a moving ion with the atoms of the target substance. In this case, the fore ion of a diatomic molecule prevents its rear ion from colliding with the atoms. The rear ion can thus be shadowed by the fore ion; as a result, the yield of the low-energy electrons (in the range $R_\gamma(E) < 1$) in the case of an H_2^+ ion is smaller than that in the case of two H^+ ions. Moreover, in a hydrogen molecule moving through a medium, the rear ion is in the wake of the fore ion; hence, the rear ion may be additionally screened by the electrons of the medium. Since slow electrons are produced in distant collisions, their number can be much smaller than that in the case of two individual protons. Consequently, the presence of the spectral interval over which $R_\gamma(E) < 1$ in the spectra of the secondary electrons can also be explained as being due to the additional screening of the rear ion in a diatomic molecule by the electrons of the medium.

The above two possible causes of the smaller efficiency of the production of low-energy electrons by molecular ions imply that the collisional mechanism for producing slow secondary electrons is hindered by the correlated motion of the molecule fragments in the medium.

Our experiments show that, when a fast charged particle passes through a substance, the mechanism for producing free electrons in the ionization by plasma oscillations appears to be more efficient in the case of projectile molecular (rather than atomic) ions.

5. CONCLUSION

According to the above analysis of the results obtained, the observed anisotropy of the ion-induced SEE is presumably associated with the fraction of energy that is carried away from the medium by both convoy and δ electrons. An increase in the energy (velocity) of the bombarding ions leads to an increase in the relative number of electrons with energies higher than the energy of the plasmons in the substance. In addition, it has been noted that plasma oscillations excited by an ion have a substantial impact on the pro-

duction and emission of electrons, especially in the case of projectile molecular ions.

ACKNOWLEDGMENTS

We would like to note the great contribution of Prof. S.S. Moiseev (now deceased) to the formulation of the problem and the discussion of the experimental results. This work was supported in part by the Ukrainian Center for Science and Technology, project no. 1862.

REFERENCES

1. F. Plattzman and P. Wolff, *Waves and Interactions in Solid-State Plasma* (Academic, New York, 1972; Mir, Moscow, 1975).
2. N. P. Kalashnikov, V. S. Remizovich, and M. I. Ryazanov, *Collisions of Fast Charged Particles in Solids* (Atomizdat, Moscow, 1980).
3. Yu. V. Gott, *Interaction of Particles with Substance in Plasma Research* (Atomizdat, Moscow, 1978).
4. E. J. Sternglass, Phys. Rev. **108**, 1 (1957).
5. D. Hasselkamp, S. Hippler, and A. Scharmann, Nucl. Instrum. Methods Phys. Res. B **18**, 561 (1987).
6. E. N. Batrakin, I. I. Zalyubovskiĭ, V. I. Karas', *et al.*, Zh. Éksp. Teor. Fiz. **89**, 1098 (1985).
7. D. Hasselcamp and A. Scharmann, Phys. Lett. A **96A** (5), 259 (1983).
8. D. Hasselcamp and S. Hippler, Nucl. Instrum. Methods Phys. Res. B **2** (2), 475 (1984).
9. H. J. Frischkorn, K. O. Groeneveld, P. Koschar, *et al.*, Phys. Rev. Lett. **49**, 1671 (1982).
10. H. J. Frischkorn, K. O. Groeneveld, D. Hofmann, *et al.*, Nucl. Instrum. Methods Phys. Res. **214**, 123 (1983).
11. Y. Yamazaki and N. Oda, Nucl. Instrum. Methods Phys. Res. B **10** (11), 161 (1985).
12. B. A. Brusilovskiĭ, *Kinetic Ion-Induced Electron Emission* (Énergoatomizdat, Moscow, 1990).
13. A. Clouvas, C. Potiriadis, H. Rothard, *et al.*, Phys. Rev. B **55**, 12086 (1997).
14. V. I. Karas', S. S. Moiseev, and V. E. Novikov, Zh. Éksp. Teor. Fiz. **71**, 1421 (1976).
15. E. N. Batrakin, I. I. Zalyubovskiĭ, V. I. Karas', *et al.*, Poverkhnost' **12**, 82 (1986).
16. S. I. Kononenko, Dopov. NANU, No. 1, 87 (2001).
17. D. Hasselcamp, S. Hippler, and A. Scharmann, Nucl. Instrum. Methods Phys. Res. B **18**, 561 (1987).
18. W. Brandt, A. Ratkowski, and R. H. Ritchie, Phys. Rev. Lett. **33**, 1325 (1974).
19. W. Brandt and R. H. Ritchie, Nucl. Instrum. Methods **132**, 43 (1976).

Translated by G.V. Shepekina

Plasma Physics Reports, Vol. 29, No. 2, 2003, pp. 137–150. Translated from Fizika Plazmy, Vol. 29, No. 2, 2003, pp. 157–171.

PLASMA TURBULENCE

Generation of Zonal Flows and Large-Scale Magnetic Fields by Drift-Alfvén Turbulence

V. P. Lakhin

Nuclear Fusion Institute, Russian Research Centre Kurchatov Institute, pl. Kurchatova 1, Moscow, 123182 Russia

Received June 20, 2002

Abstract—The possibility of generating zonal perturbations by drift-Alfvén turbulence in a plasma with a finite pressure ($1 > \beta > m_e/m_i$) is investigated. A set of coupled equations is derived that includes the equation for the spectral function of the turbulence and the averaged equations for zonal perturbations. It is shown that, in particular cases, the equation for the spectral function possesses action invariants; i.e., it takes the form of a conservation law for some quantities that are proportional to the spectral function of turbulence. Two types of instability of the zonal perturbations are revealed. The first type of instability generates only a zonal flow. Two regimes of this instability—resonant and hydrodynamic regimes—are examined, and the corresponding instability growth rates are determined. The second type of instability takes place when the resonant interaction of drift-Alfvén waves with electrons is taken into account. Because of this instability, the generation of a zonal magnetic field is inevitably accompanied by the generation of a zonal flow. It is found that the growth rate of the second type of instability is slower than that of the first type. © *2003 MAIK "Nauka/Interperiodica"*.

1. INTRODUCTION

During the last decade, much attention has been directed to the problem of the generation of sheared zonal flows in a magnetized plasma, i.e., poloidally and toroidally symmetric plasma perturbations with a finite radial wavenumber. This interest stems primarily from the recognition that such flows play a fundamental role in the processes regulating anomalous transport and transitions to improved confinement regimes (L–H transitions) in tokamaks [1–6]. According to present opinion, sheared zonal flows are responsible for the suppression of plasma turbulence and the reduction of the anomalous transport of heat and particles across the tokamak magnetic surfaces (see, e.g., [1, 7]). Hence, in order to gain insight into the scenarios of L–H transitions, it seems worthwhile to investigate the mechanisms for generating sheared zonal flows. The prevailing view is that the spontaneous generation of zonal flows is a consequence of the secondary instability of plasma oscillations. The physical cause for the onset of the secondary instability lies in the nonlinear interaction between the primary oscillations (as a rule, a kind of drift waves excited by some known linear mechanism) that gives rise to a zonal flow. Positive feedback is provided by the modulation of the amplitude of the primary plasma oscillations by the secondary sheared zonal flow; therefore, the instability can be regarded as belonging to the class of parametric (or modulational) instabilities.

Papers in which the generation of zonal flows is attributed to the above nonlinear mechanism may be divided into two groups. The papers of the first (historically earlier) group are based on the ideas and methods of the classical theory of coherent parametric instabilities (see, e.g., [8]). Accordingly, these papers study the models of the interaction of a finite number of waves: a pump wave, whose role is assumed to be played by one of the low-frequency plasma modes, usually of drift origin (such as a drift mode, an ion temperature gradient mode, an electron temperature gradient mode, and a drift-dissipative ballooning mode); a sheared flow (which can be treated as a wave with zero frequency); one or two satellites of the pump wave; and sometimes the second harmonic of the sheared flow [6, 9–13]. The papers of the second (alternative) group [14–19] are similar in concept to the turbulent dynamo theory [20] and to the theory of the generation of large-scale coherent structures by small-scale turbulence [21] and follow the approach that was developed in [22] based on the method of separation of the spatial scales of the turbulence (a small-scale process) and zonal flow (a large-scale process). In this approach, in which it is possible to use the method of multiscale expansions (in the case at hand, a two-scale expansion), small-scale turbulence is described by the wave kinetic equation accounting for the effect of the zonal flow; simultaneously, in the hydrodynamic equations describing the flow, it is necessary to take into consideration the turbulence-related nonlinear effects averaged over small scales. A similar approach to the problem of the generation of large-scale structures (including zonal flows) was used in [23–25], in which, however, the wave kinetic equation was not formally written out; instead, the equations for the small-scale turbulent field were solved by means of a two-scale expansion, and then the quantities averaged over small scales in the equations for the large-scale

1063-780X/03/2902-0137$24.00

field were calculated. In [26], it was shown that the above approaches with the same basic assumptions yield identical results.

The present paper attempts to generalize the theory of the generation of zonal flows that was constructed in [16, 17] in the electrostatic approximation to a plasma with a finite pressure such that $1 > \beta > m_e/m_i$. In this range of β values, which is characteristic of magnetic systems for plasma confinement, an important role is played by electromagnetic effects, specifically, by drift-Alfvén waves, which can develop in the plasma. The approach used in this paper is based on the method of separation of the spatial scales of the drift-Alfvén turbulence and zonal flow and on the equation that is to be derived for the spectral function of the turbulence and is a generalization of the wave kinetic equation obtained in [16, 17]. Earlier, the problem of the generation of a zonal flow by Alfvén turbulence (without allowance for a large-scale zonal magnetic field) and the problem of a fast dynamo, i.e., of the generation of a large-scale zonal magnetic field (without allowance for a zonal flow), were studied separately by Smolyakov *et al.* [27], who used a hydrodynamic model and neglected drift effects. As will be shown below, the neglect of the effect of the zonal flow in studying the fast dynamo problem is, generally speaking, incorrect. The problem of the generation of a large-scale zonal magnetic field by Alfvén turbulence was also investigated by Gruzinov *et al.* [28]. In contrast to [27], they described the electrons by the drift kinetic equation. An alternative approach employed by Guzdar *et al.* [29] to investigate the problem of the generation of zonal flows by drift-Alfvén waves is based on the theory of coherent parametric instabilities. For a plasma, they utilized a hydrodynamic description, which will also be used as a basis for the present study.

The paper is organized as follows. In Section 2, the basic nonlinear equations, which describe, on the one hand, small-scale drift-Alfvén waves and, on the other, large-scale zonal flows and large-scale magnetic fields, are presented. In Section 3, two different spatial scales are introduced and the equations for the large-scale zonal flows and large-scale magnetic fields are derived by averaging the basic equations over small scales. In Section 4, the equation for the spectral function of drift-Alfvén waves is derived and then analyzed for different limiting cases; in particular, it is discussed whether the equation yields results consistent with those obtained in the electrostatic approximation. The instability that results in the spontaneous generation of a zonal flow is examined in Section 5. Different instability regimes are considered in the same way as in [17, 18, 26]. In addition, in this section, the possibility of generating a large-scale zonal magnetic field is considered. Section 6 summarizes the main results of the present work.

2. BASIC EQUATIONS FOR DRIFT-ALFVÉN TURBULENCE

The basic hydrodynamic equations used here were obtained in [30, 31] (an identical set of equations was used in [29]):

$$\frac{\partial N}{\partial t} + [\phi, N] + v_{*e}\frac{\partial \phi}{\partial y} + \frac{\partial}{\partial z}\nabla_\perp^2 A - [A, \nabla_\perp^2 A] = 0, \quad (1)$$

$$\left(\frac{\partial}{\partial t} + v_{*e}\frac{\partial}{\partial y}\right)A + \frac{\partial}{\partial z}(\phi - N) - [A, \phi - N] = 0, \quad (2)$$

$$\frac{\partial}{\partial t}\nabla_\perp^2 \phi + [\phi, \nabla_\perp^2 \phi] + \frac{\partial}{\partial z}\nabla_\perp^2 A - [A, \nabla_\perp^2 A] = 0, \quad (3)$$

where $N = \ln(\tilde{n}/n_0)$ is the normalized density, $\phi = e\varphi/T_e$ is the normalized electrostatic potential, $A = ec_A\mathcal{A}/cT_e$ is the normalized parallel component of the vector potential, c_A is the Alfvén velocity, $v_{*e} = -(cT_e/eB_0L_n)(\omega_{Bi}/\rho_s)$ is the normalized electron drift velocity, and $L_n = n_0(\partial n_0/\partial x)^{-1}$ is the characteristic scale on which the equilibrium plasma density varies. In these equations, the time is in units of the reciprocal of the ion cyclotron frequency $1/\omega_{Bi}$, the transverse spatial coordinates $\mathbf{r}_\perp = (x, y, 0)$ are in units of $\rho_s = \sqrt{T_e/m_i\omega_{Bi}^2}$, and the longitudinal coordinate z is in units of c_A/ω_{Bi}. The Poisson bracket $[f, g]$ is defined as $[f, g] = \mathbf{e}_z \cdot [\nabla f \times \nabla g]$. For simplicity, we assume that the constant external magnetic field is uniform and is directed along the z-axis and that the plasma temperature is also uniform, $\nabla T_e = \nabla T_i = 0$. In addition, assuming that $T_i \ll T_e$, we neglect the finite-ion-Larmor-radius effects. Equation (1) is the electron continuity equation in which the longitudinal current $j_\parallel = -\nabla_\perp^2 A$ is associated with the electron motion. Equation (2) is the generalized Ohm's law derived from the equation for the longitudinal electron motion in which electron inertia is ignored but electron pressure is taken into account. Finally, Eq. (3) is derived from the quasineutrality condition for plasma perturbations.

In the linear approximation, Eqs. (1)–(3) describe the coupling between the electron-drift and Alfvén waves due to electromagnetic effects:

$$(\omega - \omega_{*e})(\omega^2 - k_\parallel^2) = \omega k_\parallel^2 k_\perp^2; \quad (4)$$

where $k_\parallel$ and $k_\perp$ are the projections of the wave vector of the perturbations onto the directions along and across the magnetic field, respectively, and $\omega_{*e} = k_y v_{*e}$ is the electron drift frequency. The right-hand side of dispersion relation (4) is due to the effect of the finite electron pressure in longitudinal Ohm's law (2); as a result of this effect, the longitudinal electric field of the perturbation is nonzero, $E_\parallel \neq 0$ (the so-called effects of the finite ion Larmor radius in terms of the electron temperature). In the electrostatic approximation

($k_\parallel \longrightarrow \infty$; i.e., $c_A \longrightarrow \infty$), dispersion relation (4) describes electron drift waves with the frequency $\omega = \omega_{*e}/(1 + k_\perp^2)$, and, in the approximation in which the drift effects are neglected ($\omega \gg \omega_{*e}$), it describes Alfvén waves with frequencies such that $\omega^2 = k_\parallel^2(1 + k_\perp^2)$. In the limit $k_y = k_\parallel = 0$, dispersion relation (4) yields $\omega = 0$, which corresponds to a zonal flow or a zonal magnetic field. Dissipative effects, such as resistivity and viscosity, cause these modes with zero frequency to be damped. In what follows, it will be shown that zonal flows may become unstable due to small-scale turbulence.

3. AVERAGED EQUATIONS FOR LARGE-SCALE ZONAL FLOWS AND MAGNETIC FIELDS

We assume that the spatial scales of the drift-Alfvén turbulence differ considerably from those of the zonal perturbation and use the method of two-scale expansion (see the Introduction). In Eqs. (1)–(3), we set

$$\phi = \bar{\phi}(X, T) + \tilde{\phi}(\mathbf{x}, t, X, T), \tag{5}$$

where the slow variables X and T correspond to the characteristic (long) spatial and temporal scales of the zonal perturbations and the fast variables $\mathbf{x}$ and t correspond to the characteristic (short) spatial and temporal scales of the drift-Alfvén turbulence. The quantity $\bar{\phi}(X, T)$, averaged over small scales, describes the zonal flow, and the fluctuating quantity $\tilde{\phi}(\mathbf{x}, t, X, T)$ accounts for turbulent perturbations. In what follows, we will assume that the spatial scale of the zonal perturbations is short in comparison with the characteristic scale on which the equilibrium plasma density varies, $L_n\partial/\partial X \gg 1$. Because of the interaction of small-scale turbulence with large-scale flows and magnetic fields, the turbulence-related quantities depend not only on the fast but also on the slow variables. The longitudinal vector potential A and plasma density N can also be expressed in a form similar to representation (5). As a result, we average Eqs. (1)–(3) over the fast variables to arrive at the following coupled averaged equations for the zonal flow and magnetic field:

$$\frac{\partial \bar{N}}{\partial T} + \overline{[\tilde{\phi}, \tilde{N}]} - \overline{[\tilde{A}, \nabla_\perp^2 A]} = 0, \tag{6}$$

$$\frac{\partial \bar{A}}{\partial T} - \overline{[\tilde{A}, \tilde{\phi} - \tilde{N}]} = 0, \tag{7}$$

$$\frac{\partial}{\partial T}\frac{\partial^2 \bar{\phi}}{\partial X^2} + \overline{[\tilde{\phi}, \nabla_\perp^2 \tilde{\phi}]} - \overline{[\tilde{A}, \nabla_\perp^2 \tilde{A}]} = 0. \tag{8}$$

The Poisson brackets corresponding to the nonlinear interaction among turbulent perturbations can be written as

$$[f, g] = \frac{\partial}{\partial x}\left(f\frac{\partial g}{\partial y}\right) - \frac{\partial}{\partial y}\left(f\frac{\partial g}{\partial x}\right), \tag{9}$$

$$\begin{aligned}[f, \nabla^2 f] &= \left(\frac{\partial^2}{\partial y^2} - \frac{\partial^2}{\partial x^2}\right)\left(\frac{\partial f}{\partial x}\frac{\partial f}{\partial y}\right) \\ &+ \frac{\partial^2}{\partial x \partial y}\left(\frac{\partial^2 f}{\partial x^2} - \frac{\partial^2 f}{\partial y^2}\right).\end{aligned} \tag{10}$$

Then, we perform averaging over the fast variables and retain only the terms of the leading order in the small parameter of the problem (the ratio of the spatial scales of the turbulence to those of the zonal flows). As a result, we obtain

$$[f, g] = \frac{\partial}{\partial X}\overline{f\frac{\partial g}{\partial y}}, \tag{11}$$

$$[f, \nabla^2 f] = -\frac{\partial^2}{\partial X^2}\overline{\frac{\partial f}{\partial x}\frac{\partial f}{\partial y}}, \tag{12}$$

where the derivatives in the averaged quantities are assumed to be taken only with respect to the fast variables.

Using relationships (11) and (12), we reduce the evolutionary equations for large-scale zonal perturbations to the form

$$\frac{\partial \bar{N}}{\partial T} + \frac{\partial}{\partial X}\overline{\tilde{\phi}\frac{\partial \tilde{N}}{\partial y}} + \frac{\partial^2}{\partial X^2}\overline{\frac{\partial \tilde{A}}{\partial y}\frac{\partial \tilde{A}}{\partial y}} = 0, \tag{13}$$

$$\frac{\partial \bar{A}}{\partial T} - \frac{\partial}{\partial X}\overline{\tilde{A}\frac{\partial}{\partial y}(\tilde{\phi} - \tilde{N})} = 0, \tag{14}$$

$$\frac{\partial}{\partial T}\frac{\partial^2 \bar{\phi}}{\partial X^2} - \frac{\partial^2}{\partial X^2}\left(\overline{\frac{\partial \tilde{\phi}}{\partial x}\frac{\partial \tilde{\phi}}{\partial y}} - \overline{\frac{\partial \tilde{A}}{\partial x}\frac{\partial \tilde{A}}{\partial y}}\right) = 0. \tag{15}$$

In order to simplify further calculations, it is worthwhile to expand the turbulence-related quantities in Fourier integrals over the fast spatial variables:

$$\tilde{\phi}(X, T, \mathbf{x}, t) = \int d\mathbf{k}\tilde{\phi}_k \exp(i\mathbf{k}\mathbf{x}), \quad \tilde{\phi}_{-k} = \tilde{\phi}_k^*, \tag{16}$$

where the Fourier coefficients $\tilde{\phi}_k$ depend on the fast time and on the slow variables. Then, we substitute expansion (16) into Eqs. (13)–(15) and perform averaging over the fast variables to obtain the following equations:

$$\frac{\partial \bar{N}}{\partial T} + \frac{\partial}{\partial X}\int d\mathbf{k} k_y \operatorname{Im}\overline{\tilde{\phi}_k \tilde{N}_{-k}} + \frac{\partial^2}{\partial X^2}\int d\mathbf{k} k_x k_y \overline{\tilde{A}_k \tilde{A}_{-k}} = 0, \tag{17}$$

$$\frac{\partial \bar{A}}{\partial T} - \frac{\partial}{\partial X}\int d\mathbf{k} k_y \operatorname{Im} \overline{\tilde{A}_k(\tilde{\phi}_{-k} - \tilde{N}_{-k})} = 0, \quad (18)$$

$$\frac{\partial}{\partial T}\frac{\partial^2 \bar{\phi}}{\partial X^2} - \frac{\partial^2}{\partial X^2}\int d\mathbf{k} k_x k_y (\overline{\tilde{\phi}_k \tilde{\phi}_{-k}} - \overline{\tilde{A}_k \tilde{A}_{-k}}) = 0. \quad (19)$$

Equation (18) implies that, in order for the nonlinear contribution to the equation describing (in essence) the evolution of a large-scale zonal magnetic field to be nonzero, the phase shift between $\tilde{A}$ and $\tilde{\phi}$ (or $\tilde{N}$) should be finite. This indicates that drift-Alfvén waves should be damped. According to [26, 28], the wave damping can result from the resonant interaction of the waves with electrons (Landau resonance). Under the assumption that Landau damping is insignificant, the contribution of the drift-Alfvén turbulence to averaged Ohm's law (18) is small in comparison with its contribution to averaged quasineutrality condition (19). This circumstance simplifies the further analysis of the averaged equations.

4. EQUATION FOR THE SPECTRAL FUNCTION OF DRIFT-ALFVÉN WAVES AND THE INVARIANTS OF THE EQUATION

Following [22, 16], we assume that the nonlinear interaction among small-scale drift-Alfvén waves is insignificant as compared to their interaction with large-scale fields. This assumption is equivalent to the quasilinear approximation and is justified provided that the nonlinear interaction among small-scale waves plays an insignificant role in comparison to the role played by the dispersion effects. Thus, the evolution of small-scale fields in their interaction with large-scale perturbations can be described by the equations

$$\frac{\partial \tilde{N}}{\partial t} + [\tilde{\phi}, \bar{N}] + [\bar{\phi}, \tilde{N}] + v_{*e}\frac{\partial \tilde{\phi}}{\partial y} + \frac{\partial}{\partial z}\nabla_\perp^2 \tilde{A} - [\tilde{A}, \nabla_\perp^2 \bar{A}] - [\bar{A}, \nabla_\perp^2 \tilde{A}] = 0, \quad (20)$$

$$\left(\frac{\partial}{\partial t} + v_{*e}\frac{\partial}{\partial y}\right)\tilde{A} + \frac{\partial}{\partial z}(\tilde{\phi} - \tilde{N}) - [\tilde{A}, \bar{\phi} - \bar{N}] - [\bar{A}, \tilde{\phi} - \tilde{N}] = 0, \quad (21)$$

$$\frac{\partial}{\partial t}\nabla_\perp^2 \tilde{\phi} + [\tilde{\phi}, \nabla_\perp^2 \bar{\phi}] + [\bar{\phi}, \nabla_\perp^2 \tilde{\phi}] + \frac{\partial}{\partial z}\nabla_\perp^2 \tilde{A} - [\tilde{A}, \nabla_\perp^2 \bar{A}] - [\bar{A}, \nabla_\perp^2 \tilde{A}] = 0. \quad (22)$$

In order to simplify the derivation of the equation for the spectral function of small-scale drift-Alfvén waves, we expand the large- and small-scale fields in Fourier integrals over the spatial variables and convert Eqs. (20)–(22) to the form

$$\frac{\partial \tilde{N}_k}{\partial t} - ik_\parallel k_\perp^2 \tilde{A}_k + i\omega_{*e,k}\tilde{\phi}_k = \int dppk_y\{(k_\perp^2 - 2pk_x)\bar{A}_p\tilde{A}_{k-p} + \bar{\phi}_p\tilde{N}_{k-p} - \bar{N}_p\tilde{\phi}_{k-p}\}, \quad (23)$$

$$\left(\frac{\partial}{\partial t} + i\omega_{*e,k}\right)\tilde{A}_k + ik_\parallel(\tilde{\phi}_k - \tilde{N}_k) = \int dppk_y\{(\bar{\phi}_p - \bar{N}_p)\tilde{A}_{k-p} - \bar{A}_p(\tilde{\phi}_{k-p} - \tilde{N}_{k-p})\}, \quad (24)$$

$$\frac{\partial \tilde{\phi}_k}{\partial t} + ik_\parallel \tilde{A}_k = \int dppk_y\left(1 - \frac{2pk_x}{k_\perp^2}\right)\{\bar{\phi}_p\tilde{\phi}_{k-p} - \bar{A}_p\tilde{A}_{k-p}\}, \quad (25)$$

where $\omega_{*e,k} = k_y v_{*e}$. In deriving Eqs. (23)–(25), we took into account the fact that, in the case of the zonal perturbations that we are only considering here, the wave vector of the long-wavelength perturbations has the only nonzero component, $\mathbf{p} = (p, 0, 0)$.

In the model at hand, drift-Alfvén turbulence is described by the three fields $\tilde{\phi}_k$, $\tilde{A}_k$, and $\tilde{N}_k$. By analogy with [18], we introduce the following combination of these fields: $\psi_k = \tilde{\phi}_k + \alpha_k\tilde{A}_k + \beta_k\tilde{N}_k$. Then, multiplying Eqs. (23) and (24) by β_k and α_k, respectively, and adding the resulting equations to Eq. (25), we arrive at the equation

$$\frac{\partial \psi_k}{\partial t} + i\tilde{\phi}_k(\omega_{*e,k}\beta_k + k_\parallel a_k) + i\tilde{A}_k(k_\parallel + \omega_{*e,k}\alpha_k - k_\parallel k_\perp^2\beta_k) - i\tilde{N}_k k_\parallel \alpha_k = \int dppk_y\left\{\bar{\phi}_p\left[\left(1 - \frac{2pk_x}{k_\perp^2}\right)\tilde{\phi}_{k-p} + \alpha_k\tilde{A}_{k-p} + \beta_k\tilde{N}_{k-p}\right]\right. - \bar{N}_p[\beta_k\tilde{\phi}_{k-p} + \alpha_k\tilde{A}_{k-p}] + \left.\bar{A}_p\left[\left(1 - \frac{2pk_x}{k_\perp^2}\right)(k_\perp^2\beta_k - 1)\tilde{A}_{k-p} - \alpha_k(\tilde{\phi}_{k-p} - \tilde{N}_{k-p})\right]\right\}. \quad (26)$$

The coefficients α_k and β_k can be found by converting the left-hand side of Eq. (26) for ψ_k into the canonical form:

$$\frac{\partial \psi_k}{\partial t} + i\omega_k\psi_k = \ldots, \quad (27)$$

where the eigenfrequency ω_k of the drift-Alfvén mode satisfies dispersion relation (4). As a result, we obtain

$$\alpha_k = \frac{\omega_k^2}{k_\parallel(\omega_k - \omega_{*e,k})}, \quad \beta_k = -\frac{\omega_k}{\omega_k - \omega_{*e,k}}. \tag{28}$$

The above assumption of a weak interaction among small-scale modes implies that, on the right-hand side of Eq. (26), it is sufficient to describe the coupling between the fields $\tilde{\phi}$, $\tilde{A}$, and $\tilde{N}$ in accordance with the linearized equations for drift-Alfvén modes, provided that the fields are represented as $(\tilde{\phi}_k, \tilde{A}_k, \tilde{N}_k) \propto \exp(-i\omega_k t)$. As a result, Eqs. (23) and (25) give

$$\tilde{A}_k = \frac{\omega_k}{k_\parallel}\tilde{\phi}_k, \quad \tilde{N}_k = \left(\frac{\omega_{*e,k}}{\omega_k} - k_\perp^2\right)\tilde{\phi}_k. \tag{29}$$

Using the definition of ψ_k, we finally arrive at the following formula, which relates $\tilde{\phi}_k$ to ψ_k and makes it possible to express all the terms on the right-hand side of Eq. (26) through ψ_k:

$$\begin{aligned}\tilde{\phi}_k &= \Lambda_k \psi_k,\\ \frac{1}{\Lambda_k} &= 1 + \frac{\omega_k}{k_\parallel}\alpha_k + \left(\frac{\omega_{*e,k}}{\omega_k} - k_\perp^2\right)\beta_k\\ &= \frac{2\omega_k^3 - \omega_{*e,k}(\omega_k^2 + k_\parallel^2)}{k_\parallel^2(\omega_k - \omega_{*e,k})}.\end{aligned} \tag{30}$$

We will describe the small-scale turbulence by the spectral function (the Wigner function) $I_k(x, t)$, which is defined as

$$\int dq\, \overline{\psi_k \psi_{-k+q}} \exp(iqx) = I_k(x, t). \tag{31}$$

The weak spatiotemporal dependence of $I_k(x, t)$ (it is assumed that $q \ll k$) corresponds to the modulation of small-scale waves by large-scale zonal perturbations. In Eq. (31), the overhead bar denotes ensemble averaging, which, by virtue of the ergodic hypothesis, is equivalent to time averaging (or, as is more often said, averaging over small scales). The evolutionary equation for $I_k(x, t)$ is derived in the following way. First, we multiply Eq. (26) by ψ_{-k+q}. Second, we multiply the analogous evolutionary equation for ψ_{-k+q}, which is derived by making the replacement $\mathbf{k} \longrightarrow -\mathbf{k} + \mathbf{q}$ in Eq. (26), by ψ_k. Third, we sum the two equations and perform averaging over small scales. Finally, applying the operator $\int dq \exp(iqx)$ to the resulting equation, we obtain

$$\begin{aligned}&\frac{\partial I_k}{\partial t} + i\int dq(\omega_{q-k} + \omega_k)\overline{\psi_k \psi_{q-k}}\exp(iqx)\\ &\quad = S_1 + S_2,\end{aligned} \tag{32}$$

where

$$\begin{aligned}S_1 &= \int dq \exp(iqx)\\ &\times \int dp\, p k_y \left\{-\bar{N}_p[\beta_k \overline{\tilde{\phi}_{k-p}\psi_{q-k}} + \alpha_k \overline{\tilde{A}_{k-p}\psi_{q-k}}]\right.\\ &+ \bar{\phi}_p\left[\left(1 - \frac{2pk_x}{k_\perp^2}\right)\overline{\tilde{\phi}_{k-p}\psi_{q-k}} + \alpha_k \overline{\tilde{A}_{k-p}\psi_{q-k}}\right.\\ &\qquad \left. + \beta_k \overline{\tilde{N}_{k-p}\psi_{q-k}}\right]\\ &+ \bar{A}_p\left[\left(1 - \frac{2pk_x}{k_\perp^2}\right)(k_\perp^2\beta_k - 1)\overline{\tilde{A}_{k-p}\psi_{q-k}}\right.\\ &\qquad \left.\left. - \alpha_k(\overline{\tilde{\phi}_{k-p}\psi_{q-k}} - \overline{\tilde{N}_{k-p}\psi_{q-k}})\right]\right\},\end{aligned} \tag{33}$$

$$\begin{aligned}S_2 &= -\int dq \exp(iqx)\\ &\times \int dp\, p k_y \left\{-\bar{N}_p[\beta_{q-k} \overline{\tilde{\phi}_{q-k-p}\psi_k} + \alpha_{q-k} \overline{\tilde{A}_{q-k-p}\psi_k}]\right.\\ &+ \bar{\phi}_p\left[\left(1 + \frac{2p(k_x - q)}{(\mathbf{q} - \mathbf{k}_\perp)^2}\right)\overline{\tilde{\phi}_{q-k-p}\psi_k} + \alpha_{q-k} \overline{\tilde{A}_{q-k-p}\psi_k}\right.\\ &\qquad \left. + \beta_{q-k} \overline{\tilde{N}_{q-k-p}\psi_k}\right]\\ &+ \bar{A}_p\left[\left(1 + \frac{2p(k_x - q)}{(\mathbf{q} - \mathbf{k}_\perp)^2}\right)((\mathbf{q} - \mathbf{k}_\perp)^2\beta_{q-k} - 1)\overline{\tilde{A}_{q-k-p}\psi_k}\right.\\ &\qquad \left.\left. - \alpha_{q-k}(\overline{\tilde{\phi}_{q-k-p}\psi_k} - \overline{\tilde{N}_{q-k-p}\psi_k})\right]\right\}.\end{aligned} \tag{34}$$

We assume that the eigenfrequency ω_k of drift-Alfvén waves is real. In the model developed here, the effects associated with Landau damping and dissipative processes are both neglected; thus, this assumption is always valid, and we have $\omega_{-k} = -\omega_k$. Taking into account that the ratio q/k is small, we expand the frequency ω_{-k+q} in the second term on the left-hand side of Eq. (32) in powers of this small parameter to obtain

$$\begin{aligned}&i\int dq(\omega_{q-k} + \omega_k)\overline{\psi_k \psi_{q-k}}\exp(iqx)\\ &\quad = i\int dq\, q\frac{\partial \omega_k}{\partial k_x}\overline{\psi_k \psi_{q-k}}\exp(iqx)\\ &= \frac{\partial \omega_k}{\partial k_x}\frac{\partial}{\partial x}\int dq\, \overline{\psi_k \psi_{q-k}}\exp(iqx) = \frac{\partial \omega_k}{\partial k_x}\frac{\partial I_k(x, t)}{\partial x}.\end{aligned} \tag{35}$$

In order to average expressions (33) and (34) over the ensemble, we turn to relationships (29) and (30) and invert relationship (31):

$$\overline{\psi_{k-p}\psi_{-k+q}} = \overline{\psi_{k-p}\psi_{-(k-p)+q-p}} = \frac{1}{2\pi}\int dx' I_{k-p}(x')\exp(-i(q-p)x'). \quad (36)$$

We also use the relationships

$$\alpha_{-k} = \alpha_k, \quad \beta_{-k} = \beta_k, \quad \Lambda_{-k} = \Lambda_k, \quad (37)$$

which are valid because $\omega_k = -\omega_k$. As a result, we arrive at the expressions

$$S_1 = \frac{1}{2\pi}\int\int\int dp dq dx' p k_y I_{k-p}(x')\Lambda_{k-p} \times \exp(iqx + i(p-q)x')\left\{\bar{\phi}_p\left[1 - \frac{2pk_x}{k_\perp^2} + \alpha_k\frac{\omega_{k-p}}{k_\parallel} + \beta_k\left(\frac{\omega_{*e,k}}{\omega_{k-p}} - (\mathbf{k}_\perp - \mathbf{p})^2\right)\right] + \bar{A}_p\left[\left(1 - \frac{2pk_x}{k_\perp^2}\right)(k_\perp^2\beta_k - 1)\frac{\omega_{k-p}}{k_\parallel} - \alpha_k\left(1 - \frac{\omega_{*e,k}}{\omega_{k-p}} + (\mathbf{k}_\perp - \mathbf{p})^2\right)\right] - \bar{N}_p\left[\beta_k + \alpha_k\frac{\omega_{k-p}}{k_\parallel}\right]\right\}, \quad (38)$$

$$S_2 = -\frac{1}{2\pi}\int\int\int dp dq dx' p k_y I_k(x')\Lambda_{k+p-q} \times \exp(iqx + i(p-q)x')\left\{\bar{\phi}_p\left[1 + \frac{2p(k_x - q)}{(\mathbf{k}_\perp - \mathbf{q})^2} + \alpha_{k-q}\frac{\omega_{k+p-q}}{k_\parallel} + \beta_{k-q}\left(\frac{\omega_{*e,k}}{\omega_{k+p-q}} - (\mathbf{k}_\perp + \mathbf{p} - \mathbf{q})^2\right)\right] + \bar{A}_p\left[\left(1 + \frac{2p(k_x - q)}{(\mathbf{k}_\perp - \mathbf{q})^2}\right)((\mathbf{k}_\perp - \mathbf{q})^2\beta_{k-q} - 1)\frac{\omega_{k+p-q}}{k_\parallel} - \alpha_{k-q}\left(1 - \frac{\omega_{*e,k}}{\omega_{k+p-q}} + (\mathbf{k}_\perp + \mathbf{p} - \mathbf{q})^2\right)\right] - \bar{N}_p\left[\beta_{k-q} + \alpha_{k-q}\frac{\omega_{k+p-q}}{k_\parallel}\right]\right\}. \quad (39)$$

We expand the integrands in expressions (38) and (39) in powers of the parameters $(p/k, q/k) \ll 1$, which are small under the assumption of the separation of the spatial scales of the zonal perturbations and drift-Alfvén turbulence, and keep only terms of the first and second orders. This yields

$$S_1 = S_1^{(0)} + S_1^{(1)}, \quad S_2 = -S_1^{(0)} + S_2^{(1)'} + S_2^{(1)''}, \quad (40)$$

where, with allowance for expression (30), we have

$$S_1^{(0)} = \int dp p k_y I_k(x)\exp(ipx)\left\{\bar{\phi}_p + \Lambda_k\bar{A}_p\left[(k_\perp^2\beta_k - 1)\frac{\omega_k}{k_\parallel} - \alpha_k\left(1 - \frac{\omega_{*e,k}}{\omega_k} + k_\perp^2\right)\right] - \Lambda_k\bar{N}_p\left[\beta_k + \alpha_k\frac{\omega_k}{k_\parallel}\right]\right\}, \quad (41)$$

$$S_1^{(1)} = -\int dp p^2 k_y \exp(ipx)\left\{\bar{\phi}_p\left(\frac{2k_x}{k_\perp^2}L_k I_k(x) + \alpha_k\frac{\partial}{\partial k_x}\left[\frac{\omega_k}{k_\parallel}\Lambda_k I_k(x)\right] + \beta_k\frac{\partial}{\partial k_x}\left[\left(\frac{\omega_{*e,k}}{\omega_k} - k_\perp^2\right)\Lambda_k I_k(x)\right] + \frac{\partial}{\partial k_x}[\Lambda_k I_k(x)]\right) + \bar{A}_p\left(\frac{2k_x}{k_\perp^2}(k_\perp^2\beta_k - 1)\frac{\omega_k}{k_\parallel}\Lambda_k I_k(x) + (k_\perp^2\beta_k - 1)\frac{\partial}{\partial k_x}\left[\frac{\omega_k}{k_\parallel}\Lambda_k I_k(x)\right] - \alpha_k\frac{\partial}{\partial k_x}\left[\left(1 - \frac{\omega_{*e,k}}{\omega_k} + k_\perp^2\right)\Lambda_k I_k(x)\right]\right) - \bar{N}_p\left(\beta_k\frac{\partial}{\partial k_x}[\Lambda_k I_k(x)] + \alpha_k\frac{\partial}{\partial k_x}\left[\frac{\omega_k}{k_\parallel}\Lambda_k I_k(x)\right]\right)\right\}, \quad (42)$$

$$S_2^{(1)'} = -\int dp p^2 k_y \Lambda_k I_k(x)\exp(ipx) \times \left\{\bar{\phi}_p\left(\frac{2k_x}{k_\perp^2} - \frac{\partial\alpha_k}{\partial k_x}\frac{\omega_k}{k_\parallel} - \frac{\partial\beta_k}{\partial k_x}\left(\frac{\omega_{*e,k}}{\omega_k} - k_\perp^2\right)\right) + \bar{A}_p\left(\frac{2k_x}{k_\perp^2}(k_\perp^2\beta_k - 1)\frac{\omega_k}{k_\parallel} - \frac{\omega_k}{k_\parallel}\frac{\partial(\beta_k k_\perp^2)}{\partial k_x} + \left(1 - \frac{\omega_{*e,k}}{\omega_k} + k_\perp^2\right)\frac{\partial\alpha_k}{\partial k_x}\right) + \bar{N}_p\left(\frac{\partial\beta_k}{\partial k_x} + \frac{\omega_k}{k_\parallel}\frac{\partial\alpha_k}{\partial k_x}\right)\right\}, \quad (43)$$

$$S_2^{(1)''} = -\frac{1}{2\pi}\iiint dpdqdx' p(p-q)k_y I_k(x') \times \exp(iqx + i(p-q)x') \times \left\{ \bar{A}_p \frac{\partial}{\partial k_x}\left[\Lambda_k\left((k_\perp^2\beta_k - 1)\frac{\omega_k}{k_\parallel} - \alpha_k\left(1 - \frac{\omega_{*e,k}}{\omega_k} + k_\perp^2\right)\right)\right] - \bar{N}_p \frac{\partial}{\partial k_x}\left[\Lambda_k\left(\beta_k + \frac{\omega_k}{k_\parallel}\alpha_k\right)\right]\right\}. \quad (44)$$

Expressions (40) imply that, to the lowest order (i.e., to within terms proportional to p), the quantities S_1 and S_2 cancel one another; hence, the nonzero contribution to Eq. (32) comes from the next-order terms, i.e., from the terms $S_1^{(1)}$, $S_2^{(1)'}$, and $S_2^{(1)''}$. Transforming the term $S_2^{(1)''}$ with the help of the equality

$$\int dx'(p-q)\exp(i(p-q)x')I_k(x') = i\int dx' \exp(i(p-q)x')\frac{\partial I_k(x')}{\partial x'}, \quad (45)$$

we get

$$S_2^{(1)''} = \frac{\partial}{\partial k_x}\left\{\Lambda_k\left[k_y\frac{\partial \bar{A}}{\partial x}\left((1-k_\perp^2\beta_k)\frac{\omega_k}{k_\parallel} + \alpha_k\left(1 - \frac{\omega_{*e,k}}{\omega_k} + k_\perp^2\right)\right) + k_y\frac{\partial \bar{N}}{\partial x}\left(\beta_k + \frac{\omega_k}{k_\parallel}\alpha_k\right)\right]\right\}. \quad (46)$$

To transform the terms $S_1^{(1)}$ and $S_2^{(1)'}$ is a much more difficult problem, which, however, can be simplified by using, first, dispersion relation (4); second, the relationship

$$2k_x \equiv \frac{\partial}{\partial k_x}\left[\frac{(\omega_k - \omega_{*e,k})(\omega_k^2 - k_\parallel^2)}{k_\parallel^2\omega_k}\right], \quad (47)$$

which is derived by differentiating the dispersion relation with respect to k_x; and third, the relationship

$$\frac{2k_x}{k_\perp^2} = \frac{1}{\omega_k - \omega_{*e,k}}\frac{\partial(\omega_k - \omega_{*e,k})}{\partial k_x} + \frac{1}{\omega_k^2 - k_\parallel^2}\frac{\partial(\omega_k^2 - k_\parallel^2)}{\partial k_x} - \frac{1}{\omega_k}\frac{\partial \omega_k}{\partial k_x}, \quad (48)$$

which is a consequence of the dispersion relation and relationship (47). In this way, we arrive at the expression

$$S_1^{(1)} + S_2^{(1)'} = k_y\frac{\partial^2\bar{\phi}}{\partial x^2}\frac{1}{f_k^\phi}\frac{\partial}{\partial k_x}(f_k^\phi I_k(x)) - k_y\frac{\partial^2\bar{A}}{\partial x^2}\Lambda_k\left((1-k_\perp^2\beta_k)\frac{\omega_k}{k_\parallel} + \alpha_k\left(1 - \frac{\omega_{*e,k}}{\omega_k} + k_\perp^2\right)\right)\frac{1}{f_k^A}\frac{\partial}{\partial k_x}(f_k^A I_k(x)) - k_y\frac{\partial^2\bar{N}}{\partial x^2}\Lambda_k\left(\beta_k + \frac{\omega_k}{k_\parallel}\alpha_k\right)\frac{1}{f_k^N}\frac{\partial}{\partial k_x}(f_k^N I_k(x)), \quad (49)$$

where

$$f_k^\phi = k_\perp^2\Lambda_k/\omega_k, \quad f_k^A = k_\perp^2\Lambda_k\left(1 - \frac{\omega_{*e,k}}{\omega_k}\right), \quad f_k^N = \Lambda_k\left(1 - \frac{\omega_{*e,k}}{\omega_k}\right). \quad (50)$$

Collecting together the above components (35), (46), and (49) and taking into account the fact that the spatial and temporal modulation of the spectral function is governed by the interaction of turbulent fluctuations with a zonal flow and thus depends only on the slow variables, we can write Eq. (32) for $I_k(X, T)$ in the form

$$\frac{\partial}{\partial T}I_k(X,T) + \frac{\partial}{\partial k_x}(\omega_k + \delta\omega_k^\phi + \delta\omega_k^A + \delta\omega_k^N)\frac{\partial I_k}{\partial X} - \frac{\partial\delta\omega_k^\phi}{\partial X}\frac{1}{f_k^\phi}\frac{\partial}{\partial k_x}(f_k^\phi I_k) - \frac{\partial\delta\omega_k^A}{\partial X}\frac{1}{f_k^A}\frac{\partial}{\partial k_x}(f_k^A I_k) - \frac{\partial\delta\omega_k^N}{\partial X}\frac{1}{f_k^N}\frac{\partial}{\partial k_x}(f_k^N I_k) = 0, \quad (51)$$

where

$$\delta\omega_k^\phi = k_y\frac{\partial\bar{\phi}}{\partial X},$$

$$\delta\omega_k^N = -k_y\frac{\partial\bar{N}}{\partial X}\Lambda_k\left(\beta_k + \frac{\omega_k}{k_\parallel}\alpha_k\right) = -\frac{\omega_k(\omega_k^2 - k_\parallel^2)}{2\omega_k^3 - \omega_{*e,k}(\omega_k^2 + k_\parallel^2)}k_y\frac{\partial\bar{N}}{\partial X}, \quad (52)$$

$$\delta\omega_k^A = k_y\frac{\partial\bar{A}}{\partial X}\Lambda_k\left((k_\perp^2\beta_k - 1)\frac{\omega_k}{k_\parallel} - \alpha_k\left(1 - \frac{\omega_{*e,k}}{\omega_k} + k_\perp^2\right)\right) = -\frac{2k_\parallel\omega_k[\omega_k(1+k_\perp^2) - \omega_{*e,k}]}{2\omega_k^3 - \omega_{*e,k}(\omega_k^2 + k_\parallel^2)}k_y\frac{\partial\bar{A}}{\partial X}.$$

The quantities $\delta\omega_k^\phi$, $\delta\omega_k^A$, and $\delta\omega_k^N$ are the perturbations of the eigenfrequency of the drift-Alfvén mode by the large-scale zonal perturbations of the transverse electric field, transverse magnetic field, and plasma density, respectively. This may be readily seen if we take into account large-scale zonal perturbations in dispersion relation (4) by making the corresponding replacements

$$\omega \longrightarrow \omega - k_y\frac{\partial\bar{\phi}}{\partial X}, \quad k_\parallel \longrightarrow k_\parallel - k_y\frac{\partial\bar{A}}{\partial X}, \qquad \omega_{*e} \longrightarrow \omega_{*e} - k_y\frac{\partial\bar{N}}{\partial X}. \tag{53}$$

As a result, the frequency perturbation that follows from dispersion relation (4) with replacements (53) can be written as

$$\delta\omega_k = \delta\omega_k^\phi + \delta\omega_k^A + \delta\omega_k^N. \tag{54}$$

The structure of Eq. (51) is such that, in the general case (when the large-scale mode perturbs the transverse electric field, transverse magnetic field, and plasma density), the equation cannot be represented in a divergence form (i.e., in the form of a conservation law) for a certain invariant of the basic equations that is associated exclusively with small-scale oscillations and is an analogue of the number of quanta in the theory of weak turbulence [32]. Hence, the question about the existence of an adiabatic invariant of a "small-scale oscillations + large-scale zonal perturbations" system in this general case remains open. On the other hand, the structure of Eq. (51) is such that, in particular cases, the equation can be reduced to a conservation law for a certain quantity, which can be called, by analogy with [16], the action invariant. First, we should mention the electrostatic case, i.e., the limit $k_\parallel \longrightarrow \infty$, in which the drift-Alfvén mode turns into a drift electron mode ($\omega_k = \omega_{*e,k}/(1 + k_\perp^2)$, with $\delta\omega_k^A \longrightarrow 0$), and we have

$$\Lambda_k = \frac{k_\perp^2}{1+k_\perp^2}, \quad f_k^\phi = k_\perp^4, \quad f_k^N = \frac{k_\perp^4}{1+k_\perp^2}, \qquad \delta\omega_k^N = -k_y\frac{\partial\bar{N}}{\partial X}\frac{1}{1+k_\perp^2}. \tag{55}$$

By analogy with [16], we also examine the following two cases in which Eq. (51) is represented as a local conservation law. The first of these corresponds to a refined Hasegawa–Mima model in which, because of the two-dimensional character of a large-scale mode, the long-wavelength perturbations of the electron density do not obey a Boltzmann distribution and thus can be neglected, $\bar{N} = 0$. In this case, Eq. (51) takes the form of a conservation law for the invariant $N_k = k_\perp^4 I_k$:

$$\frac{\partial}{\partial T}N_k(X,T) + \frac{\partial}{\partial k_x}(\omega_k + \delta\omega_k^\phi)\frac{\partial N_k}{\partial X} - \frac{\partial}{\partial X}(\omega_k + \delta\omega_k^\phi)\frac{\partial N_k}{\partial k_x} = 0. \tag{56}$$

Recalling relationship (30) between $\tilde{\phi}_k$ and ψ_k and taking into account relationships (55), one can actually see that Eq. (56) coincides exactly with the corresponding equation derived in [16].

Another case arises under the formal assumption that the long-wavelength density perturbation obeys a Boltzmann distribution, $\bar{N} = \bar{\phi}$ (this implies that the large-scale perturbation satisfies the conditions $\omega < q_\parallel v_{Te}$ and $q_\parallel \ll q_x$). In this case, which corresponds to the Hasegawa–Mima model, Eq. (51) can also be reduced to a conservation law but for a different invariant, $N_k = k_\perp^6 I_k/(1 + k_\perp^2)$:

$$\frac{\partial}{\partial T}N_k(X,T) + \frac{\partial}{\partial k_x}\left(\omega_k + \delta\omega_k^\phi\frac{k_\perp^2}{1+k_\perp^2}\right)\frac{\partial N_k}{\partial X} - \frac{\partial}{\partial X}\left(\omega_k + \delta\omega_k^\phi\frac{k_\perp^2}{1+k_\perp^2}\right)\frac{\partial N_k}{\partial k_x} = 0. \tag{57}$$

With allowance for expression (30), this result reproduces the corresponding equation derived in [16].

In the situation where electromagnetic effects are important (which is the main subject of our analysis), Eq. (51) can also take the form of a conservation law. If we neglect the effects of the resonant interaction of small-scale waves with electrons and the effects of other dissipative processes, then, from Eq. (18), we have $\bar{A} = 0$; on the other hand, from Eqs. (17) and (19) and with allowance for relationships (29) and dispersion relation (4), we obtain the estimate $\bar{N} \simeq (q/k_\perp)^2\bar{\phi} \ll \bar{\phi}$. This enables us to set $\bar{A} = \bar{N} = 0$ in Eq. (51), which thus reduces to the conservation law

$$\frac{\partial}{\partial T}N_k(X,T) + \frac{\partial}{\partial k_x}(\omega_k + \delta\omega_k^\phi)\frac{\partial N_k}{\partial X} - \frac{\partial}{\partial X}(\omega_k + \delta\omega_k^\phi)\frac{\partial N_k}{\partial k_x} = 0, \tag{58}$$

where $N_k = (k_\perp^2\Lambda_k/\omega_k)I_k$. This equation generalizes Eq. (56) to the case of a plasma with a finite pressure ($\beta > m_e/m_i$), in which Alfvén perturbations are important.

Finally, in the case in which the small-scale perturbations are purely Alfvénic and $k_\perp^2 \ll 1$, we have $\omega_k^2 \approx k_\parallel^2$ and Eq. (51) also converts into a conservation law. On

the one hand, since the effects associated with the Reynolds stress tensor (the term $\overline{[\tilde{\phi}, \nabla_\perp^2 \tilde{\phi}]}$) and the Maxwell stress tensor (the term $\overline{[\tilde{A}, \nabla_\perp^2 \tilde{A}]}$) mutually cancel out in Eq. (8), the quantity $\bar{\phi}$ can be neglected, as is evident from Eq. (61). On the other hand, in this limiting case, we have $\delta\omega_k^N \approx 0$. As a result, Eq. (51) can be written as

$$\frac{\partial}{\partial T} N_k(X, T) + \frac{\partial}{\partial k_x}(\omega_k + \delta\omega_k^A)\frac{\partial N_k}{\partial X} - \frac{\partial \delta\omega_k^A}{\partial X}\frac{\partial N_k}{\partial k_x} = 0, \tag{59}$$

where

$$N_k = k_\perp^2 I_k, \quad \delta\omega_k^A = -k_y \frac{k_\parallel}{\omega_k}\frac{\partial \bar{A}}{\partial X}. \tag{60}$$

In the general case in which the effects of the resonant interaction between drift-Alfvén waves and electrons (or the effects of collisional dissipation) are present, the large-scale mode perturbs the transverse electric field, transverse magnetic field, and plasma density. Although in this case Eq. (51) ceases to be a conservation law, it seems to be suitable for calculating the spectral function of the small-scale turbulence and, consequently, can be used to close the set of the averaged equations.

5. INSTABILITY OF LARGE-SCALE ZONAL PERTURBATIONS

Recall that, in the absence of the effects of resonant interaction and dissipative effects, the large-scale magnetic field is not excited and the density perturbation is negligible in comparison with the perturbation of the electrostatic potential. Consequently, in this case, a zonal plasma flow can be spontaneously generated without perturbing the plasma density. A system consisting of small-scale drift-Alfvén waves and a zonal flow is described by averaged equation (19) for the curl of the zonal flow velocity and kinetic equation (58) for drift-Alfvén waves, modified by the effects of the flow. These two equations will be used as a basis for the analysis of the possibility of generating a zonal flow.

With allowance for relationships (29) and (30) and the definition of N_k, which is given after Eq. (58), evolutionary equation (19) for the curl of the flow velocity takes the form

$$\frac{\partial^3 \bar{\phi}}{\partial T \partial X^2} = \frac{\partial^2}{\partial X^2}\int d\mathbf{k} k_x k_y \left(1 - \frac{\omega_k^2}{k_\parallel^2}\right)\frac{\omega_k \Lambda_k}{k_\perp^2} N_k. \tag{61}$$

We represent the adiabatic invariant N_k as a sum of the equilibrium and modulation-related components, $N_k = N_k^0 + \tilde{N}_k$, and consider perturbations of the form $(\bar{\phi}, \tilde{N}_k) \sim \exp(-i\Omega T + iqX)$. Linearizing Eq. (58) in long-wavelength perturbations yields

$$-i(\Omega - qV_g)\tilde{N}_k = -k_y q^2 \bar{\phi}\frac{\partial N_k^0}{\partial k_x}, \tag{62}$$

where $V_g = \partial\omega_k/\partial k_x$ is the x component of the group velocity of the drift-Alfvén waves. On the other hand, taking into account the above dependence of the perturbations on the spatial coordinates and time, Eq. (61) can be rewritten as

$$-i\Omega\bar{\phi} = \int d\mathbf{k} k_x k_y \left(1 - \frac{\omega_k^2}{k_\parallel^2}\right)\frac{\omega_k \Lambda_k}{k_\perp^2}\tilde{N}_k. \tag{63}$$

From Eqs. (62) and (63), we obtain the following dispersion relation:

$$\Omega = q^2 \int d\mathbf{k} k_x k_y^2 \left(1 - \frac{\omega_k^2}{k_\parallel^2}\right)\frac{\omega_k \Lambda_k}{k_\perp^2(\Omega - qV_g)}\frac{\partial N_k^0}{\partial k_x}. \tag{64}$$

In the electrostatic limit ($k_\parallel \longrightarrow \infty$), Eq. (64) coincides with the dispersion relation derived in [16, 17, 33] and, thus, is a generalization of the result obtained earlier to include electromagnetic effects.

Following [17], we consider two types of the instability described by Eq. (64). When the width $\Delta\omega_k$ of the spectrum of the small-scale turbulence exceeds the nonlinear growth (damping) rate, this equation describes a resonant instability, for which the phase velocity of the zonal flow is close to the group velocity V_g of a drift-Alfvén wave packet; hence, we have

$$\frac{1}{\omega - qV_g} = \mathcal{P}\frac{1}{\omega - qV_g} - i\pi\delta(\omega - qV_g). \tag{65}$$

From Eq. (64) with relationship (65), we obtain the instability growth rate

$$\gamma_q = q^2 \int d\mathbf{k} k_x k_y^2 \left(1 - \frac{\omega_k^2}{k_\parallel^2}\right)\frac{\omega_k \Lambda_k}{k_\perp^2}\delta(\Omega_q - qV_g)\frac{\partial N_k^0}{\partial k_x}, \tag{66}$$

where Ω_q is the real part of the frequency. Note that, differentiating dispersion relation (4) for the drift-Alfvén waves and taking into account expression (30), we can prove the identity

$$\left(1 - \frac{\omega_k^2}{k_\parallel^2}\right)\frac{k_x \omega_k \Lambda_k}{k_\perp^2} \equiv -\frac{1}{2}V_g. \tag{67}$$

As a result, as follows from Eq. (66), the condition for the onset of the instability has the form

$$V_g \frac{\partial N_k^0}{\partial k_x} > 0. \tag{68}$$

This instability can be interpreted as being caused by the resonant interaction of a small-scale wave packet with the slow modulations of the zonal flow.

Dispersion relation (64) also describes hydrodynamic instability, which occurs when the instability growth rate exceeds the spectrum width of the small-scale turbulence. Let us consider this instability in the limiting case of a monochromatic wave packet, $N_k^0 = N_0\delta(\mathbf{k} - \mathbf{k}_0)$. Using identity (67) and integrating Eq. (64) by parts, we arrive at the following equation, which is identical in form to the corresponding equation derived in [17]:

$$1 = \frac{q^2}{2}\int d\mathbf{k} k_y^2 N_k^0 \frac{\partial V_g}{\partial k_x}\frac{1}{(\Omega - qV_g)^2}. \tag{69}$$

For a monochromatic wave packet, we obtain

$$(\Omega - qV_g)^2 = \frac{q^2}{2}k_y^2 N_k^0 \frac{\partial V_g}{\partial k_x}, \tag{70}$$

where all of the quantities dependent on $\mathbf{k}$ are assumed to be taken at $\mathbf{k} = \mathbf{k}_0$. The instability takes place under the condition

$$N_k^0 \frac{\partial V_g}{\partial k_x} < 0, \tag{71}$$

in which case the growth rate of the instability of the zonal flow is written as

$$\Omega = qV_g + i|q||k_y|\sqrt{\left|N_k^0 \frac{\partial}{\partial k_x}\left(\frac{k_x k_\parallel^2 \omega_k^2}{2\omega_k^3 - \omega_{*e,k}(\omega_k^2 + k_\parallel^2)}\right)\right|}. \tag{72}$$

The growth rate $\gamma \sim I_k^{1/2}$ of the hydrodynamic instability exceeds the growth rate $\gamma \sim I_k$ of the resonant instability. A parametric hydrodynamic instability was investigated by Guzdar *et al.* [29], who used an approach based on the theory of coherent parametric instabilities. The condition for the onset of the instability that was obtained in [29] coincides qualitatively with condition (71).

A more detailed analysis of the dispersion relation of the form of relation (69) has been presented in a recent paper by Malkov *et al.* [34]. Because of the fairly nontrivial structure of dispersion relation (69), which stems primarily from the lengthy expression for the group velocity of the drift-Alfvén waves, it might be supposed that this relation can hardly be analyzed analytically and, in particular practical applications, it should be examined numerically. That is why we restrict our discussion to the above analysis.

Dispersion relation (4) can be modified to include the effects of the resonant interaction of drift-Alfvén waves with electrons; the result is (see, e.g., [35])

$$(\omega - \omega_{*e,k})(\omega^2 - k_\parallel^2)\left[1 + \frac{i\sqrt{\pi}\omega}{|k_\parallel|}\left(\frac{m_e}{m_i\beta}\right)^{1/2}\right] = \omega k_\parallel^2 k_\perp^2. \tag{73}$$

Under the assumption $\omega \sim k_\parallel \sim \omega_{*e,k}$, Eq. (73) yields the approximate relation $\omega = \omega_k + i\gamma_k$, where the real part ω_k of the frequency is determined from Eq. (4) and the imaginary part $\gamma_k \ll \omega_k$ of the frequency, which is governed by the Landau resonance, has the form

$$\gamma_k = -\sqrt{\pi}\frac{k_\perp^2 \omega_k^3 \Lambda_k}{|k_\parallel|(\omega_k - \omega_{*e,k})}\left(\frac{m_e}{m_i\beta}\right)^{1/2}. \tag{74}$$

Since relationships (29) were derived from equations that do not incorporate longitudinal electron motion, they also remain valid when the resonant interaction is taken into account. We thus arrive at the following set of averaged equations:

$$\begin{aligned}\frac{\partial \bar{N}}{\partial T} &= -\frac{\partial}{\partial X}\int d\mathbf{k} k_y \frac{\omega_{*e,k}}{\omega_k}\frac{\gamma_k}{\omega_k}\Lambda_k^2 I_k \\ &\quad -\frac{\partial^2}{\partial X^2}\int d\mathbf{k} k_x k_y \frac{\omega_k^2}{k_\parallel^2}\Lambda_k^2 I_k,\end{aligned} \tag{75}$$

$$\frac{\partial \bar{A}}{\partial T} = \frac{\partial}{\partial X}\int d\mathbf{k} k_y \frac{\gamma_k}{k_\parallel}\left(1 + k_\perp^2 - 2\frac{\omega_{*e,k}}{\omega_k}\right)\Lambda_k^2 I_k, \tag{76}$$

$$\frac{\partial}{\partial T}\frac{\partial^2 \bar{\phi}}{\partial X^2} = \frac{\partial^2}{\partial X^2}\int d\mathbf{k} k_x k_y \left(1 - \frac{\omega_k^2}{k_\parallel^2}\right)\Lambda_k^2 I_k. \tag{77}$$

Together with Eq. (51), these equations constitute a closed set of equations describing the interaction of the small-scale drift-Alfvén turbulence with long-wavelength zonal perturbations.

When the weak resonant interaction of the small-scale turbulence with electrons is taken into account (under the assumption that $|\gamma_k/\omega_k| \ll (k_x/q)k_\perp^2$), we can see from Eqs. (75)–(77) that, as before, there exists a mode that causes negligibly small perturbations of the plasma density and magnetic field and corresponds to the zonal flow. The above instability analysis for this mode remains valid. Along with the zonal flow, there can exist a slower mode satisfying the condition (see the Appendix for details)

$$\frac{\partial^2}{\partial X^2}\int d\mathbf{k} k_x k_y \left(1 - \frac{\omega_k^2}{k_\parallel^2}\right)\Lambda_k^2 I_k \simeq 0. \tag{78}$$

For simplicity, we restrict ourselves to considering the perturbations for which $qk_x \ll |\gamma_k/\omega_k|$ (under the origi-

nal assumption $q \ll k_\perp$, this condition does not contradict the above restriction on the maximum possible values of the quantity γ_k) and assume that $|\omega_{*e,k}/\omega_k| \ll 1$ and that the small-scale oscillations are Alfvénic, $\omega_k^2 = k_\parallel^2(1 + k_\perp^2)$. In this formulation, the problem was investigated by Smolyakov *et al.* [27]. Equation (75) implies that, in the case in question, long-wavelength density perturbations can be neglected, $\bar{N} = 0$. We represent I_k as a sum of the equilibrium component and a perturbation caused by the long-wavelength modulation, $I_k = I_k^0 + \tilde{I}_k$. Then, we linearize Eq. (51) in the perturbations of the form $(\bar{\phi}, \tilde{I}_k) \sim \exp(-i\Omega t + iqx)$ to obtain

$$\tilde{I}_k = -\frac{ik_y q^2}{\Omega - qV_g}\left\{\frac{(1+k_\perp^2)^{3/2}}{k_\perp^2}\frac{\partial}{\partial k_x}\left[\frac{k_\perp^2 I_k^0}{(1+k_\perp^2)^{3/2}}\right]\bar{\phi} - \frac{\omega_k}{k_\parallel}\frac{1+k_\perp^2}{k_\perp^2}\frac{\partial}{\partial k_x}\left[\frac{k_\perp^2 I_k^0}{1+k_\perp^2}\right]\bar{A}\right\}. \quad (79)$$

Substituting relationship (79) into Eq. (78) yields

$$\bar{\phi} = (\lambda/S)\bar{A}, \quad (80)$$

where

$$\lambda = \int d\mathbf{k}\frac{k_x k_y^2}{\Omega - qV_g}\frac{k_\parallel}{\omega_k}\frac{\partial}{\partial k_x}\left[\frac{k_\perp^2 I_k^0}{1+k_\perp^2}\right], \quad (81)$$

$$S = \int d\mathbf{k}\frac{k_x k_y^2}{(\Omega - qV_g)(1+k_\perp^2)^{1/2}}\frac{\partial}{\partial k_x}\left[\frac{k_\perp^2 I_k^0}{(1+k_\perp^2)^{3/2}}\right]. \quad (82)$$

In this case, expression (74) for the damping rate of Alfvén waves also reduces to a far simpler form:

$$\gamma_k = -\frac{\sqrt{\pi}}{2}k_\perp^2|k_\parallel|\left(\frac{m_i}{m_i\beta}\right)^{1/2}. \quad (83)$$

Finally, substituting relationships (79), (80), and (83) into Eq. (76), we arrive at the dispersion relation

$$\Omega = -\frac{iq^3\sqrt{\pi}}{8}\left(\frac{m_e}{m_i\beta}\right)^{1/2}\int d\mathbf{k}\frac{k_y^2|k_\parallel|}{(\Omega - qV_g)k_\parallel} \times\left\{\frac{\lambda}{S}(1+k_\perp^2)^{1/2}\frac{\partial}{\partial k_x}\left[\frac{k_\perp^2 I_k^0}{(1+k_\perp^2)^{3/2}}\right] - \frac{\omega_k}{k_\parallel}\frac{\partial}{\partial k_x}\left[\frac{k_\perp^2 I_k^0}{1+k_\perp^2}\right]\right\}. \quad (84)$$

Under the assumption $qV_g > \Omega$, which is analogous to the corresponding assumption used in [35], Eq. (84) yields

$$\Omega = \frac{iq^2\sqrt{\pi}}{4}\left(\frac{m_e}{m_i\beta}\right)^{1/2}\int d\mathbf{k}\frac{k_y^2}{|k_\parallel|}\frac{\omega_k}{k_\parallel} \times\left\{\frac{\lambda}{S}(1+k_\perp^2)^{1/2}\frac{\partial}{\partial k_x^2}\left[\frac{k_\perp^2 I_k^0}{(1+k_\perp^2)^{3/2}}\right] - \frac{\omega_k}{k_\parallel}\frac{\partial}{\partial k_x^2}\left[\frac{k_\perp^2 I_k^0}{1+k_\perp^2}\right]\right\}. \quad (85)$$

Qualitatively, dispersion relation (85) is similar in structure to the relation derived in [27]; however, quantitatively, they are significantly different. This stems primarily from the fact that Smolyakov *et al.* [27] neglected long-wavelength perturbations of the transverse electric field, $\bar{\phi} = 0$ (i.e., they set $\lambda = 0$), which does not seem to be justified, except for the particular case $k_\perp^2 \ll 1$ and $\omega_k^2 \approx k_\parallel^2$ mentioned above. In addition, the second term in the integrand in dispersion relation (85) is opposite in sign to that in the corresponding relation obtained in [27]. The reason for this is the following. Equation (76) was derived using only linear relationships between $\tilde{\phi}_k$, $\tilde{A}_k$, and $\tilde{N}_k$; these relationships follow from the equations that do not incorporate the longitudinal electron motion and remain valid when the resonant interaction of drift-Alfvén waves with electrons is taken into account. On the other hand, in deriving the averaged equation describing the evolution of the large-scale magnetic field, Smolyakov *et al.* [27] expressed the quantity $\tilde{\phi}_k - \tilde{N}_k$ in terms of $\tilde{A}_k$ using the equation for the longitudinal electron motion (Ohm's law) but neglecting the Landau resonance, which was taken into account only in the expression for the wave frequency. One can readily see that incorporating these effects into the longitudinal Ohm's law changes the sign of the averaged term, i.e., leads to the same sign of the averaged term as that in dispersion relation (85). Note also that the dispersion relation is misprinted in [27]: its correct form should include the factor $|k_\parallel|^{-1}$.

From dispersion relation (85), we obtain the following instability criterion:

$$\int d\mathbf{k}\frac{k_y^2}{|k_\parallel|}\frac{\omega_k}{k_\parallel}\left\{\frac{\lambda}{S}(1+k_\perp^2)^{1/2}\frac{\partial}{\partial k_x^2}\left[\frac{k_\perp^2 I_k^0}{(1+k_\perp^2)^{3/2}}\right] - \frac{\omega_k}{k_\parallel}\frac{\partial}{\partial k_x^2}\left[\frac{k_\perp^2 I_k^0}{1+k_\perp^2}\right]\right\} > 0. \quad (86)$$

Even in the simplest case considered above, the expression for the growth (damping) rate of the instability of a large-scale zonal magnetic field is very nontrivial; therefore, it is not sufficient to know (as in the case of the generation of a zonal flow) only the sign of the product of the spectral function of the small-scale turbulence and a certain factor [see Eqs. (66), (71)]. Indeed, it is necessary to know the explicit dependence of the spectral function on the wavenumber. In a more general case such that $qk \simeq |\gamma_k/\omega_k|$ and $|\omega_{*e,k}/\omega_k| \simeq 1$, it is also necessary to take into account the long-wavelength perturbation of the plasma density. As a result, the dispersion relation becomes too lengthy, and we will not analyze it here. It seems that, for practical purposes, the dispersion relation should be analyzed numerically with allowance for the observed spectra of the small-scale oscillations.

Recall that, in the particular case $\omega_k^2 \approx k_\parallel^2$, only a large-scale zonal magnetic field may be perturbed. Presumably, it is this case to which the analysis carried out in [27] is applicable. In the situation at hand, the dispersion relation of the mode can formally be derived from Eq. (84) with $\lambda = 0$ and $k_\perp^2 \ll 1$. Under the assumption that $qV_g > \Omega$, we obtain

$$\Omega = -\frac{iq^2\sqrt{\pi}}{4}\left(\frac{m_e}{m_i\beta}\right)^{1/2}\int d\mathbf{k}\frac{k_y^2}{|k_\parallel|}\frac{\partial}{\partial k_x^2}(k_\perp^2 I_k^0). \quad (87)$$

Here, the sign of Ω is opposite to that in the corresponding expression of [27]. The reasons for this and other discrepancies have been explained above. Dispersion relation (87) implies that the instability occurring under the condition

$$\frac{\partial}{\partial k_x^2}(k_\perp^2 I_k^0) < 0, \quad (88)$$

leads to the generation of a zonal magnetic field.

6. MAIN RESULTS AND CONCLUSIONS

In the present work, the possibility of generating large-scale zonal structures by drift-Alfvén turbulence in a plasma with a finite pressure ($\beta > m_e/m_i$) has been investigated. The interaction between drift-Alfvén turbulence and large-scale zonal perturbations is described by a set of coupled equations (17)–(19) and (51), which were derived in the quasilinear approximation. Equation (51) for the spectral function was obtained with allowance not only for the perturbation of the transverse electric field that is responsible for generating a zonal flow but also for the perturbations of the zonal magnetic field and plasma density. Generally, this equation ceases to be a conservation law for a certain invariant that is determined exclusively by small-scale oscillations and may be considered an analogue of the number of quanta. On the other hand, in the electrostatic limit $c_A \longrightarrow \infty$ (or $k_\parallel \longrightarrow \infty$, in terms of the normalized quantities used above), Eq. (51), in the cases of two-dimensional large-scale perturbations and quasi-two-dimensional perturbations (the Hasegawa–Mima model), reproduces the results obtained earlier in [16] and has the form of a conservation law applying to small-scale oscillations. In the case of Alfvén turbulence such that $\omega_k^2 \approx k_\parallel^2$, this equation can also be reduced to a conservation law.

It has been shown that, when the zonal flow alone is taken into account while the perturbations of the plasma density and zonal magnetic field are neglected, Eq. (51) represents a conservation law for the action invariant, even with allowance for the electromagnetic effects. This approximation is justified when the effects of the resonant interaction of drift-Alfvén waves with electrons are ignored, in which case the eigenfrequency of the waves is real. The stability of the drift-Alfvén turbulence against a large-scale zonal flow has been investigated. By analogy with [17], two instability regimes have been analyzed and the corresponding two criteria (66) and (71) for the onset of the instability have been derived for different ratios of the width $\Delta\omega_k$ of the spectrum of the drift-Alfvén turbulence to the instability growth rate.

The possibility of the spontaneous zonal magnetic field generation by the instability of the turbulence spectrum has been investigated neglecting the drift effects but taking into account the weak resonant damping of Alfvén waves. The growth rate of this instability is slower than that of the instability generating a zonal flow. It has been shown that the spontaneous generation of the zonal magnetic field is accompanied by the generation of a zonal flow and that the instability criterion depends essentially on the effects associated with this flow. The instability criterion for the zonal flow is determined primarily by the sign of the derivative of the action invariant with respect to the wavenumber. In contrast, the instability at hand is highly sensitive to the turbulence spectrum; hence, answering the question about the possibility of the spontaneous zonal magnetic field generation requires knowledge of the explicit dependence of the spectral function of turbulence on the wavenumber. In the case of Alfvén turbulence such that $\omega_k^2 \approx k_\parallel^2$, the spontaneous generation of the zonal magnetic field is not accompanied by the generation of a zonal flow. The criterion for the onset of this instability is determined only by the sign of the derivative of the action invariant with respect to the wavenumber.

The above analysis has been carried out based on the simplest model of the interactions in a "drift-Alfvén waves + large-scale zonal flows" system. Such a model may thus be regarded as the first step toward the construction of the theory of the generation of zonal flows and magnetic fields in a plasma with a finite pressure (i.e., with allowance for electromagnetic effects). Ongoing studies will be aimed at generalizing the theory to include finite-ion-Larmor-radius effects by using as a starting point model hydrodynamic equations that are similar to those derived in [36, 37] and are based on the Padé approximation of the exact kinetic expressions for the ion response.

The above analysis has been concerned exclusively with the linear stage of the instability of zonal flows. That is why another possible way of generalizing the theory is to include the effects associated with the finite amplitude of the zonal flows (e.g., in the spirit of [38]). Thus, it may be hypothesized that a "drift-Alfvén waves + zonal perturbations" system is self-organized in the sense that, during the secondary instability of drift-Alfvén waves, a fraction of their energy is transferred to the zonal perturbations; as a result, the wave amplitudes should decrease and, accordingly, at certain amplitudes of the drift-Alfvén turbulence and zonal

perturbations, the system may reach equilibrium. However, confirming this hypothesis requires a detailed analytic examination and, possibly, numerical analysis of the equations derived in the present paper.

ACKNOWLEDGMENTS

I am grateful to A.I. Smolyakov for bringing to my attention a number of papers on the subject and for useful discussions. This work was supported in part by the Council on the Grants of the President of the Russian Federation, the Council of the Federal Program "Government Support of the Leading Scientific Schools" (project no. 00-15-96526), and the Russian Foundation for Basic Research (project no. 02-02-16089).

APPENDIX

Derivation of the Dispersion Relation with Allowance for the Resonant Interaction of Alfvén Oscillations with Electrons

Under the conditions $qk_x \ll \gamma_k/k_\parallel \ll (k_x/q)k_\perp^2$ and $\omega_{*e,k}/\omega_k \longrightarrow 0$, large-scale zonal perturbations of the plasma density can be neglected, $\bar{N} = 0$. Using relationship (79), we can represent Eqs. (76) and (77) in the form

$$\Omega\bar{A} = a(\alpha_1\bar{\phi} + \beta_1\bar{A}), \tag{A.1}$$

$$\Omega\bar{\phi} = b(\alpha_2\bar{\phi} + \beta_2\bar{A}), \tag{A.2}$$

where the coefficients a, b, α_1, α_2, β_1, and β_2 depend on the spectrum of Alfvén oscillations and on the wave vector of the long-wavelength perturbations; moreover, $(\alpha_i, \beta_i) \simeq 1$; $i = (1, 2)$; and, under the above assumptions, $b \gg a$. Then, from Eqs. (A.1) and (A.2), we obtain the following expression for the growth rate of the instability of large-scale zonal perturbations:

$$\begin{aligned}\Omega &= \frac{a\beta_1 + b\alpha_2}{2} \pm \sqrt{\frac{(a\beta_1 + b\alpha_2)^2}{4} - ab(\alpha_2\beta_1 - \alpha_1\beta_2)} \\ &\approx \frac{a\beta_1 + b\alpha_2}{2} \\ &\pm \frac{1}{2}\sqrt{b^2\alpha_2^2 + 2ab\alpha_2\beta_1 - 4ab(\alpha_2\beta_1 - \alpha_1\beta_2)} \\ &\approx \frac{a\beta_1 + b\alpha_2}{2} \pm \frac{b\alpha_2}{2}\sqrt{1 + \frac{2a(2\alpha_1\beta_2 - \alpha_2\beta_1)}{b\alpha_2^2}} \\ &\approx \frac{a\beta_1 + b\alpha_2}{2} \pm \frac{1}{2}\left\{b\alpha_2 + \frac{a}{\alpha_2}(2\alpha_1\beta_2 - \alpha_2\beta_1)\right\}.\end{aligned} \tag{A.3}$$

This expression implies that, in the case under consideration, there exist two modes. The upper sign in formula (A.3) corresponds to the mode with the higher frequency, which is the electrostatic mode (the zonal flow):

$$\Omega = b\alpha_2. \tag{A.4}$$

The slower electromagnetic mode is described by the lower sign and satisfies the equation

$$\begin{aligned}\Omega &= \frac{1}{2}\left[a\beta_1 - \frac{a}{\alpha_2}(2\alpha_1\beta_2 - \alpha_2\beta_1)\right] \\ &\equiv a\left(\beta_1 - \alpha_1\frac{\beta_2}{\alpha_2}\right).\end{aligned} \tag{A.5}$$

Relationships (A.4) and (A.5) can be derived directly from Eqs. (A.1) and (A.2). Thus, relationship (A.4) follows from Eq. (A.2) under the assumption that $\bar{A} = 0$. Using an equation analogous to Eq. (78), i.e., setting the right-hand side of Eq. (A.2) equal to zero, we get

$$\bar{\phi} = -\frac{\beta_2}{\alpha_2}\bar{A}. \tag{A.6}$$

Substituting formula (A.6) into Eq. (A.1), we arrive at relationship (A.5).

REFERENCES

1. Z. Lin, T. S. Hahm, W. W. Lee, *et al.*, Science **281**, 1835 (1998).
2. T. S. Hahm, M. A. Beer, Z. Lin, *et al.*, Phys. Plasmas **6**, 922 (1999).
3. R. E. Waltz, R. L. Dewar, and X. Garbet, Phys. Plasmas **5**, 1784 (1998).
4. X. Garbet, Plasma Phys. Controlled Fusion **39**, 91 (1997).
5. B. Scott, Phys. Plasmas **7**, 1845 (2000).
6. F. Jenko, W. Dorland, M. Kotschenreuther, and B. N. Rogers, Phys. Plasmas **7**, 1904 (2000).
7. P. H. Diamond and Y.-B. Kim, Phys. Fluids B **3**, 1626 (1991).
8. V. N. Oraevskiĭ, in *Handbook of Plasma Physics*, Ed. by A. A. Galeev and R. N. Sudan (Énergoatomizdat, Moscow, 1984; North-Holland, Amsterdam, 1984), Vol. 2.
9. P. N. Guzdar, J. F. Drake, D. McCarthy, *et al.*, Phys. Fluids B **5**, 3712 (1993).
10. P. N. Guzdar, Phys. Plasmas **2**, 4174 (1995).
11. L. Chen, Z. Lin, and R. White, Phys. Plasmas **7**, 3129 (2000).
12. M. V. Osipenko, Fiz. Plazmy **23**, 909 (1997) [Plasma Phys. Rep. **23**, 837 (1997)].
13. P. N. Guzdar, R. G. Kleva, and L. Chen, Phys. Plasmas **8**, 459 (2001).
14. V. B. Lebedev, P. H. Diamond, V. D. Shapiro, and G. I. Soloviev, Phys. Plasmas **2**, 4420 (1995).
15. B. Dubrulle and S. V. Nazarenko, Physica D **110**, 123 (1997).
16. A. I. Smolyakov and P. H. Diamond, Phys. Plasmas **6**, 4410 (1999).
17. A. I. Smolyakov, P. H. Diamond, and V. I. Shevchenko, Phys. Plasmas **7**, 1349 (2000).

18. A. I. Smolyakov, P. H. Diamond, and M. V. Medvedev, Phys. Plasmas **7**, 3987 (2000).
19. J. A. Krommes and C. B. Kim, Phys. Rev. E **62**, 8508 (2000).
20. S. I. Vaĭnshtein, Ya. B. Zel'dovich, and A. A. Ruzmaĭkin, *Turbulent Dynamo in Astrophysics* (Nauka, Moscow, 1980).
21. H. Branover, A. Eidelman, E. Golbraikh, and S. Moiseev, *Turbulence and Structures* (Academic, San Diego, 1999).
22. A. A. Vedenov and L. I. Rudakov, Dokl. Akad. Nauk SSSR **159**, 767 (1964) [Sov. Phys. Dokl. **9**, 1073 (1965)].
23. A. V. Gruzinov, P. H. Diamond, and V. B. Lebedev, Phys. Plasmas **1**, 3148 (1994).
24. A. V. Chechkin, M. I. Kopp, V. V. Yanovskiĭ, and A. V. Tur, Zh. Éksp. Teor. Fiz. **113**, 646 (1998) [JETP **86**, 357 (1998)].
25. V. P. Lakhin, Fiz. Plazmy **27**, 777 (2001) [Plasma Phys. Rep. **27**, 733 (2001)].
26. A. I. Smolyakov, P. H. Diamond, and Y. Kishimoto, Phys. Plasmas **9**, 3826 (2002).
27. A. I. Smolyakov, P. H. Diamond, I. Gruzinov, *et al.*, in *Proceedings of the Joint Lausanne–Varenna International Workshop on Theory of Fusion Plasmas, Varenna, 2000*, Ed. by J. W. Connor (Compository, Bologna, 2001), p. 199.
28. I. Gruzinov, A. Das, P. H. Diamond, and A. I. Smolyakov, Phys. Lett. A (in press).
29. P. N. Guzdar, R. G. Kleva, A. Das, and P. Kaw, Phys. Plasmas **8**, 3907 (2001).
30. P. K. Shukla, M. Y. Yu, and R. K. Varma, Phys. Fluids **28**, 1719 (1985).
31. V. P. Lakhin, A. B. Mikhaĭlovskiĭ, and O. G. Onishchenko, Fiz. Plazmy **13**, 188 (1987) [Sov. J. Plasma Phys. **13**, 104 (1987)].
32. A. Galeev and R. Sagdeev, in *Reviews of Plasma Physics*, Ed. by M. A. Leontovich (Atomizdat, Moscow, 1973; Consultants Bureau, New York, 1979), Vol. 7.
33. P. H. Diamond, M. N. Rosenbluth, F. L. Hinton, *et al.*, in *Proceedings of the 17th IAEA Conference on Fusion Energy, Yokohama, 1998* (IAEA, Vienna, 1998), paper IAEA-CN-69/TH3/1.
34. M. A. Malkov, P. H. Diamond, and A. I. Smolyakov, Phys. Plasmas **8**, 1553 (2001).
35. A. B. Mikhaĭlovskiĭ, *Theory of Plasma Instabilities* (Atomizdat, Moscow, 1977; Consultants Bureau, New York, 1974), Vol. 2.
36. B. N. Kuvshinov and A. B. Mikhaĭlovskiĭ, Fiz. Plazmy **22**, 582 (1996) [Plasma Phys. Rep. **22**, 529 (1996)].
37. T. J. Schep, B. N. Kuvshinov, and F. Pegoraro, Phys. Plasmas **1**, 2843 (1994).
38. M. A. Malkov and P. N. Diamond, Phys. Plasmas **8**, 3996 (2001).

Translated by I.A. Kalabalyk

Plasma Physics Reports, Vol. 29, No. 2, 2003, pp. 151–160. Translated from Fizika Plazmy, Vol. 29, No. 2, 2003, pp. 172–181.

PLASMA OSCILLATIONS AND WAVES

Theory of Longitudinal Plasma Waves with Allowance for Ion Motion

G. N. Kichigin

Institute of Solar and Terrestrial Physics, Siberian Division, Russian Academy of Sciences, Irkutsk, 664033 Russia

Received December 18, 2001; in final form, July 31, 2002

Abstract—A study is made of the propagation of steady-state large-amplitude longitudinal plasma waves in a cold collisionless plasma with allowance for both electron and ion motion. Conditions for the existence of periodic potential waves are determined. The electric field, potential, frequency, and wavelength are obtained as functions of the wave phase velocity and ion-to-electron mass ratio. Taking into account the ion motion results in the nonmonotonic dependence of the frequency of the waves with the maximum possible amplitudes on the wave phase velocity. Specifically, at low phase velocities, the frequency is equal to the electron plasma frequency for linear waves. As the phase velocity increases, the frequency first decreases insignificantly, reaches its minimum value, and then increases. As the phase velocity increases further, the frequency continues to increase and, at relativistic phase velocities, again becomes equal to the plasma frequency. Finally, as the phase velocity approaches the speed of light, the frequency increases without bound. © *2003 MAIK "Nauka/Interperiodica"*.

1. INTRODUCTION

A fairly detailed review of the results of theoretical investigations on steady-state plasma waves in a collisional plasma was given in a fundamental paper by Akhiezer and Polovin [1] (see also monograph [2]). In [1], an analysis was made of plane waves in an unbounded plasma consisting of electrons (which were assumed to be cold) and heavy ions (which were assumed to be immobile). However, it is questionable whether the assumption that the ions are immobile can be used to describe large-amplitude nonlinear waves. In fact, recent papers on relativistic waves in plasmas [3–7] and works on laser–plasma interactions [8–10] clearly showed that, at sufficiently large wave amplitudes, it is necessary to take into account the ion motion. The effect of ion dynamics on the wave structure was considered by Khachatryan [7], who investigated the dependence of the maximum possible (limiting) electric field in a longitudinal plasma wave and the wavelength of this wave on the parameter μ for different values of the relativistic factor $\gamma = (1 - u^2/c^2)^{-1/2}$ (here, μ is the ion-to-electron mass ratio, u is the wave phase velocity, and c is the speed of light in vacuum). In studying the interaction of laser pulses with plasma, Bulanov *et al.* [8] estimated the laser field strengths at which it is necessary to take into account the plasma ion motion. Also, incorporating the ion mass, they determined the wavelength, electric potential, and electric field of the wake waves as functions of the laser field amplitude.

Here, in contrast to [1], the problem of the propagation of longitudinal plasma waves is solved with allowance for ion motion, and the solution is sought in the wave frame of reference, in which the physical processes occurring in the wave are easier to understand. In other respects, the problem is treated in the same formulation and under the same assumptions as those in [1].

The investigations carried out in this paper show that, for the values of the relativistic factor ranging from 1 to $\mu/2$, the results obtained coincide with the results of [1] (here and below, it is assumed that $\mu \gg 1$). For $\gamma > \mu/2$, only the maximum possible electric field amplitude depends on γ in essentially the same manner as in [1], while the dependence of the remaining parameters on γ differs from that obtained in the theory in which the ion motion is neglected. In the most interesting and important case of relativistic waves ($\gamma \gg 1$), the characteristics of longitudinal plasma waves such as (i) the positive and negative amplitudes of oscillations of the potential, (ii) the limiting electric field of the wave, (iii) the wave frequency, and (iv) the wavelength are obtained analytically as functions of the parameters γ and μ.

The paper is organized as follows. In Section 2, the problem is formulated. In Section 3, the procedure for determining the profiles of the potential and of the electric field in the wave is described. In Section 4, the frequency and wavelength of the waves with the maximum possible amplitudes are determined as functions of the phase velocity. In Section 5, the main results obtained in this study are discussed.

2. FORMULATION OF THE PROBLEM

We are interested in the wave motions in an unbounded cold plasma consisting of the ions with the rest mass M and the electrons with the rest mass m. We

1063-780X/03/2902-0151$24.00

assume that the ions are protons, so that the charge q_i of an ion is equal to the charge of an electron: $q_i = e$, where e is the absolute value of the electron charge. In contrast to [1, 2], in which the ions in a nonlinear plasma wave were treated as immobile, we take into account the ion motion in all of the cases to be investigated (including the relativistic case). We also assume that there is no external magnetic field and restrict ourselves to considering steady-state longitudinal plane waves propagating along the x-axis.

In studying a steady-state wave, it is convenient to switch to the wave frame of reference, in which the problem under consideration is time-independent and all of the sought-for variables depend only on the x coordinate. The set of equations needed to solve the problem consists of Maxwell's equations, the relativistic equations of motion, and the continuity equations for the electrons and ions.

We seek a solution to these equations in the form of an alternating-sign periodic potential wave. In this case, over a spatial interval equal to the wavelength λ, the electric field reaches its extreme values at points lying between the points where the potential is maximum and minimum. Maxwell's equation for the electric field $E(x)$,

$$\frac{dE(x)}{dx} = 4\pi e[n_i(x) - n_e(x)] \tag{1}$$

implies that, at the points of extreme electric-field values, the ion density $n_i(x)$ is equal to the electron density $n_e(x)$. Let the coordinate of one of the extreme point be $x = 0$. At this point, we have $n_i(0) = n_e(0) = n$ and $E(0) = E_0$, where E_0 is the corresponding extreme value of the electric field. Without any loss of generality, the wave potential $\varphi(x)$ can be set at zero at the extreme points; hence, we have $\varphi(0) = 0$ at $x = 0$.

The electron and ion continuity equations

$$\frac{d}{dx}[n_e(x)v_e(x)] = 0, \quad \frac{d}{dx}[n_i(x)v_i(x)] = 0$$

yield $n_i(x)v_i(x) = C_1$ and $n_e(x)v_e(x) = C_2$, where $v_e(x)$ and $v_i(x)$ are the electron and ion velocities and the constants C_1 and C_2 are independent of x. We determine these constants by setting $x = 0$. Since $n_i(0) = n_e(0) = n$, we obtain $C_1 = nv_i(0)$ and $C_2 = nv_e(0)$, where $v_e(0)$ and $v_i(0)$ are constant velocities.

Unequal values of the constants $v_e(0)$ and $v_i(0)$ indicate that a constant current flows in the plasma along the x-axis. This current will give rise to a time-independent magnetic field transverse to the wave propagation direction. Since solving the problem with allowance for both the magnetic field and the electron and ion motion seems to be a fairly difficulty task, we make an assumption with which the problem is much simpler to solve. Namely, we assume that $v_e(0) = v_i(0) = u$, where u is a constant velocity. Then, the net current vanishes everywhere, $e[n_i(x)v_i(x) - n_e(x)v_e(x)] = 0$, which indicates that, in the wave under consideration, the magnetic field is absent.

For a cold plasma with no magnetic field present, the dynamics of electrons and ions in the wave electric field can be described in the single-particle approximation by the following relativistic equations of motion, which are written in the wave rest frame:

$$v_e(x)\frac{dp_e(x)}{dx} = mc^2\frac{d\gamma_e(x)}{dx} = -eE(x), \tag{2}$$

$$v_i(x)\frac{dp_i(x)}{dx} = Mc^2\frac{d\gamma_i(x)}{dx} = eE(x); \tag{3}$$

where $\gamma_e(x) = (1 - v_e(x)/c^2)^{-1/2}$ and $\gamma_i(x) = (1 - v_i^2(x)/c^2)^{-1/2}$. The variables $p_e(x) = mv_e(x)\gamma_e(x)$ and $p_i(x) = Mv_i(x)\gamma_i(x)$ are the momenta of electrons and ions, respectively.

Substituting the relationship $E(x) = -d\varphi(x)/dx$ between the electric field and the potential into Eqs. (2) and (3), we obtain the energy conservation laws for electrons and ions:

$$Mc^2\gamma_i(x) + e\varphi(x) = Mc^2\gamma, \tag{4}$$

$$mc^2\gamma_e(x) - e\varphi(x) = mc^2\gamma. \tag{5}$$

The constants in these laws have been found by determining the energy and the potential at the point $x = 0$, at which we have set $\varphi(0) = 0$ and $v_e(0) = v_i(0) = u$. Here, we have also introduced the notation $\gamma = 1/\sqrt{1-\beta^2}$ with $\beta = u/c$. With the parameter γ so defined, the problem to be solved is physically meaningful only for velocities u below the speed of light.

We add conservation laws (4) and (5) termwise to obtain the conservation low for the total electron and ion energy in the wave:

$$Mc^2\gamma_i(x) + mc^2\gamma_e(x) = (M + m)c^2\gamma. \tag{6}$$

Using Eq. (1), we express the ion and electron densities in terms of the velocity, $n_e(x) = nu/v_e(x)$ and $n_i(x) = nu/v_i(x)$. Then, we multiply both sides of Eq. (1) by $E(x)$ and, using Eqs. (2) and (3), express the resulting terms $eE(x)/v_e(x)$ and $eE(x)/v_i(x)$ through the electron and ion momenta, respectively. As a result, we arrive at the equation

$$\frac{d}{dx}\left\{\left[\frac{E^2(x)}{8\pi}\right] - nu[p_e(x) + p_i(x)]\right\} = 0,$$

which yields one more conservation law:

$$\begin{aligned} &E^2(x)/(8\pi) - nu[p_e(x) + p_i(x)] \\ &\quad = E_0^2/(8\pi) - n\gamma(M + m)u^2, \end{aligned} \tag{7}$$

where $E_0 = E(0)$ and the constant were determined at $x = 0$.

Generally, conservation laws (6) and (7) can be deduced from the energy and momentum conservation laws stated in terms of the four-dimensional energy–momentum tensor T_{ik} of the electromagnetic field, represented as a sum of the tensors for the field, $T_{ik}^{(f)}$, and for the particles, $T_{ik}^{(p)}$: $T_{ik} = T_{ik}^{(f)} + T_{ik}^{(p)}$ [11].

In the case under consideration, these conservation laws in the wave frame have the form $dT_{4x}/dx = 0$ and $dT_{xx}/dx = 0$. Since the magnetic field is absent and, consequently, the Poynting vector equals zero, we have $T_{4x}^{(f)} = 0$. The remaining nonzero tensor components have the form

$$T_{4x}^{(p)} = mcn_e v_e \gamma_e + Mcn_i v_i \gamma_i,$$

$$T_{xx}^{(f)} = -E^2/(8\pi), \quad T_{xx}^{(p)} = mn_e v_e^2 \gamma_e + Mn_i v_i^2 \gamma_i.$$

With allowance for these tensor components and the above relationship $n_e v_e = n_i v_i = nu$, the condition $dT_{4x}/dx = 0$ yields conservation law (6) and the condition $dT_{xx}/dx = 0$ gives conservation law (7).

Having introduced the velocity u, we can use a frame of reference moving at this velocity with respect to the wave frame. We will call this frame the laboratory frame of reference (or, simply, the lab frame) and will mark the quantities in this reference frame by the superscript L. In the lab frame, the wave propagates at the velocity u in the negative direction along the x-axis, has the wavelength λ^L, and is characterized by the period of oscillations $T = u/\lambda^L$ of the potential and the electric field.

Let us transform the above conservation laws to the lab frame. To do this, we can determine all the required quantities using the Lorentz transformation formulas for inertial frames of reference. First, we write the transformation formulas for the wave vector $k = 2\pi/\lambda$ and wave frequency: $k = k^L/\gamma$ and $0 = \gamma(\omega + uk^L)$, where $\omega = 2\pi/T$ is the wave frequency in the lab frame and the wave frequency in the wave frame is naturally set equal to zero. We can see that the velocity $u = -\omega/k^L$ is the wave phase velocity in the lab frame.

In the lab frame, conservation law (6) has the form

$$K_e^L(x) + K_i^L(x) + u[p_e^L(x) + p_i^L(x)] = 0, \qquad (8)$$

where $x = x^L + ut^L$ (t^L being the time in the lab frame), $K_e^L(x) = mc^2[\gamma_e^L(x) - 1]$ is the electron kinetic energy, and $K_i^L(x) = Mc^2[\gamma_i^L(x) - 1]$ is the ion kinetic energy.

Using conservation law (6), we can write conservation law (7) in the lab frame as

$$E^2(x)/8\pi + n_0[K_e^L(x) + K_i^L(x)] = E_0^2/8\pi \qquad (9)$$

or, taking into account conservation law (8), as

$$E^2(x)/8\pi - n_0 u[p_e^L(x) + p_i^L(x)] = E_0^2/8\pi, \qquad (10)$$

where $n_0 = n/\gamma$ is the plasma density in the lab frame. A comparison between conservation laws (7) and (10) leads to an interesting conclusion: in both frames considered, the quantity $E^2(x)/(8\pi) - nu[p_e(x) + p_i(x)]$ is a constant.

If we assume that the ions in the lab frame are immobile, then we have $K_i^L = 0$; in this case, we can see that conservation law (9) coincides with the equation that relates the wave energy to the electron energy and that was obtained in [1, 2] for nonlinear plasma waves in the absence of a magnetic field.

In the lab frame, the characteristic point at the wave profile whose coordinate in the wave frame is $x = 0$ moves with the velocity $-u$. At this point, the plasma in the wave frame is quasineutral. Clearly, the plasma at this point is quasineutral in all inertial reference frames, including the lab frame. However, the most noteworthy result is that, in the lab frame, the ions and electrons at this point are immobile. This immediately yields that, in the absence of a wave and the field perturbations driven by it, all plasma electrons and ions in the lab frame will be at rest and the plasma will be quasineutral, the particle density being n_0.

The above considerations imply that, in the lab frame, the density of an immobile plasma that is not perturbed by the wave is n_0, the frequency of the wave is ω, and its wavenumber is k^L, the wave phase velocity in the lab frame being $u = -\omega/k^L$. Notably, taking into account these results and the fact that, at $K_i^L = 0$, conservation law (9) coincides with the equation that relates the wave energy to the electron energy and was derived in [1, 2], we can conclude that the lab frame introduced by us is precisely the frame of reference in which the problem of waves in a plasma is treated in [1, 2].

The above set of equations (1)–(7) is sufficient to solve the problem as formulated. The parameters of the problem are n_0, μ, and γ.

3. DETERMINATION OF THE WAVE PROFILE

One of the main objectives of our study is to determine the profiles of the potential and electric field of the wave. This can be done by using conservation law (7). We introduce the dimensional coordinate and potential, $\xi = x\omega_p\sqrt{\beta}/c$ and $\psi(\xi) = \varphi(x)/(mc^2)$, where $\omega_p = \sqrt{4\pi e^2 n/m}$ is the electron plasma frequency. Using energy conservation laws (4) and (5), we express the electron and ion momenta in terms of the potential.

Then, in dimensionless variables, conservation law (7) can be written as

$$V(\psi) = \mathcal{E} - [d\psi(\xi)/d\xi]^2/2$$
$$= \mu\beta\gamma - \sqrt{\mu^2\beta^2\gamma^2 - \psi(2\mu\gamma - \psi)} + \beta\gamma \qquad (11)$$
$$- \sqrt{\beta^2\gamma^2 + \psi(2\gamma + \psi)}.$$

Here, the variable ψ is a function of ξ; the constant parameters μ, β, and γ were defined above; and the constant parameter $\mathcal{E} = (1/2)(d\psi/d\xi)_0^2$ is the dimensionless density of the electric field energy at the point $\xi = 0$, at which $\psi = 0$ and the electric field is maximum.

From conservation law (11), we can determine the sought-for dependences of the potential and electric field on the coordinate. In the case at hand, the function $V(\psi)$, which has the meaning of the dimensionless density of the electric field energy, obviously satisfies the equation $d^2\psi/d\xi^2 = -dV/d\psi$, whose form implies that $V(\psi)$ plays the role of the potential energy in the problem of the motion of a particle of unit mass, where the variables ψ and ξ present the coordinate and time, respectively. The parameter $\mathcal{E}$ plays the role of the total energy of a particle moving in the potential well in question. In order to understand the general structure of the sought-for solution, it is convenient to turn to the formalism that was developed to analyze particle motion in a potential well in classical mechanics [12]. It is well known that, by analyzing the spatial profile of the potential energy, it is possible to describe the particle motion qualitatively. In the case at hand, this indicates that, from the shape of the profile $V(\psi)$, it is possible to find the dependence $\psi = \psi(\xi)$. This way of qualitative analysis will be used below.

Now, we consider the properties of the function $V(\psi)$. In examining analytic expression (11) for $V(\psi)$, one can readily see that the function is defined in a finite range of the variable ψ, namely, in the closed interval $-(\gamma - 1) \le \psi \le \mu(\gamma - 1)$. We denote the boundaries of this interval of the variable ψ by $\psi_-^* = -(\gamma - 1)$ and $\psi_+^* = \mu(\gamma - 1)$. That this interval of the potential is actually finite can be justified on the basis of physical considerations. In doing so, we begin by noting that, if the potential humps in the wave are lower than ψ_-^* and ψ_+^*, then the ions and electrons at different points on the wave potential profile move with different velocities but in the same direction. Consequently, in this case, the particle flow and the direction of the flow velocity vector are both constant and are the same at all points on the potential profile.

Further, in the wave frame, an electron moving in the positive direction along the x-axis is decelerated when it climbs up the potential hump of the negative polarity and is accelerated when it falls in the potential well of the positive polarity. An electron located at the point $\xi = 0$ on the wave profile (at this point, we have $\psi = 0$) moves with the velocity u, which is still sufficient for it to climb up the potential hump of height ψ_-^*. For larger potential amplitudes, the electrons will be reflected from the humps of the wave potential. The appearance of reflected electrons gives rise to a multistream motion, thereby breaking up the laminar (single-stream) motion, which is necessary for the existence of the steady-state wave under consideration. Analogously, the reflected ions that appear in the wave at amplitudes of the positive potential larger than ψ_+^* will also break up the laminar character of the flow, as is the case with electrons.

These considerations imply that, in our problem of a potential wave in a plasma, the values ψ_-^* and ψ_+^* are, respectively, the negative and positive maximum amplitudes of the dimensionless potential at which the motions of the electron and ion fluids in the wave are laminar, i.e., single-stream. Consequently, for potential amplitudes larger than ψ_-^* and ψ_+^*, the function $V(\psi)$ is undefined, as is clear from the analysis of its domain of existence, and, in addition, nonlinear laminar plasma waves cannot propagate, which follows from the above physical considerations.

Analyzing the function $V(\psi)$, we can easily see that its value at the boundary point $\psi = \psi_+^*$ is always larger than that at the other boundary point $\psi = \psi_-^*$. As a result, the maximum depth of the potential well is determined by the value ψ_-^*, which is, in turn, the maximum value of the negative amplitude of oscillations of the potential. It is clear that, at a given value of the parameter $\mathcal{E}$, the peak-to-peak oscillation amplitude is determined by expression (11) at $V(\psi) = \mathcal{E}$. Consequently, setting $V(\psi) = \mathcal{E}$ at $\psi = \psi_-^*$, we can use expression (11) to find the limiting value of the parameter $\mathcal{E}$ and, accordingly, the maximum possible amplitude of the electric field in the wave:

$$\mathcal{E}_m = \mu\beta\gamma + \beta\gamma - \sqrt{\mu^2\beta^2\gamma^2 + (\gamma - 1)(2\mu\gamma + \gamma - 1)}. \qquad (12)$$

From relationship (12), we can determine the amplitude $\mathcal{E}_m$ for nonrelativistic waves ($\beta \ll 1$, $\gamma \approx 1 + \beta^2/2$): $\mathcal{E}_m \approx \beta/2$, or, in dimensional form, $E_0^2/(8\pi) \approx n_0 m u^2/2$. For relativistic waves ($\beta \approx 1$, $\gamma > 1$), we have

$$\mathcal{E}_m \approx (\gamma - 1)/(\beta\gamma). \qquad (13)$$

From this, we obtain the following expression for the limiting value of the dimensional electric field in the wave in the lab frame:

$$(E_0)_m \approx (mc/e)\omega_{p0}\sqrt{2(\gamma - 1)}, \qquad (14)$$

where $\omega_{p0} = \sqrt{4\pi n_0 e^2/m}$ is the electron frequency of the linear plasma oscillations in the lab frame. The lim-

iting field $(E_0)_m$ corresponding to large γ values was obtained for the first time by Akhiezer and Polovin [1], so that, in the literature, it is referred to as the Akhiezer–Polovin field.

It is of interest to analyze the limiting field as a function of the parameter μ. For $\gamma > 1$, relationship (12) yields the dependence

$$(E_0)_m \approx \{1 + 1/[4\mu(\gamma + 1)]\}(mc/e)\omega_{p0}\sqrt{2(\gamma - 1)},$$

which differs from dependence (14) in the factor containing the parameters μ and γ. We can see that, for $\gamma \gg 1$, the limiting field is essentially independent of μ. A similar dependence on μ was obtained by Khachatryan [7].

The dependence of the function $V(\psi)$ on the variable ψ is illustrated graphically in Fig. 1 for several values of the parameter γ (in this and other figures, $\mu = 1836$). It can be seen from Fig. 1 that, as γ increases, the potential well, on the one hand, becomes increasingly asymmetric with respect to the vertical axis, and, on the other hand, acquires a pronounced rectangular shape. The degree to which the potential well is asymmetric depends on the value of μ, and the asymmetry itself causes the oscillations of the electric potential to become asymmetric. As a result, as the phase velocity increases, the negative amplitude of the oscillations becomes small in comparison with their positive amplitude. In addition, we can see that, as the phase velocity approaches the speed of light, the spatial scale on which the potential amplitude is negative also becomes much smaller than the scale on which the potential amplitude is positive.

Figure 1 shows that, at $\gamma > 10^5$, the potential well is almost rectangular in shape. This indicates that the potential profile should be sawtooth-shaped and, accordingly, that the electric field in the wave should be alternating in polarity: intervals of a nearly constant field of positive polarity alternate with intervals of a nearly constant field of the same amplitude but of negative polarity.

As may be seen from the plot of the function $V(\psi)$, the potential oscillates about the equilibrium point $\psi = 0$. At low wave velocities ($\beta \ll 1$, $\gamma \approx 1 + \beta^2/2$), and, accordingly, at low values of the parameter $\mathscr{E}$, the oscillation amplitude is small. Let us determine the shape of the potential well in the case of small oscillations. To do this, we expand the right-hand side of conservation law (11) in a series around the point $\psi = 0$ and obtain

$$V(\psi) \approx \frac{\beta}{2}\left(1 - \frac{\psi^2}{\beta^4}\right)\Big/\left(1 + \frac{1}{\mu}\right). \qquad (15)$$

This indicates that small oscillations occur in a parabolic potential well, the amplitude of small harmonic oscillations being $\psi_+ \approx \psi_- \approx \beta^2$.

Recall that a periodic relativistic wave ($\gamma \gg 1$) with a nearly maximum amplitude ($\mathscr{E} \approx \mathscr{E}_m$) is strongly nonlinear. In the lab frame, this is a periodic wave that propagates at the velocity $-u$ and in which the intervals where the potential is positive are much longer than the intervals where it is negative and the amplitude of the positive potential is much larger than that of the negative potential.

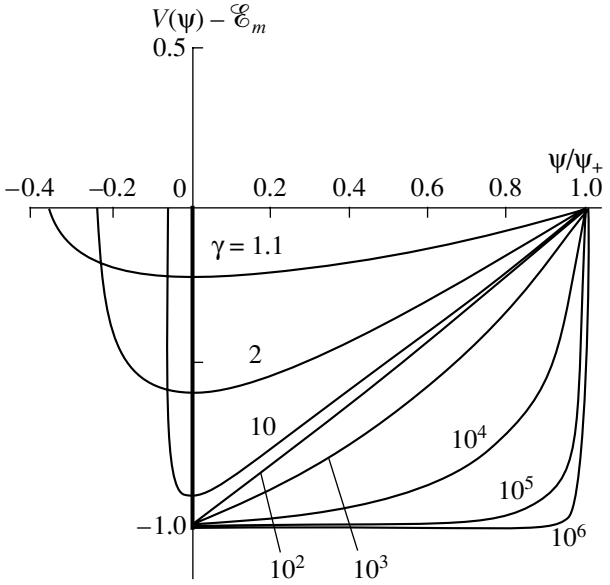

Fig. 1. Plots of the function $V(\psi) - \mathscr{E}_m$, showing the shape of the potential well for different values of the parameter γ. Numerals near the curves show the γ values. The potential ψ is normalized to the positive potential amplitude ψ_+^m.

As was noted above, at given values of the parameters γ and $\mathscr{E}$, the peak-to-peak amplitude of oscillations of the potential can be determined from the relationship

$$\sqrt{\mu^2\beta^2\gamma^2 - \psi(2\mu\gamma - \psi)} - \mu\beta\gamma + \sqrt{\beta^2\gamma^2 + \psi(2\gamma + \psi)} - \beta\gamma = \mathscr{E}.$$

Assuming that $\mu \gg 1$ and setting $\mathscr{E} = \mathscr{E}_m$, we can use this relationship to derive formulas for the limiting amplitudes of the wave potential for $\gamma \gg 1$. It is known that, at a given γ value, the maximum negative amplitude of oscillations of the potential is equal to the boundary value, $\psi_-^m = \psi_-^*$. The maximum positive amplitude can be found from the relationship $\mathscr{E}_m \approx 1$, which holds for $\gamma \gg 1$. As a result, we obtain

$$\psi_-^m = \psi_-^* \approx -\gamma, \quad \psi_+^m \approx 2\beta\mu^2\gamma^2/(\mu^2 + 2\beta\mu\gamma). \qquad (16)$$

We present the amplitude ψ_+^m for two limiting cases: (i) for $1 \ll \gamma \ll \mu$, we have $\psi_+^m \approx 2\gamma^2$ and (ii) for $\gamma \gg \mu$, we have $\psi_+^m \approx \psi_+^* \approx \mu\gamma$. Note that, for relativistic waves ($\gamma \gg 1$), the ratio ψ_+^m/ψ_-^m in the range $1 \ll \gamma \ll$

μ is equal to 2γ, while, for $\gamma > \mu$, this ratio is a constant equal to μ.

At this point, we would like to depart from our discussion and compare the above relationships with those obtained in the wave frame by solving the problem with immobile ions (in [1, 2], this problem was treated in the lab frame).

In the case of immobile ions, the potential well is described by the expression

$$V(\psi) = \beta\gamma - [\beta^2\gamma^2 + \psi(2\gamma + \psi)]^{1/2} + \psi/\beta,$$

which can be readily obtained by multiplying both sides of Eq. (1) by $d\psi/dx$ and by integrating the resulting equation under the assumption $n_i = n$ = const. Note that, in the case at hand, the function $V(\psi)$ is defined in the half-interval $\infty < \psi < -(\gamma - 1)$; hence, the value $\psi_-^* = -(\gamma - 1)$ is one of the boundary values of the variable ψ.

Setting $V(\psi) = \mathscr{E}$, we arrive at the following formulas, determining the peak-to-peak amplitude of oscillations of the potential:

$$\psi_- = \beta\gamma^2\mathscr{E}^2 - (\beta^2\gamma^4\mathscr{E} + 2\beta^3\gamma^3\mathscr{E} - \beta^2\gamma^2\mathscr{E}^2)^{1/2},$$

$$\psi_+ = \beta\gamma^2\mathscr{E}^2 + (\beta^2\gamma^4\mathscr{E} + 2\beta^3\gamma^3\mathscr{E} - \beta^2\gamma^2\mathscr{E}^2)^{1/2}.$$

The exact limiting amplitude of the electric field is determined from the relationship $\mathscr{E}_m = V(\psi_-^*)$:

$$\mathscr{E}_m = (\gamma - 1)/(\beta\gamma), \quad (17)$$

which coincides with approximate limiting amplitude (13), deduced above for $\beta \approx 1$ and $\gamma > 1$.

Setting $\mathscr{E} = \mathscr{E}_m = (\gamma - 1)/(\beta\gamma)$ and fixing γ, we obtain exact values of the maximum possible amplitude of oscillations of the potential:

$$\psi_-^m = \psi_-^* = -(\gamma - 1), \quad \psi_+^m = 2\gamma^2 - \gamma - 1. \quad (18)$$

Comparing these formulas with formulas (16), we can see that, in the case of immobile ions, the limiting negative amplitude of oscillations of the potential is the same as that in the problem in which the ion motion is taken into account. The limiting positive amplitude of oscillations of the potential coincides with that obtained above in the range $1 \ll \gamma < \mu$ and increases in proportion to γ^2 as $\gamma \longrightarrow \infty$. For $\gamma \gg 1$, the ratio of the amplitudes in the case of immobile ions is $\psi_+^*/\psi_-^* \approx 2\gamma$ and, accordingly, it approaches infinity as $\gamma \longrightarrow \infty$, in contrast to the case at hand, in which it approaches the finite value μ in the limit $\gamma \longrightarrow \infty$.

An analysis of the motion of an electron in the wave potential field in the wave frame against the background of immobile ions shows that the electron energy γ_e, which can be determined from the conservation law $\gamma_e = \psi + \gamma$ [see formula (5)], is equal to $\gamma_e = 1$ at $\psi = \psi_-^* = -(\gamma - 1)$; consequently, the dimensionless electron velocity is minimum and is equal to $\beta_e = 0$. At the point on the wave profile at which $\psi = \psi_+^* = 2\gamma^2 - \gamma - 1$, the electron energy is $\gamma_e = 2\gamma^2 - 1$ and the electron velocity is maximum, $\beta_e = 2\beta/(1 + \beta^2)$.

It is easy to show that, in the lab frame, the minimum and maximum electron velocities are $-u$ and u, respectively. This indicates that the quantity u_{max}, which is the maximum electron velocity in the laminar wave under analysis (in [1, 2], this quantity was treated as an arbitrary constant), is equal to the phase velocity: $u_{max} = u$. Taking into account this relationship, one can readily see that, for $\gamma \gg 1$, formula (14) for the limiting electric field coincides with the corresponding formula obtained in [1, 2].

Having found the positive and negative potential amplitudes and the maximum electric field in the wave, we can determine the spatial wave profile. In order to evaluate the dependence of the potential ψ on the coordinate ξ, we use the differential equation $d\psi(\xi)/d\xi = \{2[\mathscr{E} - V(\psi)]\}^{1/2}$, which is derived from conservation law (11) and in which the function $V(\psi)$ is given by the same conservation law and the variable ψ is a function of ξ. This differential equation was solved numerically by the Runge–Kutta method. For a known dependence $\psi = \psi(\xi)$, it is a fairly simple matter to determine from the equation the dependence of the electric field $d\psi(\xi)/d\xi$ on ξ.

The results of calculating the profiles of the potential and the electric field are demonstrated in Fig. 2. Before proceeding to the discussion of these calculations, we should emphasize that this figure is, in a sense, illustrative because the scales on the four semiaxes are different. Merely the shapes of the profiles of the potential and electric field are shown in Fig. 2. The profiles of the potential of negative and positive polarities are shown, respectively, in the left and right half-planes (with respect to the vertical axis) on different scales; to save space, the half-planes in the figure are simply joined together.

The values of the potential of positive polarity are normalized to the positive potential amplitude, and the values of the potential of negative polarity are normalized to the negative potential amplitude; note that, for relativistic waves, the positive amplitude may be three orders of magnitude larger than the negative amplitude (as was mentioned earlier, $\psi_+^m/\psi_-^m \approx \mu$ at $\gamma > \mu$). The spatial scales on the positive and negative semiaxes are also different.

An actual potential profile calculated for $\gamma = 5$ is displayed in Fig. 3, which shows that, even at relatively small γ values, the peak-to-peak oscillation amplitude is determined primarily by the positive potential amplitude and the length of the interval where the potential is positive is, in fact, equal to the wavelength. This shape of the potential profile has been predicted above from a

qualitative analysis of the particle motion in a potential well.

Now, we again turn to Fig. 2, in which the potential of negative polarity is seen to become essentially triangular in shape at $\gamma > 10$ (see also Fig. 3), while the potential of positive polarity acquires a triangular shape at $\gamma > 10^4$. For a triangular profile, the electric field is rectangular in shape. It is of interest to note that, for the shape of the potential of positive polarity in the range $2 < \gamma < 10^3$ (in the right half-plane in Fig. 2), the electric field also has a nearly triangular shape.

Hence, we have obtained the sought-for solutions in the form of periodic waves of the potential and have determined the range of the parameters of the problem in which the solutions exist. A comparison of formulas (16) and (18) shows that, in studying relativistic waves (or, more precisely, waves for which $\gamma > \mu$), it is of fundamental importance to take into account the ion motion in a finite-amplitude longitudinal plasma wave. In fact, for γ values in the range $1 < \gamma < \mu$, the dependence of the peak-to-peak amplitude of oscillations of the potential on γ in the problem in which ion motion is taken into account coincides with that in the problem in which the ions are assumed to be immobile, whereas, for γ values significantly above μ, these dependences are very different.

On the other hand, the maximum amplitude E_0 of the electric field in the wave [see formulas (12), (13)] agrees with a high accuracy with that given by formula (17) for the electric field in the case of immobile ions; this indicates that the maximum amplitude E_0 is independent of whether the ions are mobile or not.

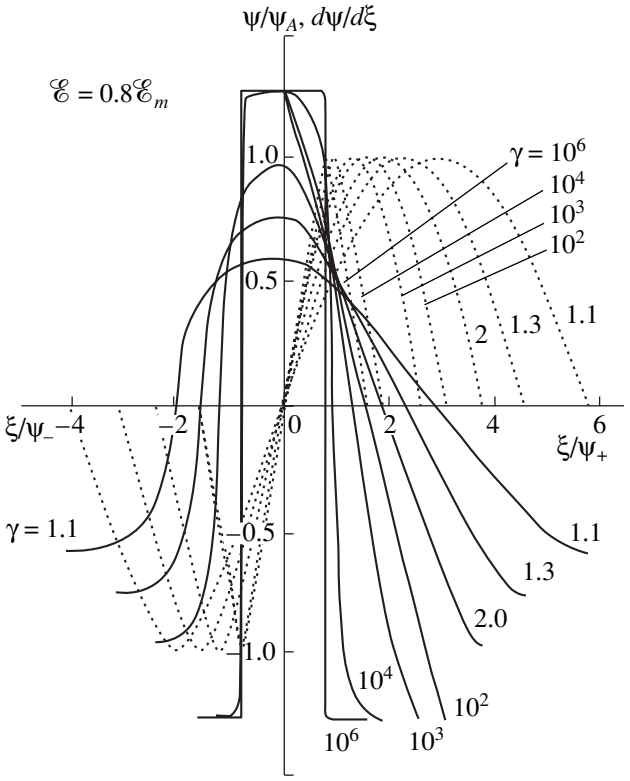

Fig. 2. Profiles of the potential $\psi(\xi)$ (dotted curves) and the electric field $d\psi/d\xi$ (solid curves) in the wave. The potential of positive polarity and positive values of the coordinate are normalized to the potential amplitude ψ_+, and the potential of negative polarity and negative values of the coordinate are normalized to the potential amplitude ψ_-. Numerals near the curves show the γ values.

4. DETERMINATION OF THE WAVE FREQUENCY

The wave frequency in the lab frame can be found from the formula $\omega = 2\pi u\gamma/\lambda$, where the spatial period λ of oscillations of the potential in the wave frame has the form

$$\lambda = \sqrt{\frac{2}{\beta}}(c/\omega_{p0})\int_{\psi_-}^{\psi_+}\frac{d\psi}{\sqrt{\mathscr{E} - V(\psi)}},$$

with $V(\psi)$ given by expression (11). This yields the following relationship for the frequency ω:

$$\omega = \omega_{p0}\frac{\pi\sqrt{2}(\beta\gamma)^{3/2}}{\int_{\psi_-}^{\psi_+}\frac{d\psi}{\sqrt{\mathscr{E} - V(\psi)}}}. \qquad (19)$$

The exact value of the frequency can only be determined by calculating the integral in formula (19) numerically. However, approximate estimates of ω can be obtained in the two limits: (i) $\gamma \approx 1$ and (ii) $\gamma \gg 1$. In this section, all calculations and estimates are made for

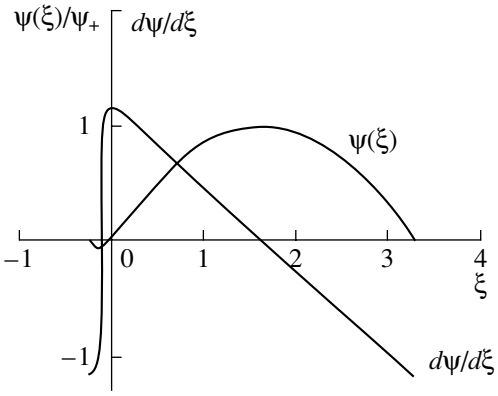

Fig. 3. Profiles of the potential $\psi(\xi)$ and the electric field $d\psi/d\xi$ in a plasma wave for $\gamma = 5$ and $\mathscr{E} = 0.8\mathscr{E}_m$.

waves that have the maximum possible amplitude, $\mathscr{E} = \mathscr{E}_m$. In the case of low phase velocities ($\gamma \approx 1$, $\beta \ll 1$), when $\mathscr{E}_m \approx \beta/2$ and $\psi_+ \approx \psi_- \approx \beta^2$, the function $V(\psi)$ is given by formula (15) and the integral in relationship (19) is calculable. As a result, we find that the fre-

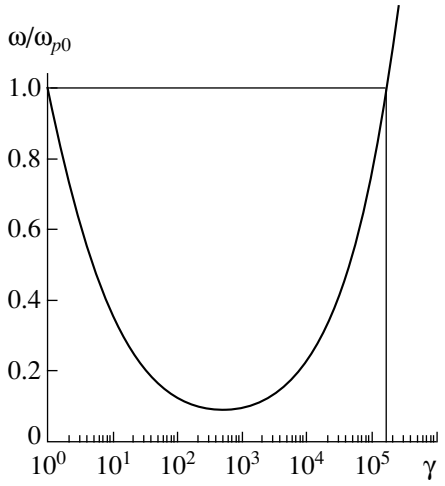

Fig. 4. Frequency of longitudinal plasma waves with the maximum possible amplitudes of the potential as a function of the parameter γ.

quency of small-amplitude oscillations is equal to the plasma frequency with allowance for ion motion [2]: $\omega = \omega_{p0}\sqrt{1 + 1/\mu} \approx \omega_{p0}$. For a relativistic plasma wave ($\beta \approx 1$, $\gamma \gg 1$), the integral can be estimated by noting that, at large values of the parameter γ, the quantity $\mathcal{E}_m - V(\psi)$ is almost constant at all ψ values and by using the relationship $\mathcal{E}_m - V(\psi) \approx 1$, which holds for the limiting amplitudes of the electric field ($\mathcal{E} \approx \mathcal{E}_m$) [see formula (11) and Fig. 1]. As a result, relationship (19) yields the estimate $\omega \approx \omega_{p0}\pi\sqrt{2}\,\gamma^{3/2}/(\psi_+^m - \psi_-^m)$. Setting $\beta \approx 1$ and $\mathcal{E}_m \approx 1$, we insert the values ψ_-^m and ψ_+^m from formulas (16) into this estimate to obtain

$$\omega \approx \omega_{p0}\frac{\pi(\mu^2 + 2\mu\gamma)}{\mu^2\sqrt{2\gamma}}. \qquad (20)$$

Formula (20) shows that, first, in the range $1 \ll \gamma \ll \mu$, the wave frequency decreases in proportion to $\gamma^{-1/2}$ and, second, in the range $\gamma > \mu$, it increases with γ in proportion to $\gamma^{1/2}$. This dependence of ω on γ indicates that, at a certain γ value, the frequency reaches its minimum value, which can be found from the condition $d\omega/d\gamma = 0$. Equating the derivative of the frequency, $d\omega/d\gamma$, calculated from formula (20), to zero, we find that the frequency is minimum ($\omega_{min} = 2\pi\omega_{p0}/\sqrt{\mu}$) at $\gamma_{min} = \mu/2$.

It is obvious that, at a certain value $\gamma = \gamma_0 \gg 1$, the frequency of the relativistic waves is again equal to the plasma frequency, as in the case of linear oscillations ($\gamma \approx 1$). The γ_0 value at which $\omega = \omega_{p0}$ can be found by using formula (20): $\gamma_0 \approx \mu^2/(2\pi^2)$.

To illustrate, we consider a plasma consisting of electrons and protons. In this case, the minimum frequency is equal to $\omega_{min} \approx \omega_{p0}/7$ at $\gamma_{min} \approx 10^3$; for relativistic waves, the frequency of waves with the maximum possible amplitudes becomes equal to the plasma frequency at $\gamma_0 \approx 2 \times 10^5$.

The above approximate dependence of ω on γ and the above estimates of γ_0, γ_{min}, and ω_{min} are confirmed by the results of exact computations in which the integral in formula (19) was evaluated numerically. The results obtained for an electron–proton plasma and for nonlinear waves with a maximum peak-to-peak amplitude of the potential ($\mathcal{E} = \mathcal{E}_m$) at a given value of γ are illustrated in Fig. 4, which shows the dependence $\omega = \omega(\gamma)$ for γ values in the range $1 \le \gamma \le \gamma_0$. For $\gamma > \gamma_0$, the frequency is described with high accuracy by the dependence $\omega \approx \omega_{p0}\pi\sqrt{2\gamma}/\mu$.

Now, we consider another wave parameter related to the wave frequency, namely, the wavelength. By definition, in the lab frame, we have $\lambda^L = 2\pi u/\omega$. For nonrelativistic waves, we have $\lambda^L = 2\pi u/\omega_{p0}$. For relativistic waves, we set $\beta \approx 1$ and $\mathcal{E}_m \approx 1$ and use formula (20) to obtain $\lambda^L \approx (c/\omega_{p0})2\sqrt{2\gamma}\,\mu^2/(\mu^2 + 2\mu\gamma)$. This shows that the wavelength of the slow waves is equal to $\lambda^L = 2\pi u/\omega_{p0}$. With increasing wave phase velocity, the wavelength increases and reaches its maximum value $\lambda^L_{max} = \sqrt{\mu}\,(c/\omega_{p0})$ at $\gamma = \gamma_{min} \approx \mu/2$. As γ increases further, the wavelength begins to decrease and becomes equal to $\lambda^L = c/\omega_{p0}$ at $\gamma \approx 2\mu^2$. For even larger γ values, the law according to which the wavenumber decreases can be written as $\lambda^L \approx (c/\omega_{p0})\mu\sqrt{2/\gamma}$.

5. THE MAIN RESULTS AND DISCUSSION

Generally, the problem of the propagation of nonlinear waves in a collisionless plasma is fairly difficult to solve. However, the problem can be substantially simplified by assuming that the plasma is cold and by turning to a hydrodynamic description of the plasma processes. In the hydrodynamic approximation, which was used here, the electron and ion components are regarded as two fluids moving in self-consistent fields. The problem can be further simplified by assuming that the ions are immobile and by considering only the electron motion (as was done in [1, 2]). In this approximation, the equations were found to have analytic solutions expressed in terms of elliptic functions [1, 2].

Let us analyze the consequences of applying the theory constructed in [1, 2] under the assumption of immobile ions to nonlinear waves propagating in a plasma with a finite ion-to-electron mass ratio μ. Formula (18) implies that, in the model with immobile ions, the maximum possible positive amplitude ψ_+^m of the wave potential at $\gamma \gg 1$ is equal to $2\gamma^2$. For ions of a finite mass, it can be shown that, as the parameter γ increases, a laminar wave whose amplitude depends on γ in this manner should inevitably break at a certain γ value. In

fact, recall that, for a laminar wave to exist, there should be no particles reflected from the potential humps, as follows from physical considerations. Assuming that the mass of the ions is finite and using the dimensionless condition $\mu(\gamma - 1) \geq 2\gamma^2$, which implies that there are no ions reflected from the potential humps in a wave with $\gamma \gg 1$, we can see that the solution describing a laminar wave is possible only for $\gamma \leq \mu/2$.

These considerations indicate that the solutions obtained in [1, 2] for an actual plasma, for which the parameter μ is finite, are valid in the finite applicability range $1 \leq \gamma \leq \mu/2$, in which their use is physically justified. Note that the value $\gamma = \mu/2$ coincides with the estimate obtained above for the value γ_{min}, at which the wave frequency is minimum. For ultrarelativistic waves ($\gamma > \mu$) with the maximum possible amplitude, the assumption of mobile ions is of fundamental importance, because it yields results that differ considerably from those of [1, 2].

When ion motion is taken into account, the dependence of the wave frequency on the phase velocity is more complicated than the dependence obtained in [1, 2]. As was shown above, the frequency of a wave propagating at a very low velocity is equal to the electron plasma frequency, in accordance with the linear theory. With increasing phase velocity, the wave frequency decreases (as is the case in [1, 2]), but only to a certain minimum value. As the phase velocity increases further, the frequency starts to increase and again becomes equal to the electron plasma frequency at a certain phase velocity. In a cold plasma, the frequency of ultrarelativistic waves with the maximum possible amplitudes increases without bound as the phase velocity approaches the speed of light. This indicates that, in the case of immobile ions, the wave frequency ω decreases monotonically with increasing γ; however, when the ion dynamics is incorporated, the frequency inevitably ceases to decrease monotonically and, as the ion motion in the wave becomes more active, the frequency begins to increase with increasing γ. Similar effects were pointed out by Khachatryan [7].

Having analyzed the above dependence of the frequency of the wave on its phase velocity, we can anticipate that the ion dynamics begins to influence the wave when its parameters become such that its frequency is minimum (i.e., at $\gamma \approx \mu/2$). In other words, the ion activity in a plasma starts at electric field amplitudes of about $(E_0)_m \approx (mc/e)\omega_{p0}\gamma^{1/2} \approx (mc/e)\omega_{p0}\mu^{1/2}$. If, as assumed in [8], the amplitude $(E_0)_m$ is comparable in order of magnitude to the maximum amplitude of the electric field in a laser pulse, $(E_L)_m \sim (E_0)_m$, then the value obtained above for $(E_0)_m$ agrees with the estimate for the maximum electric field $(E_L)_m$ that was obtained by Bulanov *et al.* [8] and above which, in their opinion, the motion of the ion plasma component should be taken into account.

We should make one remark about the electron–proton plasma considered above. According to formula (20) and Fig. 4, the wave frequency ω differs from the electron plasma frequency by less than one order of magnitude (at most, by a factor of seven) in a fairly wide range of γ values ($1 \leq \gamma < 10^5$).

The shapes of the potential and the electric field in longitudinal plasma waves possess interesting features. For a chosen point on the wave profile at which the potential is set at zero and, accordingly, with respect to which the potential is measured, we have found that the peak-to-peak amplitude of oscillations of the potential of relativistic waves is determined primarily by the positive potential amplitude.

It has been found that, in a certain range of wave velocities, the electric field in a relativistic wave is of a nearly sawtooth shape. For $\gamma > 10$, the negative component of the potential also acquires a sawtooth shape. As the phase velocity of ultrarelativistic waves increases, the entire profile of the potential in the wave becomes sawtooth-shaped, and the electric field profile becomes rectangular in shape.

Finally, let us make the following remarks. In our analysis, it was assumed that the role of the positively charged plasma component is played by protons. It is easy to see that the results obtained can be generalized to arbitrary ions whose mass and charge differ from those of protons. In this case, the behavior of the waves in a plasma consisting of electrons and one ion species with the atomic number A and charge eZ is described by Eqs. (1)–(3) with conservation laws (4)–(7), in which the mass $M^* = AM/Z$ should be used in place of the mass M of a hydrogen atom and the parameter μ should be replaced by the quantity $\mu^* = A\mu/Z$. Another interesting result is the following: for $\mu = 1$ (i.e., for an electron–positron plasma), the frequency of finite-amplitude longitudinal plasma waves with $\gamma > 1$ is always higher than the frequency of the linear plasma oscillations. This circumstance was pointed out in [7].

In summary, the main results obtained in the present study are as follows.

(i) The boundaries of the parameter range in which the periodic potential waves with phase velocities lower than the speed of light exist have been determined. In order for the waves to remain laminar, the peak-to-peak amplitude of oscillations of the potential in the wave should be finite: the positive amplitude is restricted by the value $\psi_+^* = \mu(\gamma - 1)$, and the negative amplitude is restricted by $\psi_-^* = -(\gamma - 1)$.

(ii) The profiles and amplitudes of the potential and the electric field have been calculated for plasma waves with velocities ranging from zero to the speed of light. It has been found that the absolute value of the maximum possible negative amplitude of oscillations of the potential is equal to $\gamma - 1$ and that the maximum possible positive amplitude in the range $1 < \gamma < \mu$ is approximately equal to $2\gamma^2$ and approaches the value $\mu(\gamma - 1)$ as the phase velocity approaches the speed of light.

(iii) The frequency of the wave and its wavelength have been obtained as functions of the wave phase velocity. It has been shown that, in a fairly wide range of phase velocities (the minimum velocity being zero), the frequency of the wave whose amplitude is close to the limiting amplitude in the electron–proton plasma under consideration changes only slightly, remaining of the same order of magnitude as the electron plasma frequency. The frequency of ultrarelativistic waves with the maximum possible amplitudes in a cold plasma becomes higher than the electron plasma frequency and increases without bound as the phase velocity approaches the speed of light.

ACKNOWLEDGMENTS

I am grateful to S.M. Churilov and I.G. Shukhman for useful discussions.

REFERENCES

1. A. I. Akhiezer and R. V. Polovin, Zh. Éksp. Teor. Fiz. **30**, 915 (1956) [Sov. Phys. JETP **3**, 696 (1956)].
2. *Plasma Electrodynamics*, Ed. by A. I. Akhiezer, I. A. Akhiezer, R. V. Polovin, *et al.* (Nauka, Moscow, 1974; Pergamon, Oxford, 1975).
3. W. Lünow, Plasma Phys. **10**, 879 (1968).
4. C. Max, Phys. Fluids **16**, 1277 (1973).
5. V. A. Kozlov, A. G. Litvak, and E. V. Suvorov, Zh. Éksp. Teor. Fiz. **76**, 148 (1979) [Sov. Phys. JETP **49**, 75 (1979)].
6. D. Farina and S. V. Bulanov, Fiz. Plazmy **27**, 680 (2001) [Plasma Phys. Rep. **27**, 641 (2001)].
7. A. G. Khachatryan, Phys. Rev. E **58**, 7799 (1998).
8. S. V. Bulanov, V. A. Vshivkov, G. I. Dudnikova, *et al.*, Fiz. Plazmy **25**, 764 (1999) [Plasma Phys. Rep. **25**, 701 (1999)].
9. L. M. Gorbunov, P. Mora, R. R. Ramazashvili, and A. A. Solodov, Phys. Plasmas **7**, 375 (2000).
10. L. M. Gorbunov, P. Mora, and A. A. Solodov, Phys. Rev. Lett. **86**, 3332 (2001).
11. L. D. Landau and E. M. Lifshitz, *The Classical Theory of Fields* (Nauka, Moscow, 1967; Pergamon, Oxford, 1975).
12. L. D. Landau and E. M. Lifshitz, *Mechanics* (Nauka, Moscow, 1965; Pergamon, New York, 1988).

Translated by O.E. Khadin

Plasma Physics Reports, Vol. 29, No. 2, 2003, pp. 161–165. Translated from Fizika Plazmy, Vol. 29, No. 2, 2003, pp. 182–186.

LOW-TEMPERATURE PLASMA

The Critical Electric Field in Heated SF_6

D. A. Aleksandrov*, N. L. Aleksandrov*, É. M. Bazelyan, and A. M. Konchakov***

**Moscow Institute of Physics and Technology, Institutskiĭ proezd 9, Dolgoprudnyĭ, Moscow oblast, 141700 Russia*

***Krzhizhanovskiĭ Power Engineering Institute, Leninskiĭ pr. 19, Moscow, 117927 Russia*

Received June 20, 2002; in final form, September 26, 2002

Abstract—The critical electric field at which the ionization rate is equal to the rate of electron attachment to neutral particles in heated sulfur hexafluoride (SF_6) is calculated by numerically solving the Boltzmann equation for electrons. It is shown that the main causes of a decrease in the critical field with increasing gas temperature are the change in the electron energy distribution due to gas dissociation and the reduction in the rate of electron attachment to neutral particles. The calculated results are in qualitative agreement with the available experimental data. © *2003 MAIK "Nauka/Interperiodica".*

1. INTRODUCTION

Gaseous sulfur hexafluoride (SF_6) is widely used as an insulator in high-voltage engineering. It is for this reason that the processes underlying the development of electrical breakdowns in SF_6 attract interest. The high insulating properties of SF_6, which is an electronegative gas, are largely explained by the high rate of electron attachment to SF_6 molecules, which results in the production of negative fluorine-containing ions with large binding energies.

One of the most important parameters of an electric breakdown in an electronegative gas is the critical electric field at which the electron production rate by impact ionization of neutral particles is equal to the rate of electron attachment to them. It is well known that, under normal conditions, the critical field in SF_6 is about $E \approx 89$ kV/cm, which corresponds to a reduced critical electric field of $E/N \approx 3.6 \times 10^{-15}$ V cm^2, where N is the neutral density [1]. The temperature dependence of the critical field has been studied (both theoretically and experimentally) very little, although this point is very important for describing different kinds of breakdown. For instance, it is thought that the electric field in a leader channel heated to several thousand degrees is established at a critical level [2–4]. Previously obtained estimates for the critical electric field [2, 3] were based on a rough empirical approach [5] in which this field was assumed to be determined exclusively by the ionization potential and the polarizability of neutral particles. For estimates, it was also assumed that all SF_6 molecules dissociate into atoms with the S atoms being neglected. Kinetic calculations of the critical electric field for plasma conditions in a leader channel have not yet been carried out.

The question of the critical electric field in heated SF_6 is also important for current switches, as well as in situations with spark rebreakdown of a gas gap. In the latter case, one of the main processes is the recovery of the electric strength of a heated gas channel that remains after an electric arc has come to an end. The first attempts to develop a systematic kinetic description of this process in SF_6-based current switches were made comparatively recently. Thus, the decay of an arc plasma was investigated theoretically by Cliteur *et al.* [6] with allowance for an external electric circuit, and the critical field in a channel after its cooling to 3000 K was determined by Yan *et al.* [7] by using a simplified approach.

In this paper, the critical electric field in SF_6 is determined as a function of gas temperature and gas pressure by applying a systematic kinetic approach. We calculate the mean production and loss rates of electrons by numerically solving the Boltzmann equation for them under the assumption that the neutral components of the gas are in thermodynamic equilibrium.

2. DESCRIPTION OF THE APPROACH

Based on a numerical solution of the Boltzmann equation, we determined the electron energy distribution in a gas at different temperatures and different pressures. Calculations were carried out in the two-term approximation: in the expansion of the electron distribution function in spherical harmonics [8], we retained the first two terms, which correspond to a slight anisotropy of the distribution function. The effects of the unsteady nature of the plasma and of its inhomogeneity (due to the processes of electron production and electron losses) on the electron distribution were neglected, which is valid for a near-critical electric field, when these effects cancel one another. Using the distributions obtained, we calculated the rate constants for the ionization and the electron attachment to neutral particles by averaging the rates of the corresponding processes over all neutral components. The critical electric field was determined by equating the mean rate constants for ionization and electron attach-

1063-780X/03/2902-0161$24.00 © 2003 MAIK "Nauka/Interperiodica"

ment. Note that, at sufficiently high gas temperatures, electrons are detached from the negative ions (thermal electron detachment); this indicates that, in determining the critical electric field, it is also necessary to take into account the electron detachment from negative ions in their collisions with neutral particles. However, the estimates that were made with allowance for ion heating in an electric field showed that, at $T < 4000$ K, the effect of electron detachment from F^- ions can be ignored.

In modeling electron scattering by SF_6 molecules, we took into account elastic collisions, the excitation of vibrational and electronic levels, ionization, and electron attachment. The scattering cross sections for the corresponding processes were taken from [9]. The consistency of the scattering cross sections was checked by test computations of the electron transport and rate parameters in a cold SF_6 gas. The calculated results were found to agree well with the available experimental data [1] on the electron drift velocity, the characteristic electron energy (the ratio of the transverse electron diffusion coefficient to the electron mobility), and the ionization and attachment rates. During the gas heating, an SF_6 molecule dissociates into radicals, which ultimately decompose into F and S atoms. The cross sections for elastic electron scattering, the excitation of electronic levels, and the ionization of F and S atoms were taken from [6]. The electron attachment to atoms was neglected. In fact, there is no dissociative attachment to atoms, whereas under the conditions adopted here, the rates of the three-body and radiative attachment processes are several orders of magnitude lower than the rate of dissociative attachment to radicals. For the ionization cross sections for radicals, we used the experimental data obtained on SF_5 and SF_3 by Tarnovsky *et al.* [10] and the results calculated by Ali *et al.* [1] for SF_4, SF_2, and SF (note that these calculated results agree with the experimental data [10] on the ionization cross sections for SF_5 and SF_3). Since we failed to find other data on the cross sections for electron scattering by the radicals of an SF_6 molecule in the literature, we set them equal to the cross sections for electron scattering by this molecule.

The gas components were assumed to be in thermodynamic equilibrium, and the gas composition was determined with the numerical code described in [11]. The computations were carried out for the temperature range $T = 300$–5000 K and the pressure range $p = 0.5$–5 atm.

3. DISCUSSION OF THE RESULTS

Figure 1 illustrates how the composition of an SF_6 gas depends on its temperature at atmospheric pressure. The results shown in this figure agree with the results from thermodynamic calculations [12] to within 10–15%. In a gas heated above 1600 K, the SF_6 molecules are subject to thermal dissociation. At $T > 1750$ K, the main particles in the gas mixture are F atoms, although the amount of different radicals remains sufficiently large to determine electron losses over the entire temperature range in question. As T increases, complex radicals decompose into atoms and simpler radicals.

Figure 2 shows how the mole fractions of the neutral components predominating in the gas (SF_6 molecules and F atoms) depend on temperature at two different

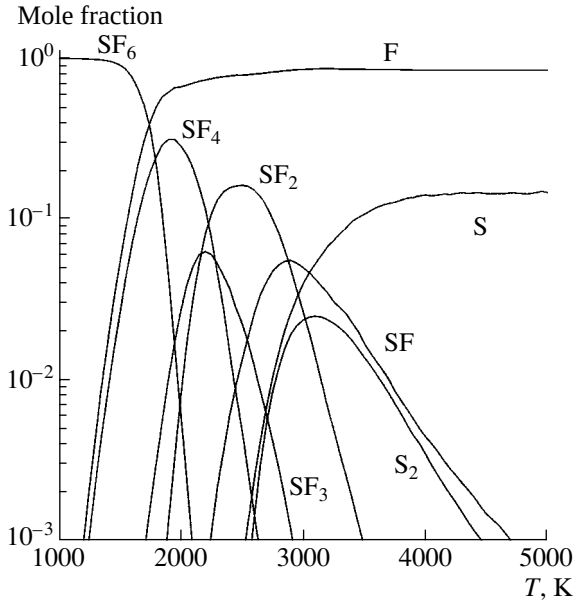

Fig. 1. Composition of an SF_6 gas vs. temperature at atmospheric pressure.

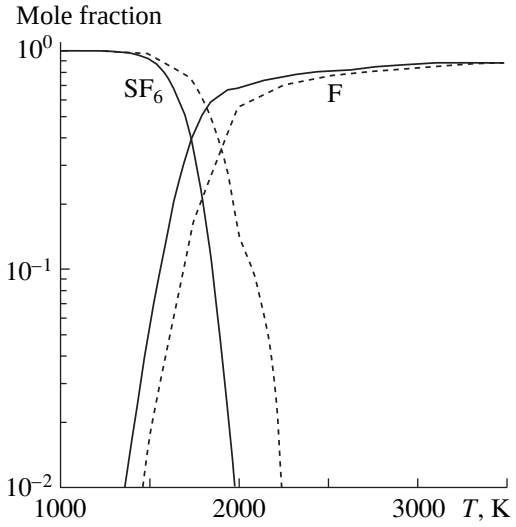

Fig. 2. Mole fractions of SF_6 and F vs. temperature at a gas pressure of 1 atm (solid curves) and 5 atm (dashed curves).

pressures. An increase (or a decrease) in pressure is seen to somewhat slow (or hasten) dissociation processes, without changing them qualitatively.

The heating of SF_6 molecules should not only induce them to dissociate, but should also exert considerable influence on the production and loss rates of the electrons and, consequently, on the critical electric field. In this case, we can distinguish between three different effects. First, even when the electron energy distribution remains unchanged, the efficiency of electron attachment to neutral particles changes as the gas composition changes with increasing *T*. Second, the same is true of the efficiency of electron-impact ionization of neutral particles (the ionization efficiencies of different particle species are characterized by the corresponding ionization potentials, which are given in the table). Finally, a change in the gas composition affects the mean energy of the electrons and their energy distribution, thereby affecting the rates of electron attachment and ionization.

Figure 3 shows how the mean ionization and attachment rate constants depend on the reduced electric field in SF_6. The calculations were carried out for $T = 1000$ K (when there is no dissociation) and for $T = 2000$ K (when the degree of dissociation is high). We can see that decomposition of molecules has a substantial influence on the rates of both ionization and electron attachment, in which case the total attachment rate decreases while the ionization rate increases. These two effects reduce the critical electric field at which the ionization and attachment rates are equal.

Ionization potentials (in eV) of neutral particles [1, 13]

SF_6	SF_4	SF_3	SF_2	SF	S_2	F	S
15.7	12.0	11.0	10.1	10.1	9.4	17.4	10.4

The influence of different effects on the evolution of the critical electric field in an SF_6 gas whose temperature *T* increases with time was clarified by successively including them in simulations. Figure 4 illustrates the results of these simulations in the form of the dependence of the critical reduced electric field on *T*. The upper curve was obtained from simulations in which the electron attachment rate changed with temperature (the electron attachment to atoms being neglected) and the ionization rate and electron energy distribution are taken to be the same as those in a cold gas. The middle curve refers to simulations in which we took into account the changes in the rates of both electron attachment and ionization in a gas whose composition changes with increasing temperature, but used the same electron energy distribution as in the previous series of simulations. Finally, the lower curve demonstrates the results of simulations in which we took into account not only the change in the attachment and ionization efficiencies but also the change in the electron energy distribution, which forms as a result of elastic and inelastic collisions of electrons with neutral particles.

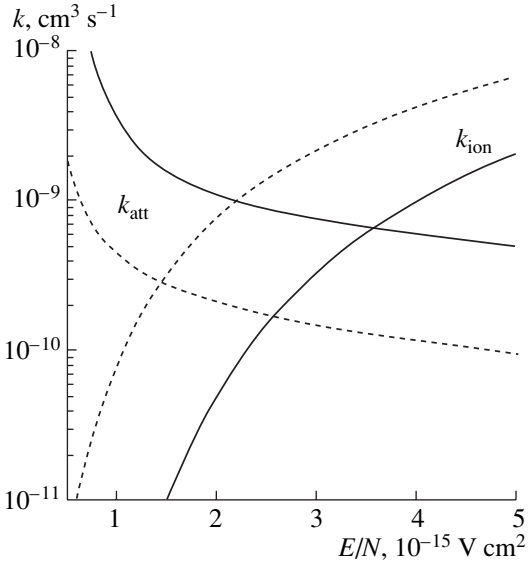

Fig. 3. Ionization and attachment rate constants vs. reduced electric field in an SF_6 gas at atmospheric pressure and at $T = 1000$ K (solid curves) and 2000 K (dashed curves). The rate constants were obtained by averaging the rates of the corresponding processes over all neutral components.

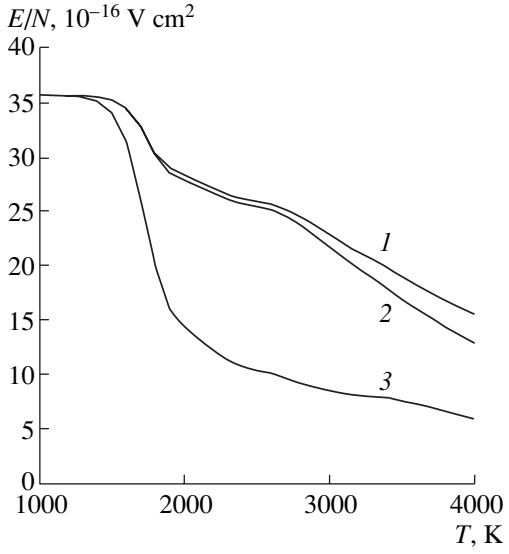

Fig. 4. Critical reduced electric field vs. temperature in an SF_6 gas at atmospheric pressure: (*1*) calculation with allowance for only the change in the electron attachment efficiency, (*2*) calculation with allowance for the changes in the attachment and ionization efficiencies, and (*3*) calculation with allowance for the changes in the attachment and ionization efficiencies and in the electron energy distribution.

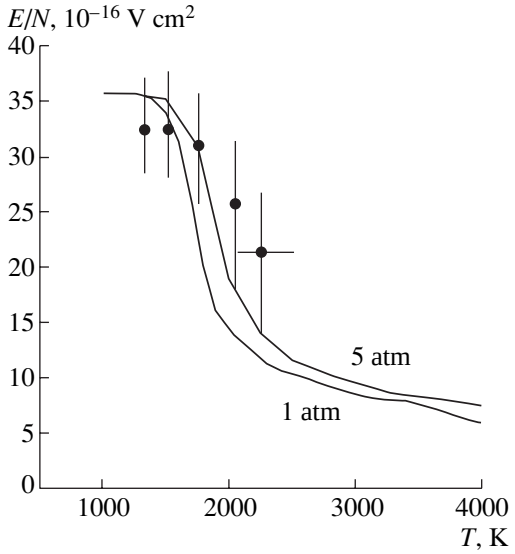

Fig. 5. Critical reduced electric field vs. temperature in an SF_6 gas at pressures of 1 and 5 atm. The closed circles show the experimental data measured at a pressure of 2 atm in [14, 15].

From Fig. 4, we can see that, because of the absence of electron attachment to atoms, the critical electric field becomes substantially weaker: at $T = 2000$ K, the field decreases by 25% and, at a temperature of 4000 K, it decreases by a factor of more than two. The effect associated with the change in the efficiency of ionization of neutral particles in a heated gas is far less because of the production of particles not only with lower ionization energies (radicals and S atoms) but also with higher ionization energies (F atoms). In this case, the amount of easily ionized particles is substantially less than that of F atoms; consequently, the total effect of a change in the ionization efficiency is relatively weak. The last effect, which is associated with the evolution of the electron energy distribution, is the greatest: as the gas is heated up to 2000 K, the critical electric field decreases by a factor of nearly three. Such a decrease might be explained as being due to the absence of the vibrational and rotational degrees of freedom of F atoms, which are the dominant particles in a heated gas; as a result, the mean electron energy increases. However, under the conditions described, i.e., when the electric field is sufficiently strong, a fraction of the electron energy transferred to these degrees of freedom is small [6] and the electrons lose their energy almost exclusively by the excitation of electronic levels and by ionization. A comparison between the cross sections for exciting the electronic levels of an F atom and an SF_6 molecule shows that the excitation efficiencies for F are approximately one order of magnitude smaller than those for other neutral particles. Consequently, in a gas heated in a given electric field, this property should make (due to dissociation) electron heating more efficient and, accordingly, should decrease the critical electric field (calculations show that, as the gas is heated from 300 to 4000 K at a given reduced electric field E/N, the mean electron energy increases by 30–35%).

In studying the electrical breakdown of gaps filled with an SF_6 gas, it is of interest to investigate the breakdown discharge parameters in the pressure range from 0.5 to 5 atm. That is why we carried out simulations not only for the atmospheric pressure but also for pressures between 0.5 and 5 atm. A change in the pressure p affects the gas composition: as p increases, the dissociation processes in the gas begin to occur at higher temperatures. Figure 5 illustrates the dependence of the critical electric field on the gas temperature at pressures of 5 and (for comparison) 1 atm. The critical electric field calculated for 0.5 atm is not shown, because it nearly coincides with the field calculated for 1 atm. We can see that, at the higher pressure, the plot of the critical electric field versus gas temperature is shifted toward somewhat higher temperatures.

Figure 5 also presents the measurement data obtained in [14, 15] (see also [4]), namely, the reduced electric field in a heated SF_6 gas at a pressure of $p = 2$ atm. The results of our calculations are seen to agree qualitatively with experiment. The observed differences can be attributed to uncertainties in the data on the cross sections for inelastic electron scattering by F atoms and for electron attachment to radicals. Increasing either the excitation cross sections for F atoms or the cross sections for electron attachment to radicals by a factor of 1.5 to 2 is quite sufficient to achieve agreement with the experimental data (to within measurement errors).

It is believed [2–4] that the electric field in a leader channel in SF_6 is equal to the critical field. Let us show that the results of our study do not contradict the data obtained from measurements in a leader channel propagating in an SF_6 gas. In [16] (see also [3]), the mean electric field in a leader channel was estimated by dividing the difference between the threshold voltage for the appearance of a leader and the breakdown voltage by the length of the projection of the leader channel onto the axis between the electrodes. The mean electric field in the channel at a pressure of 1 atm was estimated to be $E_L \approx 2$ kV cm^{-1}. The gas temperature in the leader channel was not measured; however, strong spectroscopic lines in the emission spectra of F atoms provide evidence for the intense dissociation of SF_6 molecules [3]. For this reason, it is usually assumed [2–4] that the gas temperature in a leader channel in SF_6 may reach several thousand degrees. Setting $T = 3000$ K, and using the data presented in Figs. 4 and 5, we obtain the following estimate for the critical reduced electric field at atmospheric pressure: $E/N \approx 8 \times 10^{-16}$ V cm^2. Therefore, the critical electric field is approximately equal to 2 kV cm^{-1}, which agrees with the above experimental estimate for the critical field in a leader channel.

The results obtained differ substantially from the estimates that were used earlier for the critical electric field in a heated SF_6 gas [2, 3]. The experimentally observed decrease in the critical field in SF_6 with increasing T is also interpreted in different ways. Thus, according to [2–4], the main cause of this decrease is that the rate at which electrons are attached to an SF_6 molecule is higher than the electron attachment rate to its decomposition products. However, our calculations show that a far greater role is played by the change in the electron energy distribution and more efficient electron heating by the electric field in a heated SF_6 due to the small cross sections for the excitation of the electronic levels of F atoms.

4. CONCLUSION

The kinetic calculations presented here allowed us to determine the temperature dependence of the critical electric field in an SF_6 gas at different pressures. We have also analyzed the main causes of a decrease in the critical field during the dissociation of gas molecules. We have found that, contrary to the accepted opinion, the weak critical electric field in a heated gas is associated not only with the low cross section for electron attachment but also with the change in the electron energy distribution and with a more efficient electron heating in the field because of the anomalously small cross sections for the excitation of the electronic levels of F atoms.

ACKNOWLEDGMENTS

We are grateful to V.K. Gryaznov and I.L. Iosilevskiĭ for providing us with the computational data on the thermodynamic composition of a heated SF_6 gas. This work was supported by the Russian Foundation for Basic Research, project no. 00-02-17399.

REFERENCES

1. L. G. Christophorou and J. K. Olthoff, J. Phys. Chem. Ref. Data **29**, 267 (2000).
2. L. Niemeyer and F. Pinnekamp, J. Phys. D **16**, 1031 (1983).
3. N. Wiegart, L. Niemeyer, F. Pinnekamp, *et al.*, IEEE Trans. Power Deliv. **3**, 939 (1988).
4. L. Niemeyer, L. Ullrich, and N. Wiegart, IEEE Trans. Electr. Insul. **24**, 309 (1989).
5. K. P. Brand, IEEE Trans. Electr. Insul. **17**, 451 (1982).
6. G. J. Cliteur, K. Suzuki, K. C. Paul, and T. Sakuta, J. Phys. D **32**, 494 (1999).
7. J. D. Yan, M. T. C. Fang, and Q. S. Liu, IEEE Trans. Dielectr. Electr. Insul. **4**, 114 (1997).
8. V. E. Golant, A. P. Zhilinskii, and S. A. Sakharov, *Fundamentals of Plasma Physics* (Atomizdat, Moscow, 1977; Wiley, New York, 1980).
9. J. P. Novak and M. F. Frechette, J. Appl. Phys. **55**, 107 (1984).
10. V. Tarnovsky, H. Deutsch, K. E. Martus, and K. Becker, J. Chem. Phys. **109**, 6596 (1998).
11. V. K. Gryaznov, I. L. Iosilevskiĭ, Yu. G. Krasnikov, N. I. Kuznetsova, V. I. Kucherenko, G. B. Lappo, B. N. Lomakin, G. A. Pavlov, É. E. Son, and V. E. Fortov, *The Thermal Properties of Working Fluids of a Gas-Phase Nuclear Reactor* (Atomizdat, Moscow, 1980).
12. B. Chervy and A. Gleizes, J. Phys. D **31**, 2557 (1998).
13. A. A. Radtsig and B. M. Smirnov, *Reference Data on Atoms, Molecules, and Ions* (Atomizdat, Moscow, 1980; Springer-Verlag, Berlin, 1985).
14. B. Eliasson and E. Schade, in *Proceedings of the XIII International Conference on Phenomena in Ionized Gases, Leipzig, 1977*, p. 409.
15. E. Schade, in *Invited Lectures of the XVII International Conference on Phenomena in Ionized Gases, Budapesht, 1985*, p. 277.
16. N. Wiegart, in *Proceedings of the 8th International Conference on Gas Discharges, Oxford, 1985*, p. 227.

Translated by G.V. Shepekina

Plasma Physics Reports, Vol. 29, No. 2, 2003, pp. 166–175. Translated from Fizika Plazmy, Vol. 29, No. 2, 2003, pp. 187–197.

LOW-TEMPERATURE PLASMA

Plasma-Waveguide Model of Electric Breakdown in Gas

A. V. Shelobolin

Lebedev Institute of Physics, Russian Academy of Sciences, Leninskiĭ pr. 53, Moscow, 119991 Russia

Received April 25, 2002; in final form, July 31, 2002

Abstract—Drawbacks of the conventional model of electric breakdown in high-pressure gases are discussed. A new model that associates the propagation of a breakdown wave with the propagation of a traveling electromagnetic wave in a plasma waveguide is proposed. Based on the new model, the main physical parameters of a medium are estimated. *© 2003 MAIK "Nauka/Interperiodica".*

1. INTRODUCTION

The physics of electric gas breakdown (EGB) seems to have the widest range of applications than any other division of physical science. However, the elementary processes in EGB are still far from being completely understood. The overwhelming majority of applied problems are dealt with at the empirical level, whereas the data from fundamental investigations are used only to achieve qualitative agreement between the experimental and theoretical results. The EGB theory itself, which is based on an incomplete set of experimental data, is still of fragmentary nature.

The commonly accepted EGB model, which was developed in the beginning of the 20th century, has not yet undergone any qualitative revision and still bears its main disadvantage: being capable of describing some experimental data, it cannot predict new effects or propose methods for their experimental verification. The disadvantages of both the theory and the experiment are associated with the following two circumstances. First, from an experiment standpoint, the object is extremely complicated and difficult to deal with. The requirements on the parameters of the measurement technique are hardly satisfied even with modern devices. The main equations describing EGB processes are rather complicated and, generally, cannot be simplified. Second, the EGB studies were stimulated by practical needs when the device base was poorly developed and plasma physics had just originated.

That is why the theory was constructed based on contradictory experimental results, without considering alternative plasma models. The only model that could be developed in this situation was that in which the dispersion characteristics of a medium were assumed to be similar to those of a vacuum. Consequently, taking into account the phase relations in a medium when describing EGB was unlikely to be helpful. For this reason, a model is now commonly accepted in which an electron bunch moving through a viscous medium undergoes multiplication and converts into a secondary ionization wave. Because of its limited opportunities, this model is incapable of adequately describing a variety of phenomena, the most important of which is the spatiotemporal EGB behavior.

In this paper, the drawbacks of the conventional EGB model are analyzed and an alternative plasma-waveguide model is proposed that is to a large extent free of these drawbacks (although it is still far from being completed). An analysis is carried out by successive steps. We start from qualitative considerations of the experimental data when choosing the model foundations and conclude with order-of-magnitude estimates of the main physical characteristics of the medium. Comparing the results of future experiments with these estimates will allow one to finally decide among the models.

2. INCONSISTENCY OF THE CONVENTIONAL AVALANCHE–STREAMER EGB MODEL

The conventional model of EGB at pressures of about atmospheric pressure is based on a rather wide range of experimental techniques; however, the ideology of the model mainly relies on the two-dimensional photos of breakdown waves that were first obtained by Raether in 1935 with the use of a cloud chamber [1]. Two such photos (taken from [2]) are shown in Fig. 1. Generally, the model, which is based on an analysis of photos, can be briefly described as follows.

An electron or a group of electrons starts from the cathode after applying a pulsed voltage to the discharge gap and multiplies itself in an avalanche due to impact ionization at the wave front, where energy dissipation is of a collisional nature. In the transverse (with respect to the external electric field) direction, the head of the breakdown wave (avalanche) spreads out because of diffusion. The longitudinal avalanche velocity is determined by the model of electron motion in a viscous medium under the action of a constant electrostatic force. The spatial electron density distribution can be written as [3]

$$n = (4\pi Dt)^{-3/2}\exp\left(-\frac{x^2 + y^2 + (z-ut)^2}{4Dt} + \alpha ut\right), \quad (1)$$

1063-780X/03/2902-0166$24.00

where D is the diffusion coefficient; α is the first Townsend coefficient; u is the electron drift velocity; t is time; and x, y, and z are Cartesian coordinates.

Starting from a certain instant determined by the empirical criteria of Raether, Meek, and Toll, another gas ionization mechanism becomes operational at the avalanche front and the avalanche transforms into a streamer in a stepwise manner. The avalanche diameter reduces by several times, which is seen on the photos of the avalanche-to-streamer transition [4], and the avalanche velocity increases by an order of magnitude. Qualitatively, the drawbacks and inconsistencies of the model are as follows:

(i) By virtue of the law of charge conservation and because the ions shift only slightly during the development of an avalanche, the avalanche can be regarded as a progressively stretching dipole (rather than a growing charge). Hence, the avalanche drift velocity continuously decreases and becomes zero at the instant when the internal electric field in the avalanche becomes comparable with the external one. The conventional model empirically relates this instant via Meek's criterion to the avalanche-to-streamer transition [5]. However, no decrease in the avalanche velocity just before its transformation into a streamer was observed even in the most correct experiments performed with the help of an image-converter tube [6] because of the insufficient sensitivity of the method and the speckle structure of the avalanche image. The authors of the studies [2, 5, 6], in which other techniques for avalanche recording were used, assume that, throughout the entire range of the experimental conditions, the drift velocity u depends linearly on the external electric field E:

$$u = u_0 + \beta E/N, \tag{2}$$

where N is the initial gas atom density and β is a dimensional coefficient independent of E.

(ii) Expression (2) implies that, at $E \longrightarrow 0$, the velocity u tends to u_0. The physical meaning of u_0 is the initial electron velocity at the cathode in the absence of an external electric field. The positive values of u_0 can be treated as a result of photoeffect at the cathode, because, to ensure a single-avalanche process, the cathode is usually illuminated with an external source. However, in methane, u_0 is negative [2], which cannot be qualitatively explained in terms of the conventional model.

(iii) The avalanche shape shown in Fig. 1b is not the only possible one. Figure 2, which is taken from [7], presents a photo of an avalanche whose glow has a waist. In [7], this constriction was assumed to be related to the waveform of the voltage pulse applied to the electrodes. However, this is not so, because, according to [8], the voltage waveform used in [7] did not show such a behavior. Consequently, the longitudinal profile of the avalanche glow obtained in [7] (Fig. 2) should be related to certain fundamental processes in the avalanche that are not taken into account by the conventional model.

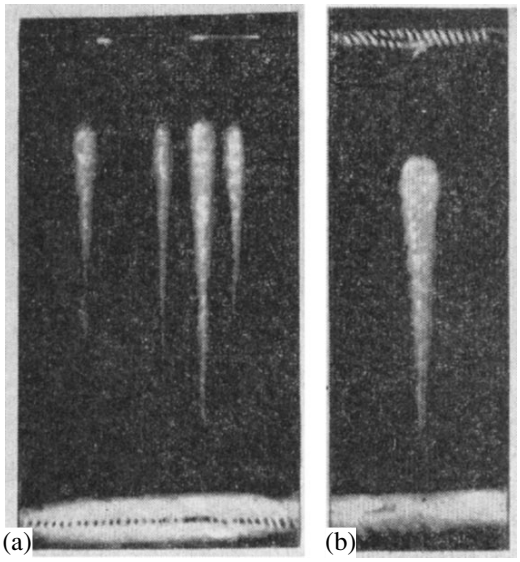

Fig. 1. Avalanche photos in (a) N_2 at a pressure of 280 torr and (b) CO_2 at a pressure of 150 torr [2].

(iv) Using the data from [7], one can extrapolate the position of the avalanche head to $t = 0$, i.e., determine its initial spatial coordinate z_0, which turns out to be $z_0 = 1.6 \pm 0.8$ mm. Thus, the avalanche starts from a point located at the distance z_0 from the cathode (rather than from the cathode itself). This fact also cannot be explained in terms of the conventional model.

(v) According to the conventional model, the avalanche-to-streamer transition is related to the switching-on of a certain additional ionization mechanism. At present, there is no consensus regarding the nature of this mechanism. Raether [2] and Lozanskiĭ and Firsov [3] believe that this is photoionization, whereas other authors [5, 9] assume that this is the increasing electrostatic ionization at the avalanche front. Each of these mechanisms implies the increase in the velocity of the breakdown wave; however, none of them explains the decrease in its transverse size. Moreover, in the dipole approximation, both mechanisms assume that the directivity diagram of the ionization factor is maximum in the direction perpendicular to the external electric field.

(vi) In addition to unsatisfactory description of the avalanche-to-streamer transition, the conventional model is incapable of describing the inertial streamer propagation after switching off the discharge voltage. In [10], it was experimentally shown that the inertial path can be longer than 1 cm, which is certainly longer than all the relaxation lengths of the gas particles at pressures close to atmospheric. In principle, the conventional model can only describe energy relaxation, rather than momentum relaxation, which was actually

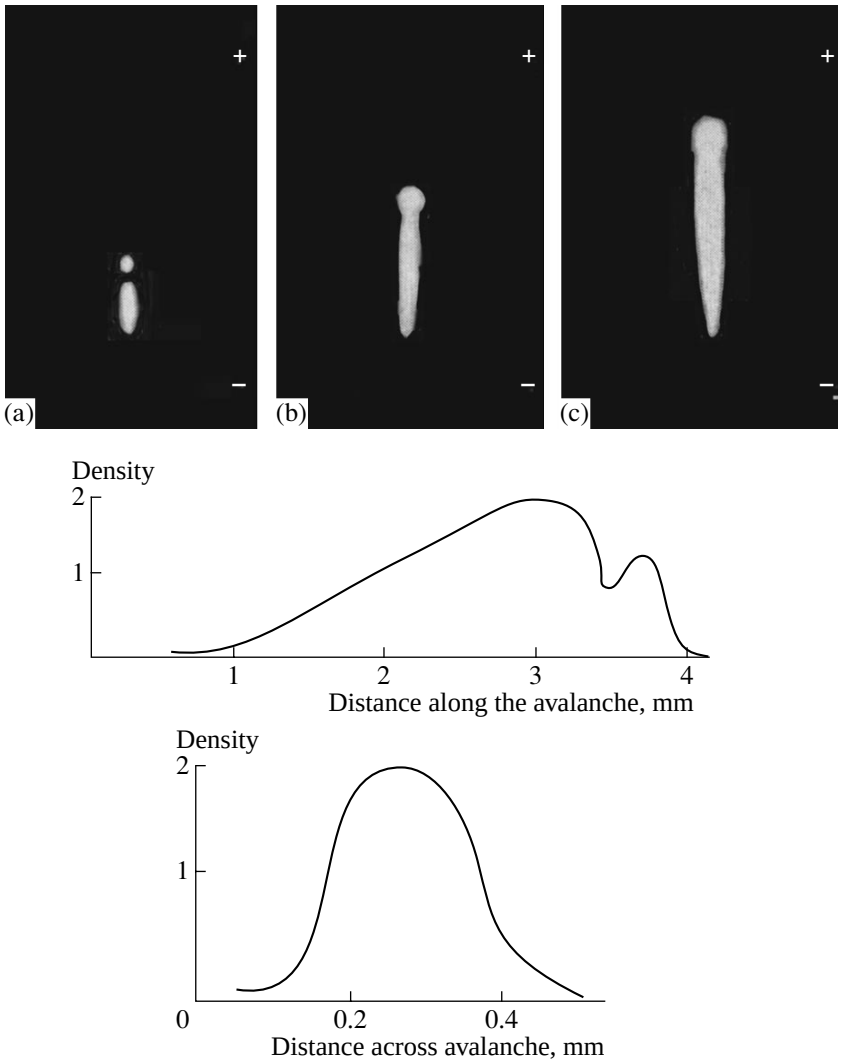

Fig. 2. Avalanche photos in air for different durations of the voltage pulse at a cloud chamber: (a) 0.05, (b) 0.08, and (c) 0.11 μs, and the blackening density for photo (b) [7].

observed in [10]. An attempt [11] to formulate a plasma model capable of describing this phenomenon will be discussed below.

Before proceeding to estimates, the following points should be discussed and following questions should be answered:

(i) What is the medium in which the breakdown wave propagates? Is it a gas or plasma? In the former case, the development of an avalanche can be described based on the assumptions of the conventional model. In the latter case, the breakdown wave can be treated as a traveling electromagnetic wave in the spatially bounded plasma—plasma waveguide. A quantity that allows one to distinguish between the gas and plasma is the Debye screening radius [12]

$$r_D = 500\sqrt{\frac{T}{n}}\ (\text{cm}), \qquad (3)$$

where T [eV] is the temperature of the colder plasma components (ions or electrons) and n [cm^{-3}] is the charge carrier density.

Assuming that the background plasma density is $n = 10^2$–10^4 cm^{-3} [13] and the ion temperature is equal to room temperature (i.e., $T = T_0 = 0.025$ eV), we obtain from formula (3) that $0.8 < r_D < 8$ cm. Thus, such an atmospheric electricity phenomenon as a stepped leader stroke is certainly an electric breakdown of plasma because the leader diameter ranges from 1 to 10 m [14]. Under laboratory conditions, before applying a pulsed voltage to the discharge gap, the medium is close to the plasma state. Up to now, reliable space and time resolved experimental data on T and n after applying the external field are still lacking.

In this context, the assumption about the plasma nature of a medium in which EGB develops still

requires experimental verification. Nevertheless, most investigators assume (directly or indirectly) that the streamer phase of breakdown occurs in a plasma; however, they do not employ this idea when analyzing the spatiotemporal characteristics of breakdown. In the conventional model, the avalanche is assumed to develop in a gas, although some investigators [15–20] suppose that, in the final stage, it occurs in a plasma.

(ii) In the conventional model, the temperature of the excessive avalanche electrons is estimated by the angle of the avalanche tail. The actual T_e value is 1–10 eV [2, 7]. However, it should be noted that, in the avalanche tail, diffusion can be accompanied by relaxation processes, in which case such estimates become senseless.

(iii) An important point of the conventional model is the estimations of the excessive charge density in the avalanche head and the electric field near its surface. It is most suitable to estimate these quantities at an instant preceding the avalanche-to-streamer transition. Three criteria for this transition can be used: Raether's criterion, Meek's criterion, and Toll's criterion. These criteria are ideologically interrelated; however, the main experimental parameters are used in different ways when estimating the medium and field parameters. Hence, these criteria should be considered independently.

According to Raether's criterion [2], the avalanche-to-streamer transition occurs when the avalanche length reaches the critical value Z_{cr}. In this case, the excessive electron density can be estimated as

$$n_{Rae} = \frac{3\exp(\alpha Z_{cr})}{4\pi R^3}, \quad (4)$$

whereas the electric field near the avalanche surface is

$$E_{Rae} = \frac{q\exp(\alpha Z_{cr})}{R^2}, \quad (5)$$

where R is the radius of the avalanche head and q is the elementary charge.

For nitrogen and air at pressures of 400 torr, we have $11.7 < \alpha Z_{cr} < 36$ [7] and $10^{-2} < R < 10^{-1}$ cm [2, 5, 7]; from here, we obtain $3 \times 10^7 < n_{Rae} < 10^{21}$ cm^{-3}. A similar estimate for E gives $2 < E_{Rae} < 6 \times 10^{12}$ V/cm.

According to Meek's criterion [5], an avalanche transforms into a streamer when the electric field of the excessive charge near the avalanche head amounts to 10–100% of the external electric field E. In this case, the excessive charge density can be estimated as

$$n_M = \frac{3(0.1–1)E}{4\pi qR}. \quad (6)$$

Consequently, for E = 20 kV/cm, we have $3 \times 10^{10} < n_M < 3 \times 10^{12}$ cm^{-3}.

According to Toll's criterion [4], an avalanche converts to a streamer at an excessive charge in its head of about $q\exp(20) \approx 10^8\, q$. Then, for the density and the electric field, we have $2 \times 10^{10} < n_T < 2 \times 10^{13}$ cm^{-3} and $10^3 < E_T < 10^5$ V/cm, respectively.

It follows from the above estimates that Raether's criterion is inapplicable to quantitatively developing the theory because the range of the main physical parameters is too wide, so that the limiting E_{Rae} and n_{Rae} values exceed the intraatomic electric field and the electron density for single ionization of gas atoms, respectively. These drawbacks of Raether's criterion are related to the facts that, on one hand, in Eq. (4) $n \sim R^{-3}$, which enlarges the range of estimates, and, on the other hand, the Z_{cr} values taken from [7] were determined by analyzing the specific features of the longitudinal streamer profile. In this respect, Meek's and Toll's criteria seem to be more preferable; however, it should be noted that, since these criteria are empirical, the above estimates are no more reliable than the basic empirical assumptions, each of which is self-contradictory. Moreover, in [20], avalanche head radii of $R = 10^{-3}$ cm were observed; therefore, the range of above estimates can be wider.

(iv) Another inconsistency of and Meek's and Toll's criteria is related to the fact that, in the observations of multiavalanche processes, the avalanche axes are equally spaced in the transverse direction by a distance of $4R$ (or multiple of $4R$) (Fig. 1a). In this case, the electrostatic interaction between the neighboring avalanches is only one order of magnitude weaker than between an individual avalanche and the external field. In view of this, it could be expected that the spatial structure of a multiavalanche breakdown will be divergent, which, however, is not the case.

(v) The above result that the avalanches in a multiavalanche breakdown are equally spaced can be a consequence of either the formation of an interference pattern in the direction perpendicular to the external electric field or the incorrect interpretation of experimental observations in those papers.

In the latter case, the probability that K avalanches will be equally spaced in the transverse direction can be estimated assuming the equal probability for them to start from any point of the electrode surface in a uniform electric field. A quantity reciprocal to this probability will show the necessary number of experiments that should be performed in order to observe the corresponding equidistant avalanche distribution. A scheme for recording electric breakdown waves in a cloud chamber is shown in Fig. 3.

The total number of cells on the electrode surface from which avalanches can start can be estimated as $m = (R_e/R)^2$, where R_e is the electrode radius. In Fig. 3, the cells that give rise to equidistant avalanches are shaded. The presence of two or more rows of such cells is related to the depth resolution x at the object, which, in turn, is related to the depth resolution x_1 at the film. If the lens produces a one-to-one image of the object on

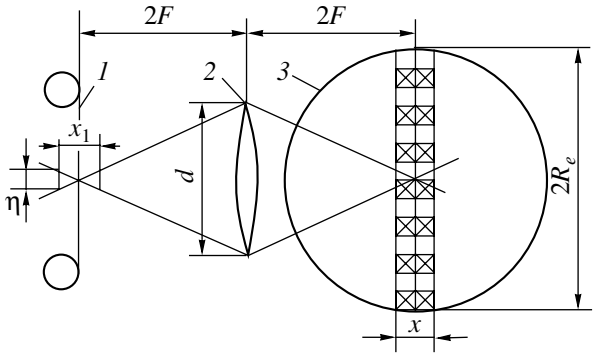

Fig. 3. Scheme for recording electric breakdown waves in a cloud chamber: (*1*) photographic film, (*2*) lens, and (*3*) cathode.

the film, then $x = x_1 = 4\eta F/d$, where η is the film grain size and F/d is the quantity reciprocal to the lens aperture ratio. Then, assuming that K avalanches start from any of m cells on the electrode surface with equal probabilities and considering the start from any of the l shaded cells to be a favorable event, the probability of observing the equidistant distribution is

$$p = \frac{l(l-1)(l-2)\ldots(l-K+1)}{m(m-1)(m-2)\ldots(m-K+1)} < \left(\frac{l}{m}\right)^K = \left(\frac{x}{4R_e}\right)^K. \quad (7)$$

Let $\eta = 50$ μm, $F/d = 11$, and $K = 20$ [8]. According to [2], for electrodes with a Rogowsky profile, an elevated uniformity of the electric field is achieved at the radius equal to the interelectrode distance. Consequently, we can set $R_e = 2$ cm. Substituting these values into formula (7), we have $p = 10^{-31}$, which almost completely excludes the possibility of the formation of an equidistant distribution of avalanches under the assumption of the equal probability for them to start from any cell on the electrode surface. This result unambiguously decides a case in favor of the formation of an interference pattern. This conclusion follows from formula (7) even for $x = 2R_e$, which corresponds to technical limitations on the depth resolution. Then, for the four avalanches shown in Fig. 1a, we have $1/p = 16$; however, under conditions of [8], $1/p = 2^{20} \approx 10^6$ and the equal probability approach is inapplicable.

3. PLASMA MODELS OF EGB

A detailed analysis of the plasma models of EGB, as well as the models of electric breakdown in plasma, is given in [21]. Generally, breakdown waves can be described by using the electron distribution function, which is calculated in one or another approximation, depending on a particular problem. However, an analysis of the basic assumptions underlying these models allows one to distinguish between two main approaches: an approach incorporating the effects of superthermal electrons and that neglecting these effects.

The former approach was used in [10, 11, 22]. The inertial streamer propagation observed in [10] was explained in [11] based on the assumption that, in a streamer, there were superthermal electrons with energies several times higher than the gas ionization energy. Moreover, the avalanche-to-streamer transition was related to the threshold for the onset of these electrons. The experimental results of [10] should be considered as fundamental. At first glance, they seem to contradict the principles of thermodynamics, according to which a closed nonequilibrium system must monotonically relax to an equilibrium state. However, the experiment showed that, after the discharge voltage was switched off, the streamer not only continued to propagate in the same direction, but also flashed before terminating.

The authors of [11] treated the volume of the streamer channel as a closed system; therefore, based on qualitative energy considerations, they arrived at the hypothesis of the presence of superthermal electrons. At the same time, plasma theory [23] predicts the existence of two characteristic time scales, namely, the relaxation times of the symmetric and asymmetric parts of the distribution function. The latter time is on the order of the reciprocal electron–neutral collision frequency and, for the streamer plasma at pressures of about atmospheric pressure, amounts to 0.1–1 ps, whereas the duration of the inertial streamer propagation is about 10 ns. This means that the plasma can "remember" the direction of the external electric field for a time significantly shorter than the streamer propagation time after the discharge voltage is switched off. It follows from this that, even if there were a superthermal peak in the distribution function, the streamer should come to a stop and emit all of the energy stored in it in a time equal to the relaxation time of the symmetric part of the distribution function.

The other plasma model of EGB does not use the hypothesis of superthermal electrons and suggests that the avalanche goes over to a plasma state even before the streamer arises [15, 16]. According to [15], the plasma density attains $\sim 10^{16}$ cm^{-3}, the excess electrons are expelled by the avalanche electric field toward the avalanche boundary, and the further diffusion expansion of the avalanche slows down because of the transition to the ambipolar diffusion regime [16]. A subsequent avalanche-to-streamer transition is related to gas photoionization ahead of the breakdown wave front [17], whereas the avalanche itself develops due to thermal fluctuations of the background electron density [18].

The main problems related to photoionization are associated with the resonant absorption of the emission from the EGB wave front by gas [3] and absolute energy calibration. The first problem is related to the fact that the mean free path of resonant photons ioniz-

ing the gas must be significantly shorter than the ~1-cm mean free path, experimentally found by Raether [2]. An attempt to resolve this contradiction by taking into account the limited width of the absorption and emission lines [3] cannot be considered satisfactory because, according the quantitative estimates of [3], the plasma density at a distance of 1 cm from the EGB wave front should be lower than the background level. The second problem is that, under the assumption of isotropic emission from the EBG wave front, the energy density of the ionized particles in the radiation source must be at least six orders of magnitude higher than that in the surrounding gas.

The problem of energy calibration was overcome in [19] by invoking the hypothesis of the laser mechanism for the amplification of ionizing radiation in the EGB wave and the corresponding decrease in the divergence angle of this radiation. The problem of transportation of ionizing radiation was resolved in [17, 18] by invoking the hypothesis of atomic ionization via intermediate excited states.

This model quite satisfactorily agrees with the hypothesis of the photoionization mechanism for the EGB wave propagation and the slowing-down of the avalanche expansion at the final stage of the avalanche development; however, it fails to eliminate other qualitative inconsistencies of the conventional model.

4. FOUNDATIONS OF THE PLASMA-WAVEGUIDE MODEL

The above list of the disadvantages of the conventional model is far from complete. However, in order to stimulate the development of a radically new model, experiments are required that would clearly demonstrate these disadvantages. Such an experiment is an electric air breakdown induced by a long laser spark [24]. The main qualitative characteristics of breakdown waves recorded in this experiment disagree with the conventional model. The main characteristics of this type of breakdown are as follows:

(i) The primary breakdown wave is a doubled piston with a characteristic size on the order of 1 cm.

(ii) The wave propagation direction is determined by the shape (rather than polarity) of the electrodes. In this case, the model of a "growing-through" electrode is not applicable because the wave always propagates from the tube to the needle, i.e., from the region with a lower electrostatic field to the region with a higher field.

(iii) The wave propagation velocity is on the order of the thermal velocity of air ions.

(iv) The primary wave starts after the electrode sheath has formed, and the starting point lies apart from the electrode at the distance on the order of the sheath thickness and the length of the EGB wave itself.

(v) The measured frequency spectrum of the electromagnetic oscillations of the channel along which the breakdown wave propagates consists of two lines in the megahertz frequency range with a frequency ratio of 3 : 1; in this case, the frequency of the excitation circuit is always three times higher than the frequency of the excited oscillations.

(vi) As the breakdown wave propagates, its leading part is damped and new waves are generated between its trailing part and the electrode.

(vii) The breakdown wave transforms into a secondary wave with a diameter one order of magnitude smaller than the diameter of the primary wave and a propagation velocity higher than that of the primary wave by one to two orders of magnitude.

(viii) Before the appearance of the secondary wave between the primary wave and the electrode toward which it propagates, a continuous glow channel with a diameter much less than the primary wave diameter is observed for a time significantly longer than the development time of the secondary wave.

These and some other less important characteristics can be understood and described only after incorporating into the model the concept of a "mode structure," which, in turn, is a consequence of the hypothesis that the breakdown wave has a phase. The conventional model does not permit such an incorporation. The reasons are that, first, it does not imply the existence of a wave phase in EGB and, second, even after being incorporated, this concept can hardly makes the model more efficient because all the electromagnetic waves in a gas have phase velocities of about $c = 3 \times 10^{10}$ cm/s (accordingly, the interaction of these waves with a medium is insignificant). In contrast, in plasma, there are certain types of waves whose phase velocities are on the order of the thermal velocities of the plasma components and that can efficiently interact with the medium.

In the absence of an external magnetic field, the longitudinal ion-acoustic and electron plasma waves are of the highest importance for the EGB problem. Both of these waves are described by similar equations and have similar dispersion characteristics $\omega(k)$ (where ω is the frequency and k is the wavenumber), shown in Fig. 4 [25, 26]. For the ion-acoustic wave, Ω is the ion Langmuir frequency and the derivative of $\omega(k)$ at the coordinate origin is equal to the ion acoustic velocity. For the electron wave, Ω is the electron Langmuir frequency and the derivative at the coordinate origin is equal to the speed of light. The dashed lines in Fig. 4 show the wave phase velocity and illustrate the graphical method for resolving the problem of determining the plasma-waveguide characteristics. This problem will be considered below. Figure 4 also graphically represent the avalanche-to-streamer transition.

When considering both of these types of waves, one should take into account not only qualitative but also quantitative similarity between them. Note that, from the experimental standpoint, it is much simpler to observe ion-acoustic waves than electron waves. Thus, preliminary computer simulations can significantly

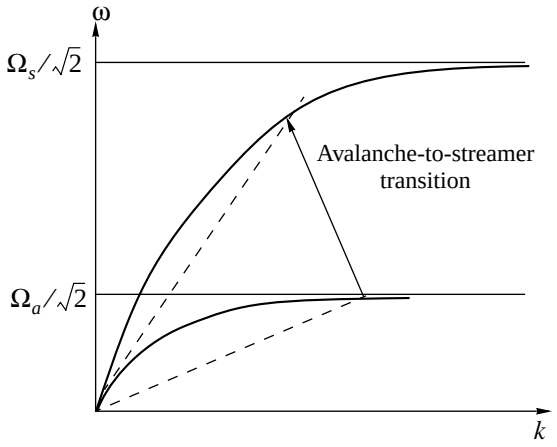

Fig. 4. Dispersion characteristics of an avalanche and a streamer and the avalanche-to-streamer transition (Ω_s is the streamer plasma frequency, and Ω_a is the avalanche plasma frequency).

reduce the cost of experiments. The presence of two types of waves also makes it necessary to formulate the principles of the plasma-waveguide model in a general form.

5. PLASMA-WAVEGUIDE MODEL

(i) After applying voltage to the discharge gap, the medium filling the gap becomes a plasma, in which cylindrical regions with a high plasma density (plasma waveguides) arise either under the action of an external ionization source or due to the formation of an interference pattern transverse to the external electric field.

(ii) Then, spatially inhomogeneous electrode sheaths arise, in which broadband electromagnetic oscillations are generated. For certain frequencies of the generated oscillations, the charge carrier density in the electrode sheaths increases to overcritical values, and the plasma waveguide becomes a plasma cavity.

(iii) Two characteristic frequencies can be distinguished in the oscillation spectrum: the pumping frequency and the carrier frequency. The pumping balances the dissipation loss in the plasma cavity and ensures the supply of energy to the oscillations at the carrier frequency, which are an energy source for the traveling ionizing wave. The pumping frequency is three times higher than the carrier frequency.

(iv) The traveling ionizing wave obeys the phase matching condition; i.e., its phase velocity is close to the thermal velocity of the charged plasma particles (the velocity corresponding to the maximum of the particle velocity distribution function).

(v) In the course of the plasma cavity evolution between the electrodes, the charge carrier temperature and density in the axial region increase. As a result, the oscillations at the pumping frequency undergo screening at the front of the ionizing wave and the pumping frequency becomes the highest carrier frequency. In this case, the third harmonic of this new carrier frequency becomes the pumping frequency. This corresponds to the avalanche-to-streamer transition.

6. EXPERIMENTAL FOUNDATIONS OF THE PLASMA-WAVEGUIDE MODEL

The simplest way to verify the plasma-waveguide model is to apply the longitudinal-wave concept [25, 26] to the experiment of [7], as was done in [27]. The solution to the corresponding set of equations is shown graphically in Fig. 4.

From Fig. 2, it can be seen that the distance from the minimum in the longitudinal profile of the avalanche glow to the avalanche front is 0.7 mm. Assuming that this distance is equal to a quarter of the longitudinal wavelength λ and the avalanche radius is $R = 0.2$ mm, we can estimate the plasma-waveguide carrier frequency ω, the plasma frequency Ω in the cylindrical part of the waveguide, and the corresponding charge carrier density n. Equating the avalanche propagation velocity (which, according to [7], can be set at $u = 10^7$ cm/s) to the wave phase velocity in the plasma waveguide and using the relations $\lambda = u/f$ and $\omega = 2\pi f$, we obtain $f = 3.6 \times 10^7$ Hz and $\omega = 2.2 \times 10^8$ s^{-1}. From the dispersion relation for the longitudinal wave [25], we find the plasma frequency Ω:

$$\Omega = 2\pi\frac{u}{\lambda}\sqrt{1-\frac{2}{4\pi^2\left(\frac{R}{\lambda}\right)^2\ln 2\pi\frac{R}{\lambda}}} \approx \frac{u}{R}\sqrt{\frac{2}{\ln\frac{1}{2\pi}\frac{\lambda}{R}}}. \quad (8)$$

Under conditions $u \ll c$ and $\omega \ll \Omega$, formula (8) is simplified. The first of these inequalities is certainly satisfied for an avalanche; the second inequality is also satisfied, but with a smaller margin. Using the first inequality, for the above values of u, R, and λ, taken from [7], we obtain that in the avalanche $\Omega_a = 8.2 \times 10^8$ s^{-1} (the subscript a stands for avalanche). The corresponding charge carrier density is $n = 2.3 \times 10^8$ cm^{-3}.

This n value agrees qualitatively with an analysis of the relaxation processes in plasma [28], which shows that $n \approx 10^8$ cm^{-3} is the threshold value above which relaxation processes that are faster than diffusion come into play. Estimates show that the avalanche mechanism for the EGB development begins to operate near this threshold, and the estimate for r_D at room temperature gives $R/r_D \approx 3$.

Going over to the estimates of the streamer parameters (marked with the subscript "s"), it is reasonable to assume that the mode structure and the ratio between the eigenfrequencies of the avalanche and streamer modes remains the same as in a cylindrical plasma waveguide [24], namely, $\Omega_s/\Omega_a \approx \omega_s/\omega_a = 3$. Then, we have $n_s = 9$, $n_a = 2 \times 10^9$ cm^{-3}. More exact calculations by formula (8) give $n_s = 10^{10}$ cm^{-3}. The relation $\omega_s/\omega_a = 3$

is confirmed by frame-to-frame streamer photos [22], which show that waists in the streamer profile occur every four nanoseconds. Without going into the waist nature, but only separating the effects linear and quadratic in the electric field, we can estimate the streamer eigenfrequency. In the former case, it is equal to 2.5×10^8 Hz, and in the latter case, to 1.25×10^8 Hz. Taking into account that the tripled avalanche frequency determined above is 1.1×10^8 Hz, we can see that it fairly well agrees with the data from [22].

Another estimate based on this relation allows us to determine the streamer longitudinal wavelength. Assuming that $u_s/u_a = 10$ and $\lambda_s = \lambda_a(u_s/u_a)(\omega_a/\omega_s)$, we have $\lambda_s = 8$ mm. Streamer photos [2, 7] show that the streamer glow is nonuniform in the longitudinal direction, the distance between the nonuniformity and the electrode being on the order of the above value. In the literature, this nonuniformity on the streamer profile is usually associated with the space coordinate where the avalanche transforms into a streamer. However, estimates of the of the medium and electric-field parameters obtained by Raether's criterion turn out to be unacceptable under this assumption. Moreover, this assumption disagrees with the results of [22], where a streamer breakdown from the middle of the gap was observed.

To conclude the discussion of the characteristic frequencies and times, we estimate the ion Langmuir frequency $\Omega_i = \Omega_e\sqrt{m/M}$ (where m is the electron mass) and the frequencies of the elastic electron–neutral and ion–neutral collisions (ν_e and ν_i, respectively) for an avalanche and a streamer. Based on the experimental data from [7], we have for an avalanche $\omega = 2.2 \times 10^8$ s^{-1}, $\Omega_e = 8.2 \times 10^8$ s^{-1}, $\Omega_i = 3.6 \times 10^6$ s^{-1}, and $\nu_i = 7 \times 10^9$ s^{-1}. For a streamer, the corresponding parameters are $\omega = 6.6 \times 10^8$ s^{-1}, $\Omega_e = 5.6 \times 10^9$ s^{-1}, $\nu_e = 10^{12}$–10^{13} s^{-1}, and $\nu_i = 7 \times 10^9$ s^{-1}. When estimating ν_i, the resonant transfer cross section (estimated at 10^{-14} cm^2 [12]) was taken as a cross section for elastic collisions.

The electron temperature T_e and the avalanche and streamer electric fields can be estimated from the phase matching condition, assuming that the EGB wave propagation velocity is equal to the electron thermal velocity, which corresponds to the maximum of the electron velocity distribution function. Experiments confirm that this principle is also applicable to an ion plasma waveguide. In [24], three EGB waves were recorded that propagated with the velocities $u_1 = 3.2 \times 10^4$ cm/s, $u_2 = 3.7 \times 10^4$ cm/s, and $u_3 = 2.4 \times 10^5$ cm/s. The first and second waves resulted in breakdown, whereas the third wave decayed and did not lead to breakdown. At $T_i = T_0 = 0.025$ eV, the thermal velocity corresponding to the maximum of the Maxwellian distribution function of the heaviest molecular ions in air,

$$V = \sqrt{\frac{2T_i}{M}}, \tag{9}$$

amounts to $V(O_2) = 3.9 \times 10^4$ cm/s and $V(N_2) = 4.2 \times 10^4$ cm/s for oxygen and nitrogen, respectively. Thus, for the first and second waves, the phase-matching condition was satisfied accurate to 20%, whereas the velocity of the third wave was six times higher than the ion thermal velocity, which resulted in its damping. An increase in the discharge voltage should lead to an increase in the density of atomic ions in air and, consequently, to a discrete distribution of breakdown delays with respect to the long laser spark initiating the discharge [24]. This phenomenon was earlier observed experimentally in [29].

Using Eq. (9) and assuming that, for a streamer, $u = V = 10^8$ cm/s, we have $T_e = 2.8$ eV. For an avalanche, a similar estimate for the electron temperature is $T_e \approx 2T_0 = 0.05$ eV. However, for an avalanche, the above problem of the initial velocity u_0 arises. In the conventional model, it should be $u_0 = 0$, whereas in the plasma-waveguide model, we have $u_0 = V_0 = \sqrt{2T_0/m} = 9.6 \times 10^6$ cm/s. Since the inequality $u_0 < V_0$ holds in all the experiments, we have to assume that there is a certain threshold value of the external electric field for the avalanche development; i.e., the dependence of the avalanche drift velocity on the external field can be approximated by $u = u_0 + \beta(E - E_0)/N$, where E_0 is the threshold external electric field. Proceeding to the estimates of the electric fields in an avalanche and a streamer, we should take into account that, according to the plasma-waveguide model, there are two modes in each of these breakdown waves, and, consequently, two types of electric fields: the traveling wave field and the pumping wave field. The electric field of the streamer traveling wave is the upper limit for the avalanche pumping field.

According to [12], the increase in the electron temperature in an avalanche traveling wave can be expressed in terms of the electric field E:

$$\Delta T_e = \frac{1}{3}\frac{M}{m}\frac{q^2E^2}{\nu_e^2} \approx T_0. \tag{10}$$

Then, we have for E

$$E = \frac{\nu_e}{q}\sqrt{1.5m\delta T_0}, \tag{11}$$

where $\delta = 2m/M$ is the coefficient of energy transfer from an electron to a gas molecule or atom with a mass M, $\nu_e = N\sigma v$ is the electron–atom collision frequency, σ is the cross section for these collisions, and v is the electron thermal velocity.

Orienting to the experiment [7], carried out with nitrogen at a pressure of 400 torr, and assuming that, according to [30], $\sigma = 8\pi a_0^2 = 7 \times 10^{-16}$ cm^2 (where $a_0 = 0.53 \times 10^{-8}$ cm is the Bohr radius), we have from formula (11) that, at $u = 1.4 \times 10^7$ cm/s, the electric field of the avalanche traveling wave is $E_a = 4$ V/cm. Taking

into account that, for a streamer, the electron–neutral collision rate is higher by one order of magnitude and the electron temperature is higher by two orders of magnitude than those for an avalanche, we obtain from formula (11) that E_s = 400 V/cm.

A qualitative comparison of the streamer electric field with the external electric field shows that they differ by two orders of magnitude. This can be related to the fact that taking into account inelastic collisions increases the effective parameter δ in formula (11) by more than two orders of magnitude [31]. On the other hand, for most gases, the parameter σ and, accordingly, ν_e are lower than in nitrogen. With allowance for these circumstances, the obtained E_a and E_s values seem to be underestimated by one order of magnitude. The indirect confirmation of this conclusion is that, in the plasma frequency multipliers [32], the energy conversion efficiency is typically on the order of 1%. Another confirmation is that the threshold fields for microwave breakdown under the nearly the same conditions with respect to the characteristic frequencies and gas pressures lie in the range 1–10 kV/cm [33].

Finally, we estimate the duration of the avalanche-to-streamer transition. The conventional model does not take into account the time behavior of the extra ionization factor and, hence, is incapable of estimating this duration. The plasma-waveguide model relates this transition to the rearrangement of the plasma cavity between the electrodes after introducing an intermediate plasma mirror in it. Accordingly, the duration of the avalanche-to-streamer transition should be either shorter or on the order of the streamer mode period (i.e., it should be in the range 1–10 ns). Of course, when analyzing the avalanche-to-streamer transition, it should be taken into account that, in the course of the avalanche development, the interelectrode cavity changes and, just before the transition, avalanches [4] or "tail waves" [24] are generated. The estimate of the characteristic transition time depends on whether or not these effects are incorporated in the model of avalanche-to-streamer transition [20].

7. CONCLUSION

The proposed plasma-waveguide model of EGB requires further development. First of all, a detailed account for the damping of breakdown waves should be made. However, since the model assumes that the traveling wave is pumped by a source, a qualitative solution to the damping problem can be found in the same way as is done for laser systems. However, the experimental data that are necessary to resolve this problem quantitatively are still lacking.

The final arguments in favor of or against the plasma-waveguide model can be obtained only experimentally. However, direct measurements of T, n, and E in avalanche and streamer experiments are still difficult to perform from the technical standpoint. Thus, the required spatial and temporal resolutions can be provided only by laser diagnostics; however, for charge carrier densities discussed above, the phase increment of the diagnostic wave can be too small to obtain the necessary data [34]. On the other hand, when measuring the avalanche temperature by the relative broadening of luminescence lines [20, 31], the scanning of the avalanche over a radius with a step on the order of 10^{-3} cm is required because of the presence of two spatial modes in the cavity. This also imposes rigid requirements on the spatial resolution and stability of the avalanche position in the transverse direction. Therefore, further improvement of the EGB diagnostic techniques is required.

Moreover, no demarcation line has yet been drawn between the spark discharge, which incorporates an avalanche and a streamer, and the arc, into which the spark discharge transforms. This can cause a discrepancy when treating the experimental data (see [31, 35]). Finally, it is very important to obtain high-quality converter-tube images that will allow one to eliminate the above discrepancy concerning the change in the velocity of an avalanche before its transition to a streamer and also to determine the characteristic time of the avalanche-to-streamer transition.

ACKNOWLEDGMENTS

I am grateful to A.A. Rukhadze for uncompromising and, thus, very helpful discussions.

REFERENCES

1. E. Flegler and H. Raether, Z. Tech. Phys., No. 16, 435 (1935).
2. G. Raether, *Electron Avalanches and Breakdown in Gases* (Butterworths, London, 1964; Mir, Moscow, 1968).
3. É. D. Lozanskiĭ and O. B. Firsov, *Theory of Spark* (Atomizdat, Moscow, 1975).
4. H. Toll, Z. Naturforsch. **19**, 346 (1964).
5. J. M. Meek and J. D. Craggs, *Electrical Breakdown of Gases* (Clarendon, Oxford, 1953; Inostrannaya Literatura, Moscow, 1960).
6. K. H. Wagner, Z. Phys. **180**, 516 (1964).
7. K. R. Allen and K. Phillips, Proc. R. Soc. London, Ser. A **274**, 19 (1963).
8. K. R. Allen and K. Phillips, Rev. Sci. Instrum. **30**, 230 (1959).
9. E. M. Bazelyan and Yu. P. Raizer, *Spark Discharge* (Mosk. Fiz.-Tekh. Inst., Moscow, 1997).
10. N. S. Rudenko and V. I. Smetanin, Zh. Tekh. Fiz. **44**, 2602 (1974).
11. N. S. Rudenko and V. I. Smetanin, Izv. Vyssh. Uchebn. Zaved., Fiz. **7**, 34 (1977).
12. V. E. Golant, A. P. Zhilinskiĭ, and S. A. Sakharov, *Principles of Plasma Physics* (Atomizdat, Moscow, 1977).
13. I. M. Imyanitov, *Insruments and Methods for Studying Atmospheric Electricity* (GITTL, Moscow, 1957).

14. M. A. Uman, *Lightning* (McGraw-Hill, New York, 1969; Mir, Moscow, 1972).
15. O. A. Omarov, M. B. Khachalov, and A. Z. Éfendiev, Fiz. Plazmy **4**, 338 (1978) [Sov. J. Plasma Phys. **4**, 189 (1978)].
16. O. A. Omarov, A. A. Rukhadze, and G. A. Shneerson, Zh. Tekh. Fiz. **49**, 1997 (1979) [Sov. Phys. Tech. Phys. **24**, 1125 (1979)].
17. A. P. Broĭtman, O. A. Omarov, S. A. Reshetnyak, and A. A. Rukhadze, Kratk. Soobshch. Fiz., No. 9, 27 (1984); Kratk. Soobshch. Fiz., No. 9, 41 (1984).
18. A. P. Broĭtman, O. A. Omarov, S. A. Reshetnyak, and A. A. Rukhadze, Kratk. Soobshch. Fiz., No. 6, 50 (1984).
19. A. P. Broĭtman and O. A. Omarov, Pis'ma Zh. Tekh. Fiz. **7**, 389 (1989).
20. O. A. Omarov and A. A. Rukhadze, Zh. Tekh. Fiz. **50**, 536 (1980) [Sov. Phys. Tech. Phys. **25**, 323 (1980)].
21. A. N. Lagar'kov and I. M. Rutkevich, *Waves of Electric Breakdown in Bounded Plasmas* (Nauka, Moscow, 1989).
22. N. S. Rudenko and V. I. Smetanin, Zh. Éksp. Teor. Fiz. **61**, 146 (1971) [Sov. Phys. JETP **34**, 76 (1971)].
23. L. M. Biberman, V. S. Vorob'ev, and I. T. Yakubov, *Kinetics of Nonequilibrium Low-Temperature Plasma* (Nauka, Moscow, 1982).
24. A. V. Shelobolin, Fiz. Plazmy **26**, 346 (2000) [Plasma Phys. Rep. **26**, 320 (2000)].
25. A. F. Aleksandrov, L. S. Bogdankevich, and A. A. Rukhadze, *Principles of Plasma Electrodynamics* (Vysshaya Shkola, Moscow, 1978).
26. A. F. Aleksandrov and A. A. Rukhadze, *Lectures on the Electrodynamics of Plasmalike Media* (Mosk. Gos. Univ., Moscow, 1999).
27. A. V. Shelobolin, Kratk. Soobshch. Fiz., No. **8**, 22 (2000).
28. D. W. Koopman and K. A. Saum, J. Appl. Phys. **44**, 5328 (1973).
29. V. D. Zvorykin, F. A. Nikolaev, I. V. Kholin, *et al.*, Fiz. Plazmy **5**, 1140 (1979) [Sov. J. Plasma Phys. **5**, 638 (1979)].
30. H. S. W. Massey and E. H. S. Burhop, *Electronic and Ionic Impact Phenomena* (Clarendon, Oxford, 1952; Inostrannaya Literatura, Moscow, 1958).
31. S. I. Andreev and G. M. Novikova, Zh. Tekh. Fiz. **45**, 1692 (1975) [Sov. Phys. Tech. Phys. **20**, 1078 (1975)].
32. A. A. Brandt and Yu. V. Tikhomirov, *Plasma Multipliers of Frequency* (Nauka, Moscow, 1974).
33. A. D. MacDonald, *Microwave Breakdown in Gases* (Wiley, New York, 1966; Mir, Moscow, 1969).
34. N. G. Basov, Yu. A. Zakharenkov, A. A. Rupasov, *et al.*, *Diagnostics of Dense Plasmas* (Nauka, Moscow, 1989).
35. L. A. Vaĭnshtein, A. M. Leontovich, A. P. Malyakin, and S. A. Mandel'shtamm, Zh. Éksp. Teor. Fiz. **24**, 326 (1953).

Translated by N.N. Ustinovskiĭ

Plasma Physics Reports, Vol. 29, No. 2, 2003, pp. 176–186. Translated from Fizika Plazmy, Vol. 29, No. 2, 2003, pp. 198–208.

LOW-TEMPERATURE PLASMA

Evolution of the Radial Structure of a Negative Corona during Its Transformation into a Glow Discharge and a Spark

Yu. S. Akishev, M. E. Grushin, V. B. Karal'nik, I. V. Kochetov, A. E. Monich, A. P. Napartovicgh, and N. I. Trushkin

Troitsk Institute of Innovation and Fusion Research, State Scientific Center of the Russian Federation, Troitsk, Moscow oblast, 142190 Russia

Received June 18, 2002; in final form, September 25, 2002

Abstract—With the proper stabilization of a negative corona, it is possible to increase the threshold current at which the corona discharge in the point–plane gap in air transforms into a spark. Then, in the current range corresponding to the transition region between the corona discharge and the spark, a new type of discharge arises—an atmospheric-pressure diffuse glow discharge. The transformation of the negative corona into a glow discharge and then into a spark is accompanied by the rearrangement of the discharge structure. The experiments show that, as the corona current increases, the radial current profile at the anode shrinks and the glow diameter near the anode increases. The radial profiles of the current and the corona glow during the transition to a glow discharge are measured. The longitudinal structure of the corona is computed using a 1.5-dimensional model that, unlike the other available models, includes gas ionization in the drift region of the corona. The experimental data are used to determine the effective cross section of the current channel at the anode. The radial glow profile near the anode is calculated using the measured current profile and assuming that the field profile is parabolic. © *2003 MAIK "Nauka/Interperiodica".*

1. INTRODUCTION

Coronas at the points of conducting objects that are at a high electric potential are observed both in nature and in laboratory conditions. A diffuse corona can easily be produced experimentally between a needle and a grounded plate. Coronas in the point–plane geometry have been studied over more than hundred years [1].

A negative diffuse corona between a needle and a plane in air is usually axisymmetric. Hence, we can speak about its radial (transverse) and longitudinal structure. In this case, the current channel of the corona (i.e., the region with a negative charge) rapidly broadens with distance away from the point; as a result, the characteristic diameter of the corona turns out to be close to its longitudinal size, which is equal to the interelectrode distance d.

Obviously, the transverse and longitudinal structures of the corona, which is a self-organizing structure, evolve and influence each other as the current varies. The influence of the transverse structure on the longitudinal one can be illustrated by the following observations. For example, if the corona diameter is limited by the wall of a dielectric tube of radius $r \le d$ [2] or if the corona is surrounded by other neighboring coronas (located at distances of $r \le d$) [3], then the voltage across the point–plane gap increases.

At the same time, in a free corona, significant changes in its longitudinal structure, which occur because the space charge in the gap increases with current, affect its radial structure only slightly. This unexpected property of the negative corona, i.e., the fact that its transverse structure near the anode depends slightly on the current, was discovered as early as at the end of the 19th century. Thus in 1899, it was found by Warburg [4] that, for a negative corona in air, the current density at the anode falls monotonically from the center and the experimental results are well approximated by the expression

$$j(\vartheta) \simeq j_0 \cos^n \vartheta \equiv j_0 (1 + \tan^2 \vartheta)^{-n/2}. \qquad (1)$$

Here, j_0 is the current density at the center of the anode (this density increases in proportion to the corona current I) and ϑ is the angle that is counted from the symmetry axis of the corona and whose vertex resides on the needle's point: $\tan\vartheta = r/d$, where r is the running radius at the anode and d is the gap length.

In other words, the radial current-density profile far from the needle (at the anode) depends neither on the electric-field structure near the corona point nor on the corona current and is only a function of the running radius at the anode. The exponent n in Eq. (1) can be different in different experiments, but it is usually within the range $n \simeq 5 \pm 0.5$. Probably, the variations in n are due to the fact that the function $j(\vartheta)$ depends weakly on the shape of the needle's point, which generates the electron flow.

1063-780X/03/2902-0176$24.00

The radial current distributions at the anode, which were obtained in many two-dimensional and simplified analytical calculations (see [5–7] and the literature cited therein) performed without an allowance for the generation of electrons by ionization and detachment in the drift region, are very similar to the Warburg profile. Thus, the authors of [7] obtained the expression

$$j(\vartheta) \simeq j_0(1 + 2\tan^2\vartheta)^{-3/2}, \quad (2)$$

whereas in [5], the following analytical formula is given:

$$j(\vartheta) \simeq j_0(1 + 0.85\tan^2\vartheta)^{-3}, \quad (3)$$

which generalizes the experimental data obtained by the authors and is valid for small radii of the corona point ($r_c < 1$ mm).

With an accuracy acceptable for practical purposes, all three of the above expressions give the same effective cross section of the current channel of a point corona:

$$S_{\text{eff}} \simeq I/j_0 = \frac{\pi d^2}{j_0}\int j(\vartheta)d(\tan\vartheta)^2 \simeq (2 \pm 0.2)d^2. \quad (4)$$

It is expected that the corona diameter will be independent of the longitudinal structure only for discharge currents below a certain level. Indeed, both the space charge of the negative ions in the interelectrode gap and the reduced electric field in the gap, $E/N \sim \sqrt{I/(Nd)}$ (where N is the gas density), increase as the current I increases. The reduced electric field, which governs the processes of ionization and detachment, increases not only with increasing current, but also with decreasing gas density due to heating. As a result, the electrons generated in these processes will make a progressively larger (and, finally, a decisive) contribution to the total current.

Since the current density in the corona decreases away from the axis, the gas is heated most intensively near the discharge axis; consequently, the value of E/N is maximum there. For this reason, it is in the center of the anode region where the conditions are first produced such that E/N reaches its critical value, starting from which electrons are intensively generated in the gap. As a result, the current density at the discharge axis sharply increases.

This effect was first observed in 1992 by Goldman *et al.* [8] in experiments with a negative corona in quiescent air. In that paper, it was shown that the current density at the anode center begins to increase more rapidly than by a liner law, $j_0 \sim \exp(I/I^* - 1)$, if the corona current I exceeds a certain critical value I^* (in the experiments of [8], the critical current was rather low: $I^* \simeq 130$ μA). The authors of [8] explained the nonlinear growth in j_0 by a local increase in E/N due to gas heating in the axial region near the anode.

It is reasonable to assume that the nonlinear growth of the current density at the corona axis, observed in [8], is due to the change of the transverse structure of the discharge, which results in a decrease in the effective cross section of the corona channel at high currents. However, the question as to the possible modification of the radial profile $j(\vartheta)$ at currents $I > I^*$ was not discussed in [8]. We only may guess as to why this question has practically not been raised in the literature till now.

In a classical low-current corona, the gas ionization in the drift region is of minor importance for the maintenance of the current. This circumstance is even considered to be one of the characteristic attributes of corona. For this reason, there has long been settled an opinion in the literature [9, 10] that an increase in the local field near the anode to a level sufficient for perceptible ionization should inevitably lead to the transformation of the corona into a spark. In other words, the limiting current at which a spark is formed only slightly exceeds the critical current I^*. Most likely, the fact that the current range in which the spatial structure of the corona is modified is rather narrow, on the one hand, complicated the study of this phenomenon and, on the other hand, was a reason why this problem did not attracted practical interest.

At the same time, our experience [3] shows that, with a proper discharge stabilization, the ionization in the discharge gap does not guarantee a transition of the corona to a spark. Among the stabilization methods, we mention the use of ballast resistors with $R > 1$ MΩ, resistive electrodes, and air circulation through the discharge. For example, the gas flow eliminates the abovementioned influence of the heating on the local increase in the reduced electric field. As a result, it becomes possible to significantly improve the corona stability against the onset of ionization instabilities and, thereby, to increase the current at which a spark is formed in a point–plane gap. It also becomes possible to sustain a diffuse discharge at high electric fields in which gas ionization in the drift region already plays a significant role. This diffuse discharge is an atmospheric-pressure glow discharge.

The transformation of a multipoint corona into a glow discharge and the change in its longitudinal structure during this transformation were studied in detail in [3]. The present paper reports on the first experimental studies on the evolution of the transverse structure of a corona on a single needle in air over a wide current range, including the transformation of the corona into a glow discharge and then into a spark. The evolution of the radial current-density profile at the anode is investigated. It is examined how the glow diameter near the anode varies as the current increases. The measured radial current profile is used to calculate the radial structure of the corona glow during the transition to a glow discharge. The electric field at the axis is calcu-

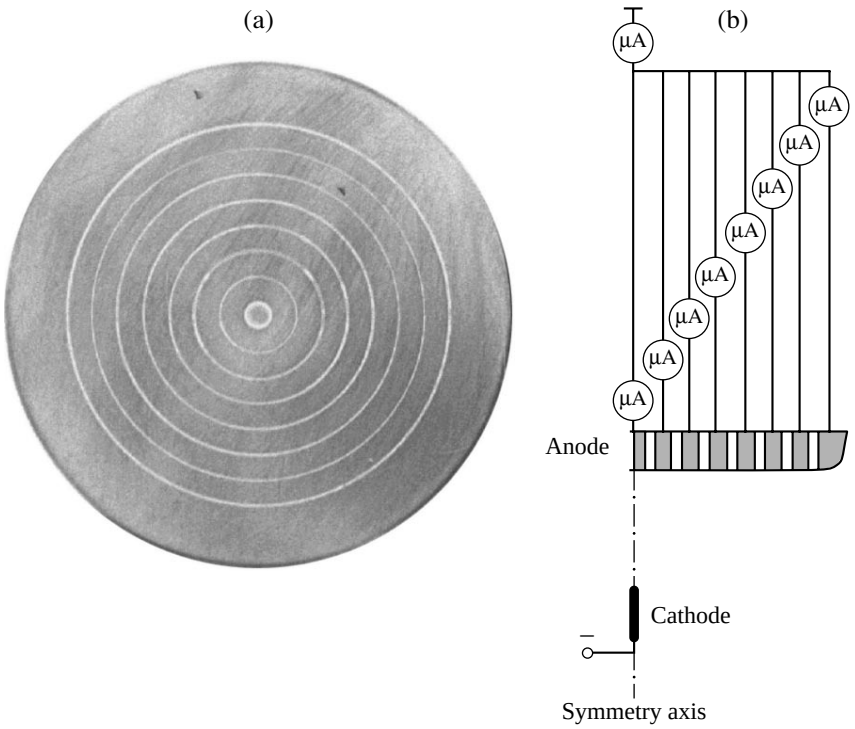

Fig. 1. (a) Photograph of the working surface of an anode consisting of nine sections (the diameter of the outer section is 65 mm) and (b) the electric circuit for measuring the current distribution over the anode sections in a steady-state corona.

lated in a 1.5-dimensional model with allowance for gas ionization in the corona drift region.

Note that, in this paper, we studied the evolution of the transverse structure of a negative corona only at a large distance from the needle (i.e., directly at the anode and near it). It is well known [1] that, in the near region of a negative corona in air, the glow structure is significantly modified at currents of $\simeq$120 μA, corresponding to the disappearance of regular current pulses (Trichel pulses). At the same time, according to the literature data and our experimental results, the change in the glow shape around the needle is not accompanied by a significant change in the radial current profile at the anode. That is why the most attention in our work is concentrated on the studies of the spatial structure of the corona far from the needle cathode.

2. MEASUREMENT OF THE RADIAL CURRENT PROFILE AT THE ANODE

In most of the available experimental papers, the radial current distribution is measured with a movable plane anode with a small hole, through which a wire probe ~1 mm in diameter, insulated from the anode by a thin-wall dielectric tube, is inserted. The end of the wire probe is flush with the anode surface. The anode with the probe is shifted in the transverse direction, and the probe current is measured at each successive position. In these experiments, the ratio between the areas of the current-collecting probe surface and the effective current-collecting anode surface is usually much less than 100. In this case, the measured probe currents are extremely low (especially at large distances from the discharge axis), which presents certain experimental difficulties and can cause significant measurement errors.

We used this method only to measure the current density j_0 at the anode center. In these experiments, we used a fixed plane anode 150 mm in diameter with a small hole at the center. A wire ~2.5 mm in diameter was inserted through a thin-wall dielectric tube. The effective area of the current-collecting probe surface was nearly 6.3 mm^2. The end of the wire probe was flush with the anode surface.

The radial current distribution $j(r)$ was measured with a plane sectioned large-diameter anode, which was assembled from narrow metal rings. The concentric rings were separated by even narrower gaps filled with a dielectric (Fig. 1). In the experiments, we measured the current trough each ring, as well as the total discharge current. The results of the measurements in each experiment were checked for the coincidence of the total discharge current with the sum of the currents through the rings.

The $j(r)$ profiles were measured in the steady-state and dynamic regimes. In the former regime, the currents from the anode sections were measured by a microammeter. In this regime, the radial current pro-

files were measured for two types of a steady-state discharge—the corona and the glow discharge. The dynamic regime was primarily used to study the fast process of the spark formation. In this regime, a voltage step was applied to the corona and several oscilloscopes simultaneously recorded the time behavior of the current through the rings until the discharge transformed into a spark. Thus, with a sectioned anode, all the information necessary for reconstructing the $j(r, t)$ distribution is gathered by applying a single voltage step. With the commonly used method of a movable anode described above, the $j(r, t)$ distribution would be reconstructed from the data obtained at different probe positions and, accordingly, by applying a large number of voltage steps. In this case, an inevitable scatter in the experimental data (which is caused, for instance, by the backlash errors of the mechanism moving the anode, by the scatter in the voltage step amplitudes, or by the drift of the initial state of the corona) would present severe problems for reconstructing the $j(r, t)$ distribution and would require fairly large time consumption.

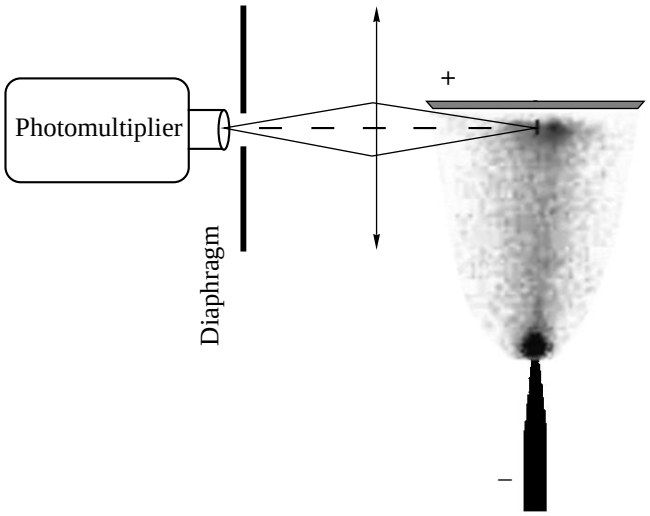

Fig. 2. Optical scheme for measuring the radial distribution of the corona glow and a photograph of a glow discharge in a point–plane gap.

3. MEASUREMENT OF THE RADIAL PROFILE OF THE CORONA GLOW

The current in the drift region of the corona can be carried by both negative ions and electrons; however, the emitting nitrogen and oxygen states are only excited by electron impact. For this reason, the transverse structure of the glow provides information about the radial distributions of the electron current and electric field in the corona. At the same time, because of the small electron component of the current in the far region of the corona, the glow intensity in the interelectrode gap (in particular, near the anode) is weak. In this situation, special measures should be undertaken in order to diminish the intensity of the background light. The radial glow profiles at different currents were measured only in a steady-state corona.

To measure the radial glow profile in the far region, we used an optical scheme with an FEU-144 photomultiplier (Fig. 2). The corona was imaged on a 1 : 1 scale onto the multiplier photocathode. In front of the cathode, a slit with a width of 0.1 mm and height of 1 mm was installed. The slit was oriented so that its long side was parallel to the discharge axis. The slit could be displaced in the radial direction with the help of a high-precision mechanism.

At each successive slit position, two photomultiplier signals were recorded—the dark-current signal (when a large opaque screen was placed between the photomultiplier and the corona) and the signal in the absence of a screen. The valid signal was the difference between these signals. The load (anode) resistance in the photomultiplier circuit was chosen such that its value guaranteed the liner photomultiplier regime at any amplitudes of the recorded signals. The measured radial glow profile was treated using the abelianization procedure.

4. DESCRIPTION OF THE 1.5-DIMENSIONAL MODEL

The commonly used two-dimensional (2D) models of the drift region of a corona [5] are fairly simplified and do not include the charge kinetics with the participation of electrons. The applicability domain of these models is limited to small currents at which the fields in the drift region are low and, thus, ionization and electron detachment only slightly affect the corona characteristics. Obviously, these simplified 2D models cannot be used to calculate the evolution of the corona during its transition to a glow discharge, in which ionization plays a decisive role.

In view of what was mentioned above, we developed a 1.5-dimensional (1.5D) model [11], in which all the corona parameters (the current density, space-charge density, electric field, etc.) are constant in all of the equipotential cross sections of the current channel and only depend on the x coordinate, directed along the symmetry axis of the discharge. In this case, the convex equipotential surfaces inside the current channel are substituted with planes that are perpendicular to the x-axis and whose effective area $S(x)$ is equal to the area of the corresponding convex surface. The 2D structure of the corona is taken into account by specifying the function $S(x)$ as an external parameter. The key problem is how to chose the shape of the current channel; this problem was discussed in detail in [3, 11].

In our case, the shape of the current channel is assumed to be a combination of two cones. At a distance X_m from the needle's point, the radius of the first channel increases from the cathode radius R_C to R_m. The radius of the second cone smoothly increases from R_m to R_A at the anode. Such a shape of the current channel

conforms with the discharge glow observed visually during the transition of the corona to a glow discharge. We note that, with this shape of the current channel, the calculated charged-particle densities and their spatial distributions near the cathode are closer to the results obtained by means of the three-dimensional (3D) model [12]. To model a corona with an interelectrode distance of d = 10.5 mm, we chose the following parameters of the corona channel: R_C = 0.06 mm, R_A = 11.6 mm, X_m = 0.1 mm, and R_m = 5.25 mm. With these parameters, the calculated current–voltage characteristic is closest to the measured one.

As was mentioned above, the particular details of the spatial structure near the corona point only slightly affect the structure of the negative corona in the far region. This means that possible inaccuracy in specifying $S(x)$ in the near region should not significantly influence the calculated average parameters of the corona in the far region.

The numerical model of a discharge in humid air is based on the well-known continuity equations for electrons and positive and negative ions; Poisson's equation; and the equation for the simplest electric circuit with parameters corresponding to the experiment:

$$\frac{\partial n_e}{\partial t} + \frac{1}{S}\frac{\partial}{\partial x}(Sn_e w_e) = (\nu_i - \nu_a)n_e + \nu_d n_n, \quad (5)$$

$$\frac{\partial n_p}{\partial t} + \frac{1}{S}\frac{\partial}{\partial x}(Sn_p w_p) = \nu_i n_e - \beta_i n_p n_n, \quad (6)$$

$$\frac{\partial n_n}{\partial t} + \frac{1}{S}\frac{\partial}{\partial x}(Sn_n w_n) = \nu_a n_e - \nu_d n_n - \beta_i n_p n_n, \quad (7)$$

$$\frac{1}{S}\frac{\partial}{\partial x}(SE) = -(n_p - n_e - n_n)\frac{e}{\varepsilon_0}, \quad (8)$$

where subscripts e, p, and n stand for electrons and positive and negative ions, respectively; n_e, n_p, and n_n are the densities of electrons and positive and negative ions; w_e, w_p, and w_n are their drift velocities; e is the electron charge; ε_0 is the permittivity of a vacuum; ν_i, ν_a, and ν_d are the ionization, attachment, and detachment frequencies; β_i is the ion–ion recombination coefficient; and $S(x)$ is the area of the discharge cross section, which is assumed to be a known function of the coordinate x. The presence of water vapor in air is taken into account by introducing an additional attachment frequency for three-body attachment to oxygen, where a water molecule is the third body (more detailed information on the kinetics of a cold plasma in atmospheric-pressure air can be found in [11]).

The current I in the external circuit was calculated from the equation

$$V = U_0 - RI, \quad (9)$$

where V is the voltage across the discharge gap, U_0 is the source voltage, and R is the ballast resistance (16.5 MΩ).

The boundary conditions for the positive and negative ions are evident: their densities are zero on the anode and cathode surfaces, respectively. For electrons, the model includes only secondary ion emission. The boundary conditions for electrons at the cathode (x = 0) are formulated using the coefficient of the ion-induced secondary electron emission γ:

$$j_e(0, t) = \gamma j_p(0, t), \quad (10)$$

where $j_e = n_e w_e$ and $j_p = n_p w_p$.

The set of Eqs. (1)–(4) was solved by an implicit difference scheme with a nonuniform spatial step (the spatial step was reduced approaching the cathode). A detailed description of this scheme is presented in [13]. Calculations were performed for the following conditions: P = 740 torr, T = 292 K, and a humidity of 30%.

5. RESULTS

5.1. Steady-State Regime

The results presented below were obtained in experiments with a steady-state discharge stabilized by air flow. In these experiments, we studied the evolution of the radial structure during the transition from the corona to a glow discharge as the current increased. The experimental parameters were chosen so as to avoid the spark regime.

Before presenting the results, we make an important comment. As was mentioned above, the gas flow allows us to substantially increase the current at which the corona discharge transforms into a spark. At the same time, the question arises as to how the gas flow affects the radial structure of the discharge. Our experiments show that, at flow velocities of up to several tens of meters per second, the gas flow directed along the discharge axis toward the anode surface stabilizes the corona against the transition to a spark, but it does not change its transverse structure. At higher velocities, close to 100 m/s, the transverse structure of the discharge is deformed by the flow. All of the results presented below were obtained at gas flow velocities no higher than 35 m/s.

A general idea of how the corona diameter varies with increasing current can be gained from data on the dependence of the current density at the anode center on the total current. According to expression (4), the ratio I/j_0 characterizes the effective cross section of the corona discharge at the anode. Figure 3 shows the dependence of the effective cross section of the current channel at the anode on the total current for different radii of the needle's point and different interelectrode distances.

The current range in which j_0 is proportional to I and the effective cross section of the discharge is indepen-

dent of the current corresponds to the true corona, which obeys the Warburg law. The nonlinear increase in j_0 with increasing I means that the current channel becomes narrower and the corona transforms into a glow discharge. It is seen that the current range corresponding to the corona discharge extends as the interelectrode distance increases or the radius of the needle's point decreases. For rather sharp points ($r_c <$ 0.5 mm), the area of the current channel is close to that predicted by the Warburg law: $S_{\text{eff}} \simeq (2 \pm 0.2)d^2$. For larger point radii, the current-channel area is somewhat smaller than $2d^2$; however, as d increases, the effective area of the current channel becomes closer to the Warburg area. In the experiments with large interelectrode distances d = 40 and 50 mm, the regime in which j_0 increases nonlinearly with I has not been achieved because of the limited voltage of the source used ($U \leq$ 60 kV).

The experiments with a sectioned anode allowed us to reveal some nontrivial features of the transition from the corona to a glow discharge. The behavior of the average current density in different sections as the total current is varied is of interest. Figure 4 shows how the currents in the central and peripheral (sixth) sections (i.e., the currents I_1 and I_6, which are proportional to the average current densities j_1 and j_6) depend on the total current I. In the true corona regime, the current densities in all of the anode sections increase linearly with current. It is clearly seen that the transition to a glow discharge first takes place in the central region of the anode, where the departure from the linear dependence occurs at a lower current as compared to the periphery. It is also seen that the transition is accompanied by the change in the current growth rates at the center and at the periphery of the corona. The current density at the center increases with current more rapidly than by a linear law (approximately, by an exponential law $j_0 \sim \exp(I/I^* - 1)$, as in [8] at currents $I \geq I^*$). In contrast, at the periphery of the anode, the current density j grows more slowly than by a linear law. This difference shows that the transition to a glow discharge is accompanied by a redistribution of the current over the anode in favor of its central part.

A complete picture of the $j(r)$ distribution was obtained by processing the current histograms over all the anode sections. First, we present the results for the steady-state corona regime. An example of the current histograms obtained for two discharge currents is shown in Fig. 5. The histograms show the average current densities in each anode section. From the measured histograms, we reconstructed the radial current profile $j(r)$ at the anode. The reconstruction procedure was as follows. For a known current at each ring, we constructed the dependence of $I_{\Sigma k}$ on R_k, where $I_{\Sigma k} = \sum_1^k I_k$,

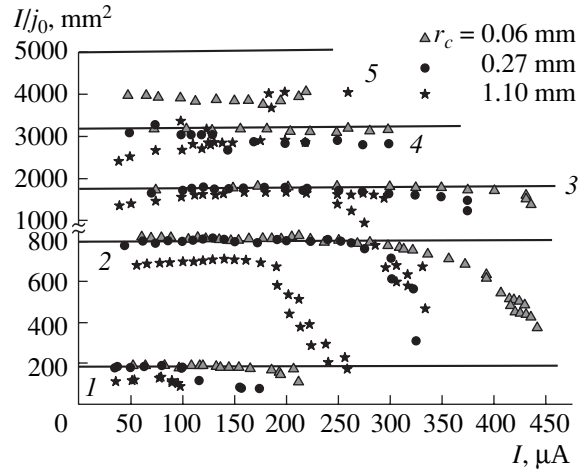

Fig. 3. Effective cross section of the current channel at the anode as a function of the total corona current at an air pressure of P = 745 torr for different radii of the cathode point and different interelectrode distances d = (*1*) 10, (*2*) 20, (*3*) 30, (*4*) 40, and (*5*) 50 mm. Solid horizontal lines correspond to $S_{\text{eff}} \simeq 2d^2$.

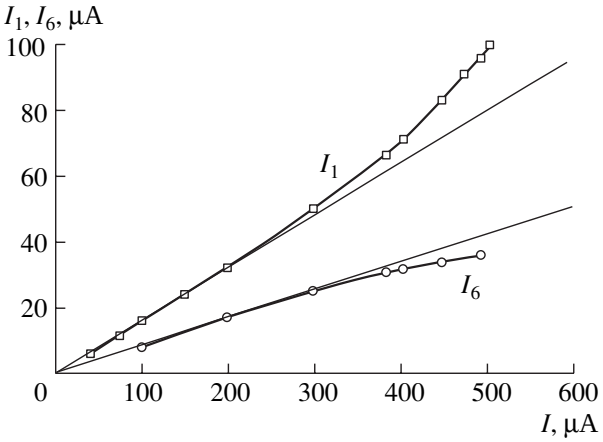

Fig. 4. Currents at the central and peripheral (sixth) anode sections as functions of the total corona current at an air pressure of P = 745 torr for the interelectrode distance d = 20 mm.

I_k is the current through the kth ring, and R_k is the outer radius of the kth ring. On the other hand, we have

$$I_{\Sigma k}(R_k) = 2\pi \int_0^{R_k} j(r) r dr = \pi d^2 \int_0^{\vartheta_k} j(\vartheta) d(\tan\vartheta)^2. \quad (11)$$

Hence, by specifying the class of function approximating $j(r)$ or $j(\vartheta)$, we can reconstruct the current profiles $j(r)$ or $j(\vartheta)$. In our case, we approximated $j(\vartheta)$ by a sum of two cosines in different powers and with different specific amplitudes:

$$j(\vartheta) = j_0(A_1 \cos^{n_1}\vartheta + A_2 \cos^{n_2}\vartheta), \quad A_1 + A_2 = 1, \quad (12)$$

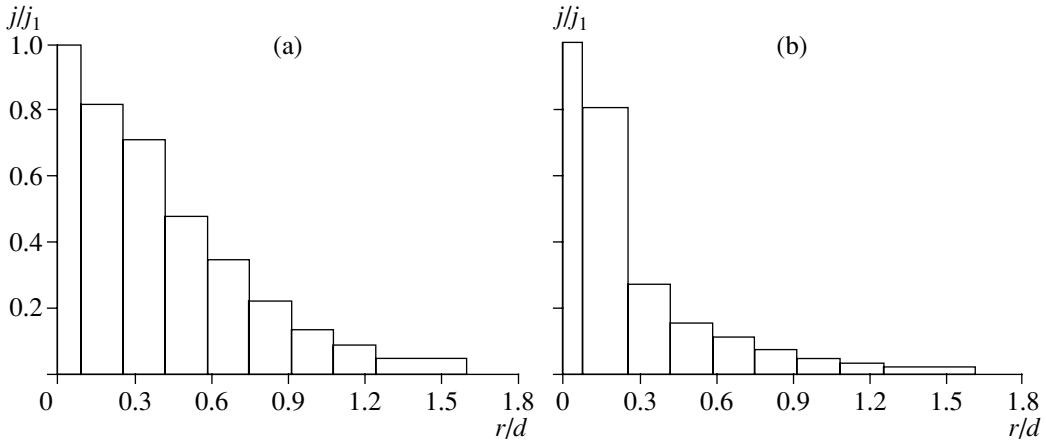

Fig. 5. Distributions of the average current density over the anode sections in the (a) corona (I = 50 μA) and (b) glow-discharge (I = 690 μA) regimes for d = 20 mm. The histograms are normalized to the average current density at the central section.

in which case $n_2 \gg n_1$ and the proportion between A_1 and A_2 changes in favor of A_2 as the current increases. At low currents, the first term corresponds to the Warburg distribution; the second term describes the peaking of $j(r)$ at the center at high currents. The parameters entering into Eq. (12) were fitted using the condition that the following sum calculated for all of the anode sections be minimum:

$$\sum_k \left(1 - \frac{j_{k\mathrm{Cal}}}{j_{k\mathrm{Exp}}}\right)^2, \qquad (13)$$

where $j_{k\mathrm{Cal}} = \dfrac{2\pi}{S_k}\int_{r_k}^{R_k} j(r) r dr$ is the calculated average current density at the kth ring of area $S_k = \pi(R_k^2 - r_k^2)$, r_k is the inner ring radius, and $j_{k\mathrm{Exp}}$ is the measured average current density at the kth ring.

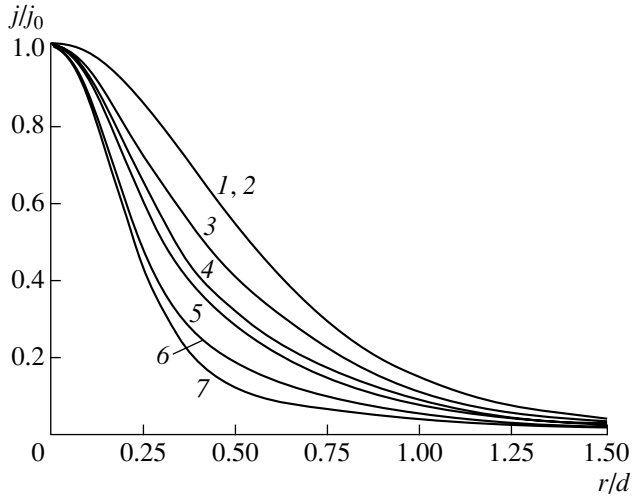

Fig. 6. Radial profiles of the normalized current density at the anode at an air pressure of P = 745 torr, d = 20 mm, and different total currents: I = (*1*) 50, (*2*) 150, (*3*) 300, (*4*) 450, (*5*) 500, (*6*) 590, and (*7*) 690 μA.

The results from the histogram processing are presented in Fig. 6, which shows how the radial profile of the current density at the anode (normalized to the current density at the discharge axis) varies with increasing total current. It can be seen that, at low corona currents, the radial profile is close to the Warburg distribution. However, starting from a certain current I^*, corresponding to the transition of the corona to a glow discharge, the current density falls more rapidly with distance away from the discharge axis. In other words, the current channel shrinks; the greater the excess of the discharge current over I^*, the narrower the channel.

The evolution of the radial glow structure with increasing current turned out to be rather surprising. The measured radial profiles of the corona glow (this is predominantly the emission of the second positive system of nitrogen) at different currents are shown in Fig. 7. When comparing the glow profiles with the current ones, we can see that the effective glow diameter is always smaller than the corona current diameter. In addition, these diameters vary differently with current: as the current increases at $I > I^*$, the effective diameter of the current channel decreases, whereas the glow diameter increases; as a result, the glow diameter in the glow-discharge regime becomes close to the current diameter.

The radial glow profile near the anode was calculated numerically. The glow intensity was assumed to be proportional to the product of the electron current density by the electron-impact excitation coefficient for the second positive system. The excitation coefficient depends exponentially on the reduced electric field. In this case, the radial glow profile is weakly sensitive to the radial electric-current distribution and is primarily determined by the radial electric-field profile. From this reason, we assumed that the radial profile of the electron current density coincided with the measured radial

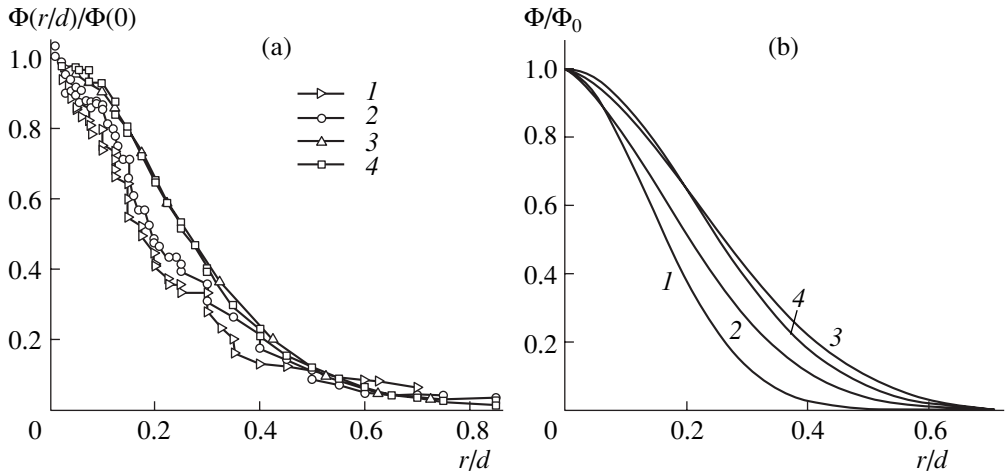

Fig. 7. (a) Unsmoothed and (b) smoothed measured radial glow profiles for d = 10 mm and different discharge currents: I = (*1*) 100, (*2*) 150, (*3*) 290, and (*4*) 320 μA.

profile of the total current density. The radial profile of the electric field was varied. The best fit to the experiment was obtained with the use of a parabolic (or cosine) approximation (see [5–7]):

$$E(r) = E(0)[1 - 0.5(r/d)^2] \quad \text{or} \quad E(\vartheta) \simeq E(0)\cos\vartheta. \quad (14)$$

The axial field $E(0)$ near the anode was calculated by the 1.5D model. An analysis of the results of the 1.5D calculations show that the axial field near the anode is described (with an accuracy no worse than 10%) by the simple expression $E(0) \simeq U/d$. Figure 8 compares the calculated radial glow profile with the measured one. A fair agreement between the calculated and measured profiles (which is primarily due to the correct calculation of the field on the axis) shows that the 1.5D model adequately describes the transition from the corona to a glow discharge in the point–plane geometry.

5.2. Dynamic Regime

The evolution of the transverse structure of the discharge until it transformed into a spark was studied in the dynamic regime of the current measurements at the anode sections. These experiments were performed without a gas flow stabilizing the corona. In this case, depending on the initial discharge voltage and the amplitude of the applied voltage step, we observed one of the two transitions: corona ⟶ corona or corona ⟶ glow discharge ⟶ spark. The transition to a steady-state glow discharge (i.e., the corona ⟶ glow discharge transition) was difficult to achieve, because a glow discharge in the absence of a gas flow was unstable and rapidly transformed into a spark.

Figure 9 shows a representative set of the current oscillograms from different anode sections. The oscillograms demonstrate the current behavior in different regions of the anode during the transitions corona ⟶ corona and corona ⟶ glow discharge ⟶ spark. A great number of such oscillograms obtained under different conditions were used to construct the current histograms over the anode sections and then to reconstruct the time evolution of the radial profile, $j(r, t)$, during the transition corona ⟶ glow discharge ⟶ spark.

At a small amplitude ΔU of the applied voltage step, the corona arrives at a new steady state that also corresponds to a corona discharge. Indeed, for the true corona, the current I (or the current density j at every point at the anode) is a parabolic function of the voltage U [1]: I (or j) ~ $U(U - U_0)$, where U_0 is the corona ignition voltage (under the conditions of Fig. 9, we have $U_0 \simeq 4.7$ kV). In this case, we can estimate the relative

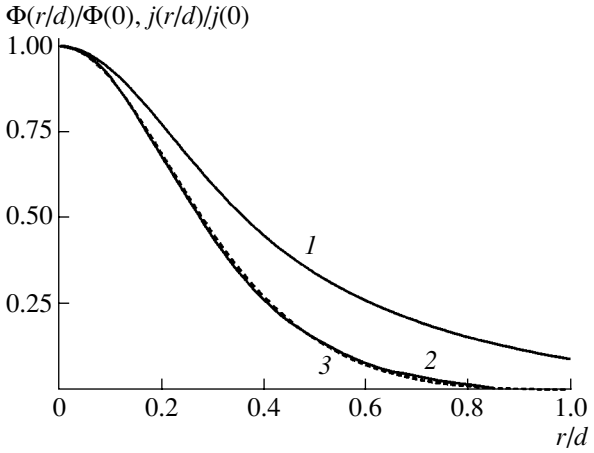

Fig. 8. Radial profiles of (*1*) the corona current and the (*2*) calculated and (*3*) measured corona glow in the far region at an air pressure of P = 745 torr, I = 320 μA, and d = 10 mm.

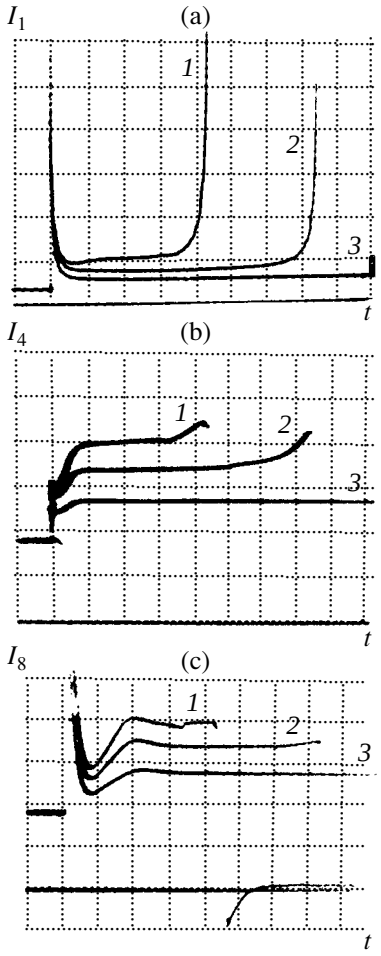

Fig. 9. Oscillograms demonstrating the time evolution of the current at the (a) central, (b) fourth, and (c) eighth anode sections during the transition corona ⟶ glow discharge ⟶ spark at an air pressure of P = 745 torr, d = 15 mm, I = 200 μA, and U = 23.6 kV for different values of the inducing voltage step: ΔU = (*1*) 4.3, (*2*) 6.8, and (*3*) 8.3 kV. The time scale is 100 μs/division for all the oscillograms; the current scale is (a) 11.2, (b) 22.4, and (c) 5.6 μA/division. The current spikes occurring immediately after applying the voltage step ΔU are associated with the transient processes in the measuring circuits and have no physical meaning.

increase in the initial corona current $\Delta I/I$ (or $\Delta j/j$) after applying the voltage step ΔU:

$$\frac{\Delta I}{I} \equiv \frac{\Delta j}{j} \simeq \frac{2U - U_0}{U - U_0}\frac{\Delta U}{U}. \qquad (15)$$

The processing of the oscillograms corresponding a steady-state discharge after applying a small-amplitude voltage step showed that the measured ratio $\Delta I/I$ for each section satisfied relationship (15). At the same time, at ΔU values at which a spark is produced, the measured ratio $\Delta I/I$ exceeds ratio (15); the higher the amplitude of the voltage step, the greater the measured ratio. This fact indicates that, at large ΔU values, the corona transforms into an unstable glow discharge, which then transforms into a spark.

We note (see Fig. 9) that this induced transition of the corona to a new steady (or quasi-steady) state occurs at different times in the axial and peripheral regions. Thus, under the conditions of Fig. 9, the new state in the axial region is reached in nearly 20 μs, which is close to the ion drift time through the interelectrode gap. At the periphery, the relaxation to a new state lasts no less than 200 μs. Therefore, the radial structure of the corona reaches its steady state in a period of time that is at least one order of magnitude longer than the ion drift time through the interelectrode gap.

In different anode regions, the time evolution of the unstable quasi-steady state corresponding to a glow discharge is also characterized by different times and has different consequences. The instability of an atmospheric-pressure glow discharge is explained by the fact that, under typical conditions required to maintain this discharge, the quasi-steady current–voltage characteristic of the anode sheath turns out to be falling; i.e., the anode sheath has a negative differential resistance and, consequently, is unstable against shrinking into a current spot with a high current density [3, 14]. Instability develops more slowly at the periphery. Up to the time when a current spike arises at the central section because of the spark generation on the discharge axis, the current at the periphery changes only slightly. The nearer the section to the discharge axis, the more pronounced the current growth. However, after the spark is formed at the central section, the current at the other sections falls off to zero, no matter how much amplitude it gained by this time. Hence, the spark terminates the discharge at all of the sections by intercepting the current from the entire anode surface, which indicates the shorting of the spark current through a small anode spot.

We can distinguish two stages in the transition of the glow discharge to a spark: the slow development of the glow-discharge instability, lasting several hundreds of microseconds, and the fast spark formation, lasting several tens of microseconds. These times are characteristic of corona gaps several centimeters in length. These times can decrease with increasing ΔU, but always remain close in order of magnitude to the above mentioned values. Note that the centimeter transverse size of a corona in combination with the characteristic growth time of the glow-discharge instability (approximately several hundreds of microseconds) gives a velocity on the order of several tens of meters per second. It is precisely these values of the flow velocity that ensure the stabilization of a glow discharge [3, 14].

In the dynamic regime, we observed a stronger shrinking of the current channel in comparison with a steady-state corona. In this case, the current flowing through the central section can exceed the total current flowing through all the other sections. For this reason,

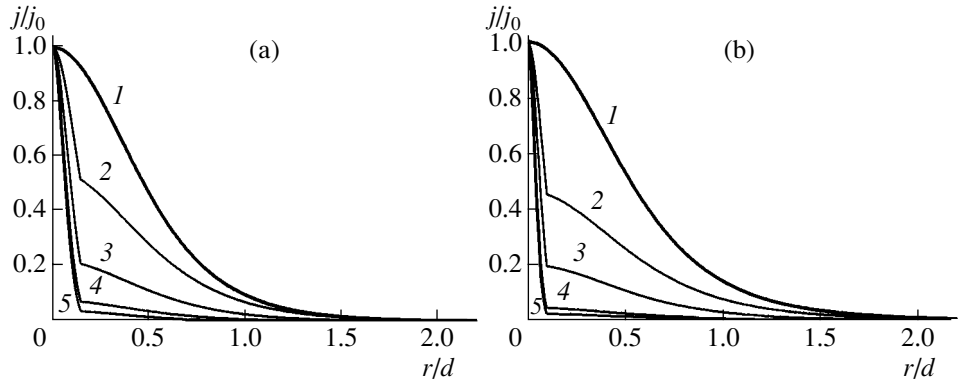

Fig. 10. Radial profiles of the normalized current density at the anode during the induced transition corona ⟶ glow discharge ⟶ spark at an air pressure of P = 745 torr for (a) d = 10 mm, U = 16 kV, I = 225 μA, and ΔU = 6 kV (*1*) in the initial state and (*2*) 50, (*3*) 150, (*4*) 180, and (*5*) 190 μs after the voltage step is applied and for (b) d = 15 mm, U = 27 kV, I = 250 μA, and ΔU = 7 kV (*1*) in the initial state and (*2*) 40, (*3*) 120, (*4*) 150, and (*5*) 160 μs after the voltage step is applied.

the current histograms of the dynamic regime were processed by a procedure different than that used for the steady-state regime. The current-density distribution at the central section was approximated separately from the other sections by the formula: $j(\vartheta)/j_0 = \cos^n\vartheta$. For the other sections, we assumed that $j(\vartheta)/j_0 = a\cos^{n_1}\vartheta$, where n_1 and a were chosen such that the current-density distribution was joined to the distribution in the central section. The fitted normalized radial current profiles are presented in Fig. 10. The point of inflection, where the distribution in the central section is jointed to that in the other sections, is only a mathematical (rather than physical) effect. It is clearly seen that, when a voltage step is applied, the current channel shrinks, which corresponds to the transition corona ⟶ glow discharge ⟶ spark. Since the diameter of the spark channel is smaller than that of the central section, it is hardly possible to extract information about the radial current profile in the spark from these experiments.

6. CONCLUSIONS

(i) In point–plane geometry, the radial current profile at the anode is observed to be independent of the total current (the Warburg profile) only in the true corona regime. As the current increases, the corona transforms into a glow discharge. During this transition, the diameter of the current channel decreases.

(ii) The transition from the corona to a glow discharge is accompanied by an increase in the glow intensity in the discharge gap, first of all, in the far region (i.e., near the anode). At all currents, the radial glow profile is narrower than the current profile; however, as the current increases, the glow profile broadens and its diameter becomes closer to the current-channel diameter.

(iii) In the absence of gas circulation, the glow discharge is unstable and transforms into a spark. The characteristic times of the processes occurring in the unstable anode region of a glow discharge are different at different distances from the discharge axis. Instability develops most rapidly at the center of the anode, where a spark is then formed.

(iv) When the voltage across the gap is rapidly changed, the relaxation times of the corona to a new state are different in the center and at the periphery. The radial profile of the corona relaxes to a steady state over a period of time significantly exceeding the ion drift time across the discharge gap.

(v) The observed sequential transition of the corona to a spark through a glow discharge is rather universal and takes place also under ordinary experimental conditions when the applied voltage increases slowly. Therefore, the elaboration of practical recommendations concerning the corona stabilization against its transformation into a spark is impossible without considering the intermediate stage, i.e., the glow discharge.

ACKNOWLEDGMENTS

We thank G.I. Aponin for his assistance in the experiments. This work was supported in part by the Russian Foundation for Basic Research, project no. 02-02-16913.

REFERENCES

1. L. B. Loeb, *Electrical Coronas* (Univ. of California Press, Berkeley–Los Angeles, 1965).
2. Yu. S. Akishev, M. E. Grushin, A. P. Napartovich, *et al.*, in *Proceedings of the 12th International Conference on Gas Discharges and Their Applications, Greifswald, 1997*, Vol. 1, p. 153.
3. Yu. S. Akishev, M. E. Grushin, I. V. Kochetov, *et al.*, Fiz. Plazmy **26**, 172 (2000) [Plasma Phys. Rep. **26**, 157 (2000)].

4. E. Warburg, Wied. Ann. **67**, 69 (1899); *Charakteristik des Spitzenstormes*, *Handbuch der Physik* (Springer-Verlag, Berlin, 1927), Bd. 4, S. 154.
5. I. P. Vereshchagin, *Corona Discharge in Electronic and Ionic Technologies* (Énergoatomizdat, Moscow, 1985).
6. J. E. Jones, M. Davies, A. Goldman, and M. Goldman, J. Phys. D **23**, 542 (1990).
7. R. S. Sigmond, J. Appl. Phys. **53**, 891 (1982).
8. A. Goldman, M. Goldman, and J. E. Jones, in *Proceedings of the 10th International Conference on Gas Discharges and Their Applications, Swansea, 1992*, p. 270.
9. N. A. Kaptsov, *Corona Discharge* (Gostekhizdat, Moscow, 1947).
10. Y. Kondo and Y. Miyoshi, Jpn. J. Appl. Phys. **17**, 643 (1978).
11. A. P. Napartovich, Yu. S. Akishev, A. A. Deryugin, *et al.*, J. Phys. D **30**, 2726 (1997).
12. Yu. S. Akishev, A. A. Deryugin, I. V. Kochetov, *et al.*, in *Proceedings of the International Symposium on High-Pressure Low-Temperature Plasma Chemistry (Hakone V), Milovy, 1996*, p. 122.
13. Yu. S. Akishev, N. N. Elkin, and A. P. Napartovich, Fiz. Plazmy **12**, 1225 (1986) [Sov. J. Plasma Phys. **12**, 706 (1986)].
14. Yu. Akishev, O. Goossens, T. Callebaut, *et al.*, J. Phys. D **34**, 2875 (2001).

Translated by N.F. Larionova

Plasma Physics Reports, Vol. 29, No. 2, 2003, pp. 97–104. Translated from Fizika Plazmy, Vol. 29, No. 2, 2003, pp. 115–123.

TOKAMAKS

Dependence of the Energy Confinement in the L- and H-modes on the Tokamak Aspect Ratio

V. M. Leonov and A. N. Chudnovskiy

Nuclear Fusion Institute, Russian Research Centre Kurchatov Institute, pl. Kurchatova 1, Moscow, 123182 Russia

Received June 26, 2002

Abstract—In the most advanced tokamak experiments, the H-mode discharges are characterized by an energy confinement time that is higher than in the L-mode by a factor of 1.5–2. For this reason, the H-mode is usually chosen as one of the basic regimes of a tokamak reactor and the presence of internal transport barriers is sometimes assumed as an additional condition. Most present-day tokamaks, which provide the main experimental information, have aspect ratios of 2.6–3.5. In this paper, attention is given to the fact that the enhancement factor (the ratio between the energy confinement times in the H- and L-modes) decreases as the tokamak aspect ratio increases. At aspect ratios ≥5, the confinement times in the L- and H-modes become equal. This result follows from a comparison of the H- and L-mode confinement scalings and is confirmed by experiments in the T-10 tokamak, which has an aspect ratio of 5, and by the results from the international confinement databases. The dependence of the enhancement factor on the aspect ratio can be important for designing steady-state fusion reactors, which are usually characterized by a rather high aspect ratio of 4–8. The possibility of using L-mode discharges with the same confinement time as in the H-mode, but with a lower peripheral temperature and in the absence of edge localized modes (ELMs), can substantially facilitate the operation of the divertor—one of the most stressed construction element of the tokamak reactor. In addition, the L-mode regime does not require overcoming the power threshold for the L–H transition; this circumstance is favorable for extending the range of the working parameters and heating scenarios. The absence of the accumulation of impurities and helium in L-mode discharges may also be important. All of these factors allow one to consider the L-mode as a possible operating regime for high-aspect-ratio tokamak reactors. © *2003 MAIK "Nauka/Interperiodica".*

1. INTRODUCTION

Most projects of the steady-state fusion reactors with superconducting toroidal magnetic coils are based on devices with aspect ratios as high as $A = R/a \sim 4$–5 [1–5] (in some projects, the aspect ratio is assumed to be even higher [6, 7]). This is dictated by the necessity of mounting a rather thick neutron protection and blanket components inside the toroidal coils and also by the desire to increase the bootstrap current, whose fraction at a fixed value of β_T (close to the limiting value) increases with aspect ratio.

Regimes with improved (as compared to the L-mode) plasma confinement, similar to that obtained in the largest present-day devices [8]) are usually considered to be basic for tokamak reactors. Most of the large tokamaks (such as JET, DIII-D, JT-60U, ASDEX-U, and TORE-SUPRA), which provide the main experimental information, have aspect ratios of 2.6–3.5. Hence, in order to well justify the concepts of steady-state tokamak reactors, it is necessary to obtain an additional experimental confirmation of the possibility of achieving improved confinement regimes at a high aspect ratio and to carry out a more detailed study of their properties.

There are few experiments in tokamaks with an increased aspect ratio. Among those are experiments carried out with a reduced minor radius of the plasma column. One of the devices with the constructive high aspect ratio is the T-10 tokamak (the major radius is $R = 1.5$ m, and the minor radius is $a \approx 0.3$ m). For this reason, the T-10 experiments are important for studying different operating conditions in high-aspect-ratio tokamaks.

The aim of this paper is to compare plasma confinement in the L- and H-modes and to discuss the prospects for using these operating regimes at aspect ratios higher than 4. In the second section, we analyze the results obtained in T-10 and compare them with the results obtained in other tokamaks with moderate aspect ratios ($A \sim 3$). In the third section, the predictions of confinement scalings for the L- and H-modes in high-aspect-ratio tokamaks are compared. In the fourth section, the energy confinement in the L- and H-modes at different aspect ratios is compared using the international tokamak databases. The main findings of the paper are presented in the conclusion.

2. ENERGY CONFINEMENT IN THE L- AND H-MODES IN THE T-10 TOKAMAK

Several years ago, improved confinement regimes with the characteristic features of the H-mode were obtained during ECR plasma heating in the T-10 tokamak [9, 10]. In these regimes, after switching on the

1063-780X/03/2902-0097$24.00

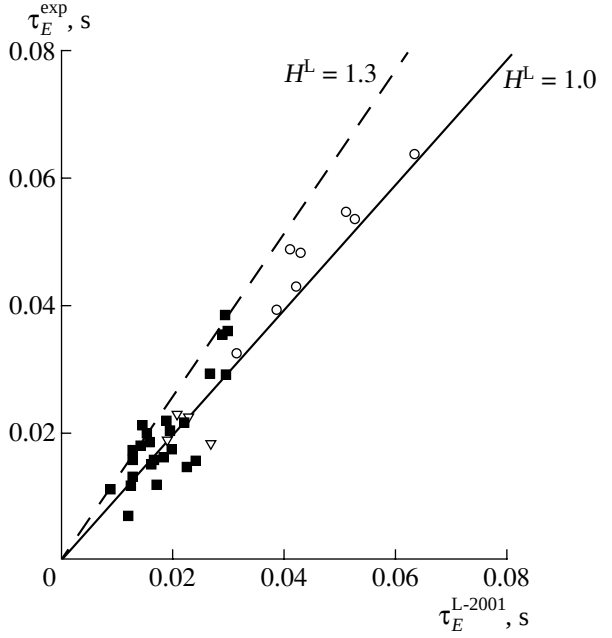

Fig. 1. Comparison of the experimental energy confinement time for different T-10 discharges with L-mode scaling (2) [11]: closed squares correspond to L-mode discharges from the L-mode database, triangles correspond to H-mode discharges from the H-mode database, and open circles correspond to H-mode discharges after the deuterium pellet injection.

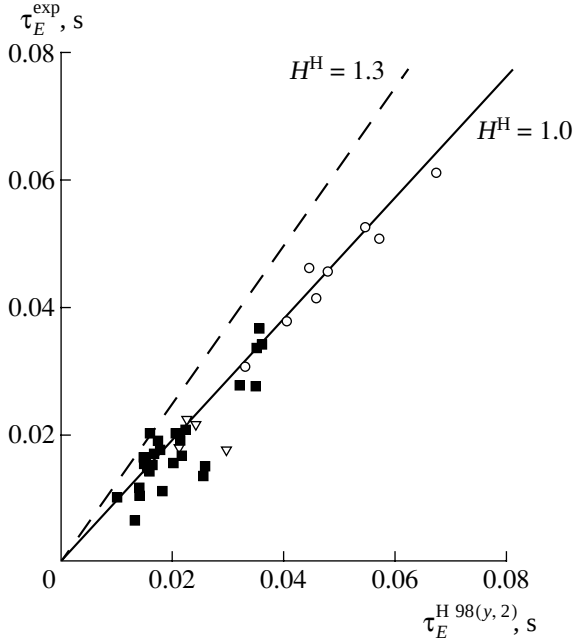

Fig. 2. Comparison of the experimental energy confinement time for different T-10 discharges with H-mode scaling (1) [16]: closed squares correspond to L-mode discharges from the L-mode database, triangles correspond to H-mode discharges from the H-mode database, and open circles correspond to H-mode discharges after the deuterium pellet injection.

auxiliary heating, a sudden decrease in the intensity of the hydrogen D_α spectral line was observed. This decrease was accompanied by an increase in the plasma density and energy. However, a similar increase in the plasma energy with increasing plasma density was also observed previously in L-mode discharges, in which the plasma density was increased by additional gas puffing. The energy confinement times in the L- and H-modes turned out to be close to each other at the same plasma densities [9]. Hence, there was no reason to tell about the improvement of the confinement in the H-mode in comparison with the L-mode at the same plasma density. The H-mode was really compared with the initial low-density L-mode stage, and it is this low-density stage with respect to which the improvement of confinement was found [9].

The characteristic features of the plasma confinement in the L- and H-modes in the T-10 tokamak are shown in Figs. 1 and 2. Figure 1 compares the experimental energy confinement time for both the L- and H-modes of the T-10 tokamak with the predictions of the L-mode scaling [11]. A comparison with the commonly used ITER-89P [12] and ITERL-96P [13] scalings gives similar results. For an analysis, we used 25 L-mode discharges of T-10 from the international L-mode database [13], four discharges from the international H-mode database [14], and H-mode discharges occurring after the injection of a deuterium pellet [15]. In Figs. 1–4 closed squares correspond to T-10 L-mode discharges, triangles correspond to T-10 H-mode discharges from the international H-mode database, and open circles correspond to T-10 H-mode discharges with the injection of a deuterium pellet.

It can be seen in the figure that, in spite of scatter in the data, both the L- and H-mode points lie about the same straight line, which corresponds to the L-mode scaling. This figure demonstrates that there is no improvement of the confinement in T-10 H-mode discharges with respect to L-mode discharges.

Fig. 2 (which, at first glance, is very similar to Fig. 1) presents an even more surprising result. In Fig. 2, the same T-10 experimental points are compared with the H-mode scaling [16]. It is interesting that all of the points that satisfactorily agree with the L-mode scaling agree with the H-mode scaling as well. It turns out that, for T-10, not only the H-mode points agree with the improved-confinement scaling, but also the L-mode points are described well by this scaling. There are individual L-mode points for which the experimental energy confinement time exceeds the prediction of the H-mode scaling, although the excess is within experimental scatter. This is rather unexpected, because it is implied that the H-mode scaling for most of the tokamaks should give a confinement time that is higher than that predicted by the L-mode scaling by a factor of 1.5–2.

There is a question as to whether this result is a specific feature of the T-10 tokamak only or if it is also typ-

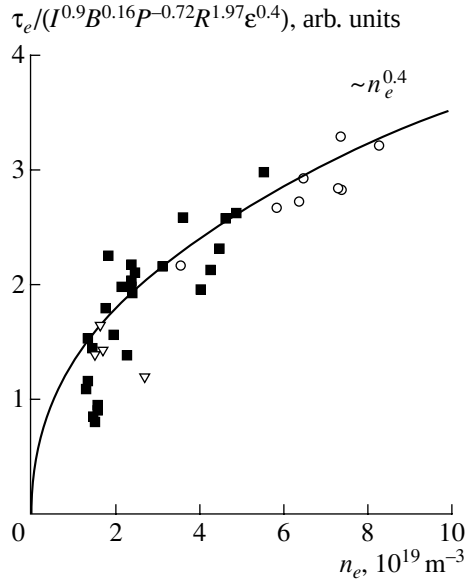

Fig. 3. Normalized experimental energy confinement time in T-10 L- and H-mode discharges as a function of the line-averaged plasma density.

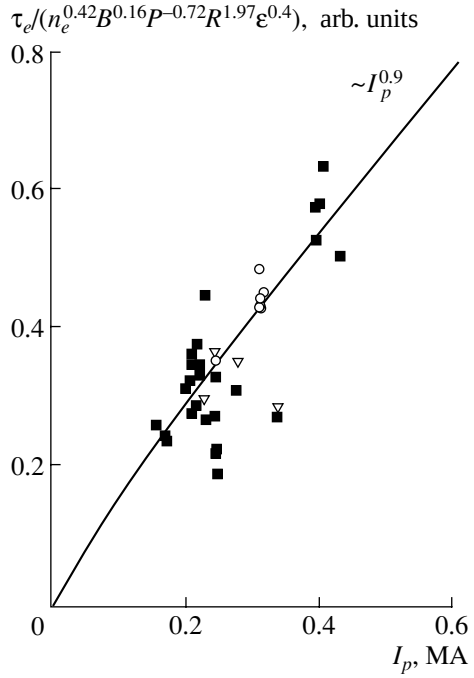

Fig. 4. Normalized experimental energy confinement time in T-10 L- and H-mode discharges as a function of the discharge current.

ical of other tokamaks. Indeed, it was stated in [17, 18] that the dependences of certain discharge parameters in T-10 differ from the dependences obtained in other tokamaks. In particular, the dependence of the energy confinement time τ_E on the average plasma density is stronger than for most of other devices and is close to linear, and the dependence of τ_E on the discharge current is very weak, whereas this dependence is almost linear for other tokamaks.

However, the fact that all of the points under examination for different T-10 regimes agree well with the scaling predictions shows that, possibly, the difference between these dependences in T-10 and the dependences given by the scalings is not as significant as has been stated in previous T-10 papers. An analysis of the parametric dependences for the set of discharges under consideration shows that, in this case, the T-10 results do not contradict the results from other tokamaks.

Figures 3 and 4 show the dependences of the experimental energy confinement time on the plasma density and discharge current for the set of T-10 discharges under consideration. To separate out the dependences on the individual parameters, the energy confinement time was normalized to the dependences on the other parameters adopted in scalings. To present both the L- and H-mode data on the same plot, they were normalized using the average exponents for the L- and H-mode scalings, taking into account that the corresponding exponents differ only slightly in these scalings.

It can be seen in Fig. 3 that the dependence on the plasma density, separated out from other dependences by the normalization, does not contradict the scaling $\tau_E \sim n^{0.4}$ within experimental scatter. Apparently, the previous conclusion about a stronger dependence can be related to both the narrow density range ($(1.5–3.5) \times 10^{19}$ m^{-3}) in the early T-10 experiments [17] and the influence of variations in the other parameters (current, toroidal field, etc.) [18]. The dependence on the current might be confused with the dependence on the density because high densities are usually achieved at high currents. We note that, in some of the previous T-10 papers, the deviation from the linear dependence of the confinement time on the density was reported [17].

The dependence of the normalized confinement time on the discharge current (see Fig. 4) for the set of T-10 discharges under consideration also does not contradict the scalings and is close to linear. Hence, we can see that the set of T-10 experimental data under consideration does not contradict the scalings and, consequently, agrees with the results obtained in other tokamaks.

Therefore, two questions still remain unanswered. First, what are the specific features of the T-10 experiments that ensure the coincidence of the experimental confinement times in the L- and H-modes? And second, why the plasma confinement in T-10 is equally well described by both the L- and H-mode scalings (or, in other words, why these scalings do not show any difference in confinement under the T-10 conditions)?

An analysis presented in the subsequent sections shows that a characteristic T-10 feature responsible for the above coincidence is the high aspect ratio, $R/a = 5$. We note that the results achieved at high aspect ratios in other tokamaks agree well with the T-10 results.

3. ASPECT-RATIO DEPENDENCE IN THE ENERGY CONFINEMENT SCALINGS

Extensive experimental databases from various tokamaks have been assembled for the ITER project. The empirical similarity laws (scalings) were developed based on thoroughly selected results from these databases. These scalings provide a brief description of the accumulated data and predict the plasma parameters in future devices. Let us analyze the difference in the aspect-ratio dependences of the confinement time in the H- and L-modes by comparing the corresponding scalings.

The energy confinement time in H-mode discharges is usually described by the ITERH-98P(y, 2) scaling [16], which is accepted as a reference scaling for the ITER design [14]:

$$\tau_E^{\mathrm{H\ 98}(y,\,2)} = 0.0562 I^{0.93} B_T^{0.15} n^{0.41} P^{-0.69} R^{1.97} \varepsilon^{0.58} k^{0.78} M^{0.19}. \quad (1)$$

To describe the L-mode confinement, we will use a scaling proposed in [11]:

$$\tau_E^{\mathrm{L\text{-}2001}} = 0.026 I^{0.81} B_T^{0.17} n^{0.43} P^{-0.75} R^{1.96} \varepsilon^{0.30} k^{0.86} M^{0.20}. \quad (2)$$

In scalings (1) and (2), the following notation is used: τ_E [s] is the thermal energy confinement time, I [MA] is the plasma current, B_T [T] is the toroidal magnetic field, n [10^{19} m^{-3}] is the line-averaged electron density, P [MW] is the heating power, R [m] is the major radius of the torus, $\varepsilon = a/R$ is the inverse aspect ratio, $k = V/(2\pi^2 R a^2)$ is the elongation of the plasma column (defined through the plasma volume V), and M [amu] is the effective ion mass.

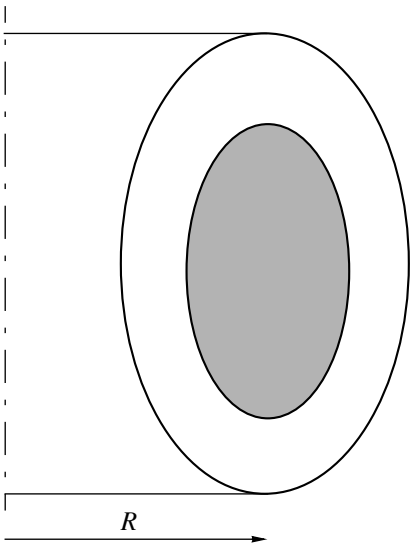

Fig. 5. Cross section of the plasma column in a tokamak.

For comparison with H-mode scaling (1), L-mode scaling (2) seems to be more convenient than the commonly used scalings of [12, 13], because a different definition of the elongation, $k = b/a$, is used in the latter scalings than in H-mode scaling (1). Note that the aspect ratio dependence in the scaling of [13] is the same as for scaling (2) (i.e., the energy confinement time is proportional to $\sim\varepsilon^{0.3}$), whereas in the scaling of [12], this dependence is given as $\sim\varepsilon^{-0.06}$, which differs even more strongly from the corresponding dependence in H-mode scaling (1). Consequently, a comparison of H-mode scaling (1) with the L-mode scalings of [12, 13] would give a similar result as the comparison with scaling (2) presented below.

Most of the exponents in scalings (1) and (2) differ slightly from each other, whereas there is a marked difference in the exponent of the inverse aspect ratio ε, which is clearly seen in the ratio between scalings (1) and (2):

$$\tau_E^{\mathrm{H}}/\tau_E^{\mathrm{L}} = 2.16 I^{0.12} B_T^{-0.02} n^{-0.02} P^{0.06} R^{0.01} \varepsilon^{0.28} k^{-0.08} M^{-0.01}. \quad (3)$$

This ratio shows the dependence of the enhancement factor of the H-mode over the L-mode on the discharge parameters. It can be seen from this expression that the exponents of most of the parameters are low, except for the exponent of the inverse aspect ratio ε. Taking into account a possible uncertainty in the exponent values ($\leq \pm 0.1$ [13, 19]), we see that only the exponent of ε exceeds this uncertainty range and the exponent of the plasma current lies near the boundary of this range. The elongation k with its exponent of –0.08 contributes insignificantly to expression (3) because k differs only slightly from unity. Hence, the energy confinement time in the H-mode can be expressed through the confinement time in the L-mode by the simplified formula

$$\tau_E^{\mathrm{H}} \approx 2.16 I^{0.12} \varepsilon^{0.28} \tau_E^{\mathrm{L}}. \quad (4)$$

This relatively simple formula shows that the difference in the confinement times in the H- and L-modes is primarily determined by the dependence on the aspect ratio and, to a lesser extent, by the dependence on the plasma current.

For T-10 with $\varepsilon = 0.2$ and a current of $I_p \approx 0.2$ MA, we obtain

$$\tau_E^{\mathrm{H}} \approx 2.16 \times 0.2^{0.4} \tau_E^{\mathrm{L}} \approx \tau_E^{\mathrm{L}}. \quad (5)$$

Thus, the fact that the confinement times in the L- and H-modes in the T-10 experiments are close to each

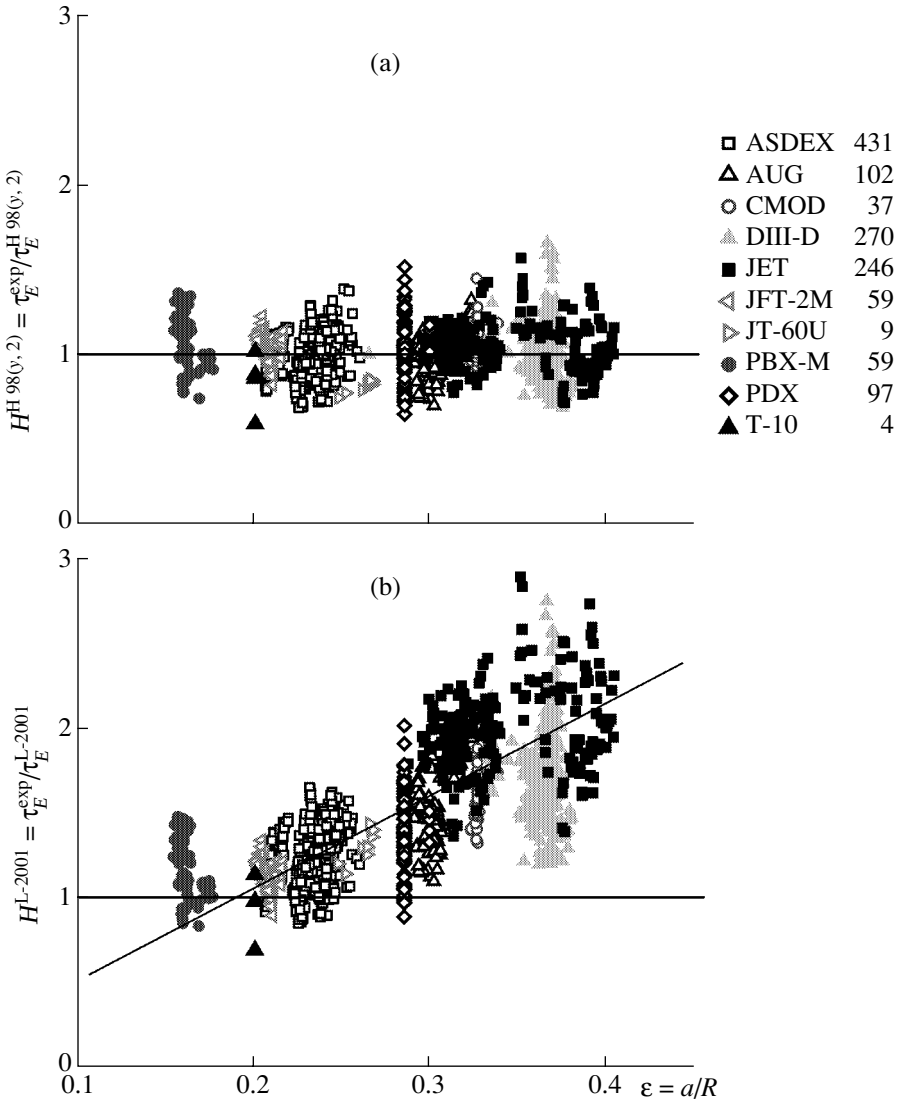

Fig. 6. Enhancement factors of the experimental energy confinement time over the predictions of the (a) H- and (b) L-mode scalings as functions of the inverse aspect ratio (results from the international H-mode database). Numbers in the right column show the number of discharges from each tokamak in the set of data under consideration.

other (Figs. 1, 2) is consistent with scalings deduced by analyzing data from various tokamaks. The above coincidence of the confinement times in T-10 can be explained by the specific parameters of this device (in particular, by the high aspect ratio and the low current) and does not contradict the results from other devices.

We note that the formal application of expression (4) at high aspect ratios (>5) even shows an excess in the confinement time for the L-mode over the H-mode. This may be explained by the extrapolation beyond the range of the experimental conditions that were used when developing the above scalings. This points to the necessity of refining the scalings at high aspect ratios. To do this, additional experiments should be carried out.

Let us consider the local value of $\varepsilon = r/R$ instead of the ε value characterizing the plasma column as a whole. In this case, for an individual tokamak with a constant R, the increase in the enhancement factor due to the increase in ε is a consequence of the fact that the energy confinement time in the H-mode increases more rapidly toward the plasma edge as compared to the L-mode. This circumstance can be illustrated by the following considerations. If one calculates the energy confinement time for the core plasma with $\varepsilon < 0.2$ (the shaded region in Fig. 5) by using the L- and H-mode scalings, these times will be close to each other. As the calculation region is extended toward the plasma boundary, the H-mode confinement time will exceed the L-mode confinement time, because both ε and the current increase when the outer regions are added. This

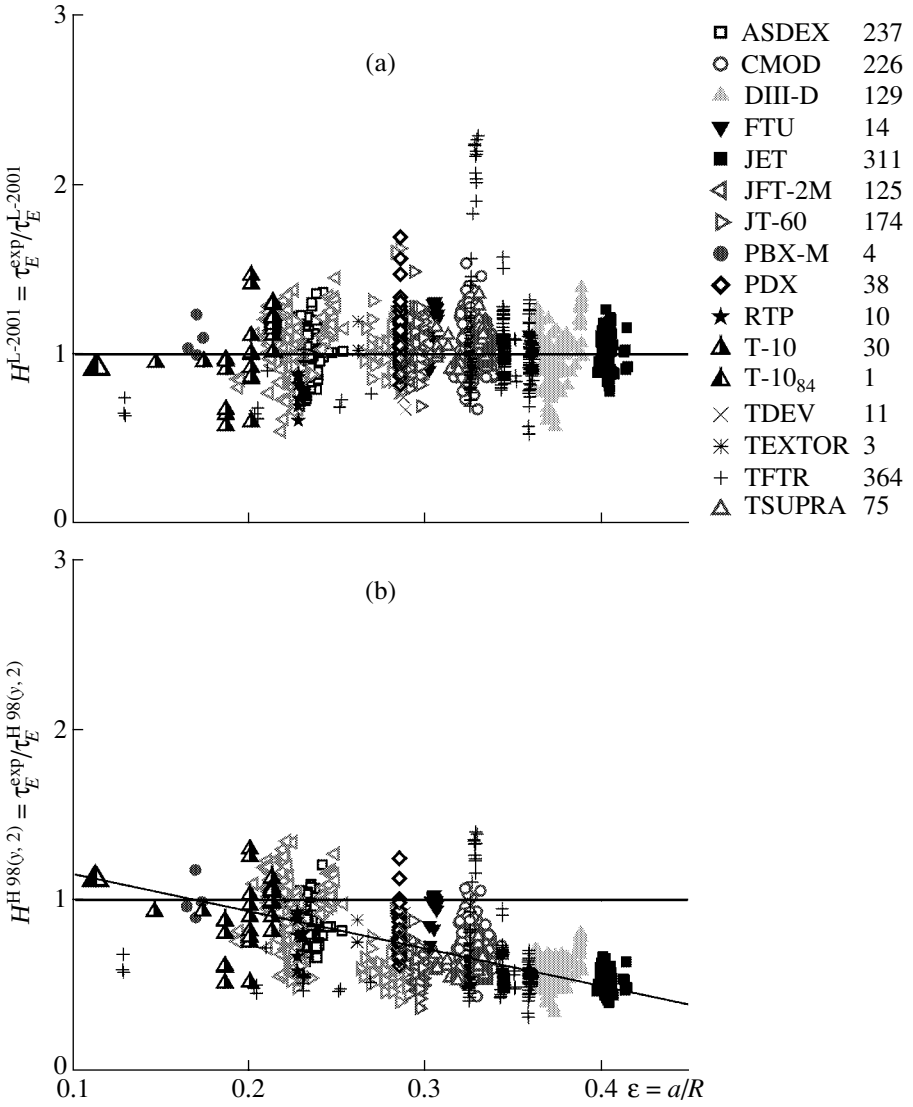

Fig. 7. Enhancement factors of the experimental energy confinement time over the predictions of the (a) L- and (b) H-mode scalings as functions of the inverse aspect ratio (results from the international L-mode database and the data from a T-10 discharge obtained in 1984). Numbers in the right column show the number of discharges from each tokamak in the set of data under consideration.

excess will be maximum at the plasma boundary, where ε is maximum.

Hence, the scaling analysis indicates that the H-mode in most of the tokamak experiments is primarily formed due to the improvement of confinement at the plasma periphery, rather than in the plasma column as a whole, as is sometimes stated.

On the other hand, from the standpoint of the construction of larger devices and tokamak reactors, it is important that the effects discussed above are associated with the more rapid improvement of the confinement in the L-mode than in the H-mode when the major radius is increased at a fixed minor radius. Ultimately, this leads to a situation in which the confinement in the L-mode becomes as good as in the H-mode. For this reason, the possibility of using L-mode discharges with the same confinement time as in the H-mode, but with a lower temperature at the plasma periphery, with a smaller accumulation of impurities and helium, without a need to overcome the power threshold for the L–H transition, and in the absence of ELMs seems to be very attractive when designing future tokamak reactors.

The conclusion that the L-mode confinement approaches the H-mode confinement as the aspect ratio increases has been made by comparing the scalings that generalize and average the experimental data from many tokamaks. However, it is also interesting to examine the whole set of experimental points in order to determine what amount of the points support this

dependence and to find out whether these results can be reliably distinguished against experimental scatter.

4. ASPECT-RATIO DEPENDENCE OF THE CONFINEMENT TIME FROM INTERNATIONAL DATABASES

In this section, we consider the dependence of the ratio between the experimental and scaling energy confinement times on the inverse aspect ratio using the results from the international L- and H-mode databases.

Figure 6 shows the ratio of the experimental H-mode confinement time to the scaling confinement time as a function of the inverse aspect ratio. Here, we used a set of discharges from the international H-mode database [20] that were analyzed when developing the ITERH-98P(y, 2) scaling (1) [16] and also T-10 H-mode discharges from the extended database [14]. Figure 6a shows the ratio H^{H} of the experimental confinement time to the time predicted by H-mode scaling (1). All the points are concentrated with some scatter about the horizontal line $H^{\mathrm{H}} = 1.0$. This is not surprising, because scaling (1) was constructed by analyzing these data.

The ratio H^{L} of the experimental confinement time to the time predicted by L-mode scaling (2) is shown in Fig. 6b for the same set of discharges as in Fig. 6a. In Fig. 6b, we can see a tendency for the points to concentrate about an inclined line. For $\varepsilon \sim 0.35$–0.4, the experimental confinement time is nearly two times higher than the time predicted by the L-mode scaling. As ε decreases, this difference decreases and, at $\varepsilon \sim 0.2$ (which corresponds to $A = 5$ and the operating conditions of the T-10), the experimental H-mode confinement time becomes close to the time calculated by the L-mode scaling. The number of discharges with a low ε in this data set is small; however, a tendency of the H^{L} factor to decrease at lower ε is observed for the entire data set under examination. This tendency shows that, as ε decreases, the confinement time in H-mode discharges approaches the time calculated by the L-mode scaling.

A similar comparison is shown in Fig. 7 for discharges from the international L-mode database [13]. This figure presents the results selected according to the rules used in [11] when deducing scaling (2) and also the result obtained in one of the early T-10 experiments [21] with the aspect ratio $R/a \approx 9$ (the large triangle in Fig. 7). The ratio H^{L} of the experimental L-mode confinement time to the time predicted by L-mode scaling (2) is plotted as a function of the inverse aspect ratio ε in Fig. 7a. The points are concentrated about the horizontal line $H^{\mathrm{L}} = 1$ because these data were used when developing scaling (2).

In Fig. 7b, the experimental confinement times in L-mode discharges are compared with the times predicted by H-mode scaling (1). At high ε (low aspect ratios), the experimental confinement times appear to be a factor of 1.5–2 lower than the times predicted by the H-mode scaling. At the same time, at high aspect ratios ($\varepsilon \le 0.2$), the confinement time in L-mode discharges is close to the time calculated by the H-mode scaling. The number of experimental points at $\varepsilon \sim 0.2$ is small. However, it can be seen that all of the points in Fig. 7b are concentrated around an inclined line, which attests that the confinement time in L-mode discharges tends toward the time predicted by the H-mode scaling at $\varepsilon \le 0.2$.

Thus, we can conclude that all the available data in the international databases testify to a tendency of the difference in the plasma confinement times in the L- and H-modes to decrease with increasing aspect ratio. To draw a more reliable conclusion on the relative behavior of confinement in these modes at aspect ratios higher than 5, additional experimental information is required.

5. CONCLUSION

A comparison of the confinement scalings for the L- and H-modes shows that the dependences of the energy confinement time on most of the parameters differ slightly in these modes, the only exception being the dependence on the aspect ratio. At low aspect ratios ($A \sim 2.5$–3.5), the energy confinement time in the H-mode is nearly twice as high as that in the L-mode. As the aspect ratio increases, this difference gradually decreases and, at aspect ratios of 5 and higher, disappears completely. This tendency, which is observed in almost all the available results from the international databases, is associated with a more rapid improvement of confinement in the L-mode as compared to the H-mode as the aspect ratio increases at a fixed minor radius.

This result is confirmed by the T-10 experiments, which demonstrated that, at the same basic discharge parameters under ECR plasma heating, the energy confinement times in the L- and H-modes turn out to be close to each other. This fact is attributed to the high aspect ratio of T-10 ($A = 5$) and can be explained without invoking the specific features of the procedure of preparing discharges in this device. It is important that L-mode confinement in T-10 coincides well with the prediction of scaling (1) for the H-mode. This result is also supported by the data from other tokamaks with a high aspect ratio.

The fact that the difference between confinement times in the L- and H-modes is mainly determined by the aspect ratio provides important information about the characteristic features of the physical processes leading to the onset of the H-mode. For a core plasma with a high aspect ratio, the confinement times in the L- and H-modes are the same. Inclusion of an outer region with a lower aspect ratio makes confinement different in these regimes. In tokamaks that have no outer regions with a low aspect ratio (devices in which the

high ratio R/a is a constructive feature), the confinement times in the L- and H-modes differ only slightly. This points to an important role of the edge plasma in the onset of the H-mode, which contradicts the hypothesis of the global improvement of the confinement in the entire plasma column during the L–H transition. These considerations can help to identify the physical mechanisms that can provide a different confinement at high values of ε.

The fact that, at high aspect ratios, the energy confinement times in the L- and H-modes become close to each other is important for designing steady-state fusion tokamak reactors and opens up prospects of using the L-mode as a basic operating regime. The possibility of using L-mode discharges with the same confinement time as in the H-mode, but with a lower temperature at the plasma periphery, with a smaller accumulation of impurities and helium, without need to overcome the power threshold for the L–H transition, and in the absence of ELMs seems to be very attractive when designing future tokamak reactors.

At present, experimental data obtained in high-aspect-ratio tokamaks are still insufficient, and additional information is needed to clarify the characteristic features and parametric dependences of plasma confinement in the L- and H-modes at high aspect ratios.

ACKNOWLEDGMENTS

We thank N.V. Ivanov and V.S. Mukhovatov for fruitful discussions. We acknowledge everyone who contributed to the international confinement databases for the possibility of working with a large amount of a thoroughly selected information. This work was supported in part by the Nuclear Science and Technology Department of the Ministry for Atomic Energy of the Russian Federation and by the Russian Foundation for Basic Research, project no. 00-15-96536.

REFERENCES

1. R. W. Conn, F. Najmabadi, and the ARIES Team, in *Proceedings of the 13th IAEA Conference on Plasma Physics and Controlled Fusion, Washington, 1990*, Vol. 3, p. 259.
2. F. Najmabadi, S. C. Jardin, M. Tillack, and the ARIES Team, in *Proceedings of the 18th IAEA Fusion Energy Conference, Sorrento, 2000*, paper IAEA-CN-77/FTP2/15.
3. I. Cook (for the SEAFP Team), Fusion Eng. Des. **30**, 171 (1995).
4. Y. Seki, M. Kikuchi, T. Ando, *et al.*, in *Proceedings of the 13th IAEA Conference on Plasma Physics and Controlled Fusion, Washington, 1990*, Vol. 3, p. 473.
5. G. Shatalov, I. Kirillov, Yu. Sokolov, *et al.*, Fusion Eng. Des. **51–52**, Part B, 289 (2000).
6. S. Nishio, S. Ueda, I. Aoki, *et al.*, in *Proceedings of the 16th IAEA Fusion Energy Conference, Montreal, 1996*, Vol. 3, p. 693.
7. Y. Murakami, K. Shinya, and S. Nishio, in *Proceedings of the 17th IAEA Fusion Energy Conference, Yokohama, 1998*, Vol. 4, p. 1263.
8. *ITER Physics Basis (Chap. 2, Sect. 3.3)*, Nucl. Fusion **39**, 2186 (1999).
9. V. V. Alikaev, A. A. Borshchegovskiĭ, V. A. Vershkov, *et al.*, Fiz. Plazmy **26**, 979 (2000) [Plasma Phys. Rep. **26**, 917 (2000)].
10. Yu. Esipchuk, V. Alikaev, A. Borshegovskij, *et al.*, in *Proceedings of the 18th IAEA Fusion Energy Conference, Sorrento, 2000*, paper IAEA-CN-77/EXP5/16.
11. G. Bracco, *Paper presented at the ITPA Meeting on Burning Plasma Transport and the Confinement Database and Modeling Group, Toki (Japan), 2001*.
12. P. N. Yushmanov, T. Takizuka, K. S. Riedel, *et al.*, Nucl. Fusion **30**, 1999 (1990).
13. S. M. Kaye and ITER Confinement Database Working Group, Nucl. Fusion **37**, 1303 (1997).
14. O. Kardaun for the International Confinement Database Working Group, in *Proceedings of the 18th IAEA Fusion Energy Conference, Sorrento, 2000*, paper IAEA-CN-77/ITERP/04.
15. Yu. D. Pavlov, Yu. N. Dnestrovskij, A. A. Borshegovskij, *et al.*, in *Proceedings of the 28th EPS Conference on Controlled Fusion and Plasma Physics, Funchal, 2001*, ECA **25A**, 1409 (2001).
16. *ITER Physics Basis (Chap. 2, Sect. 6.3)*, Nucl. Fusion **39**, 2204 (1999).
17. V. V. Alikaev, A. A. Bagdasarov, N. L. Vasin, *et al.*, Fiz. Plazmy **14**, 1027 (1988) [Sov. J. Plasma Phys. **14**, 601 (1988)].
18. V. V. Alikaev, A. A. Bagdasarov, Yu. V. Balabanov, *et al.*, in *Proceedings of the 12th International Conference on Plasma Physics and Controlled Fusion, Nice, 1988*, Vol. 1, p. 513.
19. J. P. Christiansen, J. G. Cordey, K. Thomsen, *et al.*, Nucl. Fusion **32**, 291 (1992).
20. *ITER Physics Basis (Chap. 2, Appendix A)*, Nucl. Fusion **39**, 2232 (1999).
21. V. V. Alikaev, Yu. I. Arsentiev, A. A. Bagdasarov, *et al.*, in *Proceedings of the 10th International Conference on Plasma Physics and Controlled Fusion, London, 1984*, Vol. 1, p. 419.

Translated by N.F. Larionova